Modelling and Prediction of the Effects of Dynamic Responses of Tall Buildings on an Elevator System

Submitted for the Degree of Doctor of Philosophy

At the University of Northampton

July 2016

Rafael Sánchez Crespo

Acknowledgements

The author gratefully acknowledges the financial support received from ThyssenKrupp Elevator AG and the University of Northampton during the studies of the Doctor of Philosophy.

The author would like to thank his supervisors Prof Stefan Kaczmarczyk, Prof Phil Picton, and Dr Huijuan Su.

CONTENT

List of general symbols

List of figures

List of tables

Abstract

1. INTRODUCTION 1

1.1 BACKGROUND 1

1.2 AIMS AND OBJECTIVES 4

1.3 PUBLICATIONS 4

1.3.1 Conference Publications 4

1.3.2 Report of Potential Patent 5

1.4 CONFIGURATION OF AN ELEVATOR SYSTEM 6

1.5 LITERATURE REVIEW 8

1.5.1 Rope dynamics in the elevator system 8

1.5.2 Rope impact with an obstacle 10

1.5.3 Experimental testing of rope dynamics 11

1.5.4 Measurement and monitoring of the dynamic behaviour of high-rise buildings . 12

1.5.5 Mitigation of the adverse dynamic responses of elevator ropes 13

2. METHODOLOGY 15

2.1 MATHEMATICAL MODELLING 15

2.1.1 Distributed parameter system analysis 15

2.1.2 Discretization method 16

2.2 NUMERICAL INTEGRATION TECHNIQUES 18

2.3 DAMPING ESTIMATION ON STEEL WIRE ROPES 18

2.4 VIBRATION MEASUREMENTS AND TESTING 20

3. EXPERIMENTAL SETUP, MATHEMATICAL MODEL, NUMERICAL SIMULATION, AND VALIDATION 23

3.1 EXPERIMENTAL RIG SYSTEM AND COMPONENTS 23

3.1.1 Vibration measurement and actuators 24

3.1.2 Pfeifer Drako rope properties 31

3.1.2.1 Estimation of the modal damping ratio 31

3.1.2.2 Lateral Natural Frequencies of the rope 34

3.1.2.3 Estimation of the rope modulus of elasticity 35

3.1.3 Mass attached at the end *36*
3.1.4 Steel frame properties *37*
3.1.4.1 Estimation of k_1 and k_2 ..... *38*
3.1.4.2 Determining the torsional stiffness at the support points of sections T1 and T2 *39*
3.2 DERIVATION OF THE MATHEMATICAL MODEL 45
3.3 EXPERIMENTAL VALIDATION 59
3.3.1 Free vibration analysis *60*
3.3.2 Simulation Results *63*
4. STATIONARY MODEL OF A HIGH – RISE ELEVATOR SYSTEM 74
4.1 DESCRIPTION OF THE VIBRATION MODEL 74
4.2 DERIVATION OF THE MATHEMATICAL MODEL 77
4.3 SIMULATION RESULTS 94
4.3.1 Frequency Analysis *95*
4.3.2 Mode shapes *100*
4.3.3 Response of the ropes *105*
4.3.4 Lateral response of the elevator car *112*
4.3.5 Longitudinal response of the elevator car, compensating sheave, and counterweight *114*
5. NONSTATIONARY MODEL OF A HIGH – RISE ELEVATOR SYSTEM 118
5.1 DESCRIPTION OF THE VIBRATION MODEL 118
5.2 DERIVATION OF THE MATHEMATICAL MODEL 120
5.3 SIMULATION RESULTS 130
5.3.1 Frequency Analysis *132*
5.3.2 Mode shapes *137*
5.3.3 Response of the ropes *137*
5.3.4 Longitudinal response of the elevator car, compensating sheave, counterweight *147*
5.4 AUTOPARAMETRIC RESONANCE 2:1 150
5.4.1 Lateral response of the suspension ropes *153*
5.4.2 Longitudinal response of the elevator car, compensating sheave, and counterweight *159*
6. CONCLUSIONS 162
6.1 FUTURE WORK 165

Appendix A

Orthogonality of Modes of one rope and a mass

Appendix B

Lateral Eigenvalue problem of one rope and a mass

Appendix C

Simulation Results for the experimental testing

Appendix D

Lateral Eigenvalue problem of two ropes and a mass

Appendix E

Orthogonality of Modes of two ropes and a mass

Appendix F

Coefficients for the Stationary Model of a High Rise Elevator System

Appendix G

Coefficients for the Nonstationary Model of a High Rise Elevator System

References

List of general symbols

a_{CR}, a_{CW}	Acceleration/deceleration of the elevator car and counterweight
A_v	Displacement in the lateral in plane direction
A_w	Displacement in the lateral out of plane direction
$B_{irn}(t;\tau)$	Damping coefficients that contain Coriolis and centrifugal forces that are slowly varying in time
b_1	Distance measured from the bottom landing level to the centre of the compensating sheave
b_2	Distance measured from the centre of the traction sheave to the centre of the diverter pulley
$c_{in}(t)$	Generalised coordinated in the lateral out of plane direction
d	Diameter of the Pfeifer DRAKO rope
D^{Lin}, D^{Lout}	Quadratic nonlinear coupling of the system
E_i	Modulus of elasticity of rope i^{th}
F_i^{Lin}, F_i^{Lout}	Excitation for the lateral in plane and out of plane direction
$\hat{F}_{ir}^{Lin}(\tau), \hat{F}_{ir}^{Lout}(\tau)$	Excitation for the lateral in plane and out of plane direction slowly varying in time for the ith rope
F_{CR}, F_{CS}, F_{CW}	Excitation for the elevator car, compensating sheave, and counterweight
h_0	height of the building
h_t	Position of the elevator car
h_{trav}	Height of travel
i	Subscript for the i^{th} rope represented by $i=1,2,3,4$.
j	Jerk
J_{T1}, J_{T2}	Torsional mass of sections T1, and T2
J_{eq}	Equivalent torsional mass

k_1, k_2	The equivalent spring constant represents the combined stiffness of the lift car suspension, tyre and the guide rail system for each side, in the in plane and out of plane motion.
k_{eq}	Spring of stiffness coefficient k_{eq}
$k_{\theta 1}, k_{\theta 2}$	Torsional stiffness of section T1 and T2
$\hat{k}_{irn}(t;\tau)$	Stiffness matrix that is slowly changing in time for ith rope
L	Rope length
$L_i(\tau)$	Slowly time varying length of rope i^{th}
m_i	Mass per unit length of rope i^{th}
M	Mass attached at the end of the rope termination
M_1	Mass of the elevator car
M_2	Mass of the compensating sheave
M_3	Mass of the counterweight
n_1, n_2	Number of suspension and compensating ropes
N	Number of lateral in plane and out of plane modes
$\hat{Q}$	Kinetic energy of the system
$\bar{Q}_i$	Kinetic energy density of rope i^{th}
$\bar{Q}_m$	Kinetic energy density of the rope
$q_{in}(t)$	Generalised coordinated in the lateral in plane direction
R^{Lin}, R^{Lout}	Cubic nonlinear coupling of the system
$\tilde{R}_{irn}(\tau)$	Cubic nonlinear coupling of the system slowly varying in time for the ith rope for the lateral in plane and out of plane
$S_v = A_v \sin \Omega_v t$	Kinetic excitation in the lateral in plane direction
$S_w = A_w \sin \Omega_w t$	Kinetic excitation in the lateral out of plane direction
t	Time
$T_i(x_i, t)$	Tension of rope i^{th}

U_{CR}	The dynamic displacements in the longitudinal direction of the elevator car
U_{CS}	The dynamic displacements in the longitudinal direction of the compensating sheave
U_{CW}	The dynamic displacements in the longitudinal direction of the counterweight
U_i	Dynamic displacement in the longitudinal direction of rope i^{th}
v_{CR}, v_{CW}	Velocity of the elevator car and counterweight
V_{CR}	Dynamic displacement in the lateral in plane direction of the elevator car
V_i	Dynamic displacement in the lateral in plane direction of the i^{th} rope
$\overline{V_i}$	Elastic deformations measured relative to the building motion in the lateral in plane direction of the i^{th} rope.
W_{CR}	Dynamic displacement in the lateral out of plane direction of the elevator car
W_i	Dynamic displacement in the lateral out of plane direction of the i^{th} rope
$\overline{W_i}$	Elastic deformations measured relative to the building motion in the lateral out of plane direction of the i^{th} rope.
x_i	Eulerian spatial coordinate of rope i^{th}
$\alpha_{in}(x;\tau)$	Slowly varying normal free oscillation modes of the corresponding linear undamped non stationary components in the lateral out of plane direction.
$\beta_{1n}^{Lin}, \beta_{2n}^{Lin}, \beta_{1n}^{Lout}, \beta_{2n}^{Lout}$	eigenvalues in lateral in plane and lateral out of plane direction for the suspension and compensating ropes at the car side.
ε	Rope Green strain measure
$\zeta^{Lin}, \zeta^{Lout}$	Modal damping ratio in the lateral in plane and out of plane direction

$\zeta_U, \zeta_{CR}, \zeta_{CS}, \zeta_{CW}$	Modal damping ratio in the longitudinal direction for the mass, elevator car, compensating sheave, counterweight
ξ	The lateral displacements of the structure corresponding to the top of the building at the machine room level and to the position of the elevator car and counterweight
Π	Potential energy of the system
Π_e	Cable elastic strain energy
Π_g	Gravitational energy
Π_K	Spring potential energy
τ	Slowly time scale
$\phi_{in}(x;\tau)$	Slowly varying normal free oscillation modes of the corresponding linear undamped stationary components in the lateral in plane direction.
ψ	Deformations obtained from a shape function related to the fundamental mode of a high rise building
Ω_v	External frequency of excitation lateral in plane direction
Ω_w	External frequency of excitation lateral out of plane direction
ω_{UM}	Longitudinal natural frequency of the mass
$\omega_{rr}^{Lin}, \omega_{rr}^{Lout}$	The undamped lateral in plane and out of plane natural frequencies of the rope
$\omega_{CR}(\tau), \omega_{CS}(\tau), \omega_{CW}(\tau)$	Slowly varying undamped longitudinal natural frequency of the elevator car, compensating sheave, and counterweight
$\hat{\omega}_{irr}^{Lin}(\tau), \hat{\omega}_{irr}^{Lout}(\tau)$	Slowly varying undamped lateral in plane and out of plane natural frequencies of rope i^{th}, corresponding to a length $L_i(\tau)$.

List of figures

Figure 1.1: Effect of wind in a building. (Mendis et al. 2007) 1
Figure 1.2: Traction elevator system. 6
Figure 2.1 Logarithmic decrement method 19
Figure 2.2 Frequency response of a simple structure from Gade et al. (2005) 21
Figure 3.1 Experimental rig components 24
Figure 3.2 Frequency response for piezoresistive DC sensors type 4575 from Brüel & Kjær (2015). 25
Figure 3.3 Bruel & Kjaer LAN – XI module type 3050-A-040 25
Figure 3.4 (a) Position of sensors on the mass (b) Position of sensors on the rope 11.0m away from the mass (c) Position of sensors and LVDT at the armature end/connection end with the rope 27
Figure 3.5 Diagram of a LVDT transducer from Rao (2005) 28
Figure 3.6 Diagram of the different part for the Kollmorgen electric cylinder from Kollmorgen (2014) 28
Figure 3.7 (a) Kollmorgen actuator and LVDT transducer at the excitation point (b) Portable cabinet to connect the Kollmorgen actuator and LVDT transducer 30
Figure 3.8 Control room for the experimental rig 30
Figure 3.9 Cross section of the Pfeifer Drako rope as shown in Drako (2011) 31
Figure 3.10 Band pass filtered sensor data for (a) the Lateral in plane (b) the Lateral out of plane 32
Figure 3.11 Acceleration signal from the sensor in the longitudinal direction 34
Figure 3.12 Lateral natural frequencies of the rope with a mass attached at the end of 66 kg 35
Figure 3.13 FFT spectra of the acceleration response for longitudinal natural frequency with a mass of 68 kg. Test 1 (red line), Test 2 (blue line), Test 3 (green line) 36
Figure 3.14 Mass attached at the end of the rope in the experimental test rig 37
Figure 3.15 Drawing of the mass assembly attached at the end of the rope with measured dimensions 37
Figure 3.16 Dimensions of the steel frame 38
Figure 3.17 (a) Bolt for section T1 (b) Bolts for sections T2 39
Figure 3.18 (a,b,c) Acceleration response from the accelerometers for 3 tests for section T1 bolted to the wall. (d) FFT spectrum from the acceleration response of the accelerometers for section T1 40
Figure 3.19 (a,b,c). Frequency response functions using the impact hammer test when bolted to wall section T1 40

Figure 3.20 (a,b,c) Acceleration response from the accelerometers for 3 tests for section T2 bolted to the slab. (d) FFT spectrums from the acceleration response of the accelerometers for section T2 41
Figure 3.21 (a,b,c). Frequency response functions using the impact hammer test when bolted to wall section T2 42
Figure 3.22 Acceleration response from the accelerometers for 3 tests when both beams are connected together with a bolt. (d) FFT spectrums from the acceleration response 44
Figure 3.23 Frequency response functions using the impact hammer test when both sections are bolted together 44
Figure 3.24 The model of the experimental rig 46
Figure 3.25 Equation (3.74) vs the eigenvalues 61
Figure 3.26 1st and 2nd mode shape for the lateral in plane direction 61
Figure 3.27 1st and 2nd mode shape for the lateral out of plane direction 62
Figure 3.28 Signal data after post processing in the lateral in plane and out of plane direction 64
Figure 3.29 Frequency of excitation in the lateral in plane and out of plane direction 64
Figure 3.30 Comparison of the rope displacement at the sensor attachment height from the experiment and the simulation 65
Figure 3.31 FFT spectrum of the lateral in plane displacements of the rope comparing the simulation and experimental testing 65
Figure 3.32 FFT spectrum of the lateral in plane displacements of the rope comparing the simulation and experimental testing 66
Figure 3.33 Comparison of the displacements in the lateral in plane and out of plane direction 67
Figure 3.34 Comparison of the displacements in the lateral in plane and out of plane direction between 50 seconds and 100 seconds 67
Figure 3.35 Comparison of the displacements in the lateral in plane and out of plane direction between 100 seconds and 150 seconds 68
Figure 3.36 Comparison of the displacements in the lateral in plane and out of plane direction between 150 seconds and 200 seconds 68
Figure 3.37 Comparison of the displacements in the lateral in plane and out of plane direction between 200 seconds and final time of the experiment 69
Figure 3.38 Displacement of the mass in the lateral out of plane direction 70
Figure 3.39 Displacement of the mass in the lateral in plane direction from the simulation and the experimental testing 70
Figure 3.40 Frequency of the mass of the lateral in plane displacements of the simulation and experimental testing 71

Figure 3.41 Mass displacement in the longitudinal direction comparing the response from the simulation represented by a blue line and the experimental testing represented by a black line 72
Figure 3.42 FFT spectrum over the entire time span from the longitudinal displacements of the mass of the simulation and experimental testing 72
Figure 4.1 Drawing of the full stationary elevator system.....74
Figure 4.2 Variation of frequency with the position of the elevator car (car side) 96
Figure 4.3 Variation of frequency with the position of the elevator car (car side) when comparing stiffness parameter of k_1=80 kN/m and k_1=30kN/m 98
Figure 4.4 Variation of the frequency according to the position of the car (compensating ropes at the counterweight side).....99
Figure 4.5 Variation of the frequency according to the position of the car (suspension ropes at the counterweight side) 100
Figure 4.6 The mode shape displacements of the car, compensating sheave and counterweight for case study one 101
Figure 4.7 The mode shape displacements of the car, compensating sheave and counterweight for case study two 101
Figure 4.8 The mode shape displacements of the car, compensating sheave and counterweight for case study three 102
Figure 4.9 1st and 2nd mode shapes of the system at the car side with different stiffness parameters as k_1=80 kN/m and k_1=30kN/m 103
Figure 4.10 1st and 2nd mode shapes of the system at the car side with different stiffness parameters as k_1=80 kN/m and k_1=30kN/m for case study two 104
Figure 4.11 1st and 2nd mode shapes of the compensating rope at the counterweight side for case study one 105
Figure 4.12 The mid span length displacements of the compensating rope at the car side with respect to time (a) Lateral in plane direction (b) Lateral out of plane direction for case study one comparing k1=k2=80kN/m represented as blue line and k1=k2=30kN/m represented as red line 106
Figure 4.13 The mid span length displacements of the compensating rope at the car side with respect to time (a) Lateral in plane direction (b) Lateral out of plane direction for case study two comparing k_1=k_2=80kN/m represented as blue line and k_1=k_2=30kN/m represented as red line 106
Figure 4.14 The mid span length displacements of the compensating rope at the car side with respect to time (a) Lateral in plane direction (b) Lateral out of plane direction for case study

three comparing $k_1=k_2=80kN/m$ represented as blue line and $k_1=k_2=30kN/m$ represented as red line 107
Figure 4.15 The FFT frequency spectrum of the compensating rope in the lateral in plane direction between 100 seconds and 180 seconds (a) Lateral in plane direction (b) Lateral out of plane direction for case study one 108
Figure 4.16 The FFT frequency spectrum of the compensating rope in the lateral in plane direction between 140 seconds and 180 seconds (a) Lateral in plane direction (b) Lateral out of plane direction for case study three 109
Figure 4.17 The displacements of the suspension rope at the mid span length at the car side with respect to time (a) Lateral in plane direction (b) Lateral out of plane direction for case study two comparing $k_1=k_2=80kN/m$ represented as blue line and $k_1=k_2=30kN/m$ represented as red line 109
Figure 4.18 Whirling motions of the compensating ropes at the car side for (a) case study one (b) case study two (c) case study three at the mid span length of the rope with $k_1=k_2=80kN/m$. 110
Figure 4.19 Behaviour of the compensating rope at the car side in the lateral in plane direction for case study three comparing $k_1=k_2=80kN/m$ represented as dashed blue line and $k_1=k_2=30kN/m$ represented as dashed red line 111
Figure 4.20 Behaviour of the compensating rope at the car side in the lateral out of plane direction for case study three comparing $k_1=k_2=80kN/m$ represented as dashed blue line and $k_1=k_2=30kN/m$ represented as dashed red line 111
Figure 4.21 Lateral displacements of the elevator car relative to the building structure in the lateral in plane and out of plane direction for case study one comparing stiffness parameters of $k_1=k_2=80kN/m$ represented as blue line and $k_1=k_2=30kN/m$ represented as red line 112
Figure 4.22 Lateral displacements of the elevator car relative to the building structure in the lateral in plane and out of plane direction for case study two comparing stiffness parameters of $k_1=k_2=80kN/m$ represented as blue line and $k_1=k_2=30kN/m$ represented as red line 113
Figure 4.23 Lateral displacements of the elevator car relative to the building structure in the lateral in plane and out of plane direction for case study three comparing stiffness parameters of $k_1=k_2=80kN/m$ represented as blue line and $k_1=k_2=30kN/m$ represented as red line 113
Figure 4.24 Longitudinal displacements of (a) elevator car (b) compensating sheave (c) counterweight for case study one when using a stiffness parameters of $k_1=k_2=80kN/m$ represented as blue line and $k_1=k_2=30kN/m$ represented as red line 114
Figure 4.25 Longitudinal displacements of (a) elevator car (b) compensating sheave (c) counterweight for case study two when using a stiffness parameters of $k_1=k_2=80kN/m$ represented as blue line and $k_1=k_2=30kN/m$ represented as red line 115

Figure 4.26 Longitudinal displacements of (a) elevator car (b) compensating sheave (c) counterweight for case study three when using a stiffness parameters of $k_1=k_2=80kN/m$ represented as blue line and $k_1=k_2=30kN/m$ represented as red line 115
Figure 4.27 FFT frequency spectra of (a) elevator car (b) compensating sheave (c) counterweight between the time span of 100.0 seconds – 160.0 seconds for case study one with stiffness parameters of $k_1=k_2=80kN/m$ represented as blue line and $k_1=k_2=30kN/m$ represented as red line 116
Figure 5.1 Drawing of the mathematical model taken into account. 118
Figure 5.2 The kinematic profile of the elevator car for case study one when the car is going from the bottom landing level to the top landing level with a rated velocity of *v(t)=15.00m/s* 131
Figure 5.3 The kinematic profile of the elevator car for case study two when the car is going from the bottom landing level to the top landing level with a rated velocity of *v(t)=4.00m/s* 132
Figure 5.4 Variation of frequency of the suspension ropes according to the position of the elevator car (car side) for *v(t)=15.00m/s* for case study one 134
Figure 5.5 Variation of frequency of the suspension ropes according to the position of the elevator car (car side) for *v(t)=4.00m/s* for case study two 134
Figure 5.6 Variation of frequency of the compensating ropes according to the position of the elevator car (car side) for *v(t)=15.00m/s* for case study one 136
Figure 5.7 Variation of frequency of the compensating ropes according to the position of the elevator car (car side) for *v(t)=4.00m/s* for case study two 136
Figure 5.8 1st and 2nd mode shapes of the suspension rope at the car side 137
Figure 5.9 Displacement of the suspension rope at the car side at the mid span length of the ropes in (a) Lateral in plane (b) Lateral out of plane directions when the elevator car is travelling with a rated speed of *v(t)=15.00m/s* as in case study one when the car is travelling up represented by a blue line and when going down is represented by a red line. 138
Figure 5.10 Displacement of the suspension rope at the car side at the mid span length of the ropes in (a) Lateral in plane (b) Lateral out of plane directions when the elevator car is travelling with a rated speed of *v(t)=4.00m/s* as in case study two when the car is travelling up represented by a blue line and when going down is represented by a red line 139
Figure 5.11 The FFT frequency spectrum of the suspension rope in the lateral in plane direction between 30 seconds and 50 seconds (a) Lateral in plane direction (b) Lateral out of plane direction for case study two when the elevator is travelling to the top landing level with *v(t)=4.00m/s* 140

Figure 5.12 Behaviour of the suspension rope at the car side in the lateral in plane direction for case study one comparing when the elevator car is travelling with a rated velocity of *v(t)=15.00m/s* when the car is going up represented by dashed blue line and when going down represented by dashed red line 141
Figure 5.13 Behaviour of the suspension rope at the car side in the lateral in plane direction for case study two comparing when the elevator car is travelling with a rated velocity of *v(t)=4.00m/s* when the car is going up represented by dashed blue line and when going down represented by dashed red line 141
Figure 5.14 Behaviour of the suspension rope at the car side in the lateral out of plane direction for case study one comparing when the elevator car is travelling with a rated velocity of *v(t)=15.00m/s* when the car is going up represented by dashed blue line and when going down represented by dashed red line 142
Figure 5.15 Behaviour of the suspension rope at the car side in the lateral out of plane direction for case study two comparing when the elevator car is travelling with a rated velocity of *v(t)=4.00m/s* when the car is going up represented by dashed blue line and when going down represented by dashed red line 143
Figure 5.16 Behaviour of the compensating rope at the car side in the lateral in plane direction for case study one comparing when the elevator car is travelling with a rated velocity of *v(t)=15.00m/s* when the car is going up represented by dashed blue line and when going down represented by dashed red line 144
Figure 5.17 Behaviour of the compensating rope at the car side in the lateral in plane direction for case study two comparing when the elevator car is travelling with a rated velocity of *v(t)=4.00m/s* when the car is going up represented by dashed blue line and when going down represented by dashed red line 144
Figure 5.18 Behaviour of the compensating rope at the car side in the lateral out of plane direction for case study one comparing when the elevator car is travelling with a rated velocity of *v(t)=15.00m/s* when the car is going up represented by dashed blue line and when going down represented by dashed red line 145
Figure 5.19 Behaviour of the compensating rope at the car side in the lateral out of plane direction for case study two comparing when the elevator car is travelling with a rated velocity of *v(t)=4.00m/s* when the car is going up represented by dashed blue line and when going down represented by dashed red line 146
Figure 5.20 Longitudinal displacements of (a) elevator car (b) compensating sheave (c) counterweight for case study one when the elevator car is travelling with a rated velocity of *v(t)=15.00m/s* when the car is going up represented by blue line and when going down represented by red line 147

Figure 5.21 Longitudinal displacements of (a) elevator car (b) compensating sheave (c) counterweight for case study two when the elevator car is travelling with a rated velocity of *v(t)=4.00m/s* when the car is going up represented by blue line and when going down represented by red line 148
Figure 5.22 FFT frequency spectra of (a) elevator car (b) compensating sheave between the time span of 40.0 seconds – 50.0 seconds for case study two when the elevator car is travelling at *v(t)=4.00m/s* when the car is going up represented by blue line and when going down represented by red line 149
Figure 5.23 FFT frequency spectra of (a) compensating sheave (b) counterweight between the time span of 20.0 seconds – 40.0 seconds for case study two when the elevator car is travelling at *v(t)=4.00m/s* when the car is going up represented by blue line and when going down represented by red line 150
Figure 5.24 The kinematic profile of the elevator car when the car is going from the bottom landing level to the top landing level with a rated velocity of *v(t)=2.00m/s* 152
Figure 5.25 Variation of frequency of the suspension ropes according to the position of the elevator car (car side) for *v(t)=2.00m/s* 153
Figure 5.26 Displacement of the suspension rope at the car side at the mid span length of the ropes in (a) Lateral in plane (b) Lateral out of plane directions when the elevator car is travelling with a rated velocity of *v(t)=2.00m/s* from the bottom landing level to top landing level 154
Figure 5.27 FFT frequency spectra of suspension ropes at the car side (a) Lateral in plane (b) Lateral out of plane between a time span of 40.0 seconds – 60.0 seconds when the elevator car is travelling at *v(t)=2.00m/s* when the car is going up. 155
Figure 5.28 FFT frequency spectra of suspension ropes at the car side (a) Lateral in plane (b) Lateral out of plane between a time span of 100.0 seconds – 120.0 seconds when the elevator car is travelling at *v(t)=2.00m/s* when the car is going up. 156
Figure 5.29 Displacement of the suspension rope at the car side at the mid span length of the ropes in (a) Lateral in plane (b) Lateral out of plane directions when the elevator car is travelling with a rated velocity of *v(t)=2.00m/s* from the top landing level to bottom landing level 157
Figure 5.30 FFT frequency spectra of suspension ropes at the car side (a) Lateral in plane (b) Lateral out of plane between a time span of 35.0 seconds – 45.0 seconds when the elevator car is travelling at *v(t)=2.00m/s* when the car is going down. 158
Figure 5.31 FFT frequency spectra of suspension ropes at the car side (a) Lateral in plane (b) Lateral out of plane between a time span of 90.0 seconds – 120.0 seconds when the elevator car is travelling at *v(t)=2.00m/s* when the car is going down. 159

Figure 5.32 Longitudinal displacements of (a) elevator car (b) compensating sheave (c) counterweight when the elevator car is travelling at a rated velocity of *v(t)=2.00m/s* when going up 159
Figure 5.33 FFT frequency spectra of the elevator car between the time span (a) 40.0s to 60.0s (b) 100.0s to 120.0s when the elevator car is travelling at *v(t)=2.00m/s* when the car is going up. 160

List of tables

Table 3.1 Determining the lateral modal damping ratio for the (a) Lateral in plane (b) Lateral out of plane. 33
Table 3.2 Comparison FFT and FRF for section T1 41
Table 3.3 Comparison of FFT and FRF for section T2 42
Table 3.4 Comparison of FFT and FRF of sections T1 and T2 are bolted together 45
Table 3.5 Summary of estimated experimental data to validate the mathematical model 59
Table 3.6 The first four eigenvalues obtained with equation (3.74). 60
Table 3.7 The first four linear natural frequencies when using Eq. (3.103). 62
Table 3.8 The first four natural frequencies of the rope in the lateral in plane direction using Eq. (3.104). 63
Table 3.9 The first four natural frequencies of the rope in the lateral out of plane direction using Eq. (3.105). 63

Abstract

Vibrations on a high rise building often influence all elevator components and affect the ride quality of the elevator car. The lateral and longitudinal vibrations of the suspension and compensating ropes can occur and the lateral and longitudinal vibrations at the elevator car may take place. The ropes in the elevator system can be characterized by low and high frequency modes and they are lightly damped. The elevator system in a high rise building is composed of suspension and compensating ropes, which are the pivotal components of the elevator system. An important feature of the ropes in the elevator system is that they have a time varying length. However, the rate in which the length changes can be considered as small and as a result dynamic characteristics of the system vary slowly during the elevator car travel. The design methodology of an elevator system requires a thorough dynamic analysis in order to predict the dynamic loads and to evaluate the response of the system during various operational modes. This response may be caused by a number of sources of excitation.

The main source of excitation this study is focused on is the excitation coming from the wind loading on the high rise building. Wind loading on a building structure causes high displacements at the top of the building structure, exciting all of the components of the elevator system. The main excitation from the building structure to the suspension and compensating ropes are the displacements at the machine room level. The other sources of excitation are coming from the building interface which is used to guide the elevator car and counterweight along the elevator shaft during travel. The building interface consists of guide rails and roller guides. The lateral vibration of the elevator car can result from the roller guide vibrations or due to the guide rail segments being misaligned. These various sources of excitation may lead to an adverse dynamic behaviour of the elevator system due to its nonlinear and nonstationary nature.

Due to the time varying length of the ropes in the elevator system the mass and the stiffness of the system change and consequently its dynamic characteristics such as frequencies, damping ratios and mode shapes are affected.

The aim of this research is to develop and to validate a computer model of the elevator system to predict the dynamic responses of the ropes in an elevator system due to the vibrations of a high-rise building under wind loading, when the elevator system is stationary and in motion. The three objectives of this thesis are to develop a mathematical and computer model of the elevator system to understand the behaviour of the ropes in the elevator system under the influence of the building vibrations caused by wind action, to develop an experimental programme involving a lift testing tower facilities and/or alternative tall building sites, in order to validate the computer model through experimental testing, and to develop a computer

software tool as an executable program on Windows operating system to predict the behaviour of the ropes in the elevator system based on the final mathematical models of a stationary and moving elevator system.

The experimental testing was conducted at the National Lift Tower in Northampton using an experimental rig. A set of experiments were developed and various measurements were carried out. The equations that accurately describe the motion of the mass-rope suspension system in the rig were derived. The mathematical model takes into account the stationary and nonlinear nature of the mass rope suspension system in the rig. The linear and nonlinear resonance phenomena were predicted through simulation and they were compared with the experimental results.

The equations of motion that describe the elevator system comprised of the elevator car, compensating sheave, and counterweight connected by the suspension and compensating ropes were derived. A method to account for the nonstationary and nonlinear nature of the elevator system was developed. The linear and nonlinear phenomena were observed. The nonstationary and nonlinear behaviour of the ropes in the elevator system was demonstrated through simulation. The results showed that nonlinear coupling in the lateral in plane and out of plane directions of the suspension and compensating ropes can generate modal interaction between the elevator car, compensating sheave, and counterweight. Thus, the displacements of the elevator car, compensating sheave, and counterweight can be predicted.

CHAPTER 1

1. INTRODUCTION

1.1 Background

The trend in metropolitan cities is to expand vertically instead of horizontally. More demand is applied to architects and structural engineers to design taller, safer, more economical, and aesthetic buildings. In the past great effort has been placed in the structural design of the building to be able to withstand adverse environmental loads which may cause the building to vibrate and/or collapse affecting the residents of the building at that moment in the building. Recently Kijewski-correa (2003)a; Kijewski-correa (2003)b, studied the sway and torsional response of high rise buildings in full scale monitoring projects under real wind loads in order to better understand the in-situ dynamic response of these structures and to compare design conditions with in-situ response of a high rise building. Under the action of wind, high rise buildings suffer from coupled vibrations in the alongwind, crosswind and torsional directions, see Figure 1.1. These coupled vibrations are due to the different gust patterns of wind in the windward side of the building and the turbulence at the leeward side of the building, see Figure 1.1. In many structures the crosswind and torsional response may exceed the alongwind response in terms of both serviceability and survivability designs. Also, Kwon et al. (2008); Zhou et al. (2003) developed a database and analysis procedure for the crosswind and torsional loads of wind on tall buildings.

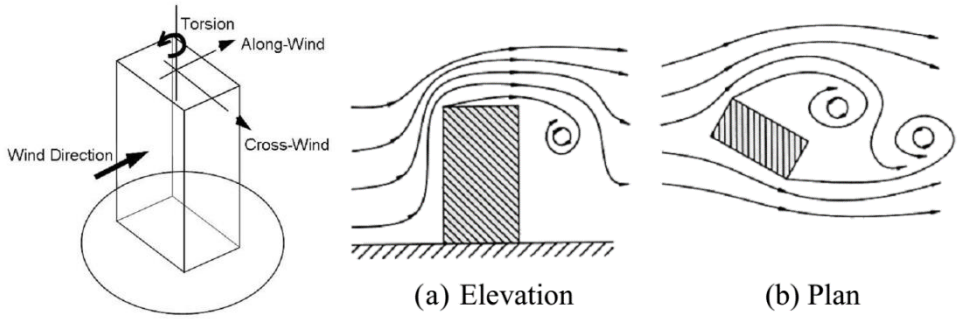

Figure 1.1: Effect of wind in a building. (Mendis et al. 2007)

Due to all of these and past efforts to better understand and analyse the behaviour of tall buildings under the action of alongwind, crosswind, and torsional wind loads, currently high rise buildings are being designed and constructed in metropolitan cities with a considerable level of safety.

There has been considerable number of studies to determine the frequency of occupant comfort in high rise buildings. According to Burton et al. (2015), if a building is vibrating at 5 milli-g is unlikely to cause significant adverse response, provided that the building motion does not occur frequently or continuously for an extended period of time. However, if a building is vibrating at 10 milli-g will be perceptible to the vast majority of occupants; this type of building may not be acceptable to some occupants.

However, inside a high rise building there is another structure that also suffers from the effects of wind and earthquakes loads on the building and this is the elevator system. The elevator system is an integral part of high rise buildings to transport the occupants in a very short period of time. This electro-mechanical system can be treated like a structure, which is supported at the top end by a concrete slab where the elevator machine is positioned to drive the elevator car up or down using the suspension means through tractive forces developed between the grooves of the traction sheave and the suspension ropes. In high rise buildings, compensating ropes are installed at the bottom of the elevator car and counterweight to take into account the transfer of mass of the suspension ropes from the car side to the counterweight side and vice versa. To control the loop of the compensating ropes below the elevator car and counterweight a compensating sheave is placed at the pit floor of the elevator shaft. The compensating sheave is constrained horizontally at the pit floor and is only permitted to move vertically. The elevator car and counterweight when traveling along the elevator shaft have a guiding interface between the building structure. Thus, the elevator motor traction sheave at the top, the compensating sheave at the bottom, and the guiding interface of the elevator car and counterweight between the building structure are the four points of contact where the elevator system is affected by the action of wind on the building and seismic action.

All building structures vibrate under the action of wind and in special circumstances when an earthquake strikes a building. Therefore, this study is focused on the analysis of the lateral vibrations of the suspension and compensation structural elements such as ropes, belts and cables and the elevator components when the suspension and compensation structural elements are excited by the displacements of the high rise building due to the wind loading on the building.

When a building vibrates at its natural frequency and this frequency matches the natural frequency of the ropes, resonance phenomena take place, that result in high amplitude motions of the rope. These high amplitudes cause the ropes to impact between them and on

the elevator shaft, which causes damage to the elevator components and disturb building residents due to the noise of each impact.

According to Strakosch (1998), if an elevator car is in the upper part of a building when the building starts to vibrate and excites the compensating ropes so that they vibrate, once the car starts to descend at full speed, centrifugal forces are induced. These forces are proportional to the square of the speed of the elevator car. As a result the centrifugal forces cause more violent vibrations of the decreasing compensating rope length when the elevator car is approaching the bottom landing level. The increased vibrations of the compensating ropes may cause serious rope or compensating sheave damage.

The new technology currently being developed by Thyssenkrupp Elevator AG (2014), will facilitate the implementation of ropeless propulsion in lift systems. However, conventional traction driven elevators will remain in dominant use. The conventional steel wire ropes used in the elevator industry has a travel height limitation up to 1200 m which is already being used to its limit, according to Drako et al. (2011). However, according to KONE (2013), advancements in rope technology are leading to a new lightweight rope made of carbon fiber core with a special high friction coating making twice the travel height limitation currently feasible.

Building vibration causes lateral in-plane, lateral out of plane, and longitudinal vibrations at the ropes which are then transferred to the car, counterweight, and compensating sheave making ride quality of the elevator car inadequate. According to Arrasate et al. (2012), lateral vibrations of the compensating ropes can be induced by vertical vibrations of the suspension ropes caused by torque ripple effects generated at the drive system of the elevator motor.

Another form of lateral excitation to the ropes results from the roller guides and guide rails, which are the guiding interface between the building and the elevator car and counterweight. The guiding interface ensures the relative position of the elevator car and counterweight along the height of travel. A misalignment of the guide rails will produce an additional form of excitation at the car which will transfer to the elevator ropes, as discussed in Andrew and Kaczmarczyk (2011).

In all of these cases, the compensating ropes are highly affected by lateral displacements of the building structure.

All of these sources of excitations may lead to an adverse dynamic behaviour of the elevator system due to its nonlinear and nonstationary nature. As a result of the varying length of the elevator ropes, according to Kaczmarczyk (2005) the mass and stiffness of the system change,

and all of its dynamic characteristics like frequencies, damping ratios and mode shapes are affected.

In order to better understand the dynamic behaviour of the elevator system, a mathematical model comprising differential equations of motion of a complete elevator system should be developed. When the equations of motion are solved an insight into the dynamic behaviour of the elevator system and its components is obtained.

1.2 Aims and objectives

The aim is to develop and to validate a computer model of the elevator system to predict the dynamic responses of ropes and cables in an elevator system due to the vibrations of a high-rise building under wind loading, when the elevator system is stationary and in motion.

In order to achieve the above aim the following objectives have been identified and accomplished:

- To develop a mathematical and computer model of the elevator system to understand the behaviour of the ropes in the elevator system under the influence of the building vibrations caused by wind action.
- To develop an experimental programme involving lift testing tower facilities and/or alternative tall building sites, in order to validate the computer model through experimental testing.

1.3 Publications

The findings of this study were published in conferences and international journals. Furthermore, a report of a potential patent was presented to ThyssenKrupp Elevator AG.

1.3.1 Conference Publications

- Sanchez Crespo, R., Kaczmarczyk, S., Picton, P., and Su, H. (2014) Modelling and Simulation of a nonstationary high-rise elevator system to predict the dynamic interactions between its components. *In: 4th Symposium on Lift and Escalator Technologies*. Northampton, UK.

- Sánchez Crespo, R. Kaczmarczyk, S., Picton, P., and Su, H. (2014) The coupled nonlinear dynamics of a lift system. *In: International Conference in Nonlinear Problems in Aviation and Aerospace ICNPAA World Congress.* Narvik, Norway.
- Sanchez Crespo, R., Kaczmarczyk, S., Picton, P., Su, H., and Jetter, M. (2013) Modelling and simulation of a high-rise elevator system to predict the dynamic interactions between its components. *In: 3rd Symposium on Lift and Escalator Technologies.* Northampton, UK.

1.3.2 Report of Potential Patent

- Sánchez Crespo, R. (2015) *Real-Time Vibration Measurements of Steel Wire Ropes in Elevator System with Embedded Fiber Bragg Gratings Sensors in a Fibre Optic Cable.* Report to ThyssenKrupp Elevator AG. Northampton: The University of Northampton.

1.4 Configuration of an elevator system

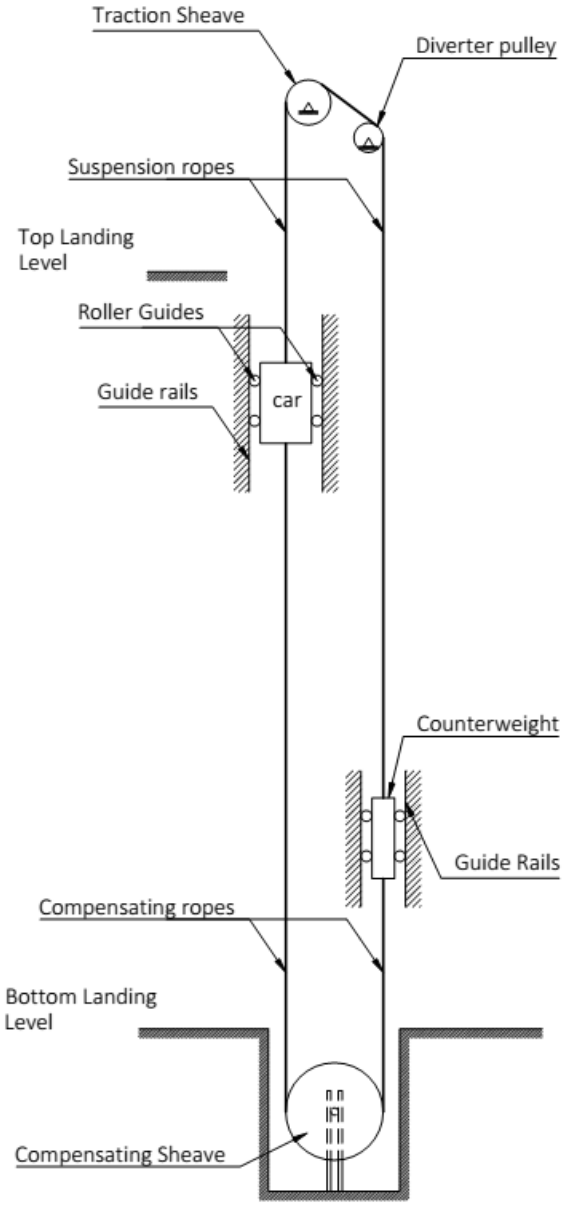

Figure 1.2: Traction elevator system.

A schematic configuration of a traction drive elevator system is shown in Figure 1.2. The elevator system consists of a traction sheave, diverter pulley, car, compensating sheave, and counterweight. The traction sheave is a part of the elevator motor and is located in the machine room of the high rise building.

The suspension ropes are connected at the upper section of the elevator car-sling assembly and pass through the traction sheave grooves and over the diverter pulley to be connected at

the top of the counterweight. The compensating ropes are connected at the bottom section of the elevator car-sling assembly and pass through the grooves of the compensating sheave to be connected at the bottom of the counterweight.

As the elevator car is travelling up and down along the elevator shaft at the car side the counterweight will be travelling in the opposite direction at the counterweight side. The mass of the counterweight is typically equal to the mass of the car-sling assembly plus 40 – 50% of the capacity of the elevator car. The car and counterweight are equipped with roller guides and are guided by rails in the elevator shaft.

1.5 Literature review

Rope dynamics has attracted interest of many researchers, especially in mine hoist ropes, cable suspension bridges, and suspended cables. In all of these areas have been the subject of many academic papers and both of their linear and nonlinear, stationary and nonstationary aspects have been researched. The work reported in this thesis is a continuation of Salamaliki-Simpson (2009) research conducted at the University. This research consisted in establishing the methodology to be used to derive the mathematical models of a stationary and nonstationary rope and mass system having a specified velocity, acceleration, and jerk according to the kinematic profile of an elevator drive control algorithm. The experimental validation of the stationary model was developed in a test rig with an aramid rope connected at one end to a shaker passing through the grooves of a pulley, which is the inclined section. From the pulley to the end termination of the rope a mass was suspended to tension the rope. The methodology developed by Salamaliki-Simpson (2009) is taken to derive the mathematical models presented in this research of the full elevator system taking into account the lateral displacements of the suspension and compensating ropes at the car and counterweight side with the interactions between the elevator car, compensating sheave, and counterweight. Therefore, the literature review section will be expanded from the publications that originated from previous research.

1.5.1 Rope dynamics in the elevator system

Kawaguti et al. (2007) studied the dynamic behaviour and passage through resonance of a cable of time varying length during its extension and retraction. The transient fluctuation of the motion amplitudes were studied and compared with the corresponding steady state motions and the results are compared with experimental results. Emory et al. (2009) analysed a simplified aramid suspension rope and elevator car system. Finite element and analytical methods were used to model the longitudinal and bending modes of the system and the results from the finite element and analytical methods were compared with experimental results. The results show that two rope sections separated by the sheave are coupled in the longitudinal motion and almost decoupled in the bending motion. Zhang et al. (2013) developed a model consisting of a rope of time-varying length and a mass attached to the end considering the longitudinal movement and flexural deformation of the rope. Kaczmarczyk et al. (2009) developed a non-stationary model of a building-compensating rope system to predict the dynamic response. The excitation is represented by a harmonic process and also as a narrow-band stochastic process. The results lead to recommendations concerning the selection of the

weight of the compensating assembly to minimize the effects of an adverse dynamic response of the system. Kaczmarczyk (2011) analysed the lateral dynamic behaviour of long non-stationary ropes, taking into account the longitudinal elastic stretching of the ropes coupled with their transverse motions which results in cubic nonlinear terms. Arrasate et al. (2013) studied the vertical vibrations caused by torque ripple generated at the elevator drive system by developing a mathematical model to validate the numerical results obtained with experimental testing. Both results show the car frame vibrates at the excitation frequencies close to the natural frequencies of the elevator system model. Kaczmarczyk et al. (2013) studied the nonlinear modal interactions taking place in a model of an aramid suspension rope system. The model consisted of an aramid suspension rope, a pulley assembly and a rigid suspended mass. The mathematical model of the system was validated with laboratory tests, the results show the nonlinear couplings may lead to adverse modal interactions in the system. Nakazawa et al. (2013) studied the effects of the compensating sheave assembly on the compensating rope winding shape around the sheave affecting the lateral vibrations of the compensating rope. An analytical model is presented to calculate the static and dynamic behaviour of the compensation rope. The model is derived as a lumped mass-spring model by using the multi-body dynamics theory. The rope bending stiffness and the contact force against the sheave are validated by several sheave weight conditions. Watanabe et al. (2013) investigated the vertical motion of the compensating sheave in an elevator dynamic model. The behaviour of the compensating sheave in different emergency cases, such as brake activation and buffer strike was studied to evaluate the maximum upward motion of the sheave. As a result, the maximum upward motion during emergency brake operation occurs in the no-loaded condition with the downward traveling near the lowest floors. Zhu and Ren (2013) first part and Ren and Zhu (2013) second part developed a spatial discretization and substructure method to accurately calculate the dynamic responses of one-dimensional structural systems, which consist of length-variant distributed-parameter components. The dependent variables of a distributed-parameter component are decomposed into boundary-induced terms and internal terms. In the first part was developed the methodology and in the second part the longitudinal, transverse, and their coupled vibrations of moving elevator cable-car systems is applied with different choices of boundary motions. Sandilo (2013), studied the vibrations of a vertical rope of changing length and applied the multiple time-scales perturbation method to construct a formal asymptotic approximations of the solutions to show the complicated dynamical behaviour of the rope. It was demonstrated that the Galerkin truncation method cannot be applied in certain type of rope problems to obtain approximations valid on a long time scales.

1.5.2 Rope impact with an obstacle

The impact of a rope without any external force and vibrating against a rigid wall, parallel to the position of the same rope at rest was studied by Amerio (1978). The set of impact points of the wall have an essential role in the study of the rope motion. Also, the elastic impact law is formulated to be used in a wider concept. Bamberger and Schatzman (1983) give an explicit formula which describes the solution of the linear elastic rope vibrating against a plane obstacle without loss of energy. Proving the dependence of the initial data and a numerical scheme is deduced from the explicit formula. Frontini and Gotusso (1990) studied a rope vibrating against an obstacle using a discrete model in the absence of obstacles. Stability conditions are analysed and numerical results are presented. Valkering (1994) analysed the impact of a string that is fixed at one end and at the other end is forced to move periodically transversely to the string. The point of impact is positioned near the string and symmetrically with respect to the endpoints. When the string impacts the obstacle the dynamics become non-linear. Hysteresis, resonance, bifurcations and chaos phenomena are analysed by changing the parameters of excitation. Han and Grosenbaugh (2004) studied the impact of a rope against a straight obstacle for 3 cases: a nearly taut string, an extensible shallow-sag cable, and an inextensible deep-sag cable. The results were accurate when compared with an analytical solution. It was found that the ratio between the initial amplitude and the equilibrium position have an important relation on how the obstacle will behave at impact. A more comprehensive model was developed by Ahn (2007), with the transverse motion of a vibrating string with fixed ends impacting a stationary rigid obstacle. The conservation of energy is also investigated. The numerical model is implemented using a numerical method solved using Fischer-Burmeister function. Additionally a rope wrapping and unwrapping around an obstacle is studied by Alsahlani and Mukherjee (2010), consisting of a string fix ends and the obstacle is located at one of the boundaries and the rope wraps and unwrap around the obstacle during vibration. However, the impacts are modelled by a series of perfectly inelastic collisions between the obstacle and adjacent segments, the unwrapping is assumed to be energy conserving. The energy during wrapping is considered to dissipate energy through inelastic collision. The obstacle serves as a passive mechanism for damping the vibrations of the rope and can be positioned anywhere to increase its effectiveness and for greater wrapping.

1.5.3 Experimental testing of rope dynamics

The majority of rope vibration measurements that has been conducted in the past have been done with piezoelectric transducers. It was of interest of this research to develop a new measuring sensor to be able to measure impact between the ropes and the elevator shaft. This literature review presents the different types of technologies that were considered for this research and discusses the difficulties encountered in the implementation of this technology.

The vibration measurements on ropes has been conducted in cable-stayed bridges using an interferometry laser system, according to Cunha and Caetano (1999). In this research a laser system was used to perform dynamic tests of the Vasco da Gama cable-stayed bridge, in Portugal, with a non-contact measuring device and with good accuracy when compared with a more conventional approach. Nassif et al. (2005) used non-contact laser Doppler vibrometer system with two types of contact sensors, which were linear variable differential transducer and geophone sensors to measure vibration in a girder of a bridge. The laser Doppler vibrometer provided measurements of vibration and deflection with good accuracy as the contact sensors and provides more versatility in the output. Kohut et al. (2013) compared two noncontact measurement methods applied to a civil structure. One system consists of high-resolution digital cameras and the second system consist of radar interferometer both measure deflections on the structure. Both systems can measure several points on a structure in a single measurement. One of the difficulties of using a laser system to measure the displacements of the ropes of the elevator system are the high amplitudes in which the ropes vibrate in the elevator shaft, which the measured point on the rope by the laser will be out of focus when it starts vibrating at high amplitudes. Also, another difficulty when using laser sensors is the limited available space between the elevator shaft walls and the elevator car when moving up or down with the elevator shaft.

Another technology considered to measure the vibrations on the ropes are high speed cameras as it is proposed in Mas et al. (2011). High speed cameras were used for measuring small vibrations in a column of a building structure after impact. Vibrations with amplitudes smaller than 0.1 mm can be registered with good accuracy. The proposed method can be applied on standard commercial cameras, thus resulting in a reliable cost-effective method. Lee and Rhee (2013) proposed a methodology to measure dynamic vibrational displacements of structures by using digital close-range photogrammetry. The displacements can be captured in various locations of the structure in 3-dimensional space, both planar and in-depth displacements relative to the cameras. The difficulties when using both high speed cameras or digital close-range photogrammetry is the short distance from the elevator shaft walls to the ropes, the

repetitive impacts of the ropes to the shaft walls, and the dark area in which the cameras will be placed. For both systems to be useful to measure the rope vibrations in the elevator shaft it would require a good source of artificial light inside the elevator shaft.

The use of fibre optic technology for vibration measurements can be employed to monitor strain. According to Martín-Pérez et al. (2010), the fibre optic sensor technology that could be used in monitoring strain of a reinforced concrete slab under service loads was based on Brillouin principle. As the result, fibre optic sensor based on Brillouin principle are capable of capturing concrete deformations and distinguish measurements between regions of tension and compression along the entire length of the sensor. Galindez-Jamioy and López-Higuera (2012) described the different applications in which fibre optic technology based on Brillouin principle has been applied to monitor loading, deflections, and material failure in civil infrastructure was used in monitoring the full length of bridges by embedding the fibre optic cable in the structure, measure deflections and fatigue during a long period of time, in rail monitoring, geotechnical structures monitoring, pipelines monitoring and material structure monitoring. The difficulties encountered with the Brillouin principle to monitor the vibrations at the ropes of the elevator system, is that at this stage is not possible to apply this principle in dynamic measurements. However, under the fibre optic technology there is the fibre Bragg principle which is used for static and dynamic measurements. Zhu et al. (2011) studied the dynamic failure signals emitted in fiber reinforced polymer stay cable using fiber Bragg gratings comparing two types of demodulation techniques for the fibre optic technology used in the study. The results of the experiment suggest that both demodulation systems may be suitable for monitoring high frequency mechanical strains in civil structures, to determine local structural damage detection. The advantage of using fiber Bragg gratings in the fibre optic cable makes it an acceptable system to measure the vibrations of the ropes in the elevator system.

1.5.4 Measurement and monitoring of the dynamic behaviour of high-rise buildings

The vibrations produced by the building along the elevator shaft and at the machine room level are the ones that give the excitation to the ropes of the elevator system. Thus, it is important to measure the displacements at different heights of the building to determine the maximum displacement and the frequency in which the building is vibrating at that moment. According to Bashor et al. (2012), developed a full scale monitoring system for buildings to evaluate the performance of dynamically sensitive structures that are under wind excitation.

The building is instrumented with four Columbia SA-107 LN high-sensitivity force-balance accelerometers that are capable of accurately measuring accelerations down to 0 Hz with a 15 V/g sensitivity. The accelerometers were installed in orthogonal pairs at opposite corners of the ceiling at the highest possible floor of each building. The data outputs of the accelerometers are sampled every 0.12s by data loggers to yield an overall system resolution of approximately 0.001 milli-g. The data logger automatically begins to capture continuous hour-long time histories of data for as long as the threshold level is exceeded. The buildings were also equipped with global positioning system to monitor its displacements, as well as wind speed sensors, according to Kijewski-Correa and Kochly (2007).

For this study global positioning system and wind speed sensors will not be required as only the displacements of the building are the ones that are affecting the ropes of the elevator system to impact on the elevator shaft and between each rope. A similar system adopted by Bashor et al. (2012) will be adopted to monitor the displacements of the high rise building at the machine room.

1.5.5 Mitigation of the adverse dynamic responses of elevator ropes

Robertson (1992) proposed the use of a retractable semaphore type or wire type limiting members positioned in the elevator shaft. The system was equipped with sensors, actuator and control unit to move the semaphore type member between the extended and retracted positions. According to Strakosch (1998), in some cases in high rise buildings a car follower rope guide is used to prevent compensation ropes and traveling cables from large-amplitude swing during high wind weather conditions. Roped 2:1, the follower rope guide travels at half the speed of the elevator car. Its purpose is to divide the free length of the hanging ropes in half, irrespective of the position of the car, thus changing the natural frequency of the ropes and cables. It is pulled upward by the elevator car and lowered by gravity of its own weight. Important factors taken into account in the design of the follower rope guide is to have sufficient weight to enable it to track properly as it rides on the car guide rails and to have proper relationship between the vertical and horizontal distances between the roller guides of the follower. The disadvantage of using a car follower system is that includes relatively high cost and the introduction of additional design members into the system.

Barker and Erlandsen (1999) designed a mechanism to control tension in compensating ropes selectively when an elevator car is parked in a critical position along the elevator shaft height.

This method is aimed at shifting the natural frequencies of the compensating ropes by increasing their tension which might not always be effective.

The application of active tendon control by Preumont and Seto (2008) could be further researched. This method has been successfully used to control vibrations in cable-stayed bridges. The tendon control of a cable structure consists of placing an actuator at one end of the cable and controlling its motion according to the control law to counteract the incoming vibrations. This method extracts the energy from the vibrating cable through axial motion.

Watanabe (2012) developed a mechanism for the elevator system which consists of rope protectors in the shaft and special emergency operation for long-period ground motion. Smith et al. (2012) designed a system and method for minimizing compensation rope vibrations by altering the natural frequency of the compensating ropes using servo actuators. The lateral vibrations of the compensating ropes may be minimized by moving the compensation sheave to adjust the tension of the compensation ropes. Smith and Kaczmarczyk (2012) proposed a shape memory alloy for dampening the vibrations in tensioned members such as ropes and cables. The frequency of the rope can be modulated by heating the shape memory alloy, thus preventing the ropes from impacting the walls of the elevator shaft. An active stiffness control of transverse vibrations of the ropes, involving the application of a longitudinal action at the rope end, is proposed by Kaczmarczyk and Picton (2012).

2. Methodology

2.1 Mathematical modelling

2.1.1 Distributed parameter system analysis

Hamilton's principle is used to derive the mathematical models and to predict the dynamic interactions between the suspension and compensating ropes in the lateral in plane, lateral out of plane, and longitudinal direction and the car, compensating sheave, and counterweight motion. The displacements are analysed in terms of the rigid body motion and the elastic deformations. Hamilton's principle can be employed to give a complete description of the dynamic behaviour on the mechanical systems. It is an integral principle which considers the entire motion of the system between the time instances t_1 and t_2. The principle considers the time integral of the difference between the kinetic and the potential with the sum of the non-conservative energies to be stationary. According to Meirovitch (2001), Hamilton principle is defined by Eq. (2.1).

$$\int_{t_1}^{t_2} (\delta\hat{Q} - \delta\Pi + \delta W_{nc})dt = 0 \tag{2.1}$$

where $\hat{Q}$, Π, and W_{nc} are the kinetic energy, potential energy, and work done by the non-conservative forces of the system respectively. Salamaliki-Simpson (2009) described the entire mass and rope suspension system based on Hamilton's principle. Therefore, the entire elevator system can be described by equation (2.1) assuming that all components are acting together as a single system due to the constraints between nearby subsystems. Additionally, the system is nonstationary, which is when the elevator car and counterweight are traveling along the elevator shaft according to the kinematic profile dictated by the drive control algorithm. The response of the system can be represented in the longitudinal, lateral in plane and lateral out of plane motions respectively for the rope as a system of partial differential equations as the following:

$$mU_{tt} + B^u U_t + K^u U + N^u + F^u = 0 \tag{2.2}$$

$$mV_{tt} + B^v V_t + K^v V + N^v + F^v = 0 \tag{2.3}$$

$$mW_{tt} + B^w W_t + K^w W + N^w + F^w = 0 \tag{2.4}$$

where

$U(x,t), V(x,t), W(x,t)$	are the dynamic displacements in the longitudinal, lateral in plane and lateral out of plane direction
x	is the Eulerian spatial coordinate and $0 \le x \le L(t)$
t	is the time
m	is the mass of the rope
$L(t)$	is the time variant length of the rope
K^u, K^v, K^w	are stiffness operators in the longitudinal, lateral in plane and lateral out of plane direction respectively
N^u, N^v, N^w	represent the nonlinear couplings in the system and are operators that acts upon displacement
B^u, B^v, B^w	are the damping operators
F^u, F^v, F^w	are the excitation functions

and $()_t$ designates partial derivatives with respect to time

2.1.2 Discretization method

The Galerkin method defined in Nayfeh and Mook (1979) as a method for converting a continuous system to a discrete problem. The method is applied to formulate the discrete mathematical models of the elevator system. The orthogonality conditions and modal shapes are applied and an ordinary differential equation that governs the temporal behaviour of the elevator system are derived, using Galerkin method the approximate solution of the system is given as

$$U(x,t;\tau) = \sum_{n=1}^{N} \gamma_n(x;\tau) p_n(t) \tag{2.5}$$

$$V(x,t;\tau) = \sum_{n=1}^{N} \phi_n(x;\tau) \mathrm{q}_n(t) \tag{2.6}$$

$$W(x,t;\tau) = \sum_{n=1}^{N} \alpha_n(x;\tau) z_n(t) \tag{2.7}$$

where $p_n(t), q_n(t), z_n(t)$ are generalised coordinated and N is the number of modes respectively, $\gamma_n(x;\tau), \phi_n(x;\tau), \alpha_n(x;\tau)$ are the linear natural modes of the system which are varying slowly in time in the longitudinal, lateral in plane and lateral out of plane direction respectively. The time varying length of the system is represented by *L(t)*. When the variation of L(t) is small over a time interval corresponding to the fundamental natural frequency of the system considered as fixed values of these parameters, the length is said to vary slowly with time, according to Kaczmarczyk (1997). The variation of *L(t)* is then observed on a slow time scale defined as $\tau = \bar{\varepsilon} T$, where T is a non-dimensional fast time scale and $\bar{\varepsilon}$ is a small parameter. Thus, the length of the rope can be represented by *L(τ)*. In order to represent the slow variability of L the fast non-dimensional time scale is defined as defined as $T = \omega_0 t$, where ω_0 is the initial fundamental natural frequency of the system and t is the time. The small parameter $\bar{\varepsilon}$ can be defined as equation (2.8).

$$\bar{\varepsilon} = \frac{v(t)}{\omega_0 L_0} \tag{2.8}$$

where L_0 is the initial lengths of the rope corresponding to ω_0. According to Kaczmarczyk (2005), for high rise elevator system the terms identified as being of the order $0(\bar{\varepsilon})$ or higher are neglected.

The frequency equations lead to an infinite sequence of eigenvalues $\beta_n^{Long}(\tau), \beta_n^{Lin}(\tau)$, and $\beta_n^{Lout}(\tau)$ that are slowly varying in time. The longitudinal, lateral in plane, lateral out of plane eigenvalues are related to the natural frequencies $\omega_n^{Long}(\tau)$, $\omega_n^{Lin}(\tau)$, and $\omega_n^{Lout}(\tau)$ and each corresponds to a value of $L(\tau)$.

When the Galerkin method is applied in the equations (2.5) - (2.7), the response of the system in the longitudinal, lateral in plane and lateral out of plane direction can be represented in the form of matrices as:

$$\dot{\vec{y}} = K(t;\tau)\vec{y} + \vec{\tilde{N}}(t;\tau) + \vec{\tilde{F}}(t;\tau) \tag{2.9}$$

where

$$\vec{y} = \left(\vec{p}^T, \vec{q}^T, \vec{z}^T, \dot{\vec{p}}^T, \dot{\vec{q}}^T, \dot{\vec{z}}^T\right) \tag{2.10}$$

is a $2(3\times N)$ dimensional modal state vector, with

$$\vec{p} = \left(p_1, p_2, p_3, ..., p_N \right)^T \tag{2.11}$$

$$\vec{q} = \left(q_1, q_2, q_3, ..., q_N \right)^T \tag{2.12}$$

$$\vec{z} = \left(z_1, z_2, z_3, ..., z_N \right)^T \tag{2.13}$$

and where dots represent differentiation with respect to time.

$K(t;\tau)$ is a slowly time variant matrix of dimension $2(3\times N)\times 2(3\times N)$, $\vec{\tilde{N}}(t;\tau)$ represents the vector of the slowly time variant nonlinear coupling terms with dimensions $2(3\times N)\times 1$ and $\vec{\tilde{F}}(t;\tau)$ is the $2(3\times N)\times 1$ dimensional external excitation vector slowly varying in time. Equation (2.9) represents a system of nonlinear differential equations with slowly varying terms. This system is a multi-degree of freedom with quadratic and cubic nonlinear terms.

2.2 Numerical Integration Techniques

The dynamics of the lift car-rope suspension system is a stiff problem. Stiff problems are the problems where the solution to be computed is slowly varying but that perturbations exist which are rapidly damped according to Söderlind et al. (2014). The numerical integration methods not designed for stiff problems are ineffective on intervals where the solution changes slowly because they use small time steps which unable to resolve fast changing solutions. These type of integrations may lead to unstable results. The numerical simulation of an elevator system is to return transient response of the system over a long time interval; the integration must be performed using a relatively large time step to cover the slow components. This time step should also be small to capture the fast components and keep the numerical integration within the acceptable boundaries according Kaczmarczyk et al. (2009), this type of problem has attracted considerable attention for research. Currently there are several numerical methods that can be implemented as Ordinary Differential Equations (ODE) solvers to give a continuous solution over the interval of integration. At each step of the integration, the ODE solver estimates the error of the solution.

2.3 Damping Estimation on steel wire ropes

Many studies have been done to estimate damping ratio in steel wire rope. Yamaguchi & Adhikari (1995) studied modal damping in structural cables. The modal damping ratio was

defined in terms of the modal potential energy ratios and the loss factors for the axial and bending deformations. Kaczmarczyk and Ostachowicz (2003) converted the lateral and longitudinal damping in steel wire ropes by equivalent viscous damping for purposes of analysis according to Inman (2001). Foss (2006) estimated modal damping ratio of wire rope isolators using quasi-static load deflection curves. The damping ratios measured from quasi-static load were compared with damping estimates from the frequency response functions. The method agreed with small amplitudes of displacement when compared with the frequency response function. Qiu and Maji (2014) estimated analytically the modal damping ratio of a carbon fibre cable through friction energy dissipation between helical wires, the stored strain energy and the initial stored energy due to the applied tension. The results obtained from the model were compared experimentally and with the logarithmic decrement method arriving to the conclusion that the accuracy of the model is affected by the manufacturing process.

The logarithmic decrement method is used in this study to determine the damping ratio of the steel wire rope used on the experimental rig in the lateral in plane and lateral out of plane directions. The logarithmic decrement method corresponds to the rate in which the amplitude of a free-damped vibration decreases. According to Rao (2005), it is defined as the natural logarithm of the ratio of any two successive amplitudes, as shown in Figure 2.1.

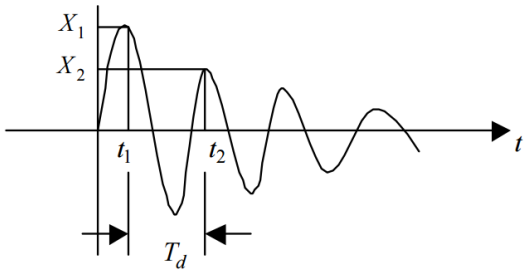

Figure 2.1 Logarithmic decrement method

The logarithmic decrement δ can be obtained using Eq. (2.14)

$$\delta = \ln \frac{x_1}{x_2} \tag{2.14}$$

The logarithmic decrement is dimensionless and is related to the dimensionless damping ratio ζ. One case of modal damping ratio is when $\zeta < 1$, thus the modal damping ratio can be obtained by solving Eq. (2.15) and this type of system is called underdamped.

$$\zeta = \frac{\delta}{2\pi} \tag{2.15}$$

For successive displacements separated by one cycle the logarithmic decrement can be obtained by solving Eq. (2.16), where *n* is an integer representing the total number of displacements used to calculate the logarithmic decrement.

$$\delta = \frac{1}{n}\ln\left(\frac{x_n}{x_{n+1}}\right) \tag{2.16}$$

Another case of modal damping ratio is when $\zeta = 1$, this happens when the system returns to the position of rest in the shortest possible time without overshooting. This type of damping is called critical damping, according to Rao (2005).

2.4 Vibration Measurements and Testing

A typical vibration measurement system is usually composed of an exciter, transducer, a signal conditioning amplifier, and a dynamic signal analysis system, Rao (2005). The exciter provides an input displacement to the rope. The two most commonly used exciters in the experimental modal testing are a shaker/actuator and an impact hammer.

To effectively estimate experimental parameters from a test rig, the modal analysis is used in this study to determine the fundamental natural frequency of a steel frame structure. According to Herlufsen (2012), modal analysis is based on measuring input/output signal responses from accelerometers. There are different techniques to determine the modal parameters but for this study a dual-channel measurement is employed, using an impact hammer. The modal parameters that describe the modes of a structure are the natural frequency, modal damping, and mode shape. According to Ewins (1994), the fundamental natural frequency and damping ratio can be obtained from any Frequency Response Function measurement on the structure. For an impact hammer excitation, each accelerometer is fixed and reflects the response of the degrees of freedom. The hammer is then moved around the structure to excite every degree of freedom. The displacements of the structure are then captured by the sensor which are converted into electric impulses and interpreted. The acceleration response from the sensor are transformed from the time domain to the frequency domain using a Fast Fourier Transform (FFT) according to Avitabile (2002). If a structure is lightly damped the frequency response can be split up into individual modes, each mode behaving as a single degree of freedom system, as shown in Figure 2.2 as shown by Gade et al. (2005). The modal parameters of a structure can be determined using Brüel & Kjaer PULSE Multi-analyzer System Type 3560 in conjunction with an impact hammer.

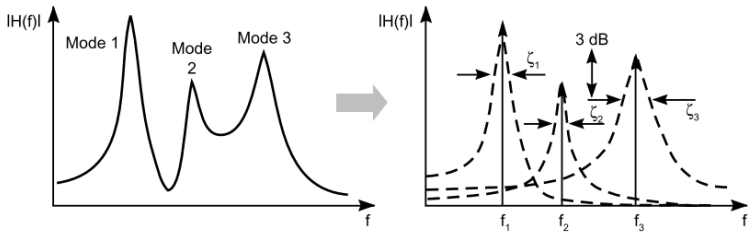

Figure 2.2 Frequency response of a simple structure from Gade et al. (2005)

Vibration measurement is useful to determine the modal parameters of a structure and to select the appropriate sensor to avoid any resonant condition or dampening of the signal. A transducer is required to transform the values of physical variables into equivalent electrical signals transducers. For the vibration measurement conducted in this research piezoelectric, piezoresistive, and linear variable displacement transducers were used. According to Rao (2005), Piezoelectric transducers work by using a natural material like quartz, tourmaline, lithium sulfate, and Rochelle salt which generate electrical charge when subjected to a deformation or mechanical stress. The electrical charge disappears when the mechanical loading is removed. Piezoresistive transducers work by measuring the change in electrical resistance of a wire using a Wheatstone bridge, potentiometer circuit, or voltage divider when a DC voltage is applied. The linear variable displacement transducer (LVDT) consists of a primary coil at the center, two secondary coils at the ends, and a magnitude core that can move freely inside the coils in the axial direction. When an AC input voltage is applied to the primary coil, the output voltage will be equal to the difference of the voltages induced in the secondary coils. The secondary coils are connected in phase opposition. When the magnetic core is in the exact middle position, the voltages in the two coils will be equal and out of phase. When the core is moved from either side of the zero position the magnetic coupling will be increased in one secondary coil and decreased in the other coil.

The piezoresistive and piezoelectric transducers were connected to portable data acquisition (DAQ) systems type 3050-A-040 from Bruel & Kjaer to acquire and store the sensor data. The LVDT transducer was connected to the Compensation Rope Test (CRT) Unit as reported by Anderson (2015). The CRT unit was then connected to the National Instruments (NI) CompactRio 9024 using NI module 9219. The signal was then converted from a voltage signal data to displacement signal data in NI LabView.

To excite the rope at different frequencies a ball screw actuator was used due to the low frequency of excitation and the applied thrust load to the rope. A ball screw actuator is a

linear actuator that translates rotational motion to linear motion with little friction. A threaded shaft provides a helical raceway for ball bearings which act as a precision screw. This type of actuator is used in high precision applications. According to Möhring & Bertram (2012), in order to avoid backlash during operation ball screw drives are preloaded. In a double nut system, preload can be applied by pre-tensioning the two nuts using spacers or by twisting the nuts against each other. The thrust is provided when a servomotor is connected at the top end. The manufacturer of the actuator used in the experimental testing was Kollmorgen (2014), which provides a drive control unit which is configured to operate the actuator. The actuator was connected to the CRT unit where the drive control unit for the actuator was positioned. The CRT unit provided the required voltage for the actuator to operate. The connection from the CRT unit for the actuator was made to the NI CompactRio 9024 using NI module 9263. The actuator was given a specified displacement and frequency using the NI LabView software which controlled the actuator to the specified parameters.

According to Anderson (2015), the configuration and design of the CRT unit with the configuration of the Kollmorgen actuator, LVDT transducer, and NI LabView software was done by Keith Anderson a ThyssenKrupp Elevator AG member.

To analyse the signal from the sensor the time signal is converted to a frequency domain. According to Inman (2001), the frequency response show one or more discrete frequencies around which the energy is concentrated. To analyse the signal in the frequency domain a frequency analyser is used by separating the energy of the signal into various frequency bands. The most common frequency analyser is a Fast Fourier Transform (FFT) which is useful for a constant bandwidth analysis.

3. Experimental Setup, Mathematical Model, Numerical Simulation, and Validation

3.1 Experimental rig system and components

In this Chapter the experimental testing components of a test rig are described in detail. The derivation of the mathematical model according to the test rig configuration setup is presented. The numerical comparison of the experimental and simulation data is shown.

The experimental testing was conducted at the National Lift Tower and is a research and testing facility located in Northampton, UK National Lift Tower (2015). The rig used in the experimental testing in this research was designed and fabricated by Kaczmarczyk (2010) to test the concept of active control theory to mitigate the vibrations of the compensating ropes. The rig was located in a void between Levels 4 and 9 of the test tower, as shown in Figure 3.1, which had a height of approximately 50.0 m. The rig was equipped with 3 cameras. The first camera was positioned at Level 4 to visualize the mass attached at the end of the rope. The second camera was positioned at the bottom of the concrete slab of Level 9 to visualize the full length of the rope during excitation. The third camera was positioned at Level 9 to capture the actuator exciting the rope. The cameras were connected to the network of the test tower. To visualize worldwide in real time all three cameras of the test rig, remote access was granted via web link when a password was provided.

The rig consisted of the following components:

a) Bruel & Kjaer AC and DC accelerometers connected to LAN-XI data acquisition hardware from Bruel & Kjaer.

b) LVDT displacement transducer model DCTH 18500C.

c) Kollmorgen actuator type EC4-AKM42G-C2R-20-25B-600-MF2 with the drive control unit type S60600.

d) National Instruments Compact Rio DAQ and control system is provided with a CRIO-9024 with the respective modules.

e) Pfeifer Drako rope.

f) Mass attached at the end.

g) Guiding rails / steel frame to restrict the motion of the mass in the lateral directions.

All of the components of the experimental test rig are discussed in full detail in this Chapter and are depicted in Figure 3.1.

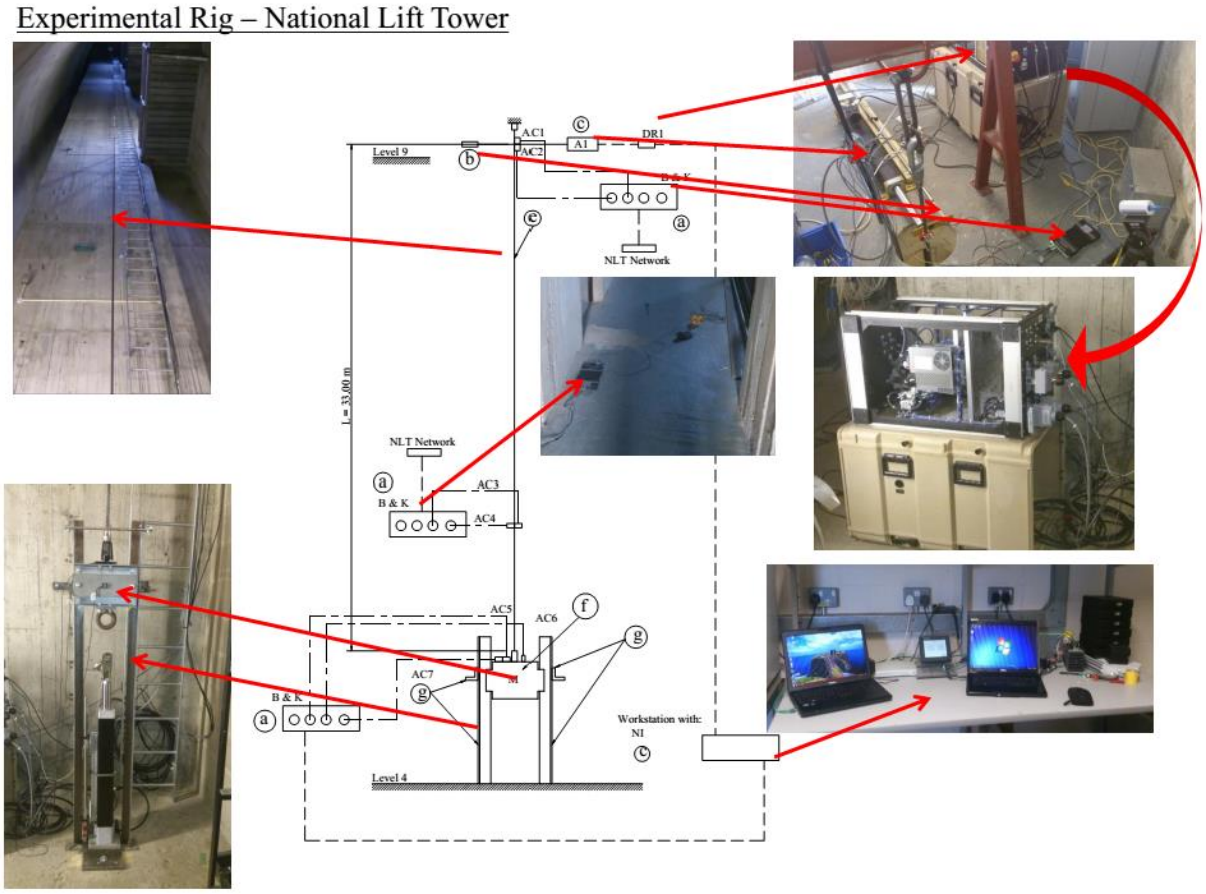

Figure 3.1 Experimental rig components

3.1.1 Vibration measurement and actuators

The Bruel & Kjaer sensors used in the experimental testing consisted of two types piezoresistive DC sensors type 4575 and piezoelectric AC sensors type 4507 B. Piezoresistive accelerometers work by measuring the electrical resistance of a material when a mechanical stress is applied, the lowest measured frequency is 0 Hz. However they have a limited high frequency response. DC sensors were used to measure low frequency vibration down to 0 Hz on the experimental rig. According to Brüel & Kjær (2015), these sensors have a nominal sensitivity of 1000 mV/g (approx. 100 mV/ms^{-2}), with a frequency range of 0 Hz to 300 Hz.

The piezoelectric accelerometer is based on piezoelectric materials, typically Quartz, which generates an electric charge output proportional to the applied force. According to Wilcoxon_Research (2009), the sensitivity of these sensors vary. Based on Brüel & Kjær

(2015), specifications the sensitivity of the sensors used for testing was 9.635 mV/g (0.9825 mV/ms^{-2}), with a frequency range of 0.1 Hz to 6 kHz.

The calibration of the sensors was done by attaching the sensors to an electrodynamic shaker from LDS model V400 series with a power amplifier from LDS model PA500 which is connected to Brüel & Kjær Pulse Front End with Brüel & Kjær Pulse Labshop software version 18.1. To control the excitation frequency of the shaker, a swept sine function was used with a frequency range from 0 Hz to 200 Hz. The typical frequency response from a piezoresistive DC sensors type 4575 is shown in Figure 3.2 according to Brüel & Kjær (2015). Similar frequency response was obtained during the calibration tests.

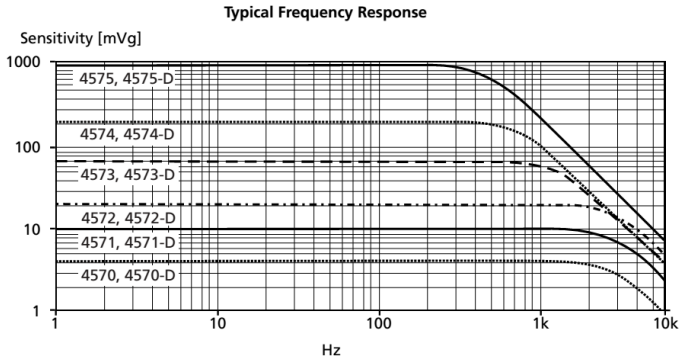

Figure 3.2 Frequency response for piezoresistive DC sensors type 4575 from Brüel & Kjær (2015).

The accelerometers were connected to Brüel & Kjær LAN-XI modules type 3050-A-040 with 4 input channels each, as shown in Figure 3.3 , with interchangeable front panel connector plate having one plate four BNC connector type UA-2100-040 and another plate LEMO connector type UA-2101-040. According to Brüel & Kjær (2013), the frequency range of this type of module is between 0 Hz to 51.2 kHz.

Figure 3.3 Bruel & Kjaer LAN – XI module type 3050-A-040

The modules have internal memory that stored the sensor data in WAV file format. This file was imported in Pulse Reflex Base 8700 – N version 18.1 for post processing the data and for exporting the post process sensor data in ASCII file format to be used in MATLAB.

To measure the vibrations at the mass in the lateral in plane, out of plane and longitudinal direction, DC sensors type 4575 were used. The sensors were attached to the mass using Bruel and Kjaer beeswax for mounting sensors, as shown in Figure 3.4 (a). At the rope, 11.0 m from the mass in the lateral in plane and out of plane direction, AC sensors type 4507B was used in each direction, as shown in Figure 3.4 (b). The sensors were attached to the rope using beeswax and tightened using plastic cable ties to avoid any detachment during testing. At the point of excitation of the actuator in the lateral in plane and out of plane direction, DC sensors type 4575 in each direction and a LVDT transducer in the lateral in plane direction was used as shown in Figure 3.4 (c).

A DC sensor was attached using beeswax, in the lateral in plane direction, in a steel metal that was positioned between the rope and the actuator to connect the LVDT transducer. In this way the LVDT would be following the displacement in the lateral in plane direction of the actuator. The distance between the LVDT and the actuator was approximately 15.0 cm, thus the bending of the steel plate can be neglected. Another DC sensor type 4575 was attached at the anchor of the rope and actuator using beeswax and tightened using a Velcro strap to avoid any detachment during testing.

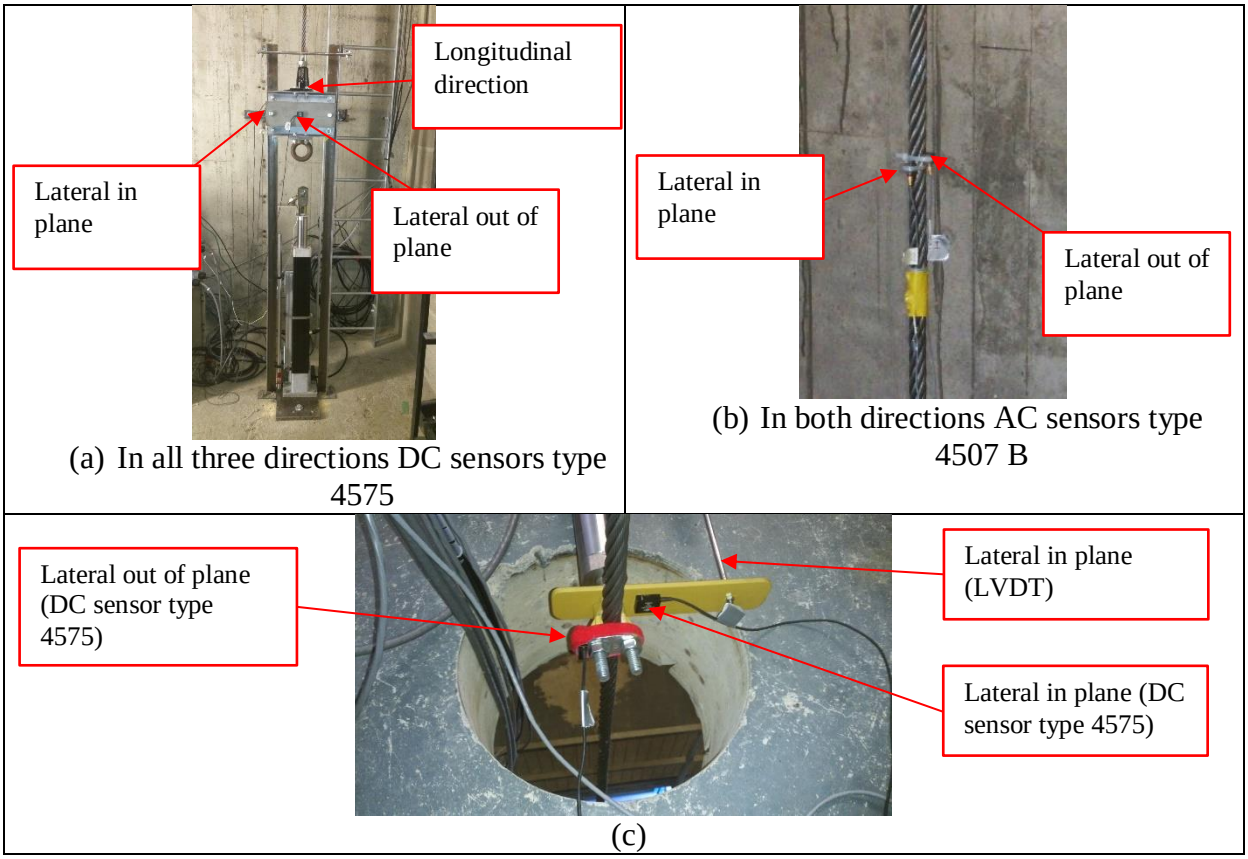

Figure 3.4 (a) Position of sensors on the mass (b) Position of sensors on the rope 11.0m away from the mass (c) Position of sensors and LVDT at the armature end/connection end with the rope

According to RDP Electronics (2014), the Linear Variable Differential Transformer (LVDT) displacement transducer used in the experimental rig was model DCTH 18500C with a measurement range of ±470mm. According to Mcdonald and Iosifescu (1998), an LVDT comprises 3 coils a primary, two secondary, and a magnetic core that can move freely inside the coils in the axial direction. When an a.c. input voltage is applied to the primary coil, the output voltage will be equal to the difference of the voltages induced in the secondary coils. This output voltage depends on the magnetic coupling between the coils and the core, which in turn depends on the axial displacement of the core. The secondary coils are connected in phase opposition so that when the magnetic core is in the exact middle position, the voltages in the two coils will be equal and out of phase. This makes the output voltage of the LVDT as zero. When the core is moved to either side of the middle position, the magnetic coupling will be increased in one secondary coil and decreased in the other coil. A diagram of an LVDT transducer is shown in

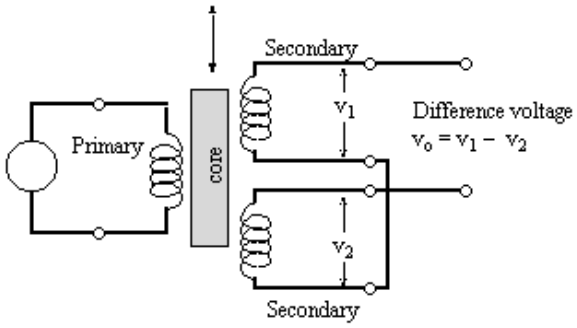

Figure 3.5 Diagram of a LVDT transducer from Rao (2005)

The actuator used as excitation at the top end of the rope was a Kollmorgen actuator type EC4-AKM42G-C2R-20-25B-600-MF2 with the drive control unit S60600. Based on Kollmorgen (2014) the actuator range are composed of different series. The EC4 series actuator is an electric cylinder that provides thrust when a servomotor is connected at the top end. The driving principle of the electric cylinder is a high precision ball screw drive which translates rotational motion to linear motion with little friction, as shown in Figure 3.6. A threaded shaft provides a helical raceway for ball bearings which act as a precision screw. This type of actuator is used in high precision applications.

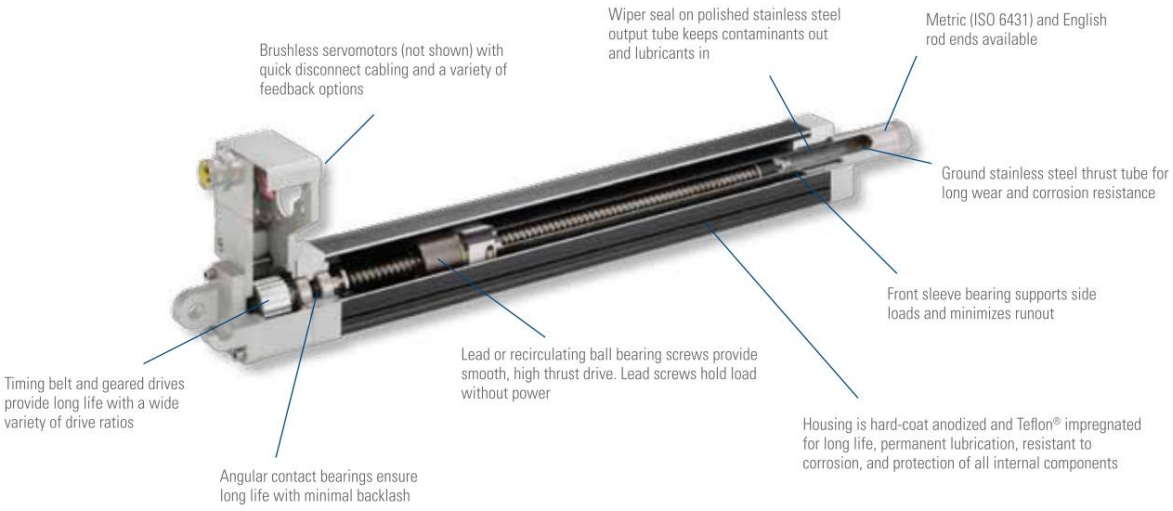

Figure 3.6 Diagram of the different part for the Kollmorgen electric cylinder from Kollmorgen (2014)

The connection between the electric cylinder and servo motor is by means of a timing belt and geared drives. The EC4 has a maximum stroke of 1500mm. The brushless servomotor attached was an AKM42G which has continuous torque of 3.51 Nm and a peak torque of 11.0

Nm according to manufacturer specifications. The AKM42G uses a drive control type AKD-X00606. The Kollmorgen drive control unit was configured using Kollmorgen Workbench software.

As reported by Anderson (2015), the Kollmorgen actuator was connected to the Compensation Rope Test (CRT) unit where the Kollmorgen drive control unit was also connected. The CRT unit provided the required voltage for the actuator to operate. The CRT unit was connected to the National Instruments (NI) CompactRio 9024 using NI module 9263 with a power supply of NI PS-15. According to National-Instruments (2010), the NI Compact Rio 9024 is an embedded real-time programmable controller that contains an industrial 800 MHz real-time freescale processor for real-time applications with 512 MB of DDR2 RAM and 4 GB storage for holding programs and logging data. The NI 9024 processor is connected to the NI Compact Rio 9111. According to National-Instruments (2014) specifications the NI Compact Rio 9111 is a reconfigurable chassis with capacity of 4 slots to insert NI modules. Based on National Instruments (2009) specifications, the NI 9263 is a four channel module with $\pm$10 V 16 Bit analog output $\pm$10 V channel to COM.

To be able to control the Kollmorgen actuator cylinder from the NI LabView software, the Kollmorgen drive control unit had to be set to remote from the Kollmorgen Handheld Machine Interface (HMI). The HMI was also connected to the CRT unit. The actuator was given a sine wave with a specified amplitude and frequency using the NI LabView software which controlled the actuator to the specified parameters. The NI LabView software tool developed by Anderson (2015), where the amplitude and frequency are specified to the actuator and the output signal from the LVDT can be compared with the prescribed sine wave of the actuator in real time during an experimental testing.

The LVDT transducer was also connected to the CRT unit which provided the required voltage. The CRT unit cables with the LVDT input signal were connected to the NI 9219 module. According to National-Instruments (2009) specifications the NI 9219 is a four channel analog input module. The input voltage signal was converted to displacement using a given factor.

The configuration and design of the CRT unit with the configuration of the Kollmorgen actuator, LVDT transducer, and NI LabView software was done by Keith Anderson a ThyssenKrupp Elevator AG member.

The prescribed sine wave was then compared with the LVDT displacement signal and shown in the NI LabView software to the user.

The configuration setup used at the top end of the rope with the Kollmorgen actuator cylinder and LVDT transducer is shown in Figure 3.7 (a) and the cabinet where the drive control unit and power supply for the actuator were placed is shown in Figure 3.7 (b).

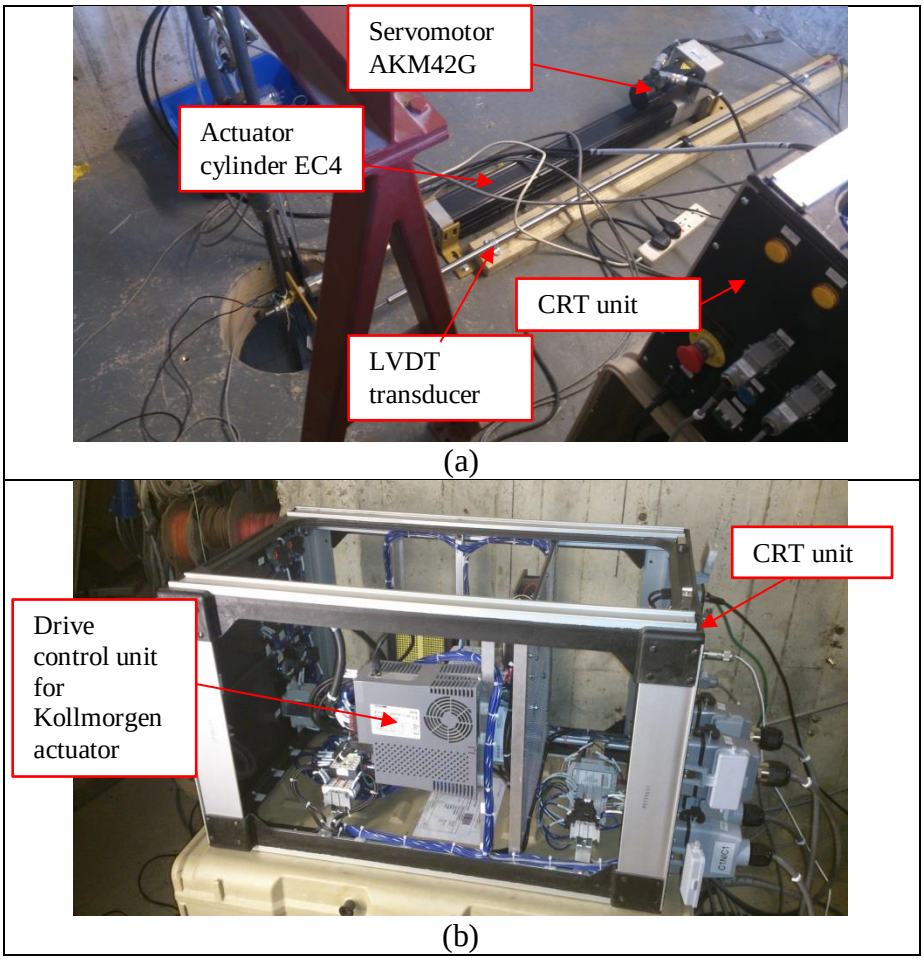

Figure 3.7 (a) Kollmorgen actuator and LVDT transducer at the excitation point (b) Portable cabinet to connect the Kollmorgen actuator and LVDT transducer

The setup at the control room for the experimental rig is shown in Figure 3.8.

Figure 3.8 Control room for the experimental rig

3.1.2 Pfeifer Drako rope properties

The Pfeifer Drako rope used in the experimental rig is the 180B compensating rope with a synthetic fibre core (SFC), according to Drako et al. (2011). The rope length was *L=32.70m*, with a diameter *d=19.10mm*, and a measured mass per unit length of *m=1.25kg/m*. Due to the synthetic fibre core and the gaps between each strand and wire, the effective area taken for the experiment is approximately half of the nominal cross section area. The nominal cross section area is $286.5mm^2$, therefore the effective cross section is $148\ mm^2$. A sample of the cross section of the Pfeifer Drako 180B is shown in Figure 3.9

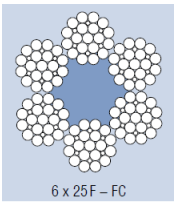

Figure 3.9 Cross section of the Pfeifer Drako rope as shown in Drako (2011)

3.1.2.1 Estimation of the modal damping ratio

The estimation of the lateral modal damping ratio with an end mass of 66 kg was determined by displacing a section of the rope. An AC sensor type 4507 B using beeswax and cable ties to secure the sensors on the rope was used to measure the displacement of the rope in the lateral in plane and out of plane direction. The sensor data was post processed in Pulse Reflex Base software using a band pass filter with the frequency range between 0.35 Hz – 0.45 Hz, shown in Figure 3.10.

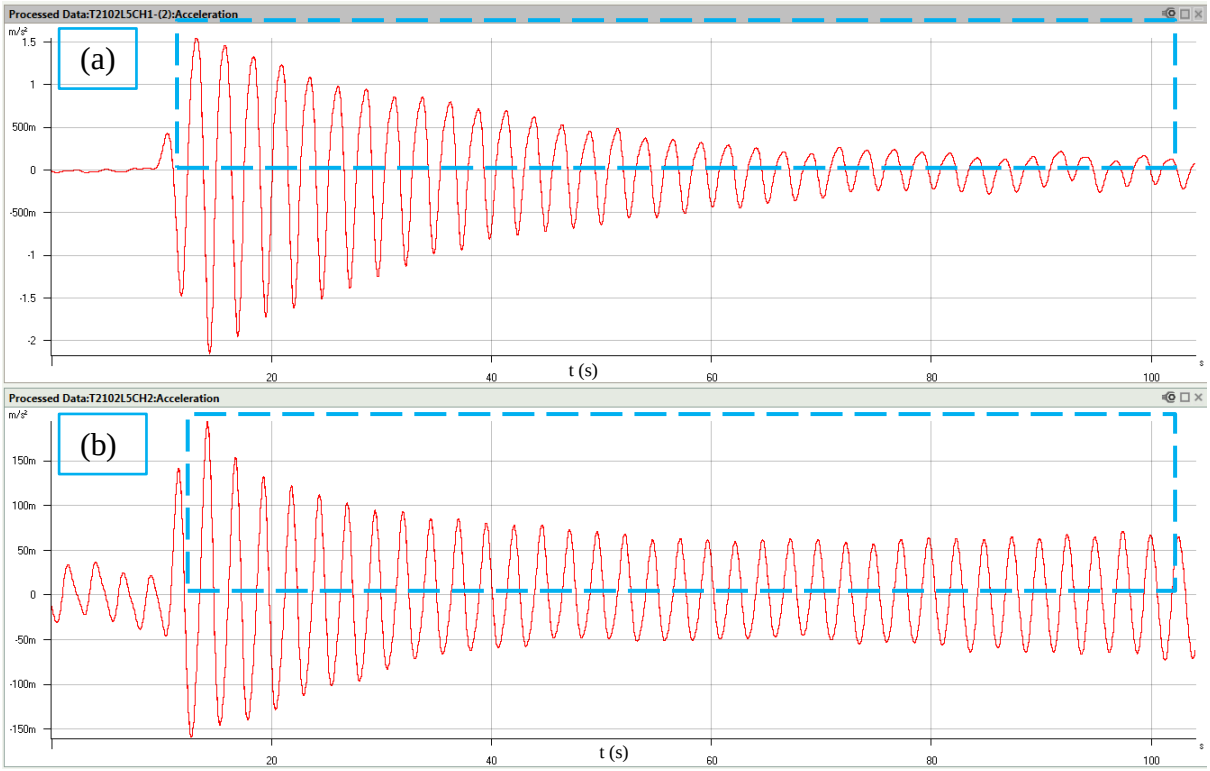

Figure 3.10 Band pass filtered sensor data for (a) the Lateral in plane (b) the Lateral out of plane

The first column in Table 3.1 (a) and (b) are shown the maximum positive acceleration peaks for the lateral in plane and out of plane direction, respectively. The acceleration values are taken from the maximum acceleration peaks inside the dashed blue square of Figure 3.10 for the lateral in plane and out of plane direction.

The second column in Table 3.1 (a) and (b) are the results when the *n* peak acceleration value is divided by the *n+1* peak acceleration value. The modal damping ratio was calculated using equations (2.16) and (2.15) when successive data from the experimental testing is available.

(a) Lateral in plane

Acceleration (m/s^2)	$\frac{x_n}{x_{n+1}}$
1.557132	1.067745705
1.458336	1.091232345
1.336412	1.065970065
1.253705	1.133169735
1.10637	1.092565436
1.012635	1.03906934

(b) Lateral out of plane

Acceleration (mm/s^2)	$\frac{x_n}{x_{n+1}}$
119.6444	1.067433935
112.086	1.092080405
102.6353	1.100460426
93.26578	1.020270465
91.4128	1.082112428
84.47625	0.996637614

0.9745596	1.093416855
0.8912974	1.011719889
0.8809725	1.072382869
0.8215093	1.102324328
0.7452519	1.04989337
0.7098358	1.122096359
0.6325979	1.139241284
0.55528	1.176243308
0.4720792	0.940651838
0.5018639	1.297904299
0.3866725	1.038661533
0.3722796	1.103795361
0.3372723	1.112220125
0.3032424	1.115873435
0.2717534	1.203645394
0.2257753	1.106772591
0.2039943	0.737747889
0.2765095	1.13522043
0.2435734	0.993942248
0.2450579	1.13958581
0.2150412	1.041552905
0.2064621	1.382867381
0.1493	1.115358555
0.1338583	0.80463564
0.1663589	0.743864841
0.2236413	1.47470452
0.1516516	1.377989474
0.1100528	0.62031842
0.1774134	1.364865447
0.129986	
$\zeta_1^{Lin} =$	**0.010891156**

84.76125	1.068061855
79.35987	1.020318068
77.77954	1.004763029
77.41083	1.08681908
71.22697	1.011346504
70.42786	1.052729399
66.90025	1.092600574
61.23029	0.977582759
62.63438	1.013652194
61.7908	1.031762994
59.88856	0.979918951
61.11583	0.966676336
63.22264	1.027808187
61.5121	1.04684822
58.75933	1.056521677
55.61583	0.902461168
61.62684	0.972424214
63.37444	1.01147433
62.65551	1.016830349
61.61845	0.946641244
65.09166	1.029384876
63.23355	0.937689904
67.43546	1.046581279
64.43404	0.911190193
70.71415	1.056419279
66.93758	1.039287223
64.4072	
$\zeta_1^{Lout} =$	**0.00305658**

Table 3.1 Determining the lateral modal damping ratio for the (a) Lateral in plane (b) Lateral out of plane

As a result the estimated lateral modal damping ratio in the lateral in plane direction was $\zeta_1^{Lin} = 0.010891156$ and in the lateral out of plane direction $\zeta_1^{Lout} = 0.00305658$. It was assumed the same lateral modal damping across all modes when doing simulation with the mathematical model.

For the estimation of the longitudinal damping ratio of the rope was determined by hitting the mass with a rubber hammer. DC sensor type 4575 was used to measure the displacements of

the rope-mass system in the longitudinal direction. The sensor was attached to the mass in the longitudinal direction using beeswax. The acceleration response without any filtering is shown in Figure 3.11

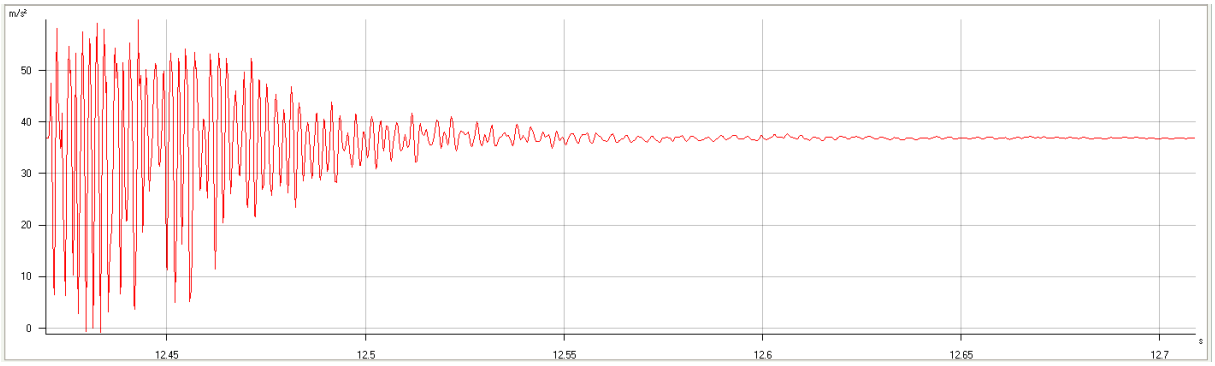

Figure 3.11 Acceleration signal from the sensor in the longitudinal direction

As it can be seen in Figure 3.11 the mass and rope system return to zero displacement in a very short period of time approximately in 0.2 seconds. According to Rao (2005), a system that returns to rest in a very short period of time usually have a critically damped ratio of 1. Therefore, the longitudinal modal damping ratio of the mass and rope system was assumed to be critically damped, $(\zeta_U = 1)$, for a case with a mass of 66 kg.

3.1.2.2 Lateral Natural Frequencies of the rope

The lateral natural frequencies of the rope were determined by displacing a section of the rope and letting the rope vibrate freely. An AC sensor type 4507 B using beeswax and cable ties to secure the sensors on the rope was used to measure the displacement of the rope in the lateral in plane and out of plane direction. The sensor data was post processed in Pulse Reflex Base software using a Fast Fourier Transform (FFT) to determine the lateral natural frequencies of the rope as shown in Figure 3.12 (using a mass of 66 kg is attached at the lower end of the rope).

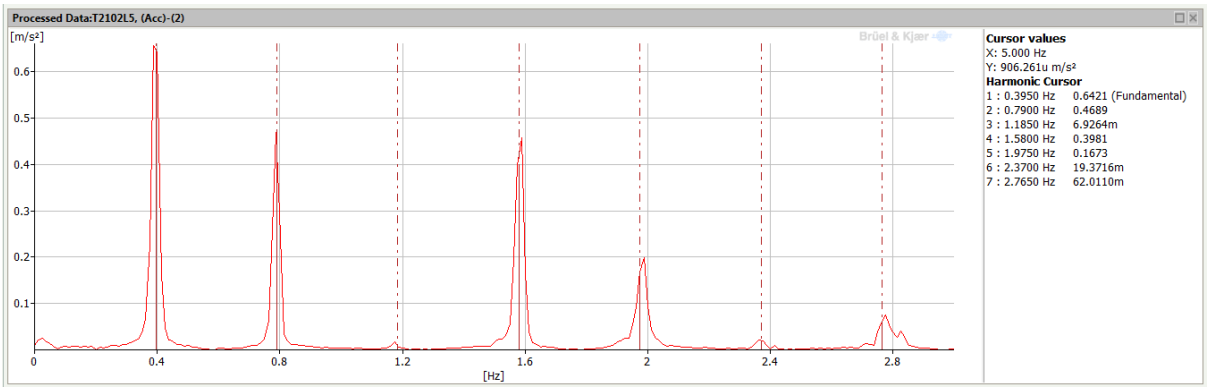

Figure 3.12 Lateral natural frequencies of the rope with a mass attached at the end of 66 kg

The fundamental natural frequency with a mass of 66 kg was identified as 0.395 Hz.

3.1.2.3 Estimation of the rope modulus of elasticity

According to Rao (2005), the governing equation of the longitudinal vibration of a bar with an end mass M attached at one end is given by equation (3.1) with a fixed end at *x=0* the boundary condition is $U(0,t)=0$.

$$EAU_x(L,t) = -MU_{tt}(L,t) \tag{3.1}$$

The longitudinal natural frequency of a bar with an end mas can be expressed as equation (3.2).

$$\omega_0^2 = \frac{EA}{LM} \tag{3.2}$$

To calculate the modulus of elasticity of a rope, the rope – mass system from the experimental rig is considered as a solid bar having a modulus of elasticity E, an effective cross sectional area A_{eff} and a length L. The mass of the rope should be taken into account as it is of considerable mass. According to Rao (2005), to take into account the mass of the spring can be accounted for by adding one third of its mass. The effective mass of the rope – mass system can be represented by equation (3.3).

$$m_e = M + \frac{mL}{3} \tag{3.3}$$

To calculate the modulus of elasticity of the rope equation (3.2) can be rewritten as equation (3.4).

$$E = \frac{\omega_0^2 L m_e}{A_{eff}} \tag{3.4}$$

The natural frequency in the longitudinal direction was determined by hitting the mass with a rubber hammer. The accelerometer was attached to the mass in the longitudinal direction of the rope. The longitudinal natural frequency of the rope – mass system was $\omega_0 = 14.88$ *Hz,* as shown in Figure 3.13.

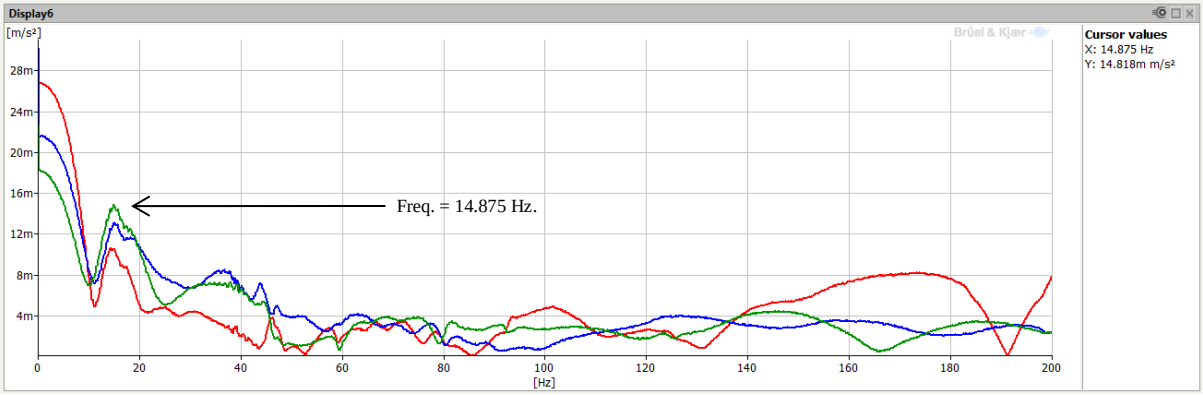

Figure 3.13 FFT spectra of the acceleration response for longitudinal natural frequency with a mass of 68 kg. Test 1 (red line), Test 2 (blue line), Test 3 (green line)

The effective mass of the rope – mass system is $m_e = 79.63$ *kg*, the length of the rope is $L = 32.70$ *m*, the effective cross sectional area of the rope is $A_{eff} = 1.433 \times 10^{-4}$ m^2. The estimated modulus of elasticity of the rope was $E = 1.5378 \times 10^{11} N/m^2$ ($EA = 2.276 \times 10^7 N$).

3.1.3 Mass attached at the end

The mass attached at the end consisted of a steel frame which two steel blocks were added to the sides. Sliding guide shoes were added to the sides of the mass, as shown on Figure 3.14. The connection to the rope was attached on the top part of the mass and a drawing with the dimensions of the mass is shown in Figure 3.14.

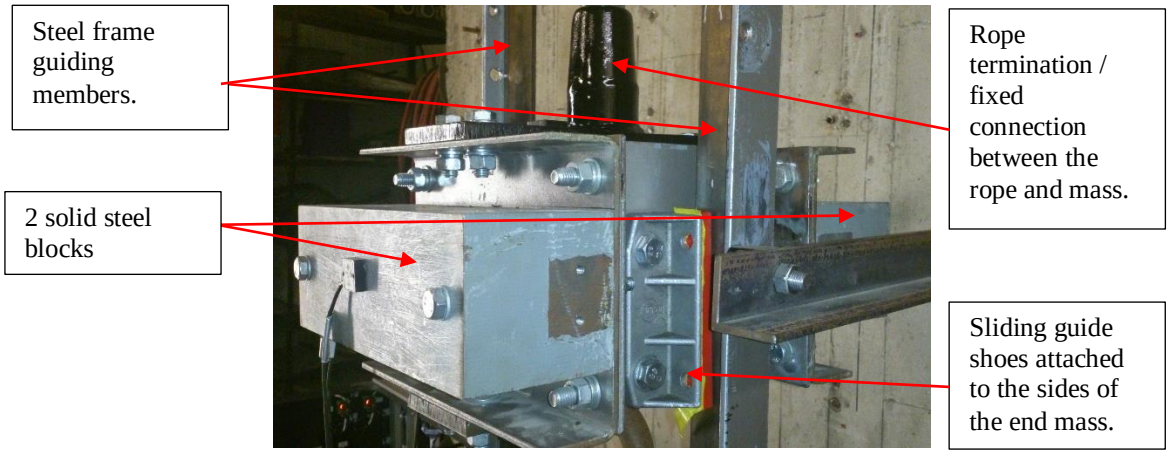

Figure 3.14 Mass attached at the end of the rope in the experimental test rig

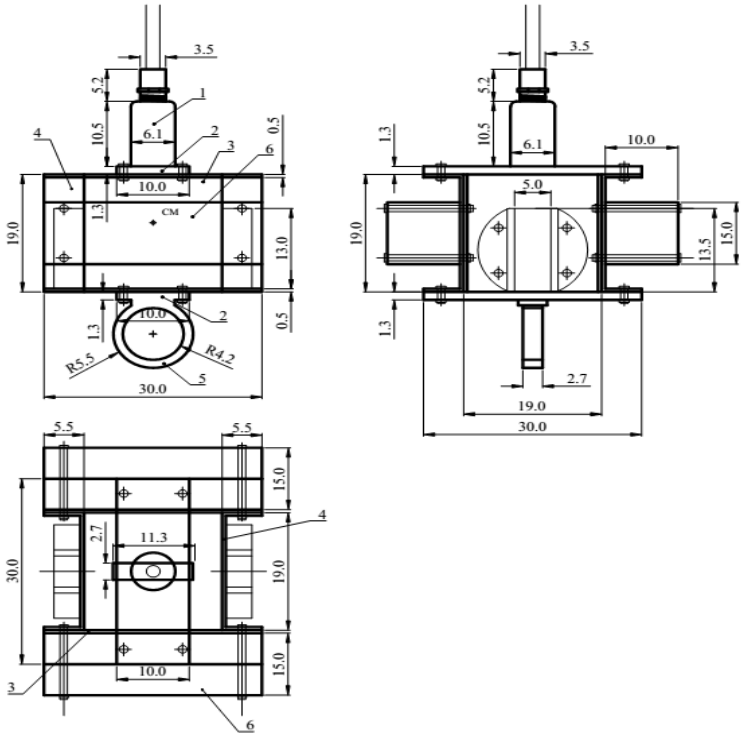

Figure 3.15 Drawing of the mass assembly attached at the end of the rope with measured dimensions

3.1.4 Steel frame properties

The steel frame consisted of four beams with the dimensions as shown in Figure 3.16. For section T1 the mass of the two beams are $m_1=3.52kg$ and $m_3=2.80kg$ with a length of $L_1=0.80m$. For section T2 the mass of the two beams are $m_2=7.42kg$ and $m_4=7.38kg$ with a length of $L_2=1.80m$.

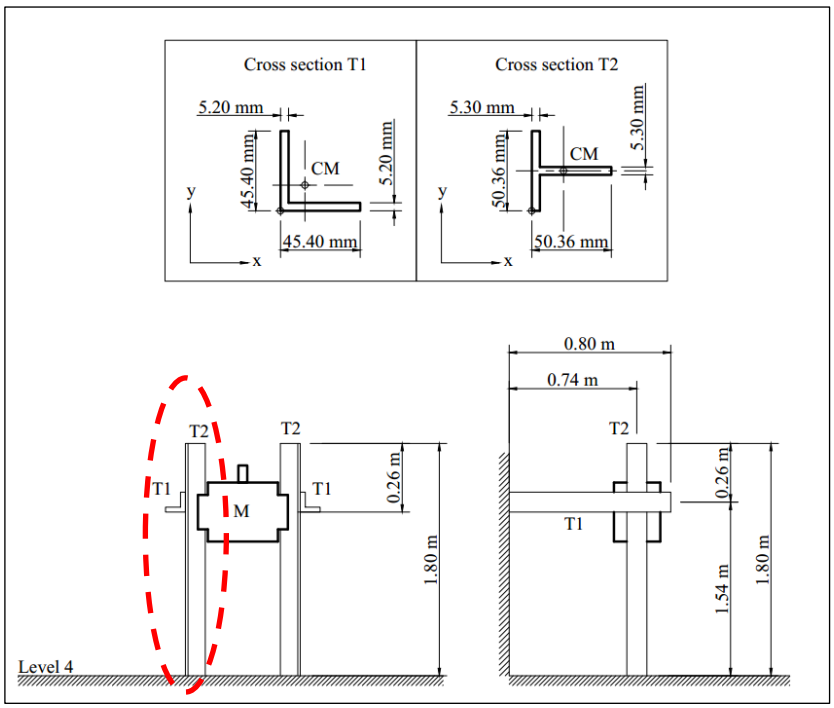

Figure 3.16 Dimensions of the steel frame

3.1.4.1 Estimation of k_1 and k_2

The attachment support to the wall and slab for sections T1 and T2 are considered as simply supported with torsional stiffness / spring, which are identified as k_1 and k_2. To determine k_1 and k_2 for the experimental test rig configuration, a preliminary approach was developed to determine all parameters of all four beams. First, all beams were individually clamped firmly from one end to a solid support to have the beam as a cantilever beam to determine the fundamental natural frequency and then to estimate the modulus of elasticity. Then each beam is anchored to the floor and wall with a single bolt, according to the support provided as it was originally. The angular natural frequency is again determined and compared with an approximate model. Afterwards, the horizontal and vertical beams of the same side are joined together by a bolt and the combined angular natural frequency is determined and compared with an approximate model.

Beams with flexible supports such as torsional (rotatory) supports with translational supports were studied by Silva et al. (2015) and Silva and Maia (2011), a beam is attached a rotatory mass (disc) at the end, the Euler Bernoulli equation was used to determine the mode shapes of the beam taking into account the flexibility of the supports by finding Rayleigh's quotient. Maiz et al. (2007) studied an Euler Bernoulli beam carrying multiple masses with

translational and rotary support ends taking into account the rotatory inertia of the mass was studied. A comparison was made when the beam has only translational supports and when having translational and torsional supports and the natural frequencies of the beam decrease when the torsional stiffness was introduced. A tapered beam with flexible supports considering as translational and rotational were studied by Rosa and Auciello (1996) and Auciello (1996) considering varying linearly the cross-section inertia of the beam the differential equation of the beam is solved using Bessel functions.

3.1.4.2 Determining the torsional stiffness at the support points of sections T1 and T2

Sections T1 and T2 were attached to the wall or slab with one bolt at the support end as a result it was not perfectly fixed or pinned, as it is shown in Figure 3.17 (a,b). Two Bruel & Kjaer DC accelerometers type 4575 were attached to the beam using beeswax. The two DC accelerometers were connected to a Bruel & Kjaer data acquisition system module type 3050-A-040. The beam was hit ones with a rubber hammer to excite the beam at the fundamental natural frequency.

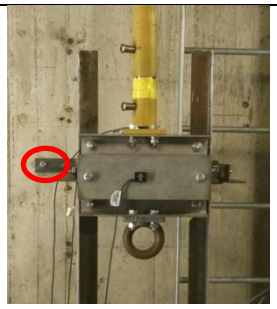

(a)

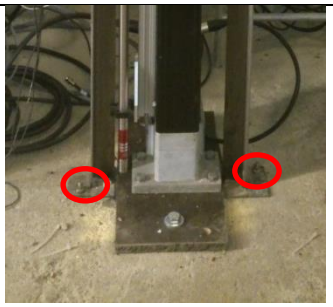

(b)

Figure 3.17 (a) Bolt for section T1 (b) Bolts for sections T2

Section T1 was bolted to the wall without being bolted to section T2. Section T1 was struck with a hammer and the acceleration response for three tests are shown in Figure 3.18(a,b,c). The section T1 was struck with a hammer and the FFT spectrum from the three tests are shown in Figure 3.18 (d). The Frequency Response Functions (FRF) when using the impact hammer test section T1 is bolted to the wall are shown in Figure 3.19 (a,b,c). A table comparing both the FFT and the FRF tests is shown in Table 3.2.

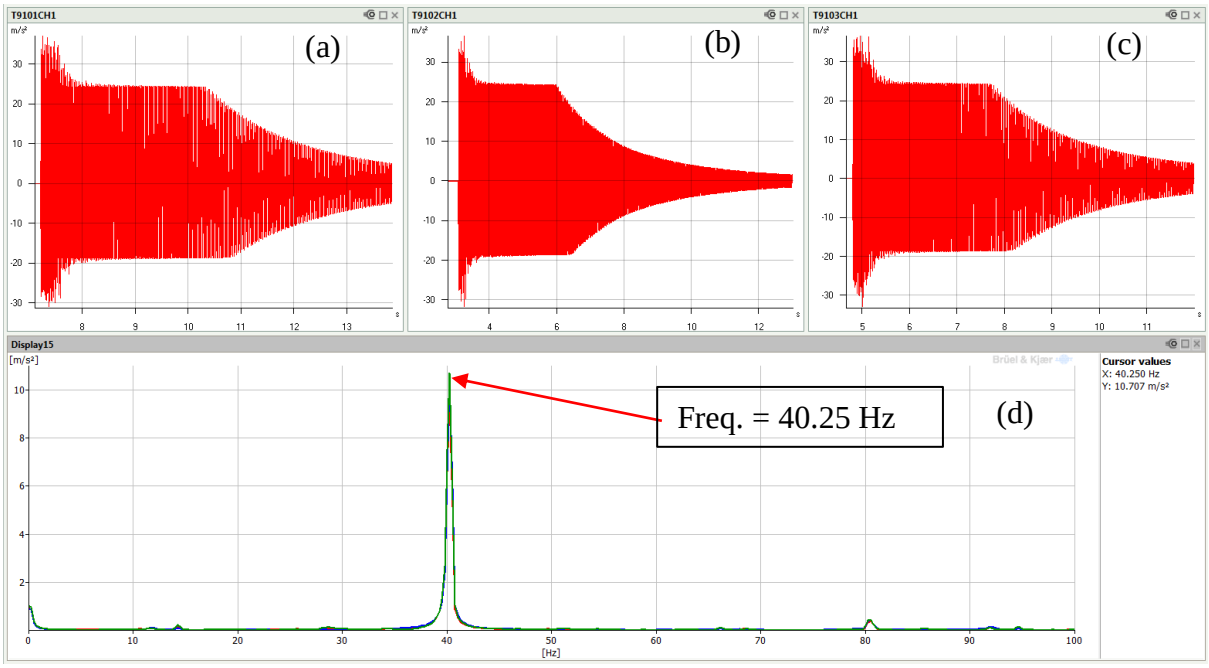

Figure 3.18 (a,b,c) Acceleration response from the accelerometers for 3 tests for section T1 bolted to the wall. (d) FFT spectrum from the acceleration response of the accelerometers for section T1

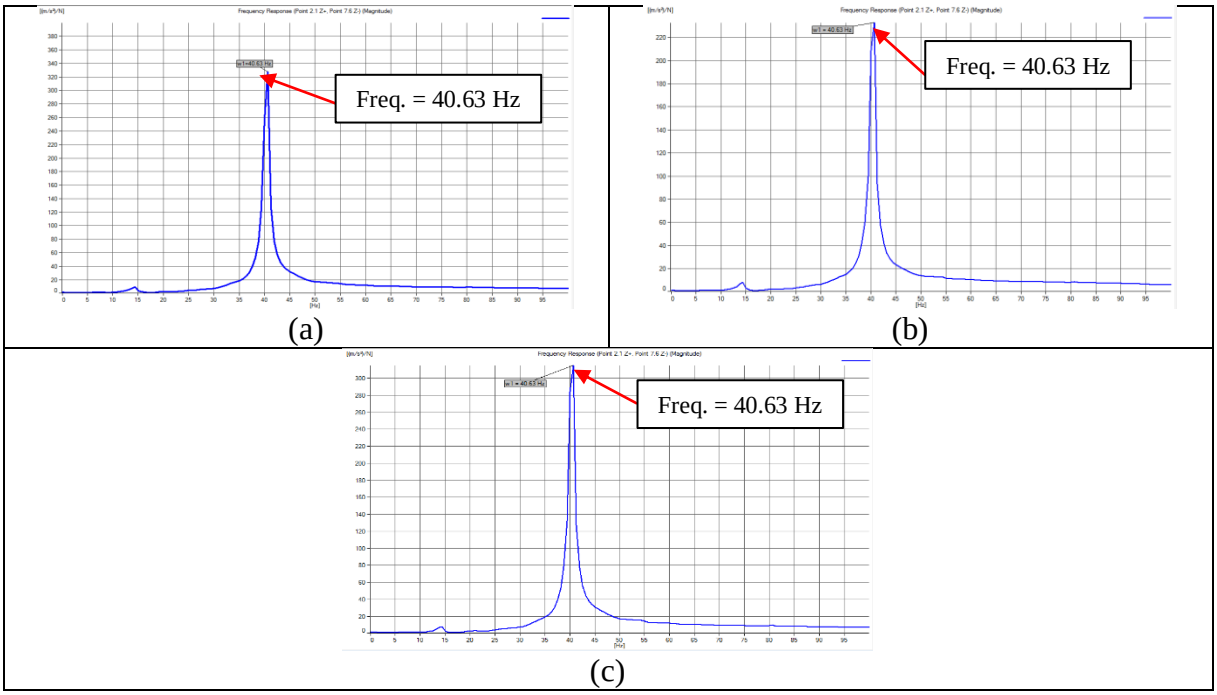

Figure 3.19 (a,b,c). Frequency response functions using the impact hammer test when bolted to wall section T1

Beam 1 Cross Section T1	Natural Frequency ω (Hz)	Average Natural Frequency ω (Hz)
From FFT spectrum	40.25	40.44
From FRF	40.63	

Table 3.2 Comparison FFT and FRF for section T1

The beam was considered as a rod of length L_1 and mass m_1, with axis of rotation at the end of the rod, where the mass moment of inertia is calculated using equation (3.5). The torsional stiffness at the support end is calculated using equation (3.6) as $k_{\theta 1}=4.848x10^4 Nm$.

$$J_{T1} = \frac{m_1 L_1^2}{3} \tag{3.5}$$

$$k_{\theta 1} = \left(2\pi\omega_{r1}\right)^2 J_{T1} \tag{3.6}$$

Section T2 was bolted to the slab without being bolted to section T1. Section T2 was struck with a hammer and the acceleration response from the sensors are shown in Figure 3.20 (a,b,c) and the FFT spectrum from the three tests is shown in Figure 3.20 (d). The Frequency Response Functions (FRF) is shown in Figure 3.21 (a,b,c) when using the impact hammer test on section T2 bolted to the slab. A table comparing both FFT and FRF test are shown in Table 3.3.

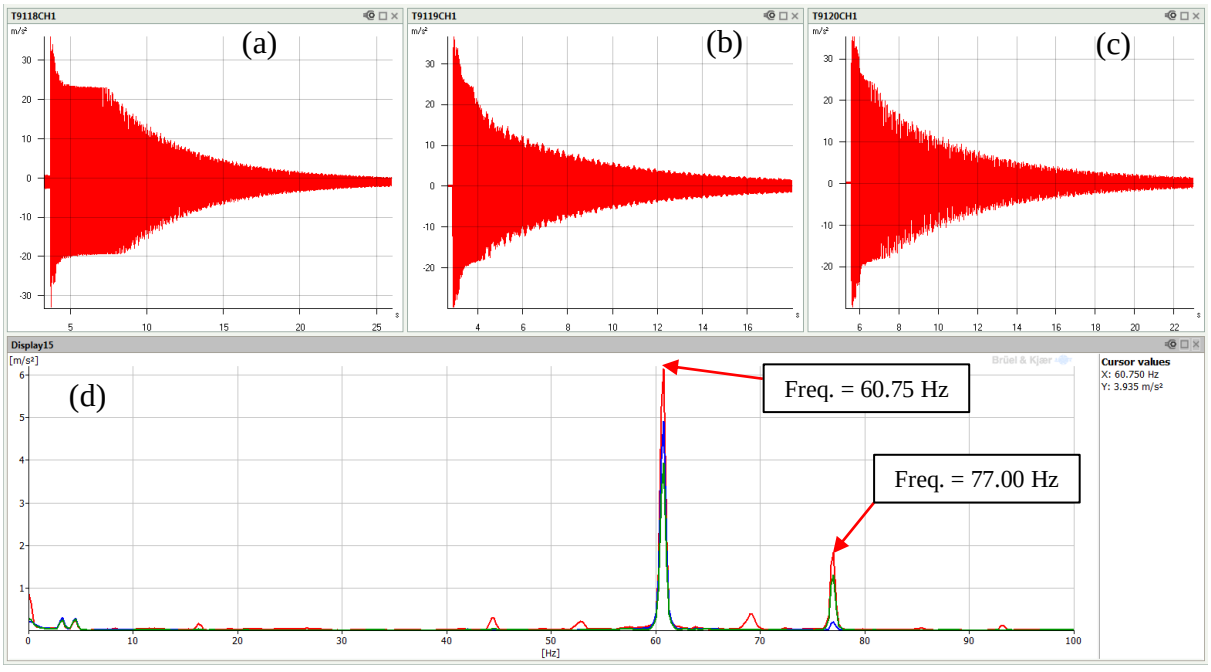

Figure 3.20 (a,b,c) Acceleration response from the accelerometers for 3 tests for section T2 bolted to the slab. (d) FFT spectrums from the acceleration response of the accelerometers for section T2.

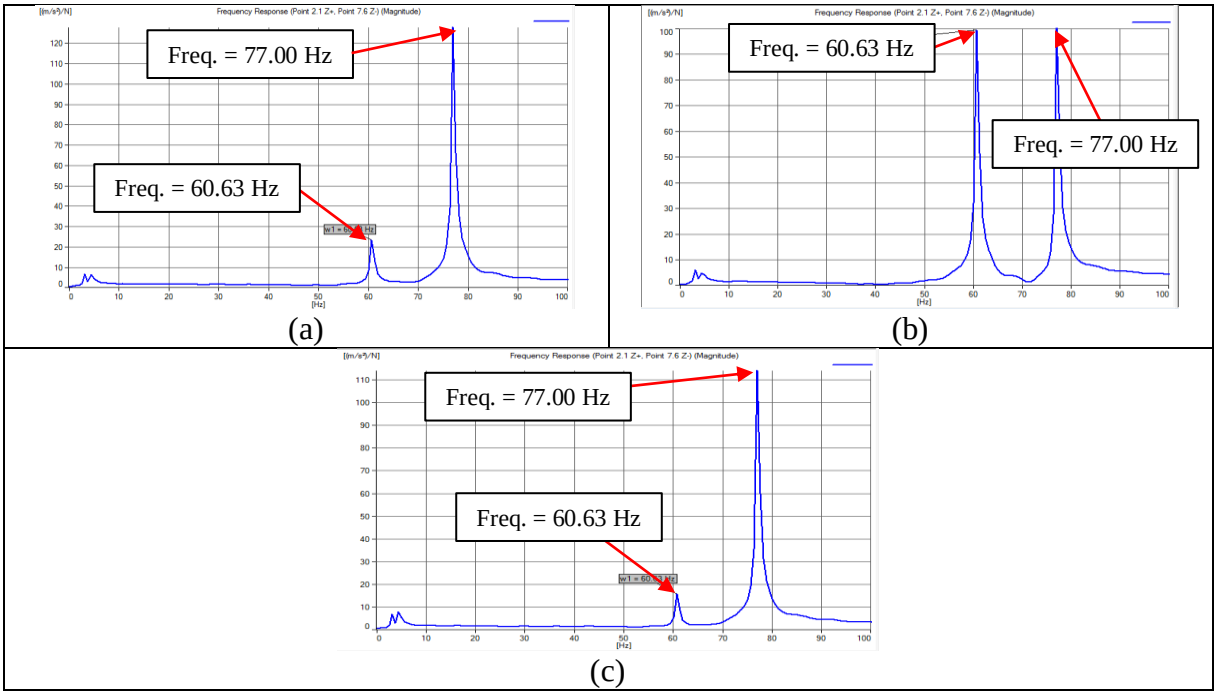

Figure 3.21 (a,b,c). Frequency response functions using the impact hammer test when bolted to wall section T2

Beam Section T2	Natural Frequency ω (Hz)	Average Natural Frequency ω (Hz)
From FFT spectrum	60.75	60.69
From FRF	60.63	

Table 3.3 Comparison of FFT and FRF for section T2

The second peak shown in Figure 3.20 and Figure 3.21 according to the frequency response function is the second natural frequency of the beam with torsional spring at the support end.

The beam was considered as a rod of length L_2 and mass m_2, with axis of rotation at the end of the rod, where the mass moment of inertia is calculated using equation (3.7). The torsional stiffness is calculated using equation (3.8) as $k_{\theta 2}=1.1653x10^{6}Nm$.

$$J_{T2} = \frac{m_2 L_2^2}{3} \tag{3.7}$$

$$k_{\theta 2} = \left(2\pi\omega_{r2}\right)^2 J_{T2} \tag{3.8}$$

When both sections are connected with a bolt as shown in Figure 3.16 (circled in red). To determine the natural frequency when both sections are bolted together can be determine using equation (3.9).

$$\omega_\theta = \sqrt{\frac{k_{eq}}{m_{eq}}} \tag{3.9}$$

The equivalent mass is determined by summing the kinetic energy as shown in equation (3.10).

$$\frac{1}{2} J_{T1} \dot{\theta}_{T1}^2 + \frac{1}{2} J_{T2} \dot{\theta}_{T2}^2 = \frac{1}{2} m_{eq} \dot{\theta}_{eq}^2 \tag{3.10}$$

The angular displacements can be converted into linear displacements by using the following transformations $\theta_{T1} = \frac{x}{L_1}$ and $\theta_{T2} = \frac{x}{L_2}$. Equation (3.10) can be rewritten as equation (3.11).

$$m_{eq} = \frac{J_{T1}}{L_1^2} + \frac{J_{T2}}{L_2^2} \tag{3.11}$$

Similarly the equivalent stiffness is obtained by summing the potential energy and is shown in equation (3.12).

$$k_{eq} = \frac{k_{\theta 1}}{L_1^2} + \frac{k_{\theta 2}}{L_2^2} \tag{3.12}$$

The fundamental frequency of the combined beam was $\omega_\theta = 54.99 Hz$, according to Eq. (3.9).

The equivalent linear stiffness estimated using equation (3.12), was $k_{eq} = 4.354x10^5 N/m$.

From the experimental testing when the beams are struck with a hammer the acceleration response from the sensors are shown in Figure 3.22 (a,b,c). The sensors were attached as close as possible where both are connected using beeswax. The FFT spectrum from the three tests is shown in Figure 3.22 (d). The Frequency Response Function (FRF) is shown in Figure 3.23 (a,b,c), when using the impact hammer test with both sections bolted together. A table comparing both test results are shown in Table 3.4.

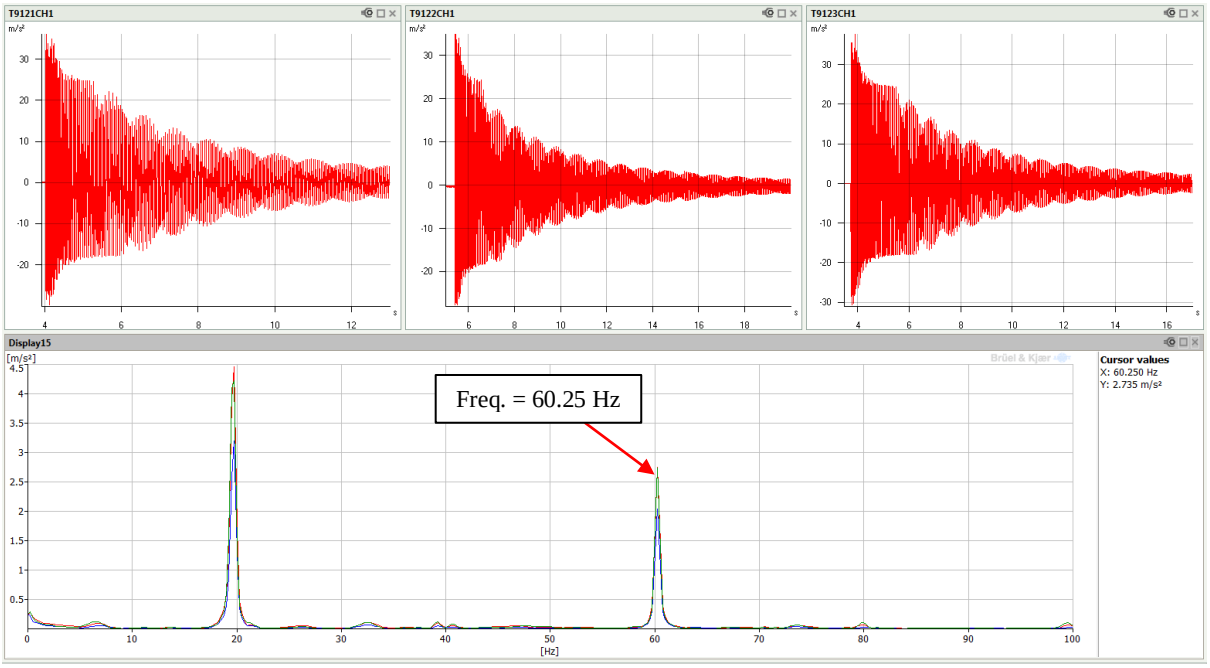

Figure 3.22 Acceleration response from the accelerometers for 3 tests when both beams are connected together with a bolt. (d) FFT spectrums from the acceleration response

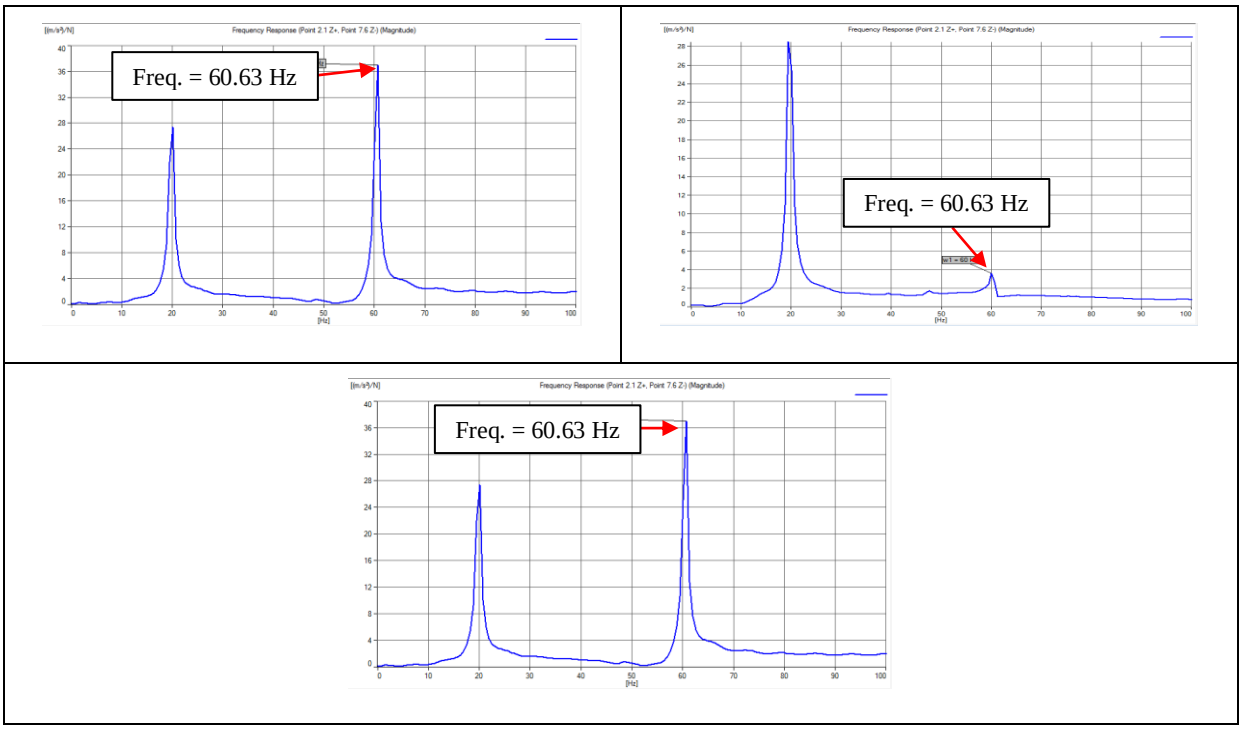

Figure 3.23 Frequency response functions using the impact hammer test when both sections are bolted together

The first prominent peak in Figure 3.22 and Figure 3.23 was approximately 20.0 Hz which is approximately equivalent when only the stiffness of section T1 is taken into account as shown in equation (3.13) with the equivalent mass, which is $\omega_{\theta 1} = 14.79Hz$.

$$\omega_{\theta 1} = \sqrt{\frac{k_{\theta 1}}{L_1^2 m_{eq}}} \tag{3.13}$$

Sections T1 – T2 connected	Natural Frequency ω (Hz)	Average Natural Frequency ω (Hz)
From FFT spectrum	60.25	60.44
From FRF	60.63	

Table 3.4 Comparison of FFT and FRF of sections T1 and T2 are bolted together

The error when comparing the estimated fundamental natural frequency of the combined beam was $\omega_{\theta} = 54.99Hz$ with the experimental frequency of $\omega_{\exp} = 60.44Hz$ was 9.91%, which shows a good agreement with the measured value.

3.2 Derivation of the mathematical model

The model of the experimental rig is shown in Figure 3.24. It consists of a vertical suspension rope of length L and a mass per unit length m, modulus of elasticity *E*, and effective cross section area *A*. The rope is fixed at the top end to a support and at the bottom end is a mass *M*. The mass is constrained to move by a steel frame structure in the longitudinal direction and in the lateral in plane direction. The equivalent linear stiffness in the lateral in plane direction is represented by k_{eq} which was deducted in section 3.1.4.1. The mass is constrained to move in the longitudinal direction by sliding guide shoes shown in Figure 3.14. The response of the rope is subjected to displacements at the top represented by $S_v(t)$ and $S_w(t)$ in the lateral in plane and out of plane directions.

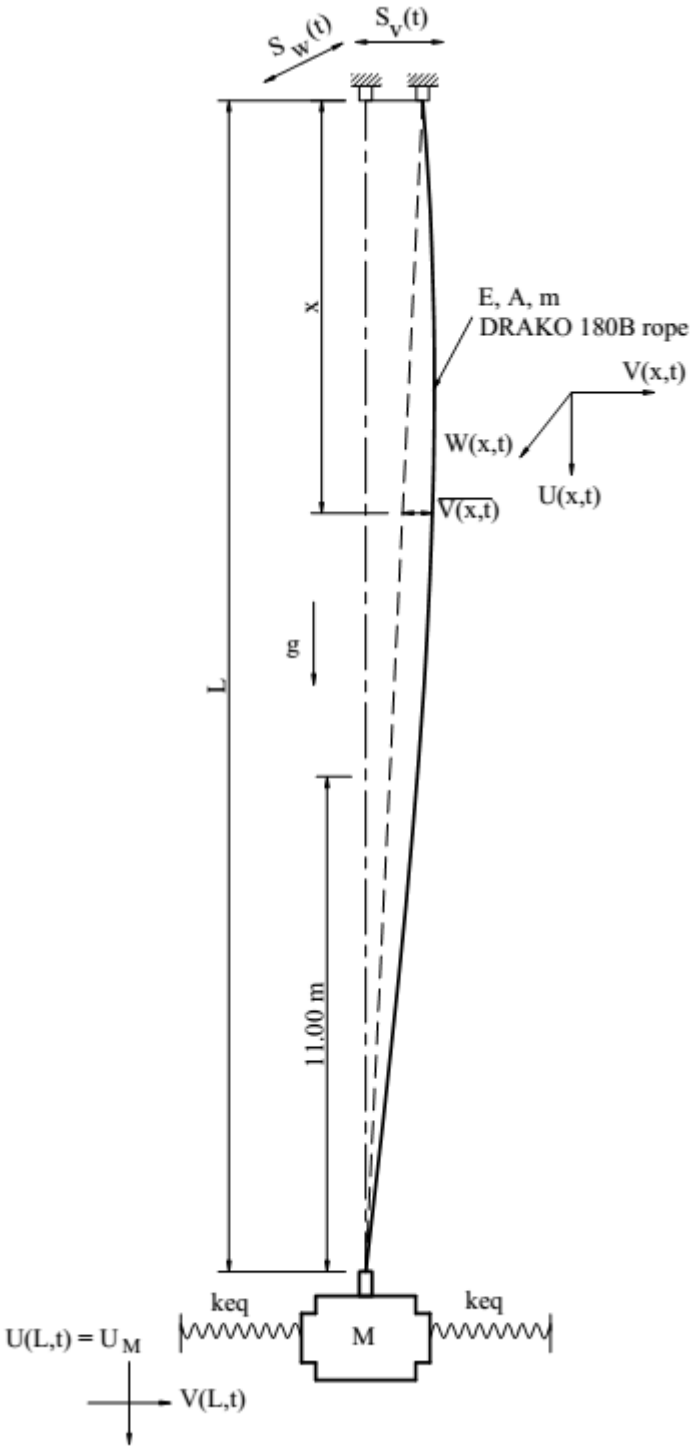

Figure 3.24 The model of the experimental rig

To develop the mathematical model the following assumptions were taken into account:

a) The rope has a constant modulus of elasticity *E*, constant cross sectional area *A*, constant mass per unit length *m*.

b) The spatial coordinate *x* is measured from the top support.

c) Damping of the rope and mass is considered.

d) The lateral damping of the rope in all modes is equal to the first lateral modal damping ratio.

e) The longitudinal damping of the mass across all modes is equal to the critical modal damping ratio.

f) Lateral in-plane *V(x,t)*, lateral out of plane *W(x,t)*, and longitudinal *U(x,t)* displacements of the rope are considered.

g) The longitudinal displacements of the mass U_M, the lateral in plane displacements of the mass *V(L,t)* of the rope are considered.

h) Equations (3.14) and (3.15) represent displacements applied to the rope at the top support in the lateral in plane and out of plane directions. The amplitudes in the lateral in plane and out of plane directions are represented by A_v and A_w, respectively. The frequency of excitation in the lateral in plane and out of plane direction are represented as λ_v and λ_w, respectively.

$$S_V(t) = A_V \sin(\lambda_V t) \tag{3.14}$$

$$S_W(t) = A_W \sin(\lambda_W t) \tag{3.15}$$

i) Elastic strain measure of the rope given in terms of Green's symmetric strain tensor as equation (3.16) where the expression $()_x$ denotes partial derivatives with respect to x.

$$\varepsilon = U_X + \frac{1}{2}\left(V_X{}^2 + W_X{}^2\right) \tag{3.16}$$

j) The displacements of the rope relative to the configuration of the rope when it is stretched by the structure motion is represented by $\bar{V}(x,t)$ and $\bar{W}(x,t)$.

k) The constant *g* is the acceleration of gravity which is equal to 9.81 m/s^2.

l) The rope length *L* is constant.

m) The mass at the bottom considered as a point mass which is constrained to vibrate in the lateral in plane direction *V(L,t)* and in the longitudinal direction U_M.

n) The longitudinal natural frequencies of the rope are higher than the lateral natural frequencies of the rope. Thus, the longitudinal inertia of the rope is neglected.

o) The bending stiffness of the rope is neglected.

p) The rope model is a nonlinear string model.

Hamilton's principle is used to derive the equations of motion. According to Meirovitch (2001), Hamilton's principle is one of the most powerful variational principle of mechanics, from which the equations of motion of a continuous system are derived. The Hamilton's principle is an integral principle which means that it considers the entire motion of a system between time t_1 and t_2. The instantaneous configuration of the system is described by n generalized coordinates $q_1, \ldots, q_n$, which corresponds to a particular point in the spatial coordinates. As time evolves, the system point moves in a configuration space, tracing out a curve. This curve describes the path of motion of the system. Thus Hamilton's principle can be defined as equation (3.17):

$$\int_{t_1}^{t_2} (\delta\hat{Q} - \delta\Pi + \delta W_{nc})dt = 0,\ \delta q_k = 0,\ k = 1,2,...,n,\ t = t_1, t_2 \tag{3.17}$$

where $\hat{Q}$, Π and W_{nc} denote the kinetic energy, the potential energy and the work due to non-conservative forces acting upon the system, respectively.

The work done by the nonconservative forces is neglected so that $\delta W_{nc}(x,t) = 0$ between t_1 and t_2 which are the initial and final time. The virtual work of the nonconservative forces in this mathematical model represents the virtual work of damping forces which are considered as modal damping ratio.

The total potential energy Π is given by the following equation

$$\Pi = \Pi_e + \Pi_g + \Pi_K \tag{3.18}$$

In the above expression Π_e is the cable elastic strain energy, Π_g is the gravitational energy, and Π_K is the potential energy of the spring. The kinetic energy of the system is expressed as follows

$$\hat{Q} = \int_0^L \bar{Q}_m \left(U_t, V_t, W_t\right) dx + Q_M \left(U_t\left(L,t\right), V_t\left(L,t\right)\right) \tag{3.19}$$

The subscript t represent the partial derivative with respect to time. The kinetic energy density of the rope is expressed as

$$\bar{Q}_m = \frac{1}{2} m \left[\left(\frac{\partial U}{\partial t}\right)^2 + \left(\frac{\partial V}{\partial t}\right)^2 + \left(\frac{\partial W}{\partial t}\right)^2 \right] \tag{3.20}$$

The kinetic energy of the mass is given as

$$Q_M = \frac{1}{2} M \left[\left(\frac{\partial V(L,t)}{\partial t} \right)^2 + \left(\frac{\partial U(L,t)}{\partial t} \right)^2 \right] \tag{3.21}$$

Assuming that the constant energy accumulated into the system during the initial static deflection is neglected, the elastic strain energy of the rope and the energy of the equivalent spring element, between the mass and steel frame in the lateral direction, are given by equations (3.22) and (3.23).

$$\Pi_e = \int_0^L \hat{\Pi}_e(U_x, V_x, W_x)\, dx \tag{3.22}$$

$$\Pi_K = \hat{\Pi}_K^V \left[V(L,t) \right] \tag{3.23}$$

where

$$\hat{\Pi}_e = \left(T(x) + \frac{1}{2} EA\varepsilon \right) \varepsilon \tag{3.24}$$

$$\hat{\Pi}_K^V = 2\left(\frac{1}{2} \right) k_{eq} \left(V(L,t) \right)^2 \tag{3.25}$$

The mean quasi static rope tension is represented by $T(x)$.The ε is the Green symmetric strain tensor measure of the rope which is defined in equation (3.16). The gravitational potential energy is given in terms of the dynamic deflections as

$$\Pi_g = \int_0^L \hat{\Pi}_g(U)\, dx - MgU_M \tag{3.26}$$

Potential Energy due to gravity of the rope

$$\hat{\Pi}_g = -mgU \tag{3.27}$$

Hamilton principle requires that any virtual displacement, arbitrary between two time instants t_1 and t_2, vanishes at the end of the time interval such as

$$\delta U(x,t) = \delta V(x,t) = \delta W(x,t) = 0 \text{ for } 0 \le x \le L \tag{3.28}$$

Applying into (3.17) equations (3.19), (3.22), and (3.23) the following equations results

$$\int_{t_1}^{t_2}\left(\begin{array}{l}\int_0^L\left(\delta\bar{Q}_m\left(U_t,V_t,W_t\right)-\delta\hat{\Pi}_g\left(U\right)-\delta\hat{\Pi}_e\left(U_x,V_x,W_x\right)\right)dx+\\ \delta Q_M\left(U_t\left(L,t\right),V_t\left(L,t\right)\right)+Mg\delta U_M-\delta\Pi_K^V\left(V\left(L,t\right)\right)\end{array}\right)dt=0 \tag{3.29}$$

where

$$\delta\bar{Q}_m=\left(\frac{\partial\bar{Q}_m}{\partial U_t}\right)\delta U_t+\left(\frac{\partial\bar{Q}_m}{\partial V_t}\right)\delta V_t+\left(\frac{\partial\bar{Q}_m}{\partial W_t}\right)\delta W_t \tag{3.30}$$

$$\delta Q_M=\left(\frac{\partial Q_M}{\partial U_t\left(L,t\right)}\right)\delta U_t\left(L,t\right)+\left(\frac{\partial Q_M}{\partial V_t\left(L,t\right)}\right)\delta V_t\left(L,t\right) \tag{3.31}$$

$$\delta\Pi_e=\left(\frac{\partial\Pi_e}{\partial U_x}\right)\delta U_x+\left(\frac{\partial\Pi_e}{\partial V_x}\right)\delta V_x+\left(\frac{\partial\Pi_e}{\partial W_x}\right)\delta W_x \tag{3.32}$$

$$\delta\hat{\Pi}_g=-mg\delta U \tag{3.33}$$

$$\delta\Pi_K^V=\frac{\partial\Pi_K^V}{\partial V\left(L,t\right)}\delta V\left(L,t\right) \tag{3.34}$$

Integrating equation (3.30) in respect to *t* and *x* the following equation is derived

$$\int_{t_1}^{t_2}\left(\int_0^L\delta\bar{Q}_m dx\right)dt=\int_{t_1}^{t_2}\left(\int_0^L\left(\left(\frac{\partial\bar{Q}_m}{\partial U_t}\right)\delta U_t+\left(\frac{\partial\bar{Q}_m}{\partial V_t}\right)\delta V_t+\left(\frac{\partial\bar{Q}_m}{\partial W_t}\right)\delta W_t\right)dx\right)dt \tag{3.35}$$

and

$$\int_{t_1}^{t_2}\delta\bar{Q}_m dt=\int_{t_1}^{t_2}\left(\frac{\partial\bar{Q}_m}{\partial U_t}\frac{\partial}{\partial t}\left(\delta U\right)+\frac{\partial\bar{Q}_m}{\partial V_t}\frac{\partial}{\partial t}\left(\delta V\right)+\frac{\partial\bar{Q}_m}{\partial W_t}\frac{\partial}{\partial t}\left(\delta W\right)\right)dt \tag{3.36}$$

can be written as

$$\begin{aligned}\int_{t_1}^{t_2}\delta\bar{Q}_m dt=&\left[\frac{\partial\bar{Q}_m}{\partial U_t}\delta U\right]_{t_1}^{t_2}-\int_{t_1}^{t_2}\frac{\partial}{\partial t}\left(\frac{\partial\bar{Q}_m}{\partial U_t}\right)\delta U dt+\left[\frac{\partial\bar{Q}_m}{\partial V_t}\delta V\right]_{t_1}^{t_2}-\int_{t_1}^{t_2}\frac{\partial}{\partial t}\left(\frac{\partial\bar{Q}_m}{\partial V_t}\right)\delta V dt\\&+\left[\frac{\partial\bar{Q}_m}{\partial W_t}\delta W\right]_{t_1}^{t_2}-\int_{t_1}^{t_2}\frac{\partial}{\partial t}\left(\frac{\partial\bar{Q}_m}{\partial W_t}\right)\delta W dt\end{aligned} \tag{3.37}$$

According to equation (3.28) the terms in red in equation (3.37) are the virtual displacements which are 0 when evaluated between t_1 and t_2. Thus, equation (3.37) can be rewritten as equation (3.38).

$$\int_{t_1}^{t_2}\delta\bar{Q}_m dt=-\int_{t_1}^{t_2}\frac{\partial}{\partial t}\left(\frac{\partial\bar{Q}_m}{\partial U_t}\right)\delta U dt-\int_{t_1}^{t_2}\frac{\partial}{\partial t}\left(\frac{\partial\bar{Q}_m}{\partial V_t}\right)\delta V dt-\int_{t_1}^{t_2}\frac{\partial}{\partial t}\left(\frac{\partial\bar{Q}_m}{\partial W_t}\right)\delta W dt \tag{3.38}$$

Similarly

$$\int_{t_1}^{t_2}\delta Q_M dt=-\int_{t_1}^{t_2}\frac{\partial}{\partial t}\left(\frac{\partial Q_M}{\partial U_t(L,t)}\right)\delta U(L,t)dt-\int_{t_1}^{t_2}\frac{\partial}{\partial t}\left(\frac{\partial Q_M}{\partial V_t(L,t)}\right)\delta V(L,t)dt \tag{3.39}$$

$$\begin{aligned}\int_0^L\delta\hat{\Pi}_e dx&=\left[\frac{\partial\hat{\Pi}_e}{\partial U_x}\delta U\right]_0^L-\int_0^L\frac{\partial}{\partial x}\left(\frac{\partial\hat{\Pi}_e}{\partial U_x}\right)\delta U dx+\left[\frac{\partial\hat{\Pi}_e}{\partial V_x}\delta V\right]_0^L-\int_0^L\frac{\partial}{\partial x}\left(\frac{\partial\hat{\Pi}_e}{\partial V_x}\right)\delta V dx\\&+\left[\frac{\partial\hat{\Pi}_e}{\partial W_x}\delta W\right]_0^L-\int_0^L\frac{\partial}{\partial x}\left(\frac{\partial\hat{\Pi}_e}{\partial W_x}\right)\delta W dx\end{aligned} \tag{3.40}$$

$$\int_{t_1}^{t_2}\delta\Pi_K^V dt=-\int_{t_1}^{t_2}\frac{\partial\hat{\Pi}_K^V}{\partial V(L,t)}\delta V(L,t)dt \tag{3.41}$$

The boundary conditions are as follows:

$$\delta U(0,t)=\delta V(0,t)=\delta W(0,t)=0 \tag{3.42}$$

$$\delta W(L,t)=0 \tag{3.43}$$

Applying into Equation (3.29) Equations (3.33) - (3.34) and Equations (3.38) - (3.43) the following equation is obtained

$$\begin{aligned}&\int_{t_1}^{t_2}\Bigg(\int_0^L\Bigg(\left[-\frac{\partial}{\partial t}\left(\frac{\partial\bar{Q}_m}{\partial V_t}\right)+\frac{\partial}{\partial x}\left(\frac{\partial\hat{\Pi}_e}{\partial V_x}\right)\right]\delta V+\left[-\frac{\partial}{\partial t}\left(\frac{\partial\bar{Q}_m}{\partial U_t}\right)+\frac{\partial}{\partial x}\left(\frac{\partial\hat{\Pi}_e}{\partial U_x}\right)+mg\right]\delta U\\&\quad+\left[-\frac{\partial}{\partial t}\left(\frac{\partial\bar{Q}_m}{\partial W_t}\right)+\frac{\partial}{\partial x}\left(\frac{\partial\hat{\Pi}_e}{\partial W_x}\right)\right]\delta W\Bigg)dx\\&\quad+\left[-\frac{\partial}{\partial t}\left(\frac{\partial Q_M}{\partial V_t(L,t)}\right)-\frac{\partial\Pi_k^V}{\partial V(L,t)}-\frac{\partial\hat{\Pi}_e}{\partial V_x}\bigg|_{x=L}\right]\delta V(L,t)\\&\quad+\left[-\frac{\partial}{\partial t}\left(\frac{\partial Q_M}{\partial U_t(L,t)}\right)+Mg-\frac{\partial\hat{\Pi}_e}{\partial U_x}\bigg|_{x=L}\right]\delta U(L,t)\Bigg)dt=0\end{aligned} \tag{3.44}$$

The virtual displacement $\delta U,\delta V,\delta W,\delta U(L,t),\delta V(L,t)$ are arbitrary and the above equation can only be valid for all the values of the virtual displacement if

$$\frac{\partial}{\partial t}\left(\frac{\partial \bar{Q}_m}{\partial V_t}\right)-\frac{\partial}{\partial x}\left(\frac{\partial \hat{\Pi}_e}{\partial V_x}\right)=0 \tag{3.45}$$

$$\frac{\partial}{\partial t}\left(\frac{\partial \bar{Q}_m}{\partial U_t}\right)-\frac{\partial}{\partial x}\left(\frac{\partial \hat{\Pi}_e}{\partial U_x}\right)-mg=0 \tag{3.46}$$

$$\frac{\partial}{\partial t}\left(\frac{\partial \bar{Q}_m}{\partial W_t}\right)-\frac{\partial}{\partial x}\left(\frac{\partial \hat{\Pi}_e}{\partial W_x}\right)=0 \tag{3.47}$$

$$\frac{\partial}{\partial t}\left(\frac{\partial Q_M}{\partial V_t(L,t)}\right)+\left.\frac{\partial \hat{\Pi}_e}{\partial V_x}\right|_{x=L}+\frac{\partial \Pi_k^V}{\partial V(L,t)_x}=0 \tag{3.48}$$

$$\frac{\partial}{\partial t}\left(\frac{\partial Q_M}{\partial U_t(L,t)}\right)+\left.\frac{\partial \hat{\Pi}_e}{\partial U_x}\right|_{x=L}-Mg=0 \tag{3.49}$$

Substituting the equations (3.20) - (3.25) into equations (3.45) - (3.49) the nonlinear equations of motion are derived.

$$\begin{aligned} &mV_{tt}+T(x)_x V_x-EA\left(U_x+\frac{1}{2}\left(V_x^2+W_x^2\right)\right)_x V_x-T(x)V_{xx} \\ &-EA\left(U_x+\frac{1}{2}\left(V_x^2+W_x^2\right)\right)_x V_{xx}=0 \end{aligned} \tag{3.50}$$

$$mU_{tt}-T(x)_x-EA\left(U_x+\frac{1}{2}\left(V_x^2+W_x^2\right)\right)_x-mg=0 \tag{3.51}$$

$$\begin{aligned} &mW_{tt}+T(x)_x W_x-EA\left(U_x+\frac{1}{2}\left(V_x^2+W_x^2\right)\right)_x W_x-T(x)W_{xx} \\ &-EA\left(U_x+\frac{1}{2}\left(V_x^2+W_x^2\right)\right)_x W_{xx}=0 \end{aligned} \tag{3.52}$$

$$\begin{aligned} &M\ddot{V}(L,t)+\left(T(\mathrm{L})+EA\left(U_x+\frac{1}{2}\left(V_x^2+W_x^2\right)\right)\Big|_{x=L}\right)V_x\big|_{x=L} \\ &+2k_{eq}V(L,t)=0 \end{aligned} \tag{3.53}$$

$$MU(L,t)_{tt}+T(\mathrm{L})+EA\left(U_x+\frac{1}{2}\left(V_x^2+W_x^2\right)\right)\Big|_{x=L}-Mg=0 \tag{3.54}$$

The equations (3.50) to (3.52) describe the dynamics of the rope and the equations (3.53) to (3.54) the boundary conditions at $x=L$ in the lateral in plane and longitudinal direction respectively.

From Figure 3.24 the tension is derived by balance of forces which is represented by equation (3.55).

$$T(x) = Mg + mg\left(L - x\right) \tag{3.55}$$

The rope system is excited at the top by displacements in the lateral in plane and out of plane direction represented by equations (3.14) and (3.15). The absolute displacements in the lateral in plane and out of plane direction can be represented as equations (3.56) - (3.57).

$$\mathrm{V}(x,t) = \bar{V}(x,t) + S_v\left(1 - \frac{x}{L}\right) \tag{3.56}$$

$$\mathrm{W}(x,t) = \bar{W}(x,t) + S_w\left(1 - \frac{x}{L}\right) \tag{3.57}$$

respectively, where $\bar{V}$ and $\bar{W}$ represent elastic deformations measured relative to the rigid-body motions of the system.

The partial derivative for *x* and *t* for the lateral in plane and out of plane direction are shown in equations (3.58) to (3.65).

$$V_{tt} = \bar{V}_{tt} + S_{tt}^{v}\left(1 - \frac{x}{L}\right) \tag{3.58}$$

$$V_x = \bar{V}_x - \frac{S_v}{L} \tag{3.59}$$

$$V_{xx} = \bar{V}_{xx} \tag{3.60}$$

$$W_{tt} = \bar{W}_{tt} + S_{tt}^{w}\left(1 - \frac{x}{L}\right) \tag{3.61}$$

$$W_x = \bar{W}_x - \frac{S_w}{L} \tag{3.62}$$

$$W_{xx} = \bar{W}_{xx} \tag{3.63}$$

$$V\left(L,t\right)_x = \bar{V}\left(L,t\right)_x - \frac{S_v}{L} \tag{3.64}$$

$$\ddot{V}\left(L,t\right)_x = \ddot{\bar{V}}\left(L,t\right)_x - \frac{S_{tt}^{v}}{L} \tag{3.65}$$

Substituting equation (3.55) into equation (3.51) results in equation (3.66)

$$mU_{tt} - EA\left(U_x + \frac{1}{2}\left(V_x^{\,2} + W_x^{\,2}\right)\right)_x = 0 \tag{3.66}$$

The longitudinal natural frequency of the rope are much higher than the lateral natural frequencies of the rope, thus the inertia in the longitudinal direction can be neglected, resulting in equation (3.67).

$$\left(U_x + \frac{1}{2}\left(V_x^{\,2} + W_x^{\,2}\right)\right)_x = 0 \tag{3.67}$$

The internal terms inside the parenthesis is represented by e(t), which is shown in equation (3.68).

$$e(t) = U_x + \frac{1}{2}\left(V_x^{\,2} + W_x^{\,2}\right) \tag{3.68}$$

Equation (3.68) is integrated with respect to x, giving equation (3.69).

$$Le(t) = \int_0^L U_x dx + \frac{1}{2}\int_0^L \left(\bar{V}_x^{\,2} - 2\frac{S_v}{L}\bar{V}_x + \frac{S_v^2}{L^2}\right)dx + \frac{1}{2}\int_0^L \left(\bar{W}_x^{\,2} - 2\frac{S_w}{L}\bar{W}_x + \frac{S_w^2}{L^2}\right)dx \tag{3.69}$$

Substituting equation (3.68) and (3.55) into equations (3.50) to (3.54) gives

$$m\bar{V}_{tt} + mS_{tt}^{v}\left(1 - \frac{x}{L}\right) + mg\bar{V}_x - mg\frac{S_v}{L} - (Mg + mgL)\bar{V}_{xx} + mgx\bar{V}_{xx} - EAe(t)\bar{V}_{xx} = 0 \tag{3.70}$$

$$\begin{aligned} &m\bar{W}_{tt} + mS_{tt}^{w}\left(1 - \frac{x}{L}\right) + mg\bar{W}_x - mg\frac{S^w}{L} - (Mg + mgL)\bar{W}_{xx} \\ &+mgx\bar{W}_{xx} - EAe(t)\bar{W}_{xx} = 0 \end{aligned} \tag{3.71}$$

$$M\bar{V}(L,t)_{tt} + Mg\bar{V}_x(L,t) - Mg\frac{S_v}{L} + EAe(t)\bar{V}_x(L,t) - EAe(t)\frac{S_v}{L} + 2k_{eq}\bar{V}(L,t) = 0 \tag{3.72}$$

$$MU(L,t)_{tt} + T(\mathrm{L}) + EAe(t) - Mg = 0 \tag{3.73}$$

The boundary conditions at $x = 0$, read $\bar{U}(0,t) = \bar{V}(0,t) = \bar{W}(0,t) = 0$. The linear natural modes of the lateral in plane and lateral out of plane motion are given as $\phi_n = sin(\beta_n^{lin} x)$ and $\alpha_n = sin\left(\frac{n\pi}{L}x\right)$ where β_n^{lin} and $\frac{n\pi}{L}$ are the eigenvalues for the lateral in plane and the lateral out of plane modes, respectively. The eigenvalues for the lateral in plane direction can be determined from the frequency equation expressed by equation (3.74).

$$T_0\beta^{Lin}\cos\beta^{Lin}L+\left(k_{eq}-\frac{MT_0}{m}\left(\beta^{Lin}\right)^2\right)\sin\beta^{Lin}L=0 \tag{3.74}$$

The natural modes and the derivation of the frequency equations are analysed in Appendices A and B.

Equations (3.69) to (3.72) can be discretised by applying the Galerkin method. In this procedure the dynamic response of the system is approximated in the lateral in plane and lateral out of plane directions by the following expansions

$$\bar{V}\left(x,t\right)=\sum_{n=1}^{N}\phi_n(x)\,\mathrm{q}_n(t) \tag{3.75}$$

$$\bar{W}\left(x,t\right)=\sum_{n=1}^{N}\alpha_n(x)\,\mathrm{c}_n(t) \tag{3.76}$$

respectively, where q_n, c_n represent the generalized (modal) coordinates and *N* represent the number of modes taken into account in the expansion. For the longitudinal direction the substitution $U(L,t)=U_M$ is applied. Substituting expansions (3.75) and (3.76) into equations (3.69) to (3.73) by applying the orthogonality conditions with respect to the linear modes a system of nonlinear ordinary differential equations results as follows.

$$\begin{aligned}e(t)=\frac{U_M}{L}+\frac{1}{2L}\int_0^L\left(\sum_{n=1}^{N}\phi_j'(x)\,\mathrm{q}_j(t)\right)^2dx-\frac{S_v}{L^2}\int_0^L\sum_{n=1}^{N}\phi_j'(x)\,\mathrm{q}_j(t)dx+\frac{1}{2L^3}\int_0^L {S_v}^2dx+\\ \frac{1}{2L}\int_0^L\left(\sum_{n=1}^{N}\alpha_j'(x)\,\mathrm{c}_j(t)\right)^2dx-\frac{1}{L^2}\int_0^L S_w\left(\sum_{n=1}^{N}\alpha_j'(x)\,\mathrm{c}_j(t)\right)dx+\frac{1}{2L^3}\int_0^L {S_w}^2dx\end{aligned} \tag{3.77}$$

The upper subscript prime represents the total derivative with respect to *x*. Finding the solution of each integral from equation (3.77) can be represented as equation (3.78).

$$\begin{aligned}e(t)=\frac{U_M}{L}+\frac{1}{2L}\sum_{j=1}^{N}\sum_{p=1}^{N}G_{jp}q_j(t)q_p(t)-\frac{S_v}{L^2}\sum_{j=1}^{N}q_j(t)\sin\left(\beta_j^{Lin}L\right)\\ +\frac{{S_v}^2}{2L^2}+\frac{1}{4}\sum_{j=1}^{N}\left(\frac{j\pi}{L}\right)^2\left(c_j(t)\right)^2+\frac{{S_w}^2}{2L^2}\end{aligned} \tag{3.78}$$

Where G_{jp} is represented as the following

$$G_{jp}=\begin{cases}j=p;\dfrac{\left(\beta_j^{Lin}\right)^2L}{2}+\dfrac{\beta_j^{Lin}\sin\left(2\beta_j^{Lin}L\right)}{4}\\ j\neq p;\beta_j^{Lin}\beta_p^{Lin}\left[\dfrac{\sin\left(L\left(\beta_j^{Lin}-\beta_p^{Lin}\right)\right)}{2\left(\beta_j^{Lin}-\beta_p^{Lin}\right)}+\dfrac{\sin\left(L\left(\beta_j^{Lin}+\beta_p^{Lin}\right)\right)}{2\left(\beta_j^{Lin}+\beta_p^{Lin}\right)}\right]\end{cases}$$

$$\ddot{q}_r(t)+2\zeta_r^{Lin}\omega_r^{Lin}\dot{q}_r(t)+\sum_{n=1}^{N}k_{rn}^{1Lin}q_n(t)+\left(\omega_r^{Lin}\right)^2 q_r(t)+k_r^{2Lin}U_M+\sum_{n=1}^{N}\sum_{j=1}^{N}D_{jnr}^{1Lin}q_j(t)q_n(t)$$
$$\sum_{n=1}^{N}D_{rn}^{2Lin}c_n^2(t)+\sum_{n=1}^{N}\sum_{j=1}^{N}\sum_{p=1}^{N}R_{jnpr}^{1Lin}q_j(t)q_p(t)q_n(t)+\sum_{n=1}^{N}\sum_{j=1}^{N}R_{jnpr}^{2Lin}c_j^2(t)q_n(t)+F_r^{Lin}=0 \quad (3.79)$$

$$\ddot{c}_r(t)+2\zeta_r^{Lout}\omega_r^{Lout}\dot{c}_r(t)+\left(\omega_r^{Lout}\right)^2 c_r(t)+\sum_{n=1}^{N}k_{rn}^{Lout}c_n(t)+\sum_{n=1}^{N}\sum_{j=1}^{N}D_{jnr}^{1Lout}q_j(t)c_n(t)$$
$$+\sum_{n=1}^{N}\sum_{j=1}^{N}R_{jnr}^{1Lout}c_j^2(t)c_n(t)+\sum_{n=1}^{N}\sum_{j=1}^{N}\sum_{p=1}^{N}R_{jnpr}^{2Lout}q_j(t)q_p(t)c_n(t)+F_r^{Lout}=0 \quad (3.80)$$

$$\ddot{U}_M+2\zeta_{UM}\omega_{UM}\dot{U}_M+\sum_{n=1}^{N}k_n^{1u}q_n(t)+\left(\omega_{UM}\right)^2 U_M+\sum_{n=1}^{N}\sum_{j=1}^{N}D_{np}^{1u}q_n(t)q_p(t)$$
$$+\sum_{n=1}^{N}\sum_{j=1}^{N}D_n^{2u}c_n^2(t)+F_U=0 \quad (3.81)$$

The modal damping coefficients have been added into the above equations in the lateral in plane, out of plane, and longitudinal direction expressed as $\zeta_r^{Lin},\zeta_r^{Lout},\zeta_{UM}$, respectively. The undamped natural frequencies in the lateral in plane, out of plane direction, and longitudinal directions are represented as $\omega_r^{Lin},\omega_r^{Lout},\omega_{UM}$, respectively. The coefficients resulting from the Galerkin method are defined. The terms for equation (3.79) which are for the lateral in plane direction of the rope are shown in equations (3.82) to (3.90).

$$m_r^{Lin}=m\int_0^L\phi_r^2(x)dx+M\phi_r^2(L) \quad (3.82)$$

$$\left(\omega_r^{Lin}\right)^2=\left(\beta^{Lin}\right)^2\frac{Mg}{m} \quad (3.83)$$

The coefficient k_{rn}^{1Lin} is defined in equation (3.84) which represents the lateral in plane linear stiffness coefficient.

$$k_{rn}^{1Lin}=\frac{mg}{m_{rr}^{Lin}}\int_0^L x\phi_n''(x)\phi_r(x)dx-\frac{mgL}{m_{rr}^{Lin}}\int_0^L\phi_n''(x)\phi_r(x)dx+\frac{mg}{m_{rr}^{Lin}}\int_0^L\phi_n'(x)\phi_r(x)dx$$
$$-\frac{EA\left(S_v{}^2+S_w{}^2\right)}{2L^2m_{rr}^{Lin}}\int_0^L\phi_n''(x)\phi_r(x)dx+\frac{EAS_v^2}{L^3m_{rr}^{Lin}}\phi_n(\mathrm{L})\phi_r(\mathrm{L})+\frac{EA\left(S_v{}^2+S_w{}^2\right)}{2L^2m_{rr}^{Lin}}\phi_n'(\mathrm{L})\phi_r(\mathrm{L}) \quad (3.84)$$
$$-\frac{EAU_M}{Lm_{rr}^{Lin}}\int_0^L\phi_n''(x)\phi_r(x)dx+\frac{EAU_M}{Lm_{rr}^{Lin}}\phi_n'(\mathrm{L})\phi_r(\mathrm{L})$$

The coefficients $D_{jnr}^{1Lin},D_{nr}^{2Lin}$ defined in equations (3.85) and (3.86) represent the quadratic lateral in plane nonlinear terms.

$$D_{jnr}^{1Lin} = \frac{EAS_v}{L^2 m_{rr}^{Lin}} \phi_r(\mathrm{L}) \int_0^L \phi_n''(x)\phi_r(x)dx - \frac{EAS_v}{L^2 m_{rr}^{Lin}} \left(\beta_j^{Lin} L\right) \phi_n'(\mathrm{L})\phi_r(\mathrm{L}) - \frac{EA}{2L^2 m_{rr}^{Lin}} S_v \phi_r(\mathrm{L}) G_{jp} \tag{3.85}$$

$$D_{jr}^{2Lin} = -\frac{EAS_v}{4Lm_{rr}^{Lin}} \phi_r(\mathrm{L}) \left(\frac{j\pi}{L}\right)^2 \tag{3.86}$$

The coefficient F_r^{Lin} defined in equation (3.87) represent the excitation coefficient for the lateral in plane direction.

$$F_r^{Lin} = \frac{m}{m_{rr}^{Lin}} S_{tt}^v \int_0^L \left(1 - \frac{x}{L}\right) \phi_r(x)dx - \frac{mg}{Lm_{rr}^{Lin}} S_v \int_0^L \phi_r(x)dx - \frac{MgS_v}{Lm_{rr}^{Lin}} \phi_r(\mathrm{L}) - \frac{EA}{2L^3 m_{rr}^{Lin}} {S_w}^2 S_v \phi_r(\mathrm{L}) - \frac{EA}{2L^3 m_{rr}^{Lin}} {S_v}^3 \phi_r(\mathrm{L}) \tag{3.87}$$

$$k_r^{2Lin} = -\frac{EAS_v \phi_r(\mathrm{L})}{L^2 m_{rr}^{Lin}} \tag{3.88}$$

The coefficients R_{jnpr}^{1Lin} and R_{jnpr}^{2Lin} defined in equations (3.89) and (3.90) represent the lateral in plane cubic nonlinear terms.

$$R_{jnpr}^{1Lin} = -\frac{EA}{2Lm_{rr}^{Lin}} G_{jp} \int_0^L \phi_n''(x)\phi_r(x)dx + \frac{EA}{2Lm_{rr}^{Lin}} G_{jp} \phi_n'(\mathrm{L})\phi_r(\mathrm{L}) \tag{3.89}$$

$$R_{jnpr}^{2Lin} = -\frac{EA}{4m_{rr}^{Lin}} \left(\frac{j\pi}{L}\right)^2 \int_0^L \phi_n''(x)\phi_r(x)dx + \frac{EA}{4m_{rr}^{Lin}} \left(\frac{j\pi}{L}\right)^2 \phi_n'(\mathrm{L})\phi_r(\mathrm{L}) \tag{3.90}$$

The terms for equation (3.80) which are for the lateral out of plane direction of the rope are shown in equations (3.91) to (3.97).

$$m_{rr}^{Lout} = m \int_0^L \alpha_r^2(x)\,dx \tag{3.91}$$

$$\left(\omega_{rr}^{Lout}\right)^2 = \left(\frac{r\pi}{L}\right)^2 \frac{(M + mL)g}{m} \tag{3.92}$$

The coefficient k_{rn}^{Lout} is defined in equation (3.93) which represents the lateral out of plane linear stiffness coefficient.

$$k_{rn}^{Lout} = \frac{mg}{m_{rr}^{Lout}} \int_0^L x\alpha_n''(x)\alpha_r(x)\,\mathrm{dx} + \frac{mg}{m_{rr}^{Lout}} \int_0^L \alpha_n'(x)\alpha_r(x)dx$$
$$-\frac{EA\left(S_v{}^2 + S_w{}^2\right)}{2L^2 m_{rr}^{Lout}} \int_0^L \alpha_n''(x)\alpha_r(x)\,\mathrm{dx} - \frac{EAU_M}{Lm_{rr}^{Lout}} \int_0^L \alpha_n''(x)\alpha_r(x)\,\mathrm{dx} \tag{3.93}$$

The coefficient D_{jnr}^{1Lout} defined in equation (3.94) represent the quadratic lateral out of plane nonlinear terms.

$$D_{jnr}^{1Lout} = \frac{EAS_v}{L^2 m_{rr}^{Lout}} \sin\left(\beta_j^{Lin} L\right) \int_0^L \alpha_n''(x)\alpha_r(x)\,\mathrm{dx} \tag{3.94}$$

The coefficients R_{jnpr}^{1Lout} and R_{jnpr}^{2Lout} defined in equations (3.95) and (3.96) represent the lateral out of plane cubic nonlinear terms.

$$R_{jnr}^{1Lout} = -\frac{EA}{4m_{rr}^{Lout}} \left(\frac{j\pi}{L}\right)^2 \int_0^L \alpha_n''(x)\alpha_r(x)\,\mathrm{dx} \tag{3.95}$$

$$R_{jnpr}^{2Lout} = -\frac{EA}{2Lm_{rr}^{Lout}} G_{jp} \int_0^L \alpha_n''(x)\alpha_r(x)\,\mathrm{dx} \tag{3.96}$$

The coefficients F_r^{Lout} defined in equation (3.97) represent the excitation coefficients for the lateral out of plane direction.

$$F_r^{Lout} = \frac{m}{m_{rr}^{Lout}} S_{tt}^w \int_0^L \left(1 - \frac{x}{L}\right)\alpha_r(x)dx - \frac{mg}{Lm_{rr}^{Lout}} S_w \int_0^L \alpha_r(x)dx \tag{3.97}$$

The terms for equation (3.81) which are for the longitudinal direction are shown in equations (3.98) to (3.102).

$$\left(\omega_{UM}\right)^2 = \frac{EA}{ML} \tag{3.98}$$

The coefficient k_n^{1u} defined in equation (3.99) represent linear coupling involving the lateral in plane modal displacements acting in the longitudinal direction.

$$k_n^{1u} = -\frac{EAS_v}{ML^2} \sin\left(\beta_n^{Lin} L\right) \tag{3.99}$$

The coefficients D_{np}^{1u}, D_n^{2u} defined in equations (3.100) and (3.101) represent the quadratic nonlinear coupling involving the lateral modal displacements acting in the longitudinal direction.

$$D_{jp}^{1u} = \frac{EA}{2ML} G_{jp} \tag{3.100}$$

$$D_{n}^{2u} = \frac{EA}{4M} \left(\frac{n\pi}{L} \right)^2 \tag{3.101}$$

The coefficients F_U defined in equation (3.102) represent the excitation coefficient for the longitudinal direction.

$$F_U = \frac{EA\left(S_v^2 + S_w^2\right)}{2ML^2} \tag{3.102}$$

3.3 Experimental Validation

As a summary the test data that has been presented in this chapter is shown in Table 3.5.

Mass attached at the end of the rope [kg]	M = 68 kg
Mass per unit length of the rope [kg/m]	*m = 1.25 kg/m*
Length of the rope [m]	L = 32.70 m
Lateral in plane modal damping coefficient	ζ_1^{Lin} *= 0.01*
Lateral out of plane modal damping coefficient	ζ_1^{Lout} *= 0.003*
Longitudinal modal damping coefficient	ζ_{Long} *= 1*
Product of Young Modulus of Material	$EA=2.276x10^7$ *N*
Linear stiffness of springs	$K_{eq}=4.354x10^5$ *N/m*

Table 3.5 Summary of estimated experimental data to validate the mathematical model

The total mass attached at the bottom end of the rope has been added half of m_{eq} to take into account the mass of the spring in the lateral in plane direction resulting in *M=68.0 kg* as it is shown in Table 3.5.

From the Galerkin method the nonlinear ordinary differential equations are given for *N* number of modes and the ODE45 solver is used in MATLAB. The solver requires that the set of differential equations be truncated to a specific number of modes to find the solution. For this validation presented with the experimental data the model was truncated at *n=4* modes. In Appendix C are shown the comparison of the displacements of the rope in the lateral in plane and out of plane direction for *n=1, n=2,* and *n=3*.

The experimental validation was accomplished by actuating the rope in the lateral in plane direction represented by $S_v(t)$, where λ_v was tuned to the fundamental natural frequency of the rope with a prescribed amplitude A_v using the Kollmorgen actuator. The frequency of excitation for the experimental test was $\lambda_v = 0.40Hz$ with A_v=0.005m of displacement. The duration of the experiment is approximately 3 minutes and 50 seconds. The objective of this validation is to demonstrate that the mathematical model presented can be used to have an accurate estimation of the displacements of the rope. The sensors attached to the rope to measure the lateral in plane and out of plane displacements of the rope were positioned at a height of 11.0 m from the mass.

3.3.1 Free vibration analysis

From the mathematical model the lateral in plane eigenvalues are obtained by finding the roots of equation (3.74) shown in Table 3.6. There are several numerical methods used to determine the roots of a function, the most common numerical method used is the bisection method. According to Dauhoo and Soobhug (2003) the method divides into two parts an interval and then selects a subinterval in which a root must lie for further processing. Equation (3.74) according to the eigenvalues is shown in Figure 3.25.

	1	2	3	4
β^{Lin}	0.0961	0.1921	0.2882	0.3843

Table 3.6 The first four eigenvalues obtained with equation (3.74)

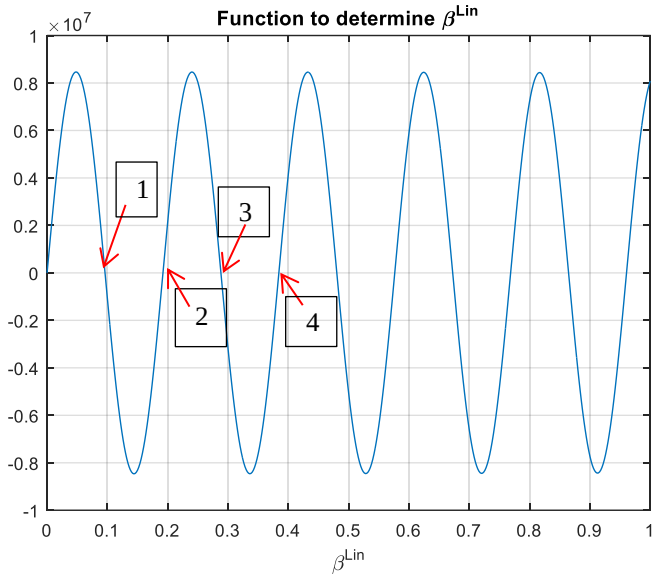

Figure 3.25 Equation (3.74) vs the eigenvalues

The natural modes shapes of the lateral in plane and lateral out of plane motion are given as $\phi_n = sin(\beta_n^{lin} x)$ and $\alpha_n = sin\left(\frac{n\pi}{L} x\right)$ using the corresponding eigenvalues, and are shown in Figure 3.26 and Figure 3.27 respectively.

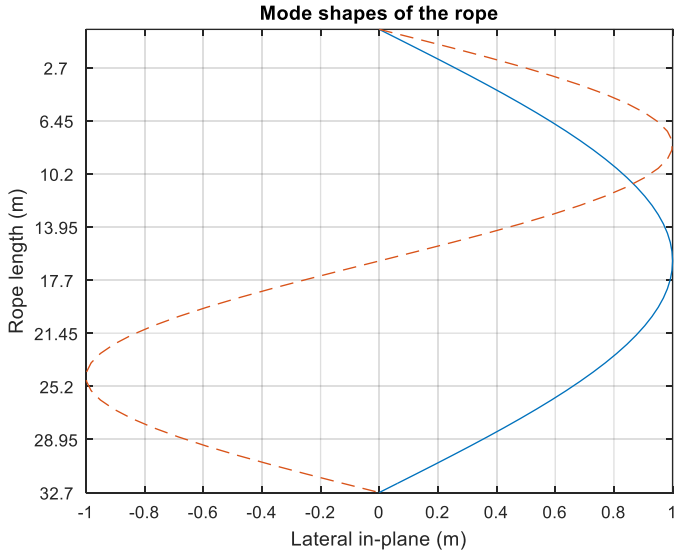

Figure 3.26 1st and 2nd mode shape for the lateral in plane direction

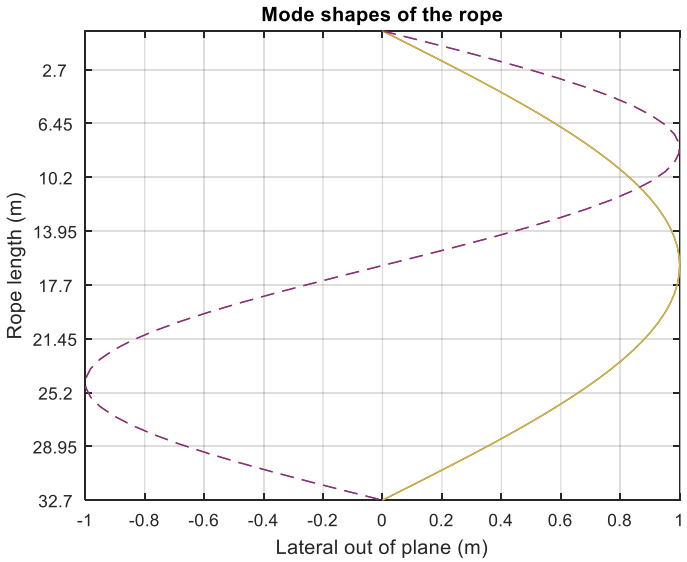

Figure 3.27 1st and 2nd mode shape for the lateral out of plane direction

The linear natural frequencies in the lateral in plane direction are obtained with the (β^{lin}) eigenvalues by using equation (3.103)

$$\omega^{Lin} = \beta^{Lin}\sqrt{\frac{Mg}{m}} \tag{3.103}$$

Resulting in the first four natural frequencies in the lateral in plane direction shown in Table 3.7.

	1 N. F. [Hz]	2 N. F. [Hz]	3 N. F. [Hz]	4 N. F. [Hz]
ω^{Lin}	0.3532	0.7064	1.0597	1.4129

Table 3.7 The first four linear natural frequencies when using Eq. (3.103).

The natural frequencies of the rope and mass system can also be calculated when taking into account all linear terms that are not time dependent in the lateral in plane direction as shown in equation (3.104).

$$\left(\omega_{rr}^{Lin}\right)^2 = -\frac{Mg+mgL}{m_{rr}^{Lin}}\int_0^L \phi_r''(x)\phi_r(x)dx + \frac{Mg}{m_{rr}^{Lin}}\phi_r'(\mathrm{L})\phi_r(\mathrm{L}) + \frac{2k_{eq}}{m_{rr}^{Lin}}\phi_r^2(\mathrm{L})$$
$$+\frac{mg}{m_{rr}^{Lin}}\int_0^L x\phi_r''(x)\phi_r(x)dx + \frac{mg}{m_{rr}^{Lin}}\int_0^L \phi_r'(x)\phi_r(x)dx \tag{3.104}$$

Resulting in the first four natural frequencies in the lateral in plane direction shown in Table 3.8, similar to the estimated in the previous sections of this chapter

	1 N. F. [Hz]	2 N. F. [Hz]	3 N. F. [Hz]	4 N. F. [Hz]
ω^{Lin}	0.4039	0.8071	1.2075	1.6234

Table 3.8 The first four natural frequencies of the rope in the lateral in plane direction using Eq. (3.104).

The natural frequencies of the rope and mass system in the lateral out of plane direction when using the linear terms that are not time dependent as shown in equation (3.105) are similar when using equation (3.104) for the lateral in plane direction.

$$\left(\omega_{rr}^{Lout}\right)^2 = -\frac{\left(Mg+mgL\right)}{m_{rr}^{Lout}}\int_0^L \alpha_r''(x)\alpha_r(x)\,\mathrm{dx} + \frac{mg}{m_{rr}^{Lout}}\int_0^L x\alpha_r''(x)\alpha_r(x)\,\mathrm{dx} + \frac{mg}{m_{rr}^{Lout}}\int_0^L \alpha_r'(x)\alpha_r(x)dx \tag{3.105}$$

Resulting in the first four natural frequencies in the lateral out of plane direction shown in Table 3.9, similar to the estimated in the previous sections of this chapter

	1 N. F. [Hz]	2 N. F. [Hz]	3 N. F. [Hz]	4 N. F. [Hz]
ω^{Lout}	0.4039	0.8071	1.2075	1.6234

Table 3.9 The first four natural frequencies of the rope in the lateral out of plane direction using Eq. (3.105).

The approximate value of the first (fundamental) natural frequency in the longitudinal direction is given by Eq. (3.98) resulting in $\omega_{UM} = 16.10Hz$, which is much higher than the lateral natural frequencies of the rope. The fundamental natural frequency in the longitudinal direction of $\omega_{UM} = 16.10Hz$ agrees with the longitudinal frequency obtained from experimental testing of a rope and mass system shown in section 3.1.2.3 which was $\omega_0 = 14.88$ *Hz* used to estimate the modulus of elasticity of the rope.

3.3.2 Simulation Results

The signal data obtained after post processing from the LVDT in the lateral in plane direction and from the DC accelerometer in the lateral out of plane direction at the excitation point of the rope is shown in Figure 3.28. The main excitation was in the lateral in plane direction with

±0.005m, which was the amplitude provided by the Kollmorgen actuator and was prescribed in the National Instruments LabView software program. The displacements for the lateral out of plane were initially small but near 100 seconds increase to ±0.002m which is when the lateral out of plane displacements of the rope start to increase due to the transfer of energy from the lateral in plane direction to the lateral out of plane direction when the whirling motion of the rope appear.

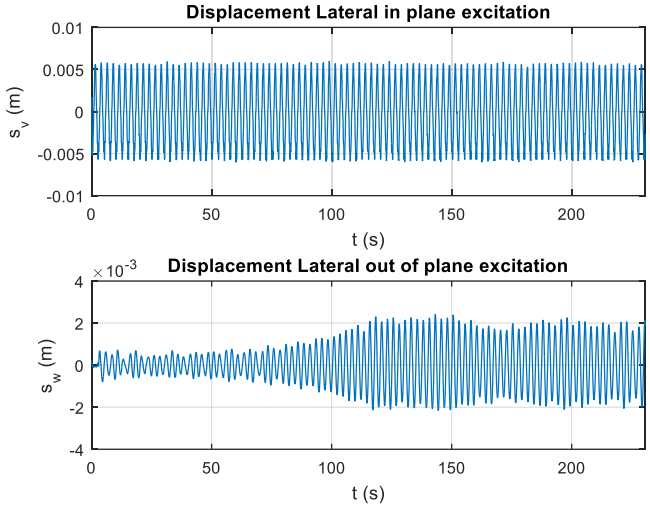

Figure 3.28 Signal data after post processing in the lateral in plane and out of plane direction

The FFT spectrum over the entire time span of the signal is shown in Figure 3.29 for the lateral in plane and out of plane direction. In both the dominant frequency is 0.40 Hz which is the prescribed frequency of the Kollmorgen actuator.

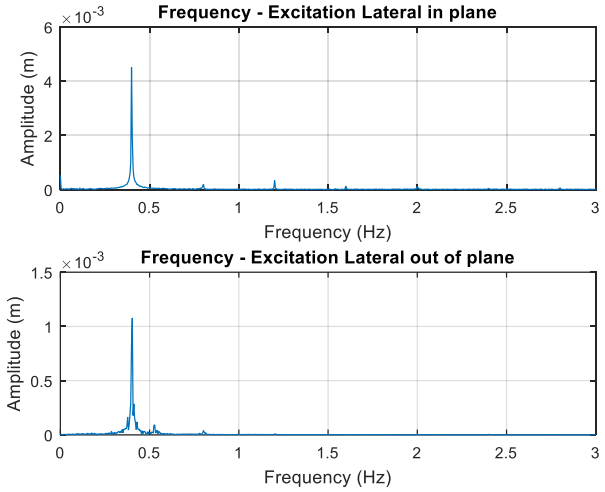

Figure 3.29 Frequency of excitation in the lateral in plane and out of plane direction

The sensor data from the experiment shown in dotted black line and the data determined from the simulation shown in blue line are compared with the displacement shown in Figure 3.30 for both the lateral in plane and out of plane direction.

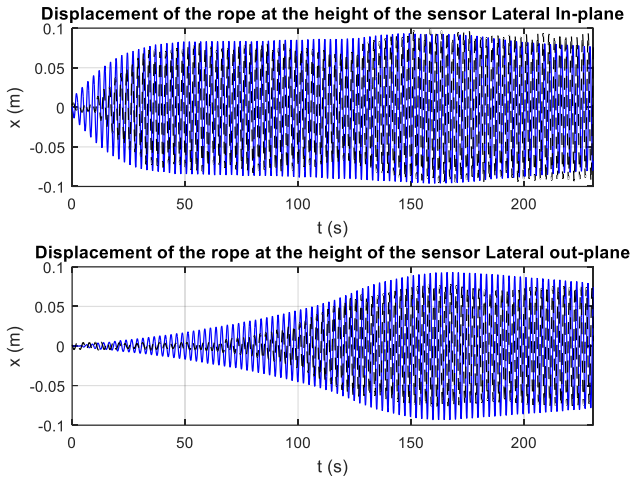

Figure 3.30 Comparison of the rope displacement at the sensor attachment height from the experiment and the simulation

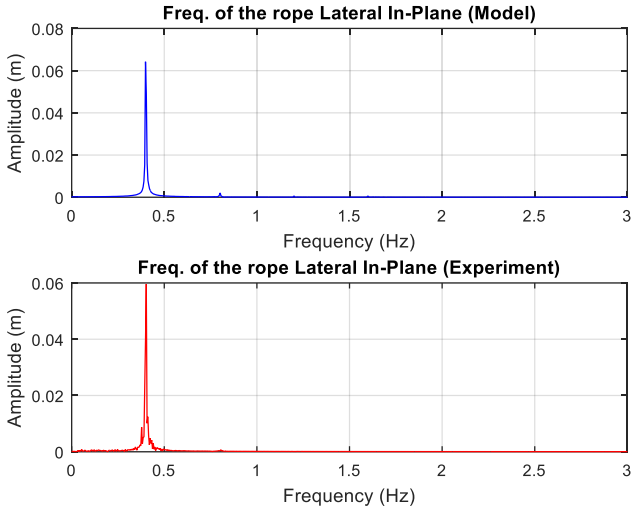

Figure 3.31 FFT spectrum of the lateral in plane displacements of the rope comparing the simulation and experimental testing

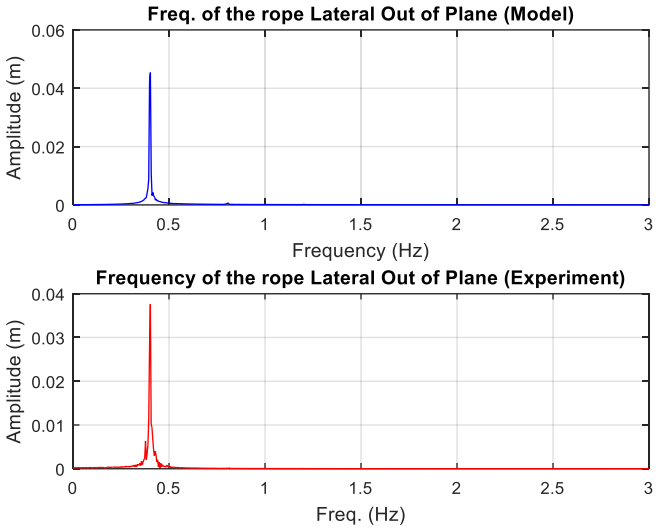

Figure 3.32 FFT spectrum of the lateral in plane displacements of the rope comparing the simulation and experimental testing

The FFT spectrum over the entire time span of the displacements of the rope in the lateral in plane direction are shown in Figure 3.31 and for the lateral out of plane direction are shown in Figure 3.32 comparing both simulation and experimental testing.

According to Nayfeh and Mook (1979), the whirling motion of the rope is an interesting phenomena which is a consequence of internal resonance. The whirling motion of a rope occurs when the energy of the rope is transferred from the lateral in plane direction to the lateral out of plane direction. The whirling motion of the rope is a direct consequence of the fact that the frequency of the motion in the plane of the excitation is the same as the frequency of the motion in the plane perpendicular to the plane of the excitation. Thus, the two components of motion are strongly coupled.

The whirling motion of the rope can be seen when the lateral in plane and out of plane displacements are graphed together. In Figure 3.33 shows the whirling motion of the rope recorded at the sensor height when comparing the displacement from the sensor represented by a dotted black line and the displacement determined from the simulation represented by a blue line during the entire time span.

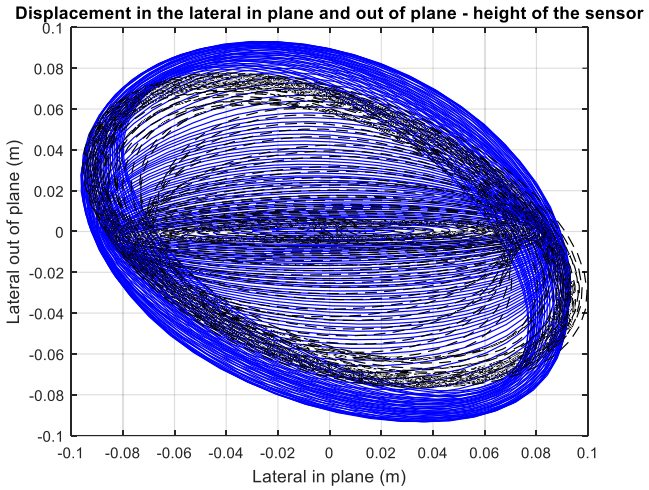

Figure 3.33 Comparison of the displacements in the lateral in plane and out of plane direction

The whirling motion of the rope is shown in different time spans between 50 seconds and 100 seconds, 100 seconds and 150 seconds, 150 seconds and 200 seconds, and 200 seconds until the end of the experiment are shown in Figure 3.34, Figure 3.35, Figure 3.36, and Figure 3.37 respectively. The blue line represents the displacements determined from the simulation and the dotted black line is the sensor data.

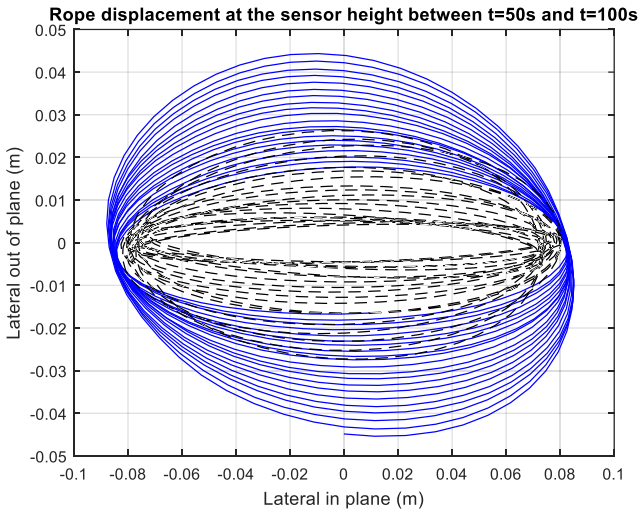

Figure 3.34 Comparison of the displacements in the lateral in plane and out of plane direction between 50 seconds and 100 seconds

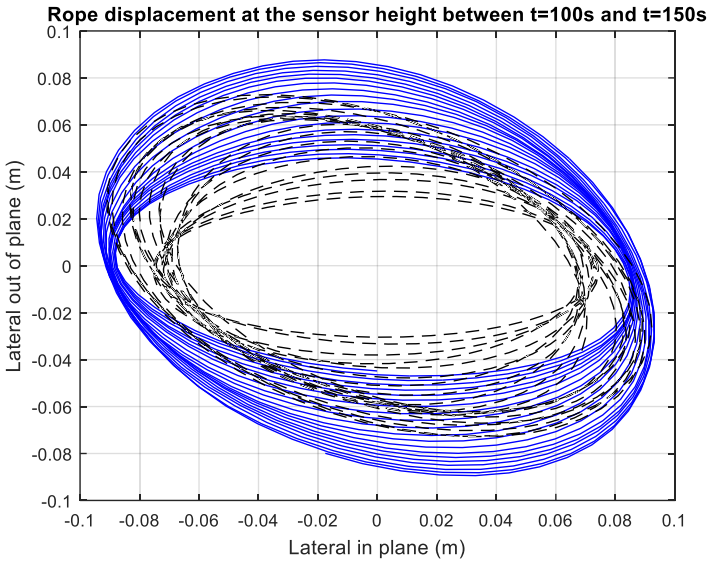

Figure 3.35 Comparison of the displacements in the lateral in plane and out of plane direction between 100 seconds and 150 seconds

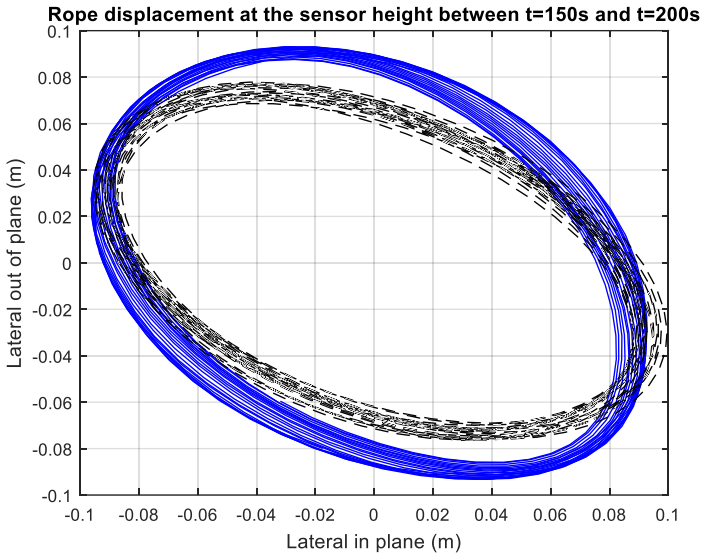

Figure 3.36 Comparison of the displacements in the lateral in plane and out of plane direction between 150 seconds and 200 seconds

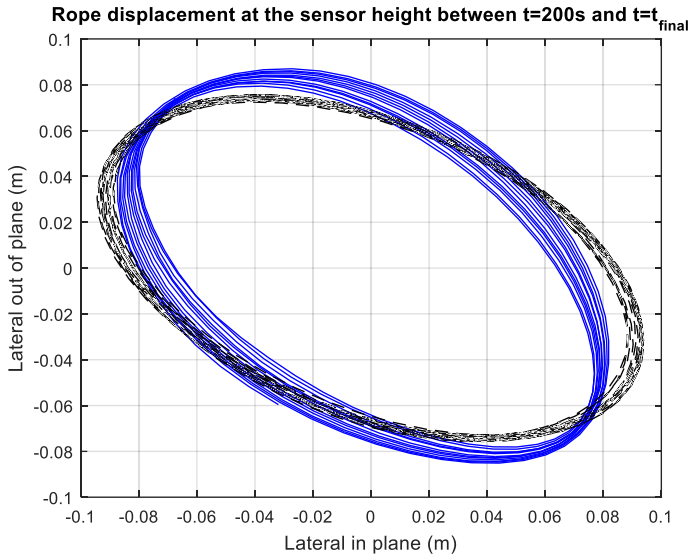

Figure 3.37 Comparison of the displacements in the lateral in plane and out of plane direction between 200 seconds and final time of the experiment

As it can be seen the response from the simulation model starts to correlate better with the experimental testing after the initial 100.0 seconds when the whirling phenomena on the rope starts to occur.

The model accommodates the lateral in plane and longitudinal motion of the mass. The lateral out of plane motion of the mass are neglected, due to the high stiffness in the lateral out of plane direction of the frame structure at the mass assembly. The displacements of the mass in the lateral out of plane direction after the initial transient phenomena were very small in the range of 0.2×10^{-4}m, as it can be seen in Figure 3.38. The high amplitudes in the lateral out of plane direction are due to the transient phenomena possibly caused by misalignment in the system. According to Meirovitch (2001), transient phenomena are initial excitations that come to rest in a system with damping, which are caused by a sudden change of state.

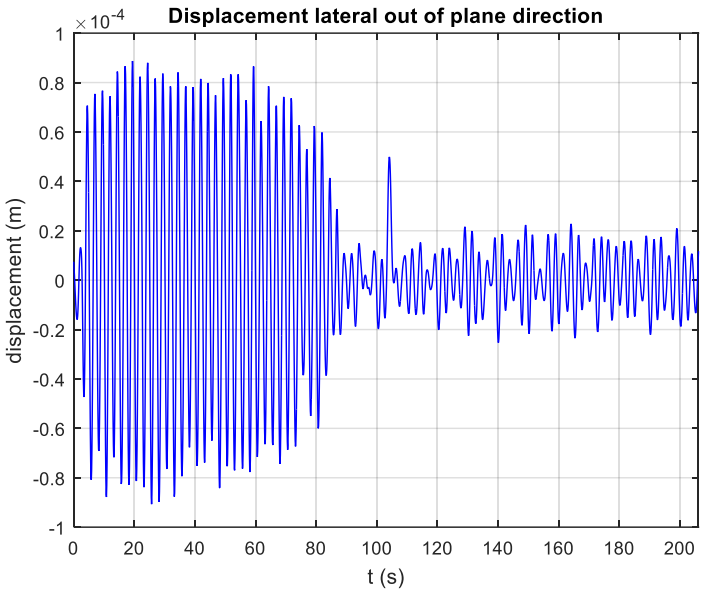

Figure 3.38 Displacement of the mass in the lateral out of plane direction

The lateral in plane displacements of the mass are shown in Figure 3.39 showing the results from the simulation in blue line and the experimental testing in black line. The displacements shown for the simulation model are much smaller than the experimental testing as the model does not accommodate the rotation of the mass during the whirling motion of the rope. The displacements from the experimental testing start increasing up to $2x10^{-4}$m due to the whirling motion of the rope.

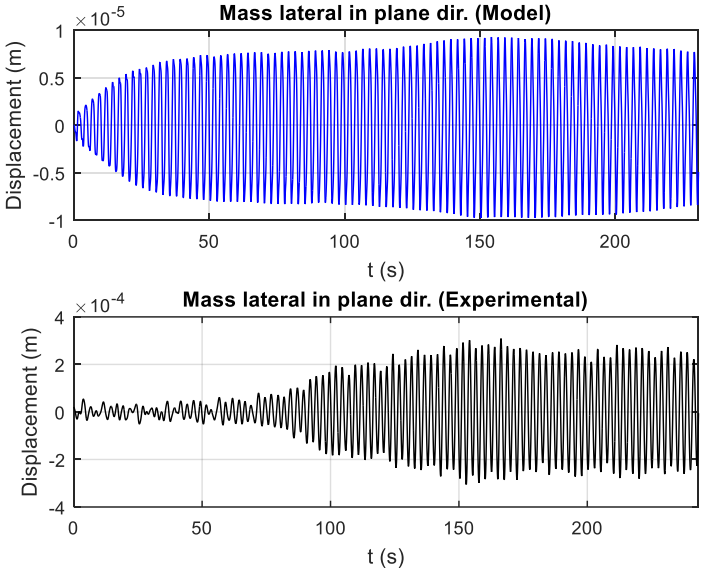

Figure 3.39 Displacement of the mass in the lateral in plane direction from the simulation and the experimental testing

The FFT spectrum of the mass in the lateral in plane over the entire time span for the simulation and the experimental testing are shown in Figure 3.40, where the predominant frequency of 0.40 Hz is shown.

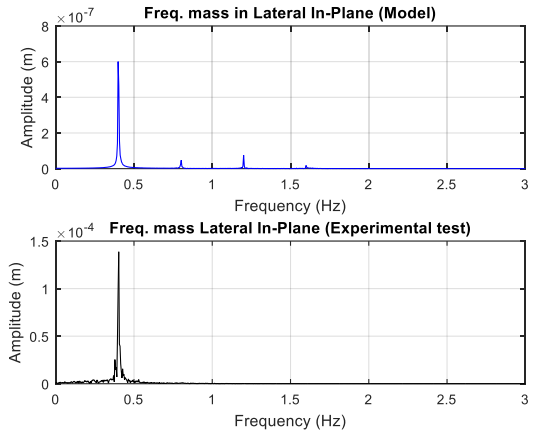

Figure 3.40 Frequency of the mass of the lateral in plane displacements of the simulation and experimental testing

The displacements of the mass in the longitudinal direction are shown in Figure 3.41 comparing the response from the simulation represented by a blue line and the response from the experimental model. The high amplitudes in the sensor data is due to the transient phenomena possibly caused by misalignment in the system. As it can be seen from the results after the initial 100.0 seconds the transient vanishes and the measured response amplitudes are within the range of the response predicted by the simulation. The steel frame was lubricated before every test exactly at the sliding guiding system of the mass and steel frame. After 100 seconds the longitudinal displacements of the mass in the experimental testing got lowered because the lateral in plane displacement of the mass started to appear.

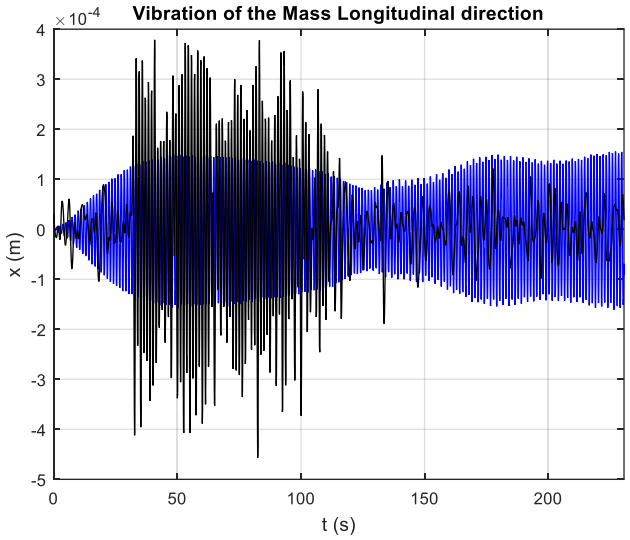

Figure 3.41 Mass displacement in the longitudinal direction comparing the response from the simulation represented by a blue line and the experimental testing represented by a black line

The FFT spectrum over the entire time span from the displacement of the mass in the longitudinal direction of the simulation and the experimental testing are shown in Figure 3.42.

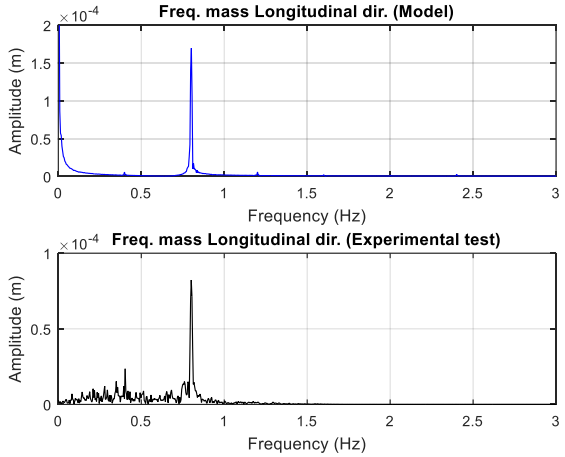

Figure 3.42 FFT spectrum over the entire time span from the longitudinal displacements of the mass of the simulation and experimental testing

The predominant frequency is 0.80 Hz which is twice the frequency of excitation to the rope, which is coming from equation (3.102) in the longitudinal direction. Thus, the mass is excited at $2\lambda_v$ due to primary external resonance.

As it was seen in the experimental testing the rotation of the mass does have influence in the lateral in plane, out of plane, and longitudinal displacements of the mass. Simplifications were made to track and understand the fundamental features and the behaviour of the system.

However, the rotational mode of the mass was observed. The imperfections or misalignment at the mass assembly, that are responsible for any additional looseness or misalignment have been difficult to eliminate and to accommodate in the current model due to project constraints. Future work is planned to improve the model.

In a real elevator system due to ever increasing efforts to achieve good ride quality characteristics, the imperfections in the elevator car mass and its guiding system are negligible. Thus, the proposed model assumptions can be applied in a full elevator system to predict the behaviour of the suspension and compensating ropes with the influence of the elevator car, compensating sheave, and counterweight.

4. Stationary Model of a High – Rise Elevator System

4.1 Description of the vibration model

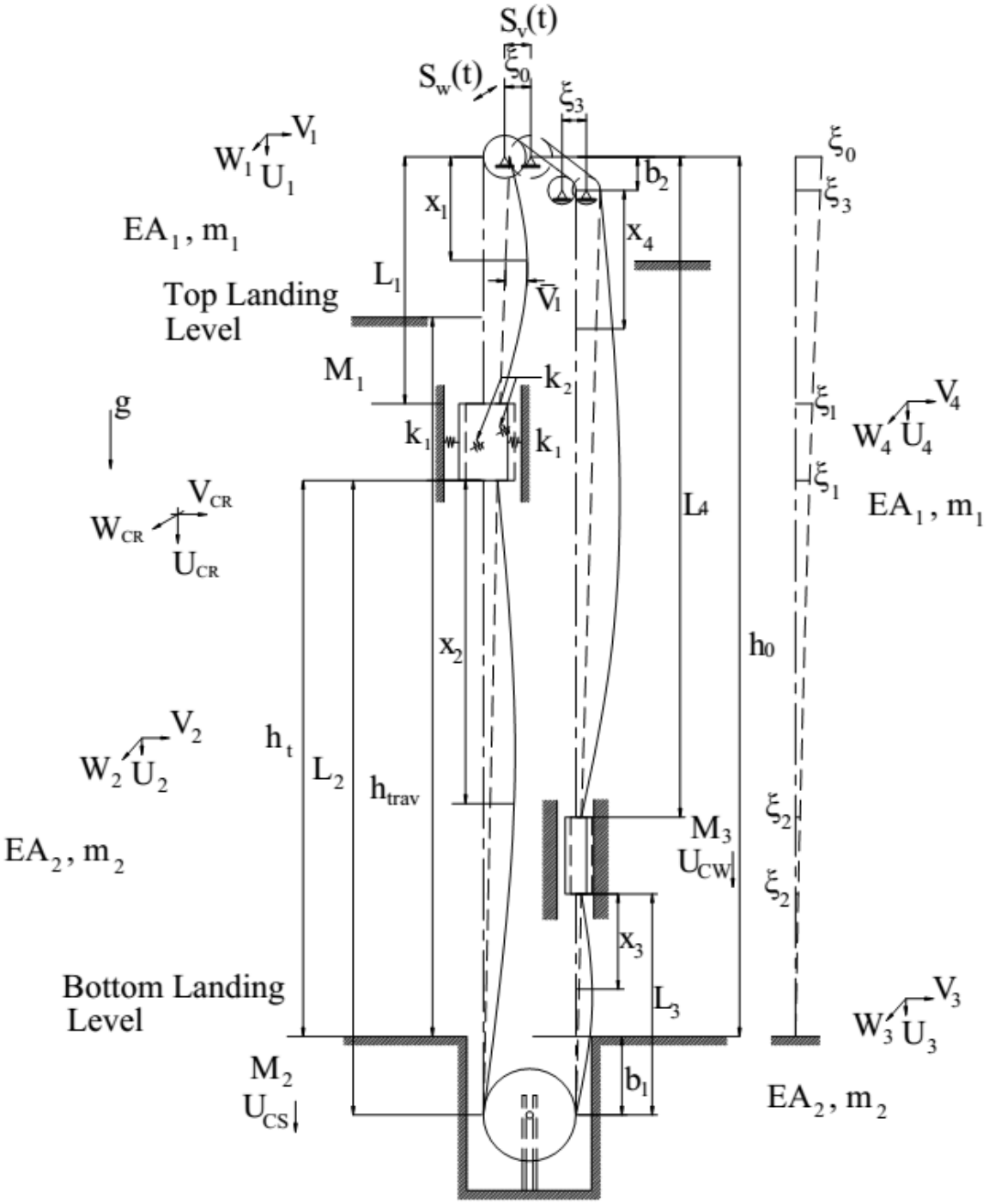

Figure 4.1 Drawing of the full stationary elevator system

In Chapter 3 was developed a mathematical model of a rope and mass system considering the lateral in plane and out of plane displacements of the rope and the lateral in plane and

longitudinal displacements of a mass attached to the end of the rope. The results obtained from the mathematical model were in the same range as with the experimental results. The mathematical model had certain limitations in predicting the rotational motion of the mass due to the imperfections or misalignments at the mass assembly that are responsible for any additional looseness or misalignment. Interesting events were discussed like the interaction between the lateral displacements of the rope coupled with the longitudinal and lateral displacements of the mass, the whirling motion of the rope through the auto parametric terms, the lateral external frequency in which the rope was excited at the top, excited the mass in the longitudinal direction at twice the frequency which is primary external excitation. Thus, the proposed assumptions to develop the mathematical model can be applied to a full elevator system to predict the behaviour of the suspension ropes, compensating ropes, elevator car, compensating sheave, and counterweight.

The model of an elevator system with an elevator car of mass M_1, compensating sheave of mass M_2, and counterweight of mass M_3, is depicted in Figure 4.1. The suspension and compensating ropes have mass per unit length m_1 and m_2, constant elastic modulus EA_1 and EA_2, respectively. The parameter b_1 represents the distance measured from the bottom landing level to the center of the compensating sheave. The parameter b_2 denotes the distance measured from the center of the traction sheave to the center of the diverter pulley and h_0 represents the distance measured from the bottom landing level to the center of the traction sheave. The parameter h_{trav} is the height of travel of the elevator car. The elevator car, compensating sheave and counterweight are considered as point masses, thus the height is neglected. The parameter h_t is the position of the elevator car measured from the bottom landing level to the elevator car.

The lengths of the suspension rope and of the compensating rope are defined as follows. The length of the suspension rope at the car side measured from the center of the traction sheave to the termination at the car crosshead beam is denoted by L_1. The length of the compensating rope at the car side measured from the termination at the car bottom to the center of the compensating sheave is denoted as L_2. The length of the compensating rope at the counterweight side measured from the termination at the counterweight to the center of the compensating sheave is denoted by L_3. The length of the suspension rope at the counterweight side measured from the center of the diverter pulley to the termination at the counterweight end is denoted by L_4. The mass moment of inertia of the diverter pulley and the short stretch of the suspension rope between the pulley and the traction sheave is neglected in the simulation model.

The response of the elevator ropes subjected to dynamic loading due to the building sway are represented by the lateral in-plane and lateral out of plane displacements denoted as $V_i(x_i,t)$ and $W_i(x_i,t)$ where the subscript $i=1,2,3,4$ corresponds to the sections of the ropes of length L_1, L_2, L_3, and L_4, respectively. The displacements of the ropes relative to the configuration of the ropes when they are stretched by the structure motion are represented by $\bar{V}_i(x_i,t)$ and $\bar{W}_i(x_i,t)$. The lateral in-plane and lateral out of plane motions of the ropes are coupled with the longitudinal motions of the ropes that are denoted as $U_i(x_i,t)$. The parameter x_i is the spatial coordinate of each rope measured from the top support of each rope. The longitudinal motions of the car, compensating sheave and counterweight are denoted as $U_{CR}(t)$, $U_{CS}(t)$, and $U_{CW}(t)$, respectively. The lateral in plane and out of plane motions of the car denoted as $V_{CR}(t)=V_1(L_1,t)=V_2(0,t)$ and $W_{CR}(t)=W_1(L_1,t)=W_2(0,t)$. The lateral motions of the counterweight are not considered in this mathematical model. More emphasis was placed at the car side due to see the effects to the ride quality of the elevator car. The compensating sheave and counterweight are restricted to move in the longitudinal direction. The parameter k_1 and k_2 represents the combined stiffness of the roller guides and guide rails in the lateral in plane and the lateral out of plane direction, respectively. The parameters k_1 and k_2 can be estimated as it was discussed in Salamaliki-Simpson (2009). The lateral displacements of the structure corresponding to the top of the building at the machine room level and to the position of the car and counterweight are represented as $\xi_0(t)$, $\xi_1(t)$, $\xi_2(t)$, and $\xi_3(t)$.

To develop the mathematical model the following assumptions were taken into account:

a) All ropes are treated as strings.

b) The elastic modulus EA of the ropes is considered constant.

c) The bending stiffness of all ropes is neglected.

d) No interactions between the ropes are accounted for in the mathematical model.

e) The elevator car, compensating sheave and counterweight are treated as concentrated mass elements.

f) The elevator system does not affect the dynamics of the building.

g) Lateral damping of suspension and compensating ropes in all modes is equal to the first lateral modal damping ratio.

h) Longitudinal damping of the elevator car, compensating sheave, and counterweight are considered with longitudinal damping ratios.

i) The $S_V(t) = A_V \sin(\lambda_V t)$ and $S_W(t) = A_W \sin(\lambda_W t)$ are the displacement applied by the building at the machine room level in the lateral in plane and out of plane directions.

j) The building displacements are considered as a cantilever beam.

k) Elastic Green strain measure of the i^{th} rope considered as equation (4.1).

$$\varepsilon_i = U_{ix} + \frac{1}{2}\left(V_{ix}{}^2 + W_{ix}{}^2\right) \tag{4.1}$$

l) The constant g is gravity which is equal to 9.81 m/s^2.

m) The coupling between the suspension and compensating ropes at the car side due to the constraints at the elevator car by the springs k_1 and k_2 in both lateral in plane and out of plane directions are considered.

n) The elastic interface with the building at the counterweight side is neglected.

o) This is a stationary model, thus the elevator car is not subjected to an overall transport motion. A typical scenario is when the elevator car is positioned at a given height and the electromechanical brake is applied at the machine room level and the elevator car is stationary.

4.2 Derivation of the mathematical model

Hamilton's principle is used to derive the equations of motion, according to equation (3.17). The total potential energy is given by equation (3.18). The kinetic energy of the system is expressed as follows

$$\begin{aligned}\hat{Q} = &\sum_{i=1}^{4}\int_0^{L_i} \bar{Q}_i\left(U_{it}, V_{it}, W_{it}\right) dx_i + Q_{M_1}\left(\left(U_{CR}\right)_t, V_{1t}\left(L_1, t\right), W_{1t}\left(L_1, t\right)\right) \\ &+ Q_{M_2}\left(\left(U_{CS}\right)_t\right) + Q_{M_3}\left(\left(U_{CW}\right)_t\right)\end{aligned} \tag{4.2}$$

The kinetic energy density of the i^{th} rope are expressed as

$$\bar{Q}_i = \frac{1}{2} m_i \left[\left(\frac{\partial U_i}{\partial t}\right)^2 + \left(\frac{\partial V_i}{\partial t}\right)^2 + \left(\frac{\partial W_i}{\partial t}\right)^2\right] \tag{4.3}$$

The kinetic energy of each mass are given as

$$Q_{M_1} = \frac{1}{2} M_1 \left[\left(\frac{\partial V_1(L_1,t)}{\partial t} \right)^2 + \left(\frac{\partial U_{CR}}{\partial t} \right)^2 + \left(\frac{\partial W_1(L_1,t)}{\partial t} \right)^2 \right] \tag{4.4}$$

$$Q_{M_2} = \frac{1}{2} M_2 \left[\left(\frac{\partial U_{CS}}{\partial t} \right)^2 \right] \tag{4.5}$$

$$Q_{M_3} = \frac{1}{2} M_3 \left[\left(\frac{\partial U_{CW}}{\partial t} \right)^2 \right] \tag{4.6}$$

Assuming that the constant energy accumulated into the system during the initial static deflection is neglected, the elastic strain energy of the rope and the equivalent spring element between elevator car and guide rails in the lateral directions is given by equations (4.7) (4.8), respectively.

$$\Pi_e = \sum_{i=1}^{4} \int_0^{L_i} \hat{\Pi}_{ie}(U_{ix}, V_{ix}, W_{ix}) dx_i \tag{4.7}$$

$$\Pi_K = \Pi_K^V \left[V_1(L_1,t) \right] + \Pi_K^W \left[W_1(L_1,t) \right] \tag{4.8}$$

where

$$\hat{\Pi}_{ie} = \left(T_i(x_i) + \frac{1}{2} E A_i \varepsilon_i \right) \varepsilon_i \tag{4.9}$$

$$\Pi_K^V = 2\left(\frac{1}{2}\right) k_1 \left(V_1(L_1,t) - f_5^v \right)^2 \tag{4.10}$$

$$\Pi_K^W = 2\left(\frac{1}{2}\right) k_2 \left(W_1(L_1,t) - f_5^w \right)^2 \tag{4.11}$$

The mean quasi static rope tension is represented by $T_i(x_i)$ and the rope strain measure is given in terms of Green's symmetric strain tensor represented in equation (4.1), where the expression $()_x$ denotes partial derivatives with respect to x. The absolute lateral in plane and out of plane displacements of the elevator car are represented as $V_1(L_1,t)$ and $W_1(L_1,t)$, respectively. The displacements of the spring attachment of the elevator car and the building structure in lateral in plane and out of plane direction are represented as f_5^v and f_5^w, defined as $f_5^v(t) = \psi_1 \mathrm{A}_v \sin(\lambda_v t)$ and $f_5^w(t) = \psi_1 \mathrm{A}_w \sin(\lambda_w t)$ are derived further in the mathematical model. This type of base excitation to the springs is due to the interaction between the guide

rails and roller guides that are being excited by the building displacements according to position of the elevator car in the shaft. The gravitational potential energy is given in terms of the dynamic deflections as

$$\Pi_g = \sum_{i=1}^{4} \int_0^{L_i} \hat{\Pi}_{ig}(U_i)dx_i - M_1 g U_{CR} - M_2 g U_{CS} - M_3 g U_{CW} \tag{4.12}$$

Potential Energy due to gravity of the i^{th} rope

$$\hat{\Pi}_{ig} = -m_i g U_i \tag{4.13}$$

Hamilton principle requires that any virtual displacement, arbitrary between two instants t_1 and t_2, vanishes at the end of the time interval, so that

$$\begin{aligned} &\delta U_i(x_i,t) = \delta V_i(x_i,t) = \delta W_i(x_i,t) = 0 \\ &\delta U_{CR} = \delta U_{CS} = \delta U_{CW} = \delta V_1(L_1,t) = \delta W_1(L_1,t) = 0 \end{aligned} \quad \text{for } 0 \le x_i \le L_i \text{ at } t_1, t_2 \tag{4.14}$$

Applying into (3.17) equations (4.2), (4.7), (4.8), and (4.12) the following equation result

$$\int_{t_1}^{t_2} \left(\begin{aligned} &\sum_{i=1}^{4} \int_0^{L_i} \left(\delta \bar{Q}_i(U_{it},V_{it},W_{it}) - \delta \hat{\Pi}_{ig}(U_i) - \delta \hat{\Pi}_{ie}(U_{ix},V_{ix},W_{ix}) \right) dx_i + \\ &\delta Q_{M_1}\left(V_{1t}(L_1,t), W_{1t}(L_1,t), (U_{CR})_t\right) + \delta Q_{M_2}\left((U_{CS})_t\right) \\ &+ \delta Q_{M_3}\left((U_{CW})_t\right) + M_1 g \delta U_{CR} + M_2 g \delta U_{CS} + M_3 g \delta U_{CW} \\ &- \delta \Pi_{\kappa}^{V}\left(V_1(L_1,t)\right) - \delta \Pi_{\kappa}^{W}\left(W_1(L_1,t)\right) \end{aligned} \right) dt = 0 \tag{4.15}$$

where

$$\delta \bar{Q}_i = \left(\frac{\partial \bar{Q}_i}{\partial U_{it}}\right)\delta U_{it} + \left(\frac{\partial \bar{Q}_i}{\partial V_{it}}\right)\delta V_{it} + \left(\frac{\partial \bar{Q}_i}{\partial W_{it}}\right)\delta W_{it} \tag{4.16}$$

$$\delta Q_{M_1} = \left(\frac{\partial Q_{M_1}}{\partial (U_{CR})_t}\right)\delta (U_{CR})_t + \left(\frac{\partial Q_{M_1}}{\partial V_{1t}(L_1,t)}\right)\delta V_{1t}(L_1,t) + \left(\frac{\partial Q_{M_1}}{\partial W_{1t}(L_1,t)}\right)\delta W_{1t}(L_1,t) \tag{4.17}$$

$$\delta Q_{M_2} = \left(\frac{\partial Q_{M_2}}{\partial (U_{CS})_t}\right)\delta (U_{CS})_t \tag{4.18}$$

$$\delta Q_{M_3} = \left(\frac{\partial Q_{M_3}}{\partial (U_{CW})_t}\right)\delta (U_{CW})_t \tag{4.19}$$

$$\delta\hat{\Pi}_{ie} = \left(\frac{\partial\hat{\Pi}_{ie}}{\partial U_{ix}}\right)\delta U_{ix} + \left(\frac{\partial\hat{\Pi}_{ie}}{\partial V_{ix}}\right)\delta V_{ix} + \left(\frac{\partial\hat{\Pi}_{ie}}{\partial W_{ix}}\right)\delta W_{ix} \tag{4.20}$$

$$\delta\hat{\Pi}_{ig} = -m_i g\delta U_i \tag{4.21}$$

$$\delta\Pi_K^V = \frac{\partial\Pi_K^V}{\partial V_1(L_1,t)}\delta V_1(L_1,t) \tag{4.22}$$

$$\delta\Pi_K^W = \frac{\partial\Pi_K^W}{\partial W_1(L_1,t)}\delta W_1(L_1,t) \tag{4.23}$$

Integrating equation (4.16) in respect to *t* and *x* the following equation is derived

$$\int_{t_1}^{t_2}\left(\int_0^{L_i}\delta\bar{Q}_i dx\right)dt = \int_{t_1}^{t_2}\left(\int_0^{L_i}\left(\left(\frac{\partial\bar{Q}_i}{\partial U_{it}}\right)\delta U_{it} + \left(\frac{\partial\bar{Q}_i}{\partial V_{it}}\right)\delta V_{it} + \left(\frac{\partial\bar{Q}_i}{\partial W_{it}}\right)\delta W_{it}\right)dx\right)dt \tag{4.24}$$

and

$$\int_{t_1}^{t_2}\delta\bar{Q}_i dt = \int_{t_1}^{t_2}\left(\frac{\partial\bar{Q}_i}{\partial U_{it}}\frac{\partial}{\partial t}(\delta U_i) + \frac{\partial\bar{Q}_i}{\partial V_{it}}\frac{\partial}{\partial t}(\delta V_i) + \frac{\partial\bar{Q}_i}{\partial W_{it}}\frac{\partial}{\partial t}(\delta W_i)\right)dt \tag{4.25}$$

Can be written as

$$\begin{aligned}\int_{t_1}^{t_2}\delta\bar{Q}_i dt &= \left[\frac{\partial\bar{Q}_i}{\partial U_{it}}\delta U_i\right]_{t_1}^{t_2} - \int_{t_1}^{t_2}\frac{\partial}{\partial t}\left(\frac{\partial\bar{Q}_i}{\partial U_{it}}\right)\delta U_i dt + \left[\frac{\partial\bar{Q}_i}{\partial V_{it}}\delta V_i\right]_{t_1}^{t_2} - \int_{t_1}^{t_2}\frac{\partial}{\partial t}\left(\frac{\partial\bar{Q}_i}{\partial V_{it}}\right)\delta V_i dt \\ &+ \left[\frac{\partial\bar{Q}_i}{\partial W_{it}}\delta W_i\right]_{t_1}^{t_2} - \int_{t_1}^{t_2}\frac{\partial}{\partial t}\left(\frac{\partial\bar{Q}_i}{\partial W_{it}}\right)\delta W_i dt\end{aligned} \tag{4.26}$$

According to equation (4.14) the terms in red in equation (4.26) are the virtual displacements which are 0 when evaluated between t_1 and t_2. Thus, equation (4.26) can be rewritten as equation (4.27).

$$\int_{t_1}^{t_2}\delta\bar{Q}_i dt = -\int_{t_1}^{t_2}\frac{\partial}{\partial t}\left(\frac{\partial\bar{Q}_i}{\partial U_{it}}\right)\delta U_i dt - \int_{t_1}^{t_2}\frac{\partial}{\partial t}\left(\frac{\partial\bar{Q}_i}{\partial V_{it}}\right)\delta V_i dt - \int_{t_1}^{t_2}\frac{\partial}{\partial t}\left(\frac{\partial\bar{Q}_i}{\partial W_{it}}\right)\delta W_i dt \tag{4.27}$$

Similarly

$$\begin{aligned}\int_{t_1}^{t_2}\delta Q_{M_1} dt &= -\int_{t_1}^{t_2}\frac{\partial}{\partial t}\left(\frac{\partial Q_{M_1}}{\partial(U_{CR})_t}\right)\delta U_{CR} dt - \int_{t_1}^{t_2}\frac{\partial}{\partial t}\left(\frac{\partial Q_{M_1}}{\partial V_{1t}(L_1,t)}\right)\delta V_{1t}(L_1,t)dt \\ &- \int_{t_1}^{t_2}\frac{\partial}{\partial t}\left(\frac{\partial Q_{M_1}}{\partial W_{1t}(L_1,t)}\right)\delta W_{1t}(L_1,t)dt\end{aligned} \tag{4.28}$$

$$\int_{t_1}^{t_2} \delta Q_{M_2} dt = -\int_{t_1}^{t_2} \frac{\partial}{\partial t}\left(\frac{\partial Q_{M_2}}{\partial \left(U_{CS}\right)_t} \right) \delta U_{CS} dt \tag{4.29}$$

$$\int_{t_1}^{t_2} \delta Q_{M_3} dt = -\int_{t_1}^{t_2} \frac{\partial}{\partial t}\left(\frac{\partial Q_{M_3}}{\partial \left(U_{CW}\right)_t} \right) \delta U_{CW} dt \tag{4.30}$$

$$\begin{aligned}\int_0^{L_i} \delta \hat{\Pi}_{ie} dx = &\left[\frac{\partial \hat{\Pi}_{ie}}{\partial U_{ix}} \delta U_i \right]_0^{L_i} - \int_0^{L_i} \frac{\partial}{\partial x}\left(\frac{\partial \hat{\Pi}_{ie}}{\partial U_{ix}} \right) \delta U_i dx_i + \left[\frac{\partial \hat{\Pi}_{ie}}{\partial V_{ix}} \delta V_i \right]_0^{L_i} - \int_0^{L_i} \frac{\partial}{\partial x}\left(\frac{\partial \hat{\Pi}_{ie}}{\partial V_{ix}} \right) \delta V_i dx_i \\ &+ \left[\frac{\partial \hat{\Pi}_{ie}}{\partial W_{ix}} \delta W_i \right]_0^{L_i} - \int_0^{L_i} \frac{\partial}{\partial x}\left(\frac{\partial \hat{\Pi}_{ie}}{\partial W_{ix}} \right) \delta W_i dx_i\end{aligned} \tag{4.31}$$

$$\int_{t_1}^{t_2} \delta \Pi_K^V dt = -\int_{t_1}^{t_2} \frac{\partial \Pi_K^V}{\partial V_1\left(L_1,t\right)} \delta V_1\left(L_1,t\right) dt \tag{4.32}$$

$$\int_{t_1}^{t_2} \delta \Pi_K^w dt = -\int_{t_1}^{t_2} \frac{\partial \Pi_K^w}{\partial W_1\left(L_1,t\right)} \delta W_1\left(L_1,t\right) dt \tag{4.33}$$

The boundary conditions are as follows:

$$V_1(0,t) = W_1(0,t) = \xi_0 \tag{4.34}$$

$$U_1(0,t) = V_2(L_2,t) = W_2(L_2,t) = V_3(L_3,t) = W_3(L_3,t) = U_4(0,t) = 0 \tag{4.35}$$

$$U_1(L_1,t) = U_2(0,t) = U_{CR} \tag{4.36}$$

$$V_1(L_1,t) = V_2\left(0,t\right) = W_1(L_1,t) = W_2\left(0,t\right) = \xi_1 \tag{4.37}$$

$$U_2(L_2,t) = U_3(L_3,t) = U_{CS} \tag{4.38}$$

$$V_3(0,t) = W_3(0,t) = V_4(L_4,t) = W_4(L_4,t) = \xi_2 \tag{4.39}$$

$$U_3(0,t) = U_4(L_4,t) = U_{CW} \tag{4.40}$$

$$V_4(0,t) = W_4(0,t) = \xi_3 \tag{4.41}$$

Applying into equation (4.15) equations (4.21), (4.27) to (4.41) the following equation is obtained

$$
\int_{t_1}^{t_2}\left(\begin{array}{l}
\sum_{i=1}^{4}\int_{0}^{L_i}\left(\begin{array}{l}
\left[-\frac{\partial}{\partial t}\left(\frac{\partial \bar{Q}_i}{\partial V_{it}}\right)+\frac{\partial}{\partial x}\left(\frac{\partial \hat{\Pi}_{ie}}{\partial V_{ix}}\right)\right]\delta V_i \\
+\left[-\frac{\partial}{\partial t}\left(\frac{\partial \bar{Q}_i}{\partial U_{it}}\right)+\frac{\partial}{\partial x}\left(\frac{\partial \hat{\Pi}_{ie}}{\partial U_{ix}}\right)+m_i g\right]\delta U_i \\
+\left[-\frac{\partial}{\partial t}\left(\frac{\partial \bar{Q}_i}{\partial W_{it}}\right)+\frac{\partial}{\partial x}\left(\frac{\partial \hat{\Pi}_{ie}}{\partial W_{ix}}\right)\right]\delta W_i
\end{array}\right)dx_i \\
+\left[-\frac{\partial}{\partial t}\left(\frac{\partial Q_{M_1}}{\partial V_{1t}(L_1,t)}\right)-\left.\frac{\partial \hat{\Pi}_{1e}}{\partial V_{1x}}\right|_{x=L_1}+\left.\frac{\partial \hat{\Pi}_{2e}}{\partial V_{2x}}\right|_{x=L_2}-\frac{\partial \Pi_K^V}{\partial V_1(L_1,t)}\right]\delta V_1(L_1,t) \\
+\left[-\frac{\partial}{\partial t}\left(\frac{\partial Q_{M_1}}{\partial W_{1t}(L_1,t)}\right)-\left.\frac{\partial \hat{\Pi}_{1e}}{\partial W_{1x}}\right|_{x=L_1}+\left.\frac{\partial \hat{\Pi}_{2e}}{\partial W_{2x}}\right|_{x=L_2}-\frac{\partial \Pi_K^W}{\partial W_1(L_1,t)}\right]\delta W_1(L_1,t) \\
+\left[-\frac{\partial}{\partial t}\left(\frac{\partial E_{M_1}}{\partial (U_{CR})_t}\right)-\left.\frac{\partial \hat{\Pi}_{1e}}{\partial U_{1x}}\right|_{x=L_1}+\left.\frac{\partial \hat{\Pi}_{2e}}{\partial U_{2x}}\right|_{x=0}+M_1 g\right]\delta U_{CR} \\
+\left[-\frac{\partial}{\partial t}\left(\frac{\partial E_{M_2}}{\partial (U_{CS})_t}\right)-\left.\frac{\partial \hat{\Pi}_{2e}}{\partial U_{2x}}\right|_{x=L_2}-\left.\frac{\partial \hat{\Pi}_{3e}}{\partial U_{3x}}\right|_{x=L_3}+M_2 g\right]\delta U_{CS} \\
+\left[-\frac{\partial}{\partial t}\left(\frac{\partial E_{M_3}}{\partial (U_{CW})_t}\right)-\left.\frac{\partial \hat{\Pi}_{4e}}{\partial U_{4x}}\right|_{x=L_4}+\left.\frac{\partial \hat{\Pi}_{3e}}{\partial U_{3x}}\right|_{x=L_3}+M_3 g\right]\delta U_{CW}
\end{array}\right)dt=0 \tag{4.42}
$$

The virtual displacement $\delta U_i, \delta V_i, \delta W_i, \delta U_{CR}, \delta U_{CS}, \delta U_{CW}, \delta V_1(L_1,t), \delta W_1(L_1,t)$ are arbitrary and the above equation can only be valid for all the values of the virtual displacement if

$$
\frac{\partial}{\partial t}\left(\frac{\partial \bar{Q}_i}{\partial V_{it}}\right)-\frac{\partial}{\partial x}\left(\frac{\partial \hat{\Pi}_{ie}}{\partial V_{ix}}\right)=0 \tag{4.43}
$$

$$
\frac{\partial}{\partial t}\left(\frac{\partial \bar{Q}_i}{\partial U_{it}}\right)-\frac{\partial}{\partial x}\left(\frac{\partial \hat{\Pi}_{ie}}{\partial U_{ix}}\right)-m_i g=0 \tag{4.44}
$$

$$
\frac{\partial}{\partial t}\left(\frac{\partial \bar{Q}_i}{\partial W_{it}}\right)-\frac{\partial}{\partial x}\left(\frac{\partial \hat{\Pi}_{ie}}{\partial W_{ix}}\right)=0 \tag{4.45}
$$

$$
\frac{\partial}{\partial t}\left(\frac{\partial Q_{M_1}}{\partial V_{1t}(L_1,t)}\right)+\left.\frac{\partial \hat{\Pi}_{1e}}{\partial V_{1x}}\right|_{x=L_1}-\left.\frac{\partial \hat{\Pi}_{2e}}{\partial V_{2x}}\right|_{x=L_2}+\frac{\partial \Pi_K^V}{\partial V_1(L_1,t)}=0 \tag{4.46}
$$

$$
\frac{\partial}{\partial t}\left(\frac{\partial Q_{M_1}}{\partial W_{1t}(L_1,t)}\right)+\left.\frac{\partial \hat{\Pi}_{1e}}{\partial W_{1x}}\right|_{x=L_1}-\left.\frac{\partial \hat{\Pi}_{2e}}{\partial W_{2x}}\right|_{x=L_2}+\frac{\partial \Pi_K^W}{\partial W_1(L_1,t)}=0 \tag{4.47}
$$

$$\frac{\partial}{\partial t}\left(\frac{\partial Q_{M_1}}{\partial\left(U_{CR}\right)_t}\right)+\left.\frac{\partial\hat{\Pi}_{1e}}{\partial U_{1x}}\right|_{x=L_1}-\left.\frac{\partial\hat{\Pi}_{2e}}{\partial U_{2x}}\right|_{x=0}-M_1 g=0 \tag{4.48}$$

$$\frac{\partial}{\partial t}\left(\frac{\partial Q_{M_2}}{\partial\left(U_{CS}\right)_t}\right)+\left.\frac{\partial\hat{\Pi}_{2e}}{\partial U_{2x}}\right|_{x=L_2}+\left.\frac{\partial\hat{\Pi}_{3e}}{\partial U_{3x}}\right|_{x=L_3}-M_2 g=0 \tag{4.49}$$

$$\frac{\partial}{\partial t}\left(\frac{\partial Q_{M_3}}{\partial\left(U_{CW}\right)_t}\right)+\left.\frac{\partial\hat{\Pi}_{4e}}{\partial U_{4x}}\right|_{x=L_4}-\left.\frac{\partial\hat{\Pi}_{3e}}{\partial U_{3x}}\right|_{x=L_3}-M_3 g=0 \tag{4.50}$$

Substituting the equations (4.3) to (4.11) into equations (4.43) to (4.50) the stationary and nonlinear equations of motion are derived. The equations (4.51) to (4.53) describe the dynamics of the i^{th} rope in the elevator system, where *i=1,2,3, and 4.*

$$\begin{aligned}&m_i V_{itt}-T_{ix}V_{ix}-EA_i\left(U_{ix}+\frac{1}{2}\left(V_{ix}{}^2+W_{ix}{}^2\right)\right)_x V_{ix}\\&-T_i V_{ixx}-EA_i\left(U_{ix}+\frac{1}{2}\left(V_{ix}{}^2+W_{ix}{}^2\right)\right)V_{ixx}=0\end{aligned} \tag{4.51}$$

$$\begin{aligned}&m_i W_{itt}-T_{ix}W_{ix}-EA_i\left(U_{ix}+\frac{1}{2}\left(V_{ix}{}^2+W_{ix}{}^2\right)\right)_x W_{ix}\\&-T_i W_{ixx}-EA_i\left(U_{ix}+\frac{1}{2}\left(V_{ix}{}^2+W_{ix}{}^2\right)\right)W_{ixx}=0\end{aligned} \tag{4.52}$$

$$m_i U_{itt}-T_{ix}-EA_i\left(U_{ix}+\frac{1}{2}\left(V_{ix}{}^2+W_{ix}{}^2\right)\right)_x-m_i g=0 \tag{4.53}$$

The equations (4.54) and (4.55) are the boundary conditions at $x_1=L_1$ in the lateral in plane and lateral out of plane direction for the elevator car.

$$\begin{aligned}&M_1 V_{1tt}\left(L_1,t\right)+\left(T_1(\mathrm{x})+EA_1\left(U_{1x}+\frac{1}{2}\left(V_{1x}{}^2+W_{1x}{}^2\right)\right)\Big|_{x_1=L_1}\right)V_{1x}\Big|_{x_1=L_1}\\&-\left(T_2(\mathrm{x})+EA_2\left(U_{2x}+\frac{1}{2}\left(V_{2x}{}^2+W_{2x}{}^2\right)\right)\Big|_{x_2=L_2}\right)V_{2x}\Big|_{x_2=0}+2k_1V_1\left(L_1,t\right)-2k_1 f_5^{v}=0\end{aligned} \tag{4.54}$$

$$\begin{aligned}&M_1 W_{1tt}\left(L_1,t\right)+\left(T_1(\mathrm{x})+EA_1\left(U_{1x}+\frac{1}{2}\left(V_{1x}{}^2+W_{1x}{}^2\right)\right)\Big|_{x_1=L_1}\right)W_{1x}\Big|_{x_1=L_1}\\&-\left(T_2(\mathrm{x})+EA_2\left(U_{2x}+\frac{1}{2}\left(V_{2x}{}^2+W_{2x}{}^2\right)\right)\Big|_{x_2=L_2}\right)W_{2x}\Big|_{x_2=0}+2k_2W_1\left(L_1,t\right)-2k_2 f_5^{w}=0\end{aligned} \tag{4.55}$$

The equations (4.56) to (4.58) are the boundary conditions at $x_1=L_1$ and $x_2=0$, $x_2=L_2$ and $x_3=L_3$, $x_3=0$, and $x_4=L_4$ in the longitudinal direction for the elevator car, compensating sheave, and counterweight respectively.

$$\begin{aligned} &M_1\left(U_{CR}\right)_{tt}+T_1(\mathrm{L}_1)+EA_1\left(U_{1x}+\frac{1}{2}\left(V_{1x}{}^2+W_{1x}{}^2\right)\right)\Big|_{x=L_1} \\ &-T_2(0)-EA_2\left(U_{2x}+\frac{1}{2}\left(V_{2x}{}^2+W_{2x}{}^2\right)\right)\Big|_{x=0}-M_1g=0 \end{aligned} \tag{4.56}$$

$$\begin{aligned} &M_2\left(U_{CS}\right)_{tt}+T_2(\mathrm{L}_2)+EA_2\left(U_{2x}+\frac{1}{2}\left(V_{2x}{}^2+W_{2x}{}^2\right)\right)\Big|_{x=L_2} \\ &+T_3(\mathrm{L}_3)+EA_2\left(U_{3x}+\frac{1}{2}\left(V_{3x}{}^2+W_{3x}{}^2\right)\right)\Big|_{x=L_3}-M_2g=0 \end{aligned} \tag{4.57}$$

$$\begin{aligned} &M_3\left(U_{CW}\right)_{tt}+T_4(\mathrm{L}_4)+EA_1\left(U_{4x}+\frac{1}{2}\left(V_{4x}{}^2+W_{4x}{}^2\right)\right)\Big|_{x=L_4} \\ &-T_3(0)-EA_2\left(U_{3x}+\frac{1}{2}\left(V_{3x}{}^2+W_{3x}{}^2\right)\right)\Big|_{x=0}-M_3g=0 \end{aligned} \tag{4.58}$$

From Figure 4.1 all tensions are derived by balance of forces which are represented by equations (4.59) to (4.62).

$$T_1(x_1)=\left(M_1+m_1\left(L_1-x\right)+m_2L_2+\frac{M_2}{2}\right)g \tag{4.59}$$

$$T_2(x_2)=\left(\frac{M_2}{2}+m_2\left(L_2-x_2\right)\right)g \tag{4.60}$$

$$T_3(x_3)=\left(\frac{M_2}{2}+m_2\left(L_3-x_3\right)\right)g \tag{4.61}$$

$$T_4(x_4)=\left(M_3+m_1\left(L_4-x_4\right)+m_2L_3+\frac{M_2}{2}\right)g \tag{4.62}$$

The elevator system is excited by the displacements at the machine room level in the lateral in plane and out of plane direction represented by equations (4.63) and (4.64).

$$S_v=A_v\sin\left(\lambda_v t\right) \tag{4.63}$$

$$S_w=A_w\sin\left(\lambda_w t\right) \tag{4.64}$$

The overall lateral in plane displacements of each rope are represented by equations (4.65) to (4.68).

$$\mathrm{V}_1(x_1,t)=\bar{V}_1(x_1,t)+S_v(t)\left(1+(\psi_1-1)\frac{x_1}{L_1}\right) \tag{4.65}$$

$$\mathrm{V}_2(x_2,t)=\bar{V}_2(x_2,t)+S_v(t)\psi_2\left(1-\frac{x_2}{L_2}\right) \tag{4.66}$$

$$\mathrm{V}_3(x_3,t)=\bar{V}_3(x_3,t)+S_v(t)\psi_3\left(1-\frac{x_3}{L_3}\right) \tag{4.67}$$

$$\mathrm{V}_4(x_4,t)=\bar{V}_4(x_4,t)+S_v(t)\left(\psi_5+(\psi_4-\psi_5)\frac{x_4}{L_4}\right) \tag{4.68}$$

The overall lateral out of plane displacements of each rope are represented by equations (4.69) to (4.72).

$$W_1(x_1,t)=\bar{W}_1(x_1,t)+S_w(t)\left(1+(\psi_1-1)\frac{x_1}{L_1}\right) \tag{4.69}$$

$$W_2(x_2,t)=\bar{W}_2(x_2,t)+S_w(t)\psi_2\left(1-\frac{x_2}{L_2}\right) \tag{4.70}$$

$$W_3(x_3,t)=\bar{W}_3(x_3,t)+S_w(t)\psi_3\left(1-\frac{x_3}{L_3}\right) \tag{4.71}$$

$$W_4(x_4,t)=\bar{W}_4(x_4,t)+S_w(t)\left(\psi_5+(\psi_4-\psi_5)\frac{x_4}{L_4}\right) \tag{4.72}$$

where $\bar{V}_i(x_i,t),\bar{W}_i(x_i,t)$ are the displacements of the rope relative to the configuration of each rope when it is stretched by the structure motion. Furthermore, ψ_1, ψ_2, ψ_3, ψ_4, and ψ_5 are the deformations obtained from the shape function $\psi(z)$ of a cantilever beam which is assumed to be related to the fundamental mode of the high rise building and is approximated by a cubic polynomial representing the lateral displacements of the structure corresponding to the top of the structure and to the position of the car and counterweight estimated by equations (4.73) to (4.77).

$$\psi_1=3\left(1-\frac{L_1}{h_0}\right)^2-2\left(1-\frac{L_1}{h_0}\right)^3 \tag{4.73}$$

$$\psi_2 = 3\left(\frac{L_2 - b_1}{h_0}\right)^2 - 2\left(\frac{L_2 - b_1}{h_0}\right)^3 \tag{4.74}$$

$$\psi_3 = 3\left(\frac{L_3 - b_1}{h_0}\right)^2 - 2\left(\frac{L_3 - b_1}{h_0}\right)^3 \tag{4.75}$$

$$\psi_4 = 3\left(1 - \frac{L_4 + b_2}{h_0}\right)^2 - 2\left(1 - \frac{L_4 + b_2}{h_0}\right)^3 \tag{4.76}$$

$$\psi_5 = 3\left(1 - \frac{b_2}{h_0}\right)^2 - 2\left(1 - \frac{b_2}{h_0}\right)^3 \tag{4.77}$$

The partial derivative with respect to *t* for the lateral in plane are shown in equations (4.78) to (4.82).

$$V_{1tt} = \bar{V}_{1tt} - A_v\lambda_v^2 \sin(\lambda_v t) - A_v\lambda_v^2 \sin(\lambda_v t)\left(\frac{\psi_1 - 1}{L_1}\right)x_1 = \bar{V}_{1tt} - S_1^v - S_2^v x_1 \tag{4.78}$$

$$V_{1tt}(L_1, t) = \bar{V}_1(L_1, t)_{tt} - \psi_1 \mathrm{A}_v \lambda_v^2 \sin(\lambda_v t) = \bar{V}_1(L_1, t)_{tt} - S_7^v \tag{4.79}$$

$$V_{2tt} = \bar{V}_{2tt} - \psi_2 A_v\lambda_v^2 \sin(\lambda_v t) + \frac{\psi_2}{L_2} A_v\lambda_v^2 \sin(\lambda_v t)\, x_2 = \bar{V}_{2tt} - S_3^v + S_4^v x_2 \tag{4.80}$$

$$V_{3tt} = \bar{V}_{3tt} - \psi_3 A_v\lambda_v^2 \sin(\lambda_v t) + \frac{\psi_3}{L_3} A_v\lambda_v^2 \sin(\lambda_v t)\, x_3 = \bar{V}_{3tt} - S_9^v + S_{10}^v x_3 \tag{4.81}$$

$$V_{4tt} = \bar{V}_{4tt} - \psi_5 A_v\lambda_v^2 \sin(\lambda_v t) - A_v\lambda_v^2 \sin(\lambda_v t)\left(\frac{\psi_4 - \psi_5}{L_4}\right)x_4 = \bar{V}_{4tt} - S_5^v - S_6^v x_4 \tag{4.82}$$

The partial derivative with respect to *x* for the lateral in plane are shown in equations (4.83) to (4.91).

$$V_{1x} = \bar{V}_{1x} + \left(\frac{\psi_1 - 1}{L_1}\right)\mathrm{A}_v \sin(\lambda_v t) = \bar{V}_{1x} - f_1^v \tag{4.83}$$

$$V_{2x} = \bar{V}_{2x} + \left(\frac{\psi_2}{L_2}\right)\mathrm{A}_v \sin(\lambda_v t) = \bar{V}_{2x} - f_2^v \tag{4.84}$$

$$V_{3x} = \bar{V}_{3x} - \left(\frac{\psi_3}{L_3}\right)\mathrm{A}_v \sin(\lambda_v t) = \bar{V}_{3x} - f_3^v \tag{4.85}$$

$$V_{4x} = \bar{V}_{4x} - \left(\frac{\psi_4 - \psi_5}{L_4} \right) \mathrm{A}_v \sin\left(\lambda_v t\right) = \bar{V}_{4x} - f_4^v \tag{4.86}$$

$$V_1\left(L_1, t\right) = \bar{V}_1\left(L_1, t\right) + \psi_1 \mathrm{A}_v \sin\left(\lambda_v t\right) = \bar{V}_1\left(L_1, t\right) + f_5^v \tag{4.87}$$

$$V_{1xx} = \bar{V}_{1xx} \tag{4.88}$$

$$V_{2xx} = \bar{V}_{2xx} \tag{4.89}$$

$$V_{3xx} = \bar{V}_{3xx} \tag{4.90}$$

$$V_{4xx} = \bar{V}_{4xx} \tag{4.91}$$

Similarly, the lateral out of plane direction derivative with respect to *x* and *t* can be deducted. Substituting equations (4.59) to (4.62) into equation (4.53) results in equation (4.92).

$$m_i U_{itt} - EA_i \left(U_{ix} + \frac{1}{2}\left(V_{ix}^{\ 2} + W_{ix}^{\ 2} \right) \right)_x = 0 \tag{4.92}$$

Considering that the longitudinal natural frequencies of the ropes are much higher than the lateral natural frequencies of the ropes, thus the inertia in the longitudinal direction can be neglected, resulting in equation (4.93).

$$EA_i \left(U_{ix} + \frac{1}{2}\left(V_{ix}^{\ 2} + W_{ix}^{\ 2} \right) \right)_x = 0 \tag{4.93}$$

The internal terms inside the parenthesis is represented by $e_i(t)$, which is shown in equation (4.94)

$$e_i\left(t\right) = U_{ix} + \frac{1}{2}\left(V_{ix}^{\ 2} + W_{ix}^{\ 2} \right) \tag{4.94}$$

Substituting equation (4.94) into equation (4.51) to (4.58) gives

$$m_i V_{itt} + T_{ix} V_{ix} - T_i V_{ixx} - EA_i e_i\left(t\right) V_{ixx} = 0 \tag{4.95}$$

$$m_i W_{itt} + T_{ix} W_{ix} - T_i W_{ixx} - EA_i e_i\left(t\right) W_{ixx} = 0 \tag{4.96}$$

$$\begin{aligned} &M_1 \bar{V}_1\left(L_1, t\right)_{tt} - M_1 S_7^v + T_1(\mathrm{L}_1)\bar{V}_{1x} - T_1(\mathrm{L}_1) f_1^v + EA_1 e_1\left(t\right)\bar{V}_{1x} - EA_1 e_1\left(t\right) f_1^v \\ &-T_2(0)\bar{V}_{2x} + T_2(0) f_2^v + EA_2 e_2\left(t\right)\bar{V}_{2x} - EA_2 e_2\left(t\right) f_2^v + 2k_1 \bar{V}_1\left(L_1, t\right) = 0 \end{aligned} \tag{4.97}$$

$$\begin{aligned} &M_1 \bar{W}_1\left(L_1, t\right)_{tt} - M_1 S_7^w + T_1(\mathrm{L}_1)\bar{W}_{1x} - T_1(\mathrm{L}_1) f_1^w + EA_1 e_1\left(t\right)\bar{W}_{1x} - EA_1 e_1\left(t\right) f_1^w \\ &-T_2(0)\bar{W}_{2x} + T_2(0) f_2^w + EA_2 e_2\left(t\right)\bar{W}_{2x} - EA_2 e_2\left(t\right) f_2^w + 2k_1 \bar{W}_1\left(L_1, t\right) = 0 \end{aligned} \tag{4.98}$$

$$M_1\left(U_{CR}\right)_{tt}+T_1(\mathrm{L}_1)+EA_1e_1\left(t\right)-T_2(0)-EA_2e_2\left(t\right)-M_1g=0 \tag{4.99}$$

$$M_2\left(U_{CS}\right)_{tt}+T_2(\mathrm{L}_2)+EA_2e_2\left(t\right)+T_3(\mathrm{L}_3)+EA_2e_3\left(t\right)-M_2g=0 \tag{4.100}$$

$$M_3\left(U_{CW}\right)_{tt}+T_4(\mathrm{L}_4)+EA_1e_4\left(t\right)-T_3(0)-EA_2e_3\left(t\right)-M_3g=0 \tag{4.101}$$

The boundary conditions at $x_1=0$ are $\bar{V}_1(0,t)=\bar{W}_1(0,t)=0$, at $x_1=L_1$ or $x_2=0$ are $\bar{V}_1\left(L_1,t\right)=\bar{V}_2\left(0,t\right)$ and $\bar{W}_1\left(L_1,t\right)=\bar{W}_2\left(0,t\right)$, and at $x_2=L_2$ are $\bar{V}_2(L_2,t)=\bar{W}_2(L_2,t)=0$. The linear natural modes of the lateral in plane and lateral out of plane motion for the suspension rope at the car side (rope 1) are given as equations (4.102) and (4.103).

$$\phi_{1n}\left(x_1\right)=sin(\beta_{1n}^{Lin}x_1) \tag{4.102}$$

$$\alpha_{1n}\left(x_1\right)=sin\left(\beta_{1n}^{Lout}x_1\right) \tag{4.103}$$

The linear natural modes of the lateral in plane and lateral out of plane motion for the compensating rope at the car side (rope 2) are represented by equations (4.104) and (4.105).

$$\phi_{2n}(x_2)=\sin\beta_{1n}^{Lin}L_1\cos\beta_{2n}^{Lin}x_2-\frac{\sin\beta_{1n}^{Lin}L_1\cos\beta_{2n}^{Lin}L_2}{\sin\beta_{2n}^{Lin}L_2}\sin\beta_{2n}^{Lin}x_2 \tag{4.104}$$

$$\alpha_{2n}(x_2)=\sin\beta_{1n}^{Lout}L_1\cos\beta_{2n}^{Lout}x_2-\frac{\sin\beta_{1n}^{Lout}L_1\cos\beta_{2n}^{Lout}L_2}{\sin\beta_{2n}^{Lout}L_2}\sin\beta_{2n}^{Lout}x_2 \tag{4.105}$$

The derivation of the linear natural modes of rope 1 and 2 are analysed in Appendix D. Where $\beta_{1n}^{Lin},\beta_{2n}^{Lin},\beta_{1n}^{Lout}$, and β_{2n}^{Lout} are the eigenvalues in lateral in plane and lateral out of plane direction for the suspension and compensating ropes at the car side, respectively. The natural frequency for the lateral in plane direction of both ropes can be obtained from equation (4.106), which is derived in Appendix D and in Appendix E are the orthogonality of modes.

$$\begin{aligned}
&\omega^{Lin}\sqrt{T_2m_2}\cos\left(\omega^{Lin}L_2\sqrt{\frac{m_2}{L_2}}\right)\sin\left(\omega^{Lin}L_1\sqrt{\frac{m_1}{L_1}}\right)\\
&+2k_1\sin\left(\omega^{Lin}L_2\sqrt{\frac{m_2}{L_2}}\right)\sin\left(\omega^{Lin}L_1\sqrt{\frac{m_1}{L_1}}\right)\\
&+\omega^{Lin}\sqrt{T_1m_1}\sin\left(\omega^{Lin}L_2\sqrt{\frac{m_2}{L_2}}\right)\cos\left(\omega^{Lin}L_1\sqrt{\frac{m_1}{L_1}}\right)\\
&-M_1\left(\omega^{Lin}\right)^2\sin\left(\omega^{Lin}L_2\sqrt{\frac{m_2}{L_2}}\right)\sin\left(\omega^{Lin}L_1\sqrt{\frac{m_1}{L_1}}\right)=0
\end{aligned} \tag{4.106}$$

The natural frequency for the lateral out of plane direction of both ropes can be obtained from equation (4.107), which is derived in Appendix D and in Appendix E are the orthogonality of modes.

$$\begin{aligned}
&\omega^{Lout}\sqrt{T_2 m_2}\cos\left(\omega^{Lout}L_2\sqrt{\frac{m_2}{L_2}}\right)\sin\left(\omega^{Lout}L_1\sqrt{\frac{m_1}{L_1}}\right)\\
&+2k_2\sin\left(\omega^{Lout}L_2\sqrt{\frac{m_2}{L_2}}\right)\sin\left(\omega^{Lout}L_1\sqrt{\frac{m_1}{L_1}}\right)\\
&+\omega^{Lout}\sqrt{T_1 m_1}\sin\left(\omega^{Lout}L_2\sqrt{\frac{m_2}{L_2}}\right)\cos\left(\omega^{Lout}L_1\sqrt{\frac{m_1}{L_1}}\right)\\
&-M_1\left(\omega^{Lout}\right)^2\sin\left(\omega^{Lout}L_2\sqrt{\frac{m_2}{L_2}}\right)\sin\left(\omega^{Lout}L_1\sqrt{\frac{m_1}{L_1}}\right)=0
\end{aligned} \tag{4.107}$$

The eigenvalues for the lateral in plane and out of plane direction for the suspension and compensating ropes at the counterweight side can be determined from equations (4.108) to (4.111).

$$\beta_{1n}^{Lin}=\omega_n^{Lin}\sqrt{\frac{m_1}{T_1}} \tag{4.108}$$

$$\beta_{2n}^{Lin}=\omega_n^{Lin}\sqrt{\frac{m_2}{T_2}} \tag{4.109}$$

$$\beta_{1n}^{Lout}=\omega_n^{Lout}\sqrt{\frac{m_1}{T_1}} \tag{4.110}$$

$$\beta_{2n}^{Lout}=\omega_n^{Lout}\sqrt{\frac{m_2}{T_2}} \tag{4.111}$$

Similarly, the boundary conditions at $x_3=0$, $x_3=L_3$, $x_4=0$, and $x_4=L_4$ are $\bar{V}_3(0,t)=\bar{W}_3(0,t)=\bar{V}_3(L_3,t)=\bar{W}_3(L_3,t)=\bar{V}_4(L_4,t)=\bar{W}_4(L_4,t)=\bar{V}_4(0,t)=\bar{W}_4(0,t)=0$. The linear natural modes of the lateral in plane and lateral out of plane motion are given as $\alpha_{in}=\phi_{in}=sin\left(\frac{n\pi}{L_i}x\right)$ where $\frac{n\pi}{L_i}$ are the eigenvalues in lateral in plane and lateral out of plane direction for the suspension and compensating rope at the counterweight side, respectively. The natural frequencies in the lateral in plane and out of plane direction are determined by equation (4.112) for ropes *i=3,4.*

$$\omega_{in}^{Lin} = \omega_{in}^{Lout} = \frac{n\pi}{L_i}\sqrt{\frac{T_i}{m_i}} \tag{4.112}$$

The equations of motion in (4.51) to (4.58) can be discretised by applying the Galerkin method. In this procedure the dynamic response of the system is approximated in the lateral in plane and lateral out of plane directions by the following expansions

$$\bar{V}_i(x_i,t) = \sum_{n=1}^{N} \phi_{in}(x_i)\,\mathrm{q}_{in}(t) \tag{4.113}$$

$$\bar{W}_i(x_i,t) = \sum_{n=1}^{N} \alpha_{in}(x_i)\,\mathrm{c}_{in}(t) \tag{4.114}$$

respectively, where q_{in}, c_{in} represent the generalized (modal) coordinates. For the suspension and compensating ropes at the car side the time dependent functions are $q_{1n}(t)=q_{2n}(t)$ due to the boundary conditions in (4.37). Substituting expansions (4.113) and (4.114) into equation (4.94) which can be expanded into equations (4.115) to (4.118).

$$\begin{aligned} e_1(t) &= \frac{U_{CR}}{L_1} + \frac{1}{2L_1}\sum_{j=1}^{N}\sum_{p=1}^{N} G_{jp}^{1Lin} q_{1j}(t) q_{1p}(t) + \frac{f_1^v}{L_1}\sum_{j=1}^{N} q_{1j}(t)\sin\left(\beta_{1j}^{Lin} L_1\right) + \frac{\left(f_1^v\right)^2}{2} \\ &+ \frac{1}{2L_1}\sum_{j=1}^{N}\sum_{p=1}^{N} G_{jp}^{1Lout} c_{1j}(t) c_{1p}(t) + \frac{f_1^w}{L_1}\sum_{j=1}^{N} c_{1j}(t)\sin\left(\beta_{1j}^{Lout} L_1\right) + \frac{\left(f_1^w\right)^2}{2} \end{aligned} \tag{4.115}$$

$$\begin{aligned} e_2(t) &= \frac{U_{CS}-U_{CR}}{L_2} + \frac{1}{2L_2}\sum_{j=1}^{N}\sum_{p=1}^{N} G_{jp}^{2Lin} q_{2j}(t) q_{2p}(t) + \frac{f_2^v}{L_2}\sum_{j=1}^{N} q_{2j}(t)\sin\left(\beta_{2j}^{Lin} L_2\right) + \frac{\left(f_2^v\right)^2}{2} \\ &+ \frac{1}{2L_2}\sum_{j=1}^{N}\sum_{p=1}^{N} G_{jp}^{2Lout} c_{2j}(t) c_{2p}(t) + \frac{f_2^w}{L_2}\sum_{j=1}^{N} c_{2j}(t)\sin\left(\beta_{2j}^{Lout} L_2\right) + \frac{\left(f_2^w\right)^2}{2} \end{aligned} \tag{4.116}$$

$$e_3(t) = \frac{U_{CS}-U_{CW}}{L_3} + \frac{1}{4}\sum_{j=1}^{N}\left(\frac{j\pi}{L_3}\right)^2 q_{3j}^2(t) + \frac{\left(f_3^v\right)^2}{2} + \frac{1}{4}\sum_{j=1}^{N}\left(\frac{j\pi}{L_3}\right)^2 c_{3j}^2(t) + \frac{\left(f_3^w\right)^2}{2} \tag{4.117}$$

$$e_4(t) = \frac{U_{CW}}{L_4} + \frac{1}{4}\sum_{j=1}^{N}\left(\frac{j\pi}{L_4}\right)^2 q_{4j}^2(t) + \frac{\left(f_4^v\right)^2}{2} + \frac{1}{4}\sum_{j=1}^{N}\left(\frac{j\pi}{L_4}\right)^2 c_{4j}^2(t) + \frac{\left(f_4^w\right)^2}{2} \tag{4.118}$$

Where $G_{jp}^{1Lin}, G_{jp}^{1Lout}, G_{jp}^{2Lin}$ and G_{jp}^{2Lout} are shown in Appendix F.

Substituting expansions (4.113) and (4.114) into (4.95) to (4.101) applying the orthogonality conditions with respect to the linear modes a system of nonlinear ordinary differential equations results as follows.

$$\ddot{q}_{1r}(t)+2\zeta_{1r}^{Lin}\omega_{1rr}^{Lin}\dot{q}_{1r}(t)+\left(\omega_{1r}^{Lin}\right)^2 q_{1r}(t)+\sum_{n=1}^{N}k_{1rn}^{Lin1}q_{1n}(t)+k_{1rn}^{Lin3}U_{CR}+k_{1rn}^{Lin4}U_{CS}$$
$$+\sum_{n=1}^{N}k_{1rn}^{Lin2}c_{1n}(t)+\sum_{n=1}^{N}\sum_{j=1}^{N}D_{irn}^{Lin1}q_{1j}(t)q_{1n}(t)+\sum_{n=1}^{N}\sum_{j=1}^{N}D_{1rn}^{Lin2}c_{1j}(t)q_{1n}(t)$$
$$+\sum_{n=1}^{N}\sum_{j=1}^{N}D_{1rn}^{Lin3}c_{1j}(t)c_{1n}(t)+\sum_{n=1}^{N}\sum_{j=1}^{N}\sum_{p=1}^{N}R1_{1rnjp}^{Lin}q_{1j}(t)q_{1p}(t)q_{1n}(t)$$
$$+\sum_{n=1}^{N}\sum_{j=1}^{N}\sum_{p=1}^{N}R2_{1rnjp}^{Lin}c_{1j}(t)c_{1p}(t)q_{1n}(t)+F_{1r}^{Lin}=0 \quad (4.119)$$

$$\ddot{c}_{1r}(t)+2\zeta_{1r}^{Lout}\omega_{1rr}^{Lout}\dot{c}_{1r}(t)+\left(\omega_{1r}^{Lout}\right)^2 c_{1r}(t)+\sum_{n=1}^{N}k_{1rn}^{Lout1}c_{1n}(t)+k_{1rn}^{Lout3}U_{CR}+k_{1rn}^{Lout4}U_{CS}$$
$$+\sum_{n=1}^{N}k_{1rn}^{Lout2}q_{1n}(t)+\sum_{n=1}^{N}\sum_{j=1}^{N}D_{irn}^{Lout1}q_{1j}(t)c_{1n}(t)+\sum_{n=1}^{N}\sum_{j=1}^{N}D_{1rn}^{Lout2}c_{1j}(t)c_{1n}(t)$$
$$+\sum_{n=1}^{N}\sum_{j=1}^{N}D_{1rn}^{Lout3}q_{1j}(t)q_{1n}(t)+\sum_{n=1}^{N}\sum_{j=1}^{N}\sum_{p=1}^{N}R1_{1rnjp}^{Lout}q_{1j}(t)q_{1p}(t)c_{1n}(t)$$
$$+\sum_{n=1}^{N}\sum_{j=1}^{N}\sum_{p=1}^{N}R2_{1rnjp}^{Lout}c_{1j}(t)c_{1p}(t)c_{1n}(t)+F_{1r}^{Lout}=0 \quad (4.120)$$

and for *i=3,4*

$$\ddot{q}_{ir}(t)+2\zeta_{ir}^{Lin}\omega_{irr}^{Lin}\dot{q}_{in}(t)+\left(\omega_{ir}^{Lin}\right)^2 q_{ir}(t)+\sum_{n=1}^{N}k_{irn}^{Lin}q_{in}(t)$$
$$+\sum_{n=1}^{N}\sum_{j=1}^{N}\sum_{p=1}^{N}R1_{irnjp}^{Lin}q_{ij}^2(t)q_{in}(t)+\sum_{n=1}^{N}\sum_{j=1}^{N}\sum_{p=1}^{N}R2_{irnjp}^{Lin}z_{ij}^2(t)q_{in}(t)+F_{ir}^{Lin}=0 \quad (4.121)$$

$$\ddot{c}_{ir}(t)+2\zeta_{ir}^{Lout}\omega_{irr}^{Lout}\dot{c}_{ir}(t)+\left(\omega_{ir}^{Lout}\right)^2 c_{ir}(t)+\sum_{n=1}^{N}k_{irn}^{Lout1}c_{in}(t)$$
$$+\sum_{n=1}^{N}\sum_{j=1}^{N}\sum_{p=1}^{N}R1_{irnjp}^{Lout}q_{ij}^2(t)c_{in}(t)+\sum_{n=1}^{N}\sum_{j=1}^{N}\sum_{p=1}^{N}R2_{irnjp}^{Lout}c_{ij}^2(t)c_{in}(t)+F_{ir}^{Lout}=0 \quad (4.122)$$

The coefficients $\zeta_{1r}^{Lin}, \zeta_{1r}^{Lout}, \zeta_{ir}^{Lin}, \zeta_{ir}^{Lout}$ represent the modal damping ratios for the i^{th} rope in the lateral in plane and out of plane direction.

$$M_1\left(U_{CR}\right)_{tt}+k1^{u1}U_{CR}(t)+k2^{u1}U_{CS}(t)+\sum_{n=1}^{N}k3_n^{u1}q_{1n}(t)+\sum_{n=1}^{N}k4_n^{u1}c_{1n}(t)$$
$$+\sum_{j=1}^{N}\sum_{p=1}^{N}R1_{jp}^{u1}q_{1j}(t)q_{1p}(t)+\sum_{j=1}^{N}\sum_{p=1}^{N}R2_{jp}^{u1}c_{1j}(t)c_{1p}(t)+f_{CR}=0 \quad (4.123)$$

$$
\begin{aligned}
&M_2\left(U_{CS}\right)_{tt}+k1^{u2}U_{CR}\left(t\right)+k2^{u2}U_{CS}\left(t\right)+k3^{u2}U_{CW}\left(t\right)\\
&+\sum_{n=1}^{N}k4_n^{u2}q_{1n}\left(t\right)+\sum_{n=1}^{N}k5_n^{u2}c_{1n}\left(t\right)+\sum_{j=1}^{N}\sum_{p=1}^{N}R1_{jp}^{u2}q_{1j}\left(t\right)q_{1p}\left(t\right)\\
&+\sum_{j=1}^{N}\sum_{p=1}^{N}R2_{jp}^{u2}c_{1j}\left(t\right)c_{1p}\left(t\right)+\sum_{n=1}^{N}R3_n^{u2}q_{3n}^2\left(t\right)+\sum_{n=1}^{N}R4_n^{u2}c_{3n}^2\left(t\right)+f_{CS}=0
\end{aligned}
\tag{4.124}
$$

$$
\begin{aligned}
&M_3\left(U_{CW}\right)_{tt}+k1^{u3}U_{CS}\left(t\right)+k2^{u3}U_{CW}\left(t\right)+\sum_{n=1}^{N}R1_n^{u3}q_{3n}^2\left(t\right)\\
&+\sum_{n=1}^{N}R2_n^{u3}c_{3n}^2\left(t\right)+\sum_{n=1}^{N}R3_n^{u3}q_{4n}^2\left(t\right)+\sum_{n=1}^{N}R4_n^{u3}c_{4n}^2\left(t\right)+f_{CW}=0
\end{aligned}
\tag{4.125}
$$

The equations of motion (4.123) to (4.125) for the elevator car, compensating sheave, and counterweight are transformed into the modal coordinates using the transformation $\vec{U}=\left[Y\right]\vec{S}$ where $\vec{U}=\left[U_{CR}\quad U_{CS}\quad U_{CW}\right]^T$ and $\vec{S}=\left[S_{CR}\quad S_{CS}\quad S_{CW}\right]^T$ is a vector of modal-coordinates corresponding to the system comprising the car, compensating sheave, and counterweight, respectively. If [Y] is the mass-normalized mode shape matrix, the following set of equations describing the vertical response of the car, compensating sheave and counterweight in terms of the modal parameters represented as (4.126) to (4.128)

$$
\ddot{S}_{CR}\left(t\right)+2\zeta_{CR}\omega_{CR}\dot{S}_{CR}\left(t\right)+\omega_{CR}^2S_{CR}\left(t\right)+\left(\vec{Y}^{(1)}\right)^T\left(\vec{\sigma}_1+\vec{\sigma}_2\right)+\left(\vec{Y}^{(1)}\right)^T\left(\vec{F}+\vec{\eta}\right)=0 \tag{4.126}
$$

$$
\ddot{S}_{CS}\left(t\right)+2\zeta_{CS}\omega_{CS}\dot{S}_{CS}\left(t\right)+\omega_{CS}^2S_{CS}\left(t\right)+\left(\vec{Y}^{(2)}\right)^T\left(\vec{\sigma}_1+\vec{\sigma}_2\right)+\left(\vec{Y}^{(2)}\right)^T\left(\vec{F}+\vec{\eta}\right)=0 \tag{4.127}
$$

$$
\ddot{S}_{CW}\left(t\right)+2\zeta_{CW}\omega_{CW}\dot{S}_{CW}\left(t\right)+\omega_{CW}^2S_{CW}\left(t\right)+\left(\vec{Y}^{(3)}\right)^T\left(\vec{\sigma}_1+\vec{\sigma}_2\right)+\left(\vec{Y}^{(3)}\right)^T\left(\vec{F}+\vec{\eta}\right)=0 \tag{4.128}
$$

where $\omega_{CR},\omega_{CS},\omega_{CW}$ represent the longitudinal natural frequencies of the elevator car, compensating sheave and counterweight, which can be estimated by finding the eigenvalues from the stiffness matrix represented in (4.129) and mass matrix represented in (4.130). The coefficients $\zeta_{CR},\zeta_{CS},\zeta_{CW}$ represent the longitudinal modal damping ration of the elevator car, compensating sheave and counterweight.

$$
\begin{bmatrix}
k1^{u1} & k2^{u1} & 0\\
k1^{u2} & k2^{u2} & k3^{u2}\\
0 & k1^{u3} & k2^{u3}
\end{bmatrix}
\tag{4.129}
$$

$$\begin{bmatrix} M_1 & 0 & 0 \\ 0 & M_2 & 0 \\ 0 & 0 & M_3 \end{bmatrix} \tag{4.130}$$

The coefficients $\vec{\sigma}_1, \vec{\sigma}_2, \vec{F}, \vec{\eta}$ are shown in equations (4.131) to (4.134).

$$\vec{\sigma}_1 = \begin{bmatrix} \sum_{n=1}^{N} k3_n^{u1} q_{1n}(t) \\ \sum_{n=1}^{N} k4_n^{u2} q_{1n}(t) \\ 0 \\ \end{bmatrix} \tag{4.131}$$

$$\vec{\sigma}_2 = \begin{bmatrix} \sum_{n=1}^{N} k4_n^{u1} c_{1n}(t) \\ \sum_{n=1}^{N} k5_n^{u2} c_{1n}(t) \\ 0 \\ \end{bmatrix} \tag{4.132}$$

$$\vec{F} = \begin{bmatrix} f_{CR} \\ f_{CS} \\ f_{CW} \end{bmatrix} \tag{4.133}$$

$$\vec{\eta} = \begin{bmatrix} \eta_{CR} \\ \eta_{CS} \\ \eta_{CW} \end{bmatrix} \tag{4.134}$$

The coefficients $\eta_{CR}, \eta_{CS}, \eta_{CW}$ are the quadratic terms from the equations of motion of the elevator car, compensating sheave, counterweight represented in equations (4.135) to (4.137).

$$\eta_{CR} = \sum_{j=1}^{N}\sum_{p=1}^{N} R1_{jp}^{u1} q_{1j}(t) q_{1p}(t) + \sum_{j=1}^{N}\sum_{p=1}^{N} R2_{jp}^{u1} c_{1j}(t) c_{1p}(t) \tag{4.135}$$

$$\begin{aligned} \eta_{CS} &= \sum_{j=1}^{N}\sum_{p=1}^{N} R1_{jp}^{u2} q_{1j}(t) q_{1p}(t) + \sum_{j=1}^{N}\sum_{p=1}^{N} R2_{jp}^{u2} c_{1j}(t) c_{1p}(t) \\ &+ \sum_{n=1}^{N} R3_n^{u2} q_{3n}^2(t) + \sum_{n=1}^{N} R4_n^{u2} c_{3n}^2(t) \end{aligned} \tag{4.136}$$

$$\eta_{CW} = \sum_{n=1}^{N} R1_n^{u3} q_{3n}^2(t) + \sum_{n=1}^{N} R2_n^{u3} c_{3n}^2(t) + \sum_{n=1}^{N} R3_n^{u3} q_{4n}^2(t) + \sum_{n=1}^{N} R4_n^{u3} c_{4n}^2(t) \tag{4.137}$$

Similarly in equations (4.119) and (4.120) the coefficients of the elevator car, compensating sheave and counterweight are transformed and rewritten as equations (4.138) and (4.139)

$$\begin{aligned}
&\ddot{q}_{1r}(t)+2\zeta_{1r}^{Lin}\omega_{1rr}^{Lin}\dot{q}_{1r}(t)+\left(\omega_{1r}^{Lin}\right)^2 q_{1r}(t)+\sum_{n=1}^{N}k_{1rn}^{Lin1}q_{1n}(t)\\
&+\bar{\sigma}_u^{lin}\vec{Y}^{(1)}S_{CR}+\bar{\sigma}_u^{lin}\vec{Y}^{(2)}S_{CS}+\bar{\sigma}_u^{lin}\vec{Y}^{(3)}S_{CW}\\
&+\sum_{n=1}^{N}k_{1rn}^{Lin2}c_{1n}(t)+\sum_{n=1}^{N}\sum_{j=1}^{N}D_{irn}^{Lin1}q_{1j}(t)q_{1n}(t)+\sum_{n=1}^{N}\sum_{j=1}^{N}D_{1rn}^{Lin2}c_{1j}(t)q_{1n}(t)\\
&+\sum_{n=1}^{N}\sum_{j=1}^{N}D_{1rn}^{Lin3}c_{1j}(t)c_{1n}(t)+\sum_{n=1}^{N}\sum_{j=1}^{N}\sum_{p=1}^{N}R1_{1rnjp}^{Lin}q_{1j}(t)q_{1p}(t)q_{1n}(t)\\
&+\sum_{n=1}^{N}\sum_{j=1}^{N}\sum_{p=1}^{N}R2_{1rnjp}^{Lin}c_{1j}(t)c_{1p}(t)q_{1n}(t)+F_{1r}^{Lin}=0
\end{aligned} \tag{4.138}$$

$$\begin{aligned}
&\ddot{c}_{1r}(t)+2\zeta_{1r}^{Lout}\omega_{1rr}^{Lout}\dot{c}_{1r}(t)+\left(\omega_{1r}^{Lout}\right)^2 c_{1r}(t)+\sum_{n=1}^{N}k_{1rn}^{Lout1}c_{1n}(t)\\
&+\bar{\sigma}_u^{lout}\vec{Y}^{(1)}S_{CR}+\bar{\sigma}_u^{lout}\vec{Y}^{(2)}S_{CS}+\bar{\sigma}_u^{lout}\vec{Y}^{(3)}S_{CW}\\
&+\sum_{n=1}^{N}k_{1rn}^{Lout2}q_{1n}(t)+\sum_{n=1}^{N}\sum_{j=1}^{N}D_{irn}^{Lout1}q_{1j}(t)c_{1n}(t)+\sum_{n=1}^{N}\sum_{j=1}^{N}D_{1rn}^{Lout2}c_{1j}(t)c_{1n}(t)\\
&+\sum_{n=1}^{N}\sum_{j=1}^{N}D_{1rn}^{Lout3}q_{1j}(t)q_{1n}(t)+\sum_{n=1}^{N}\sum_{j=1}^{N}\sum_{p=1}^{N}R1_{1rnjp}^{Lout}q_{1j}(t)q_{1p}(t)c_{1n}(t)\\
&+\sum_{n=1}^{N}\sum_{j=1}^{N}\sum_{p=1}^{N}R2_{1rnjp}^{Lout}c_{1j}(t)c_{1p}(t)c_{1n}(t)+F_{1r}^{Lout}=0
\end{aligned} \tag{4.139}$$

where $\bar{\sigma}_u^{lin}$ and $\bar{\sigma}_u^{lout}$ are represented by

$$\bar{\sigma}_u^{lin}=\begin{bmatrix}k_{1r}^{lin3} & k_{1r}^{lin4} & 0\end{bmatrix} \tag{4.140}$$

$$\bar{\sigma}_u^{lout}=\begin{bmatrix}k_{1r}^{lout3} & k_{1r}^{lout4} & 0\end{bmatrix} \tag{4.141}$$

All coefficients are shown in Appendix F.

4.3 Simulation Results

Three case study results are shown to verify the proposed mathematical model of a stationary elevator system with a comparison on each case study with a high and low stiffness for k_1 and k_2.

The parameters taken to analyse the dynamic performance of an elevator system in the three case studies consist of six ($n_1=6$) steel wire suspension ropes and six ($n_2=6$) steel wire compensating ropes, both suspension and compensating ropes have a mass of $m_1=m_2=2.15$

kg/m with a constant elastic modulus of $EA_1 = EA_2 = 95276193$ N. The modal damping ratios for the ropes are assumed as 1% across all modes and 30% for the lumped mass of the elevator car, compensating sheave and counterweight. The height measured from the ground floor level to the centre of the traction sheave is $h_0 = 248$ m, travel height $h_{trav} = 236.00$ m, the car mass with full load is $M_1 = 8600$ kg, the mass of the compensating sheave is $M_2 = 8000$ kg, and the mass of the counterweight is $M_3 = 7800$ kg. The height measured from the bottom landing level to the centre of the compensating sheave is given as $b_1 = 8.30$ m and the height from centre of the traction sheave to the centre of the diverter pulley is $b_2 = 0.50$ m. Assuming that the high rise building has a circular cross section, the fundamental natural frequency is $\Omega_v = 1.885$ rad/s (0.30 Hz) in the lateral in plane direction and in the lateral out of plane direction is $\Omega_w = 1.5708$ rad/s (0.25 Hz). Assuming, the high rise building is excited by wind harmonically, the displacement at the machine room level in the lateral in plane direction is $A_v = 0.90$ m and in the lateral out of plane direction is $A_w = 0.35$ m. From the Galerkin method the nonlinear ordinary differential equations are given for *N* number of modes and the ODE45 solver is used in MATLAB. For the simulation results presented in this Chapter, the number of modes taken into account are *N=4*, considered for all simulations of Chapter 4. The stiffness of the springs that are connected to the elevator car in the lateral in plane direction and in the lateral out of plane direction is of $k_1 = k_2 = 80000$ N/m considered as high spring stiffness and $k_1 = k_2 = 30000$ N/m considered as low spring stiffness. The simulation is started from the initial instant $t_0 = 0$ s until $t_f = 200$ s.

4.3.1 Frequency Analysis

The variation of frequency in the lateral direction of the car, suspension and compensating ropes at the car side due to different positions of the elevator car along the travel height is determined with the eigenvalues of equation (4.142).

$$\left(\bar{\omega}_{1rr}^{Lin}\right)^2 = \begin{bmatrix} -\left(M_1 + m_1L_1 + m_2L_2 + \dfrac{M_2}{2}\right) g\int_0^{L_1} \phi_{1r}''(x)\phi_{1r}(x)dx \\ +\left(M_1 + m_2L_2 + \dfrac{M_2}{2}\right) g\phi_{1r}'(\mathrm{L}_1)\phi_{1r}(\mathrm{L}_1) \\ +2k_1\phi_{1r}(\mathrm{L}_1)^2 - \left(m_2L_2 + \dfrac{M_2}{2}\right) g\int_0^{L_2} \phi_{2r}''(x)\phi_{2r}(x)dx \\ -\left(m_2L_2 + \dfrac{M_2}{2}\right) g\phi_{2r}'(0)\phi_{1r}(\mathrm{L}_1) \\ m_1g\int_0^{L_1} x\phi_{1n}''(x)\phi_{1r}(x)dx + m_1g\int_0^{L_1} \phi_{1n}'(x)\phi_{1r}(x)dx \\ +m_2g\int_0^{L_2} x\phi_{2n}''(x)\phi_{2r}(x)dx + m_2g\int_0^{L_2} \phi_{2n}'(x)\phi_{2r}(x)dx \end{bmatrix} / m_{1rr}^{Lin} \quad (4.142)$$

The variation of frequency corresponding to all lateral modes of the elevator car, suspension, and compensating ropes at the car side according to the position of the elevator car in the hoistway measured from the bottom landing level are shown in Figure 4.2, with $k_1 = k_2 = 80000$ N/m.

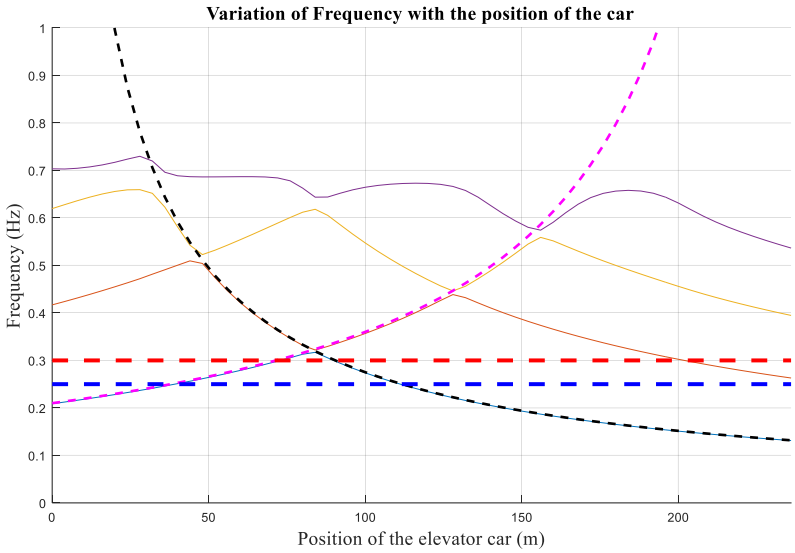

Figure 4.2 Variation of frequency with the position of the elevator car (car side)

In Figure 4.2 the solid blue, orange, yellow, purple line are the variation of frequency of the first four lateral in plane natural frequencies at the car side of the elevator car, suspension and compensating ropes. The dashed magenta and black line are the fundamental natural frequency of the suspension and compensating ropes when the lateral stiffness of the elevator car is neglected according to the change of position of the elevator car, calculated using

equations (4.143) and (4.144). The dashed red and blue lines are the excitation of the building structure in the lateral in plane and out of plane direction with 0.30 Hz and 0.25 Hz, respectively. In Figure 4.2 can be seen that the suspension ropes will be excited at the fundamental natural frequency and compensating ropes will be excited at twice the fundamental natural frequency in the lateral in plane direction due to the frequency of excitation of the building structure in the lateral in plane direction of 0.30 Hz. For the lateral out of plane direction the suspension and compensating ropes will be excited at the fundamental natural frequency due to the frequency of excitation of the building structure in the lateral out of plane direction of 0.25 Hz.

$$\left(\tilde{\omega}_{1rr}^{Lin}\right)^2 = \begin{bmatrix} -\left(M_1 + m_1 L_1 + m_2 L_2 + \dfrac{M_2}{2}\right) g \int_0^{L_1} \phi_{1r}''(x)\phi_{1r}(x)dx \\ m_1 g \int_0^{L_1} x\phi_{1n}''(x)\phi_{1r}(x)dx + m_1 g \int_0^{L_1} \phi_{1n}'(x)\phi_{1r}(x)dx \end{bmatrix} / \left(m_1 \int_0^{L_1} \phi_{1r}^2\left(x_1\right)dx_1\right) \tag{4.143}$$

$$\left(\tilde{\omega}_{2rr}^{Lin}\right)^2 = \begin{bmatrix} -\left(m_2 L_2 + \dfrac{M_2}{2}\right) g \int_0^{L_2} \phi_{2r}''(x)\phi_{2r}(x)dx \\ +m_2 g \int_0^{L_2} x\phi_{2n}''(x)\phi_{2r}(x)dx + m_2 g \int_0^{L_2} \phi_{2n}'(x)\phi_{2r}(x)dx \end{bmatrix} / \left(m_2 \int_0^{L_2} \phi_{2r}^2\left(x_2\right)dx_2\right) \tag{4.144}$$

In Figure 4.2 the curve veering phenomena is observed which is when two eigenvalues approach each other closely and suddenly veer away again, each one taking on the trajectory of the other. The curve veering phenomena is also known as mode localization, according to Giannini and Sestieri (2015) investigated curve veering with a two degrees of freedom system to analysed the adverse conditions in coupling between elastic, inertial or gyroscopic. Du Bois et al. (2011) and Bendiksen (2000) defined the veering phenomena as smooth change of normal parametric variation of two modes approaching each other but, instead of crossing, they veer away and finally diverge. The curve veering phenomena is the effect caused by modal interaction, a group of frequencies joining together and mode shape localization. The importance of eigenvalue veering and mode shape localization was demonstrated in a structural buckling case in Pierre and Plaut (1989).

The point where both the fundamental natural frequency of the suspension and compensating ropes match each other occur when the elevator car is positioned at 84.0 m from the bottom landing level with a frequency of 0.317 Hz.

The effect on the variation of frequency and veering phenomena when using high and low stiffness parameter is shown in Figure 4.3. In Figure 4.3 the solid blue, orange, yellow, and purple line for the first four natural frequencies in the lateral direction at the car side when using a stiffness parameter of k_1=80 kN/m considered as high stiffness and the dashed green, cyan, red, and blue lines represent the first four natural frequencies in the lateral direction at the car side when using a stiffness parameter of k_1=30kN/m considered as low stiffness parameter. The dashed red and blue lines are the excitation of the building structure in the lateral in plane and out of plane direction with 0.30 Hz and 0.25 Hz, respectively.

It should be noted as the stiffness parameter is lowered the variation of frequency becomes smooth and the sharp peak for the fundamental natural frequency is reduced. The point where both the fundamental natural frequency of the suspension and compensating ropes match each other was reduced from a frequency of 0.317 Hz to 0.305 Hz.

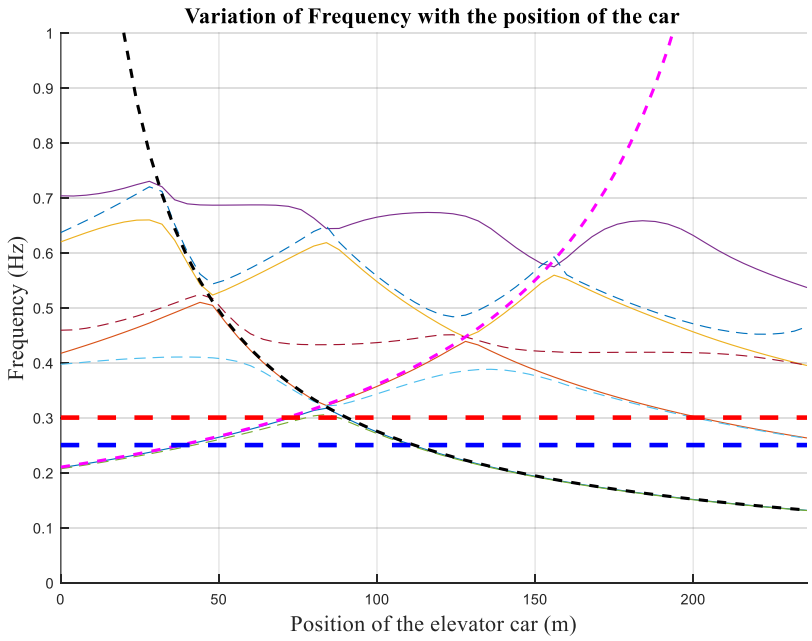

Figure 4.3 Variation of frequency with the position of the elevator car (car side) when comparing stiffness parameter of k_1=80 kN/m and k_1=30kN/m

Thus, the three case studies that will be presented consist of positioning the elevator car at the bottom landing level as case study one, when the elevator car is positioned at the veering point at a height of 84.0 m from the bottom landing level as case study two, and when the elevator car is positioned at the top landing level at a height of 236.0 m from the bottom landing level as case study three.

Similarly, the variation of the compensating and suspension ropes at the counterweight side and the variation of the longitudinal natural frequencies of the elevator car, compensating sheave, and counterweight according to the position of the car in the hoistway measured from the bottom landing level are shown in Figure 4.4 and Figure 4.5. The solid blue, orange, yellow, purple line represent the first four natural frequencies of the compensating and suspension ropes at the counterweight side, calculated using equations (4.145) and (4.146). The dashed green, magenta, and black lines represent the change of frequency in the longitudinal direction of the elevator car, compensating sheave, and counterweight according to the position of the elevator car, estimated by finding the eigenvalues from the stiffness matrix represented in (4.129) and mass matrix represented in (4.130). The dashed red and blue lines represent the frequency of excitation from the building structure at 0.30 Hz and 0.25 Hz in the lateral in plane and out of plane direction. The compensating rope at the counterweight side will be excited at twice the fundamental natural frequency due to the frequency of excitation of the building structure. Similarly, the suspension ropes at the counterweight side will be excited at higher than the fundamental natural frequency due to the frequency of excitation of the building structure.

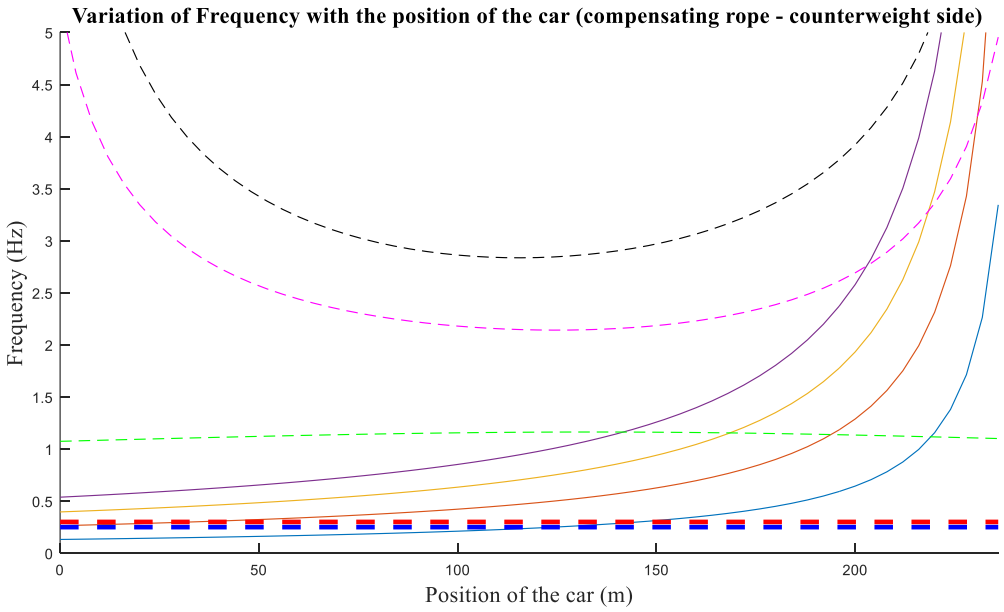

Figure 4.4 Variation of the frequency according to the position of the car (compensating ropes at the counterweight side)

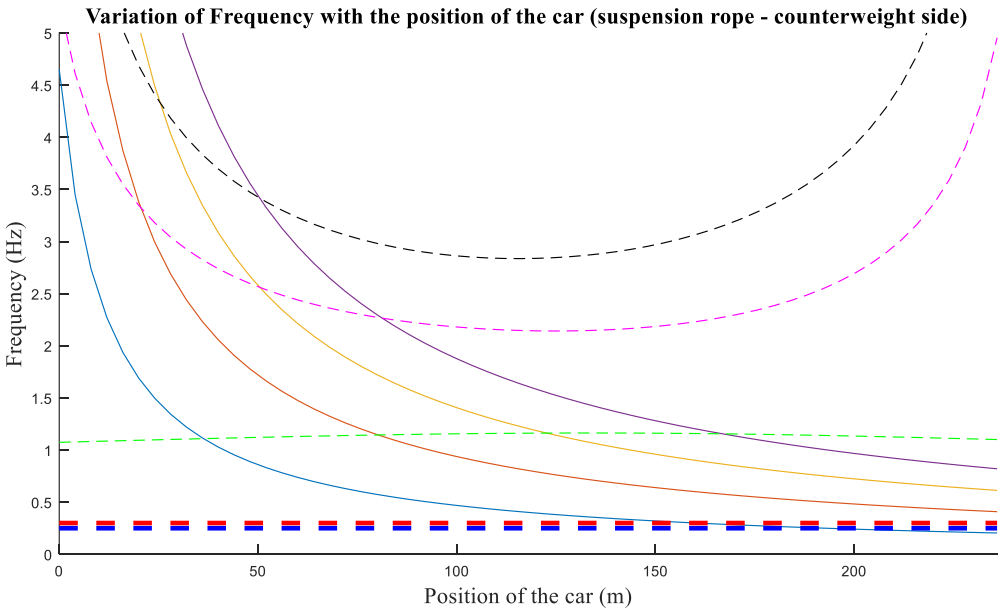

Figure 4.5 Variation of the frequency according to the position of the car (suspension ropes at the counterweight side)

$$\left(\omega_{3rr}^{Lin}\right)^2 = -\left(m_2 L_3 + \frac{M_2}{2}\right)\frac{g}{m_{3rr}^{Lin}}\int_0^{L_3}\phi_{3r}''(x)\phi_{3r}(x)dx + \frac{m_2 g}{m_{3rr}^{Lin}}\left(\begin{array}{l}\int_0^{L_3}\phi_{3r}'(x)\phi_{3r}(x)dx \\ +\int_0^{L_3}x\phi_{3r}''(x)\phi_{3r}(x)dx\end{array}\right) \tag{4.145}$$

$$\begin{aligned}\left(\omega_{4rr}^{Lin}\right)^2 &= -\left(M_3 + m_1 L_4 + m_2 L_3 + \frac{M_2}{2}\right)\frac{g}{m_{4rr}^{Lin}}\int_0^{L_4}\phi_{4r}''(x)\phi_{4r}(x)dx \\ &+ \frac{m_1 g}{m_{4rr}^{Lin}}\left(\int_0^{L_4}x\phi_{4n}''(x)\phi_{4r}(x)dx + \int_0^{L_4}\phi_{4n}'(x)\phi_{4r}(x)dx\right)\end{aligned} \tag{4.146}$$

4.3.2 Mode shapes

The mode shapes corresponding to the vertical vibrations of the car, compensating sheave and counterweight are shown in Figure 4.6 (a), (b) and (c), respectively for case study one. In the first mode (1.074 Hz) the elevator car and compensating sheave have similar displacements and are in phase than the counterweight. The second mode (5.3085 Hz) is the displacements of the elevator car and compensating sheave are in phase and the counterweight is out of phase. In the third mode (8.4475 Hz) the elevator car, compensating sheave, and counterweight motions are all out of phase.

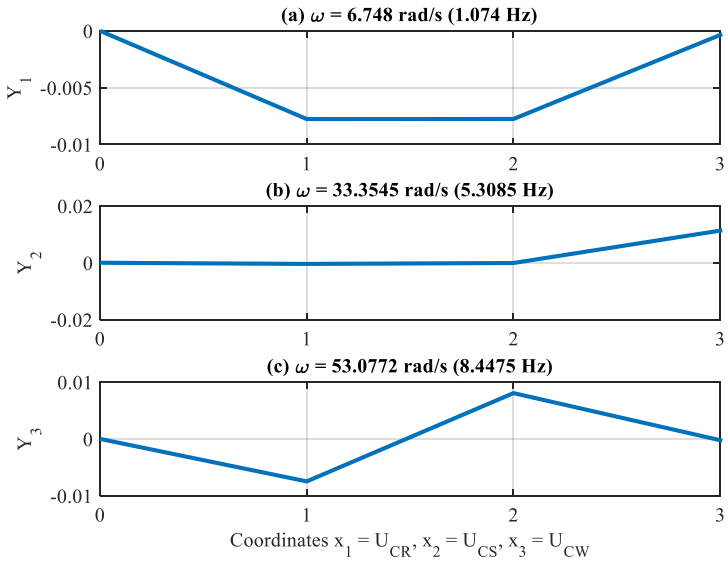

Figure 4.6 The mode shape displacements of the car, compensating sheave and counterweight for case study one

The mode shapes corresponding to the vertical vibrations of the car, compensating sheave and counterweight are shown in Figure 4.7 (a), (b) and (c), respectively for case study two. In the first mode (1.147 Hz) the elevator car and compensating sheave have greater displacements than the counterweight and they are in phase. The second mode (2.2491 Hz) the displacements of the elevator car, compensating sheave, and counterweight are all out of phase. In the third mode (2.9492 Hz) the elevator car and counterweight motions are in phase and the compensating sheave is out of phase.

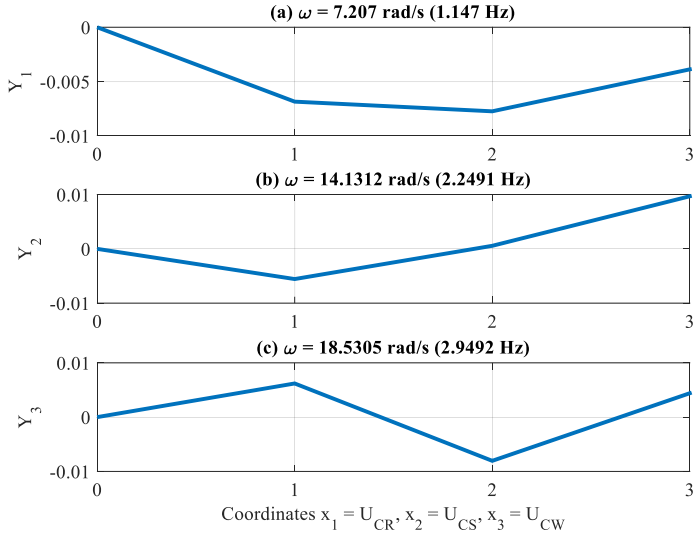

Figure 4.7 The mode shape displacements of the car, compensating sheave and counterweight for case study two

The mode shapes corresponding to the vertical vibrations of the car, compensating sheave and counterweight are shown in Figure 4.8 (a), (b) and (c), respectively for case study three. In the first mode (1.1007 Hz) the compensating sheave and counterweight are in phase and the elevator car is out of phase. The second mode (4.9549 Hz) the displacements of the compensating sheave and counterweight are in phase. The displacements of the elevator car are out of phase. In the third mode (8.6533 Hz) the elevator car, compensating sheave and counterweight motions are all out of phase.

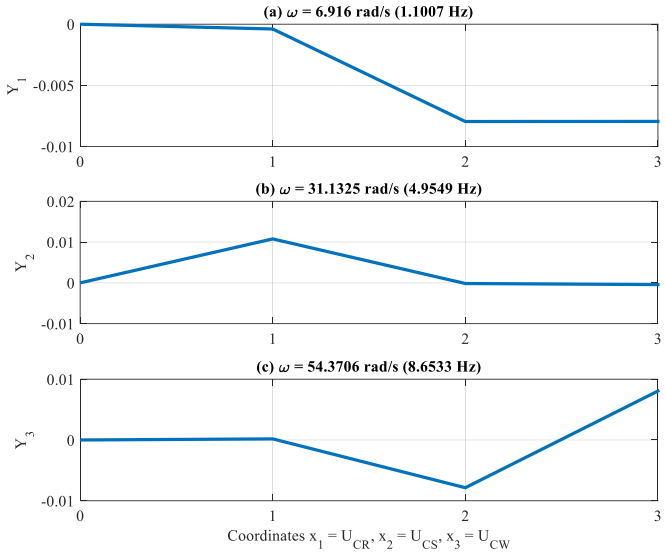

Figure 4.8 The mode shape displacements of the car, compensating sheave and counterweight for case study three

The lateral mode shapes of the system at the car side composed of the suspension and compensating rope and the elevator car when the car is at the bottom landing level as in case study one where the elevator car is positioned at the bottom landing level is shown in Figure 4.9 comparing stiffness parameters of k_1=80 kN/m and k_1=30 kN/m. The solid and dashed line represent the 1st and 2nd mode shapes of the system at the car side, where the blue and red line represent the suspension and compensating ropes and the connection point of the ropes is the elevator car considered as a lumped mass. The small linewidth represent the mode shapes calculated with a stiffness parameter of k_1=80 kN/m and the bigger linewidth represent the mode shapes calculated with a stiffness parameter of k_1=30kN/m. The mode shapes can be determined with equations (4.102) and (4.104).

The mode shape of the compensating rope is linear due to the short length of the compensating rope. The mode shape function is scaled so that the maximum amplitude is 1. The effect of having a low stiffness parameter would increase the amplitude in the lateral direction for the elevator car.

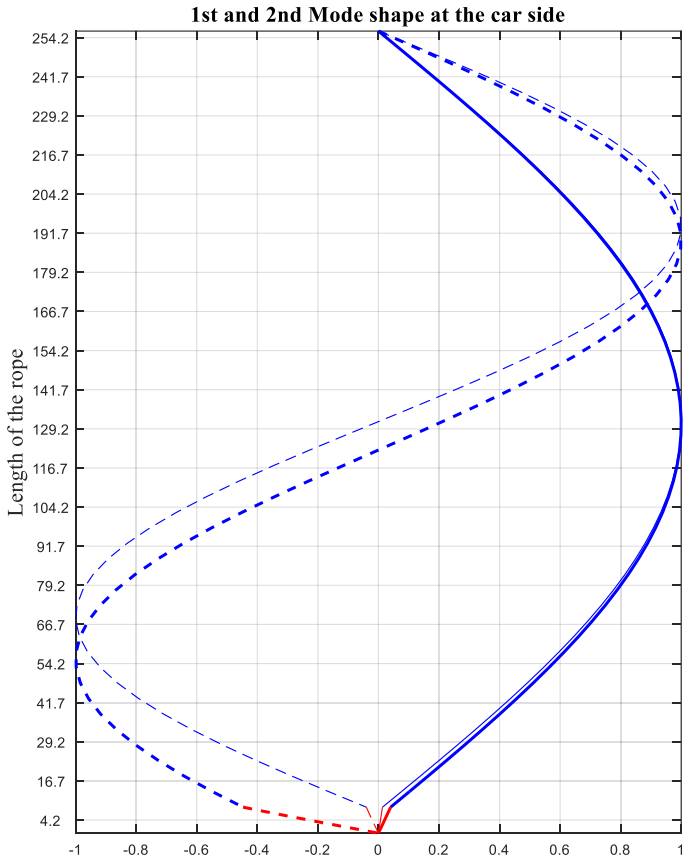

Figure 4.9 1st and 2nd mode shapes of the system at the car side with different stiffness parameters as k_1=80 kN/m and k_1=30kN/m

The lateral mode shapes of the system at the car side composed of the suspension and compensating rope and the elevator car when the car is positioned at 84.0 m from the bottom landing level as in case study two is shown in Figure 4.10 comparing stiffness parameters of k_1=80 kN/m and k_1=30 kN/m. The elevator car is positioned at 84.0 m from the bottom landing level at the veering point where the fundamental natural frequencies of the suspension and compensating ropes match. The solid and dashed line represent the 1st and 2nd mode shapes of the system at the car side, where the blue and red line represent the suspension and compensating ropes and the connection between the ropes is the elevator car considered as a lumped mass. The small linewidth represent the mode shapes calculated with a stiffness

parameter of k_1=80 kN/m and the bigger linewidth represent the mode shapes calculated with a stiffness parameter of k_1=30kN/m. The mode shapes can be determined with equations (4.102) and (4.104).

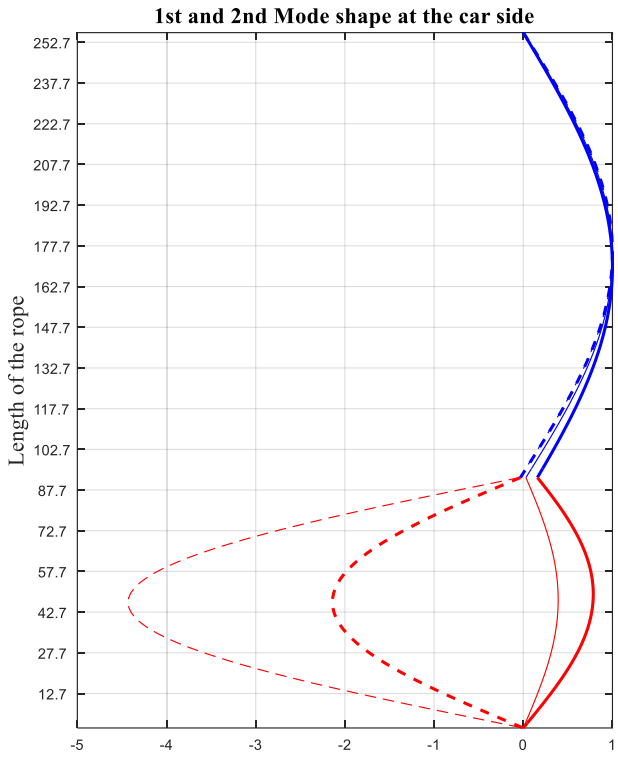

Figure 4.10 1st and 2nd mode shapes of the system at the car side with different stiffness parameters as k_1=80 kN/m and k_1=30kN/m for case study two

Similarly, the mode shapes for case study three when the car is positioned at the top landing level and the mode shapes for the three case studies in the lateral out of plane direction can be deducted.

In Figure 4.11 the 1st and 2nd mode shapes of the compensating ropes at the counterweight side for case study one are represented by a solid and dashed blue line, respectively. The mode shapes of the compensating rope at the counterweight side are scaled to show the maximum amplitude as 1. Similarly, the mode shapes for case studies two and three can be determined by using $\alpha_{in} = \phi_{in} = sin\left(\frac{n\pi}{L_i}x\right)$.

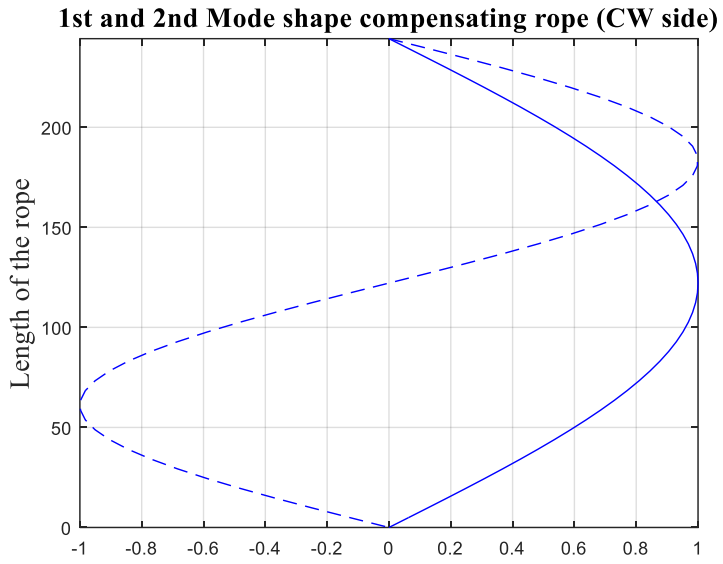

Figure 4.11 1st and 2nd mode shapes of the compensating rope at the counterweight side for case study one

4.3.3 Response of the ropes

The behaviour of all ropes of the elevator system are obtained from the mathematical model. The response of the compensating ropes at the car side for case study one, two, and three are shown in Figure 4.12, Figure 4.13, and Figure 4.14 comparing a high stiffness parameter of $k_1=k_2=80kN/m$ represented by a blue line and a low stiffness parameter of $k_1=k_2=30kN/m$ represented by a red line. The response of the compensating rope at the car side in the lateral in plane direction is obtained from equation (4.66) and in the lateral out of plane direction is obtained from equation (4.70). The response of the compensating ropes in the lateral direction at the car side is higher due to the effect of using a low spring parameter in the lateral direction of the elevator car. In case study one the elevator car is positioned at the bottom landing level, thus the compensating ropes at the car side have small displacements in the lateral directions when compared with the other two case studies.

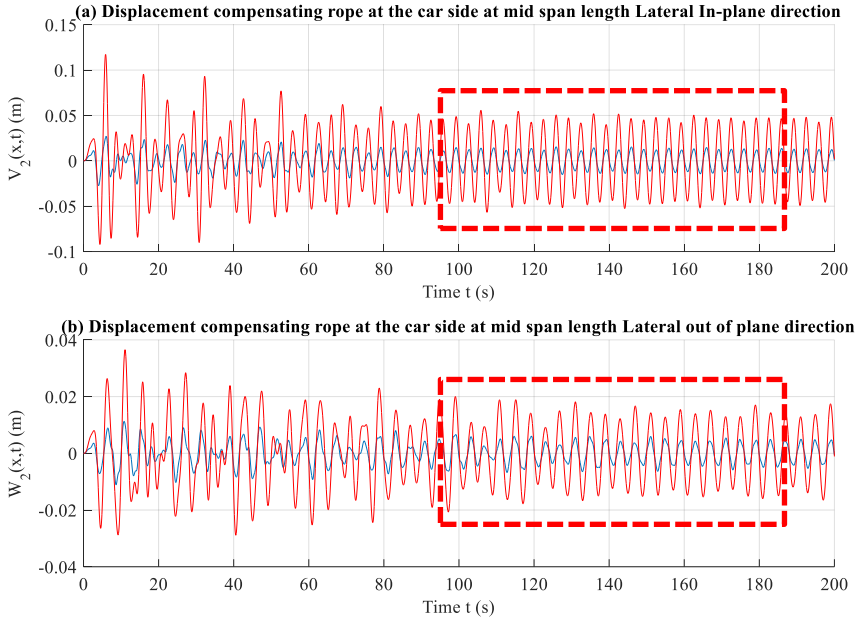

Figure 4.12 The mid span length displacements of the compensating rope at the car side with respect to time (a) Lateral in plane direction (b) Lateral out of plane direction for case study one comparing k1=k2=80kN/m represented as blue line and k1=k2=30kN/m represented as red line

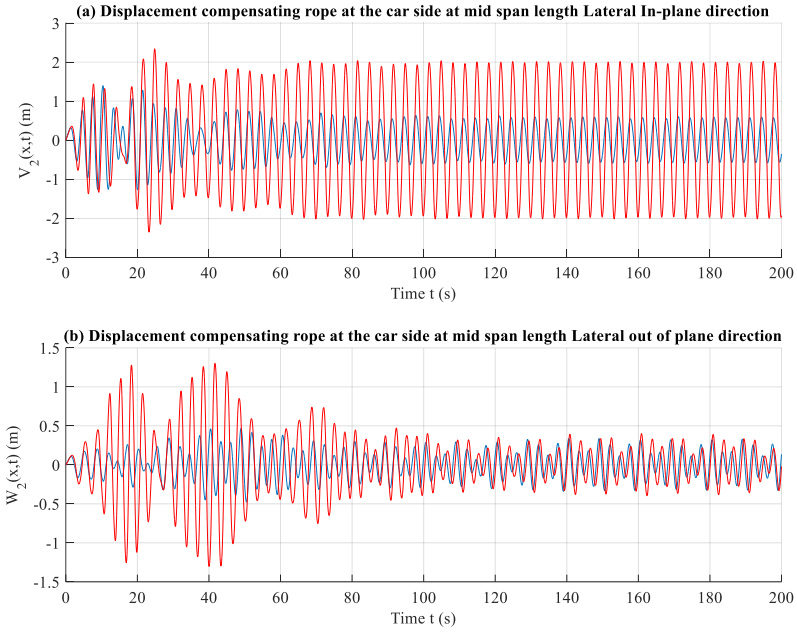

Figure 4.13 The mid span length displacements of the compensating rope at the car side with respect to time (a) Lateral in plane direction (b) Lateral out of plane direction for case study two comparing $k_1=k_2=80$kN/m represented as blue line and $k_1=k_2=30$kN/m represented as red line

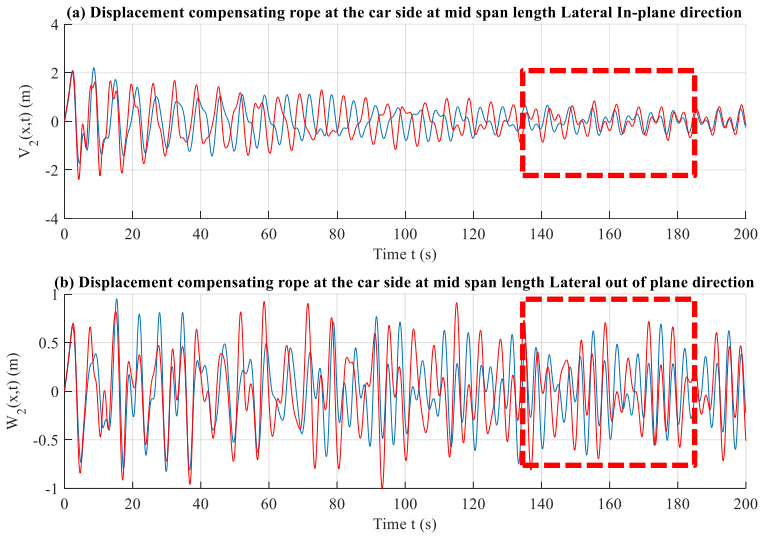

Figure 4.14 The mid span length displacements of the compensating rope at the car side with respect to time (a) Lateral in plane direction (b) Lateral out of plane direction for case study three comparing $k_1=k_2=80$kN/m represented as blue line and $k_1=k_2=30$kN/m represented as red line

The FFT frequency spectra of the lateral in plane and out of plane direction over a time span of 100.0 seconds – 180.0 seconds for case study one are shown in Figure 4.15 (a) and (b), respectively. It is evident that the dominant frequencies are 0.30 Hz and 0.25 Hz which is the frequencies in which the building structure is exciting the ropes in the lateral in plane and out of plane directions shown in Figure 4.15 (a) and (b). The frequencies of 0.30 Hz and 0.25 Hz from the lateral in plane and out of plane directions are coming from the parametric terms located in the lateral in plane and out of plane equations in the stiffness coefficients of K_{1rn}^{Lin1} and K_{1rn}^{Lout1} from equations (4.119) and (4.120). This parametric excitation is coming from the kinematic forcing terms that are exciting the ropes at the machine room level. Due to the short length of the ropes no interaction between the lateral in plane and out of plane directions is taking place.

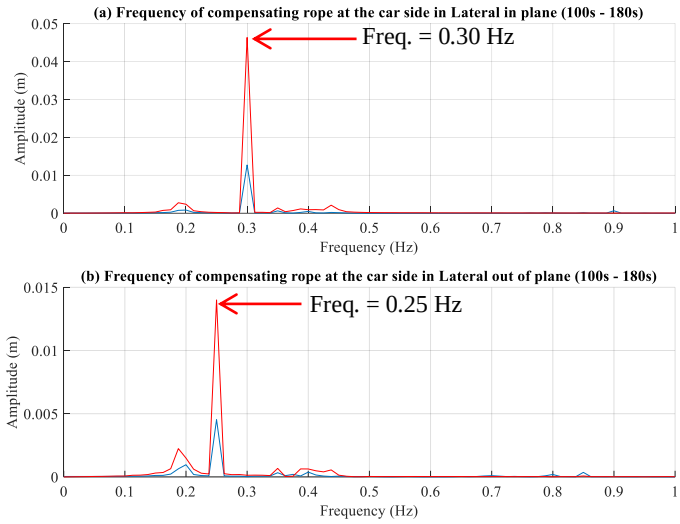

Figure 4.15 The FFT frequency spectrum of the compensating rope in the lateral in plane direction between 100 seconds and 180 seconds (a) Lateral in plane direction (b) Lateral out of plane direction for case study one

The FFT frequency spectra of the lateral in plane and out of plane direction over a time span of 140.0 seconds – 180.0 seconds for case study three are shown in Figure 4.16 (a) and (b), respectively. It is evident that the dominant frequency is 0.30 Hz which is the frequency in which the building structure is exciting the ropes in the lateral in plane direction is shown in Figure 4.16 (a) and (b). In the lateral out of plane direction the second predominant frequency is 0.25 Hz which is the lateral out of plane excitation frequency of the building structure. Thus, 1:1 autoparametric interaction is taking place between the lateral in plane and out of plane directions, through the quadratic and cubic nonlinear terms of equations (4.138) and (4.139) from coefficients $D_{1rn}^{Lin2}, R2_{1rnjp}^{Lin}, D_{1rn}^{Lout1}, R1_{1rnjp}^{Lout}$ where the coupling between the lateral in plane and out of plane modes occur.

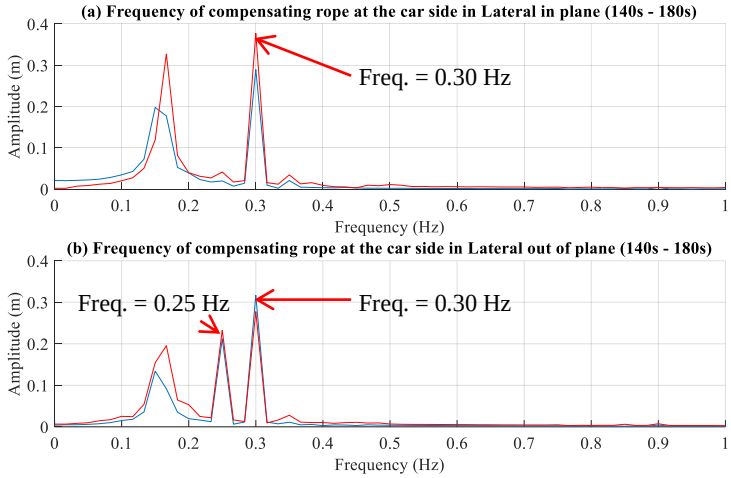

Figure 4.16 The FFT frequency spectrum of the compensating rope in the lateral in plane direction between 140 seconds and 180 seconds (a) Lateral in plane direction (b) Lateral out of plane direction for case study three

For case study two the elevator car is positioned at the veering point where the fundamental natural frequencies of the suspension and compensating ropes match and are excited at the fundamental natural frequency in the lateral in plane direction by the building structure. Thus, the response of the suspension ropes at the car side will be showing high displacements as shown in Figure 4.17.

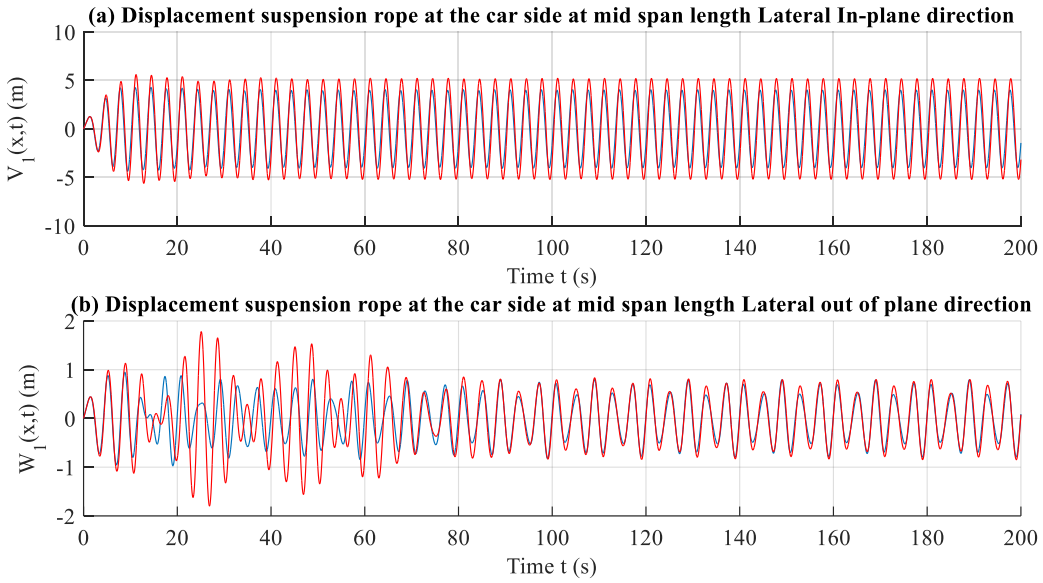

Figure 4.17 The displacements of the suspension rope at the mid span length at the car side with respect to time (a) Lateral in plane direction (b) Lateral out of plane direction for case study two comparing $k_1=k_2=80$kN/m represented as blue line and $k_1=k_2=30$kN/m represented as red line

The whirling motions at the mid span length of the compensating ropes at the car side for case studies one, two, and three are shown in Figure 4.18 with $k_1=k_2=80$kN/m using the total time span. In Figure 4.18 (a) the displacements of the rope in both directions are small due to the short length of the rope in case study one. In Figure 4.18 (b) and (c) the compensating rope at the car side is showing the whirling motion. Similarly the whirling motion of the compensating ropes at the car side with $k_1=k_2=30$kN/m can be obtained.

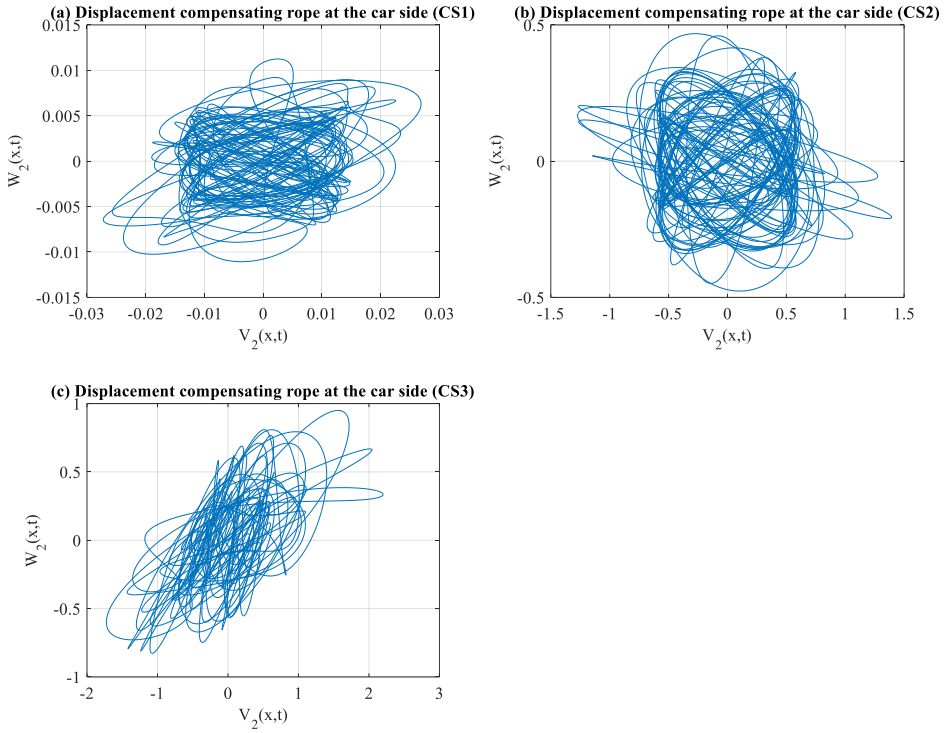

Figure 4.18 Whirling motions of the compensating ropes at the car side for (a) case study one (b) case study two (c) case study three at the mid span length of the rope with $k_1=k_2=80$kN/m

In Figure 4.19 and Figure 4.20 show the maximum displacements of the compensating ropes at the car side in the lateral in plane and out of plane direction, compared with a stiffness parameter of $k_1=k_2=80$kN/m represented by a dashed blue line and $k_1=k_2=30$kN/m represented by a dashed red line. The compensating rope length is measured from center of the compensating sheave to the elevator car considered as lumped mass where the height is not considered according to the assumption made at the beginning. In Figure 4.19 and Figure 4.20 the shapes of the ropes display the second mode shape due the excitation frequency of the building in the lateral in plane and out of plane direction is exciting the rope at twice the fundamental natural frequency of the rope as it can be seen in Figure 4.2.

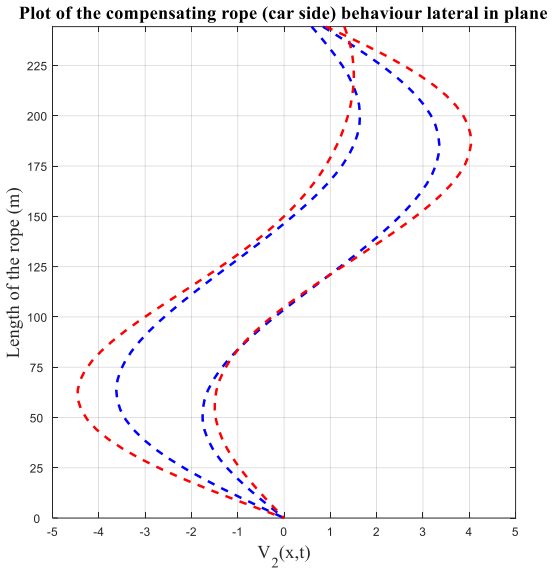

Figure 4.19 Behaviour of the compensating rope at the car side in the lateral in plane direction for case study three comparing $k_1=k_2=80$kN/m represented as dashed blue line and $k_1=k_2=30$kN/m represented as dashed red line

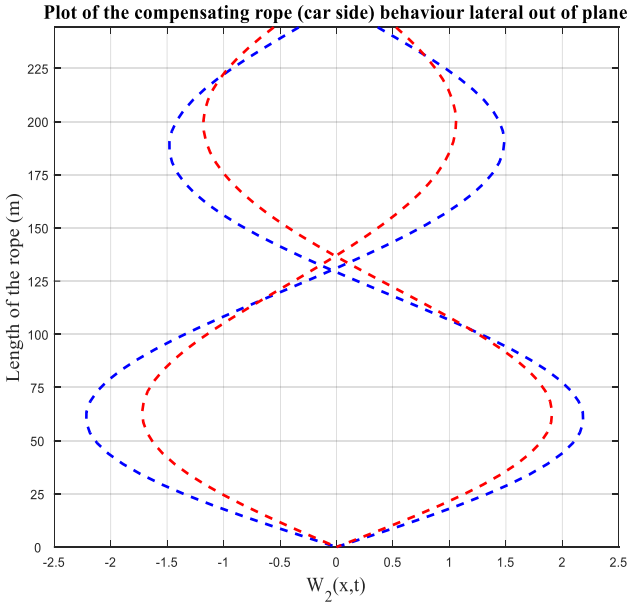

Figure 4.20 Behaviour of the compensating rope at the car side in the lateral out of plane direction for case study three comparing $k_1=k_2=80$kN/m represented as dashed blue line and $k_1=k_2=30$kN/m represented as dashed red line

The response of the suspension ropes at the car side and counterweight side and the compensating ropes at the counterweight side can be obtained, similar figures can be obtained.

4.3.4 Lateral response of the elevator car

The lateral in plane and out of plane displacements of the elevator car are shown in Figure 4.21, Figure 4.22, and Figure 4.23 corresponding to the three case studies, compared with a stiffness parameter of $k_1=k_2=80$kN/m represented by a blue line and $k_1=k_2=30$kN/m represented by a red line. The maximum displacement of the elevator car in the lateral in plane and out of plane direction is in case study two shown in Figure 4.22 with a displacement in the lateral in plane of 0.75 m and in the lateral out of plane of 0.20 m. Due to the influence of the lateral in plane and out of plane displacements of the suspension and compensating ropes as shown in Figure 4.13 and Figure 4.17 at the mid span length of the rope for the compensating and suspension ropes at the car side. As the elevator car is positioned at the veering point where the fundamental natural frequencies of the suspension and compensating ropes match as shown in Figure 4.2. The lateral displacements of the mass are increased when a low spring parameter is used compared with a high stiffness parameter.

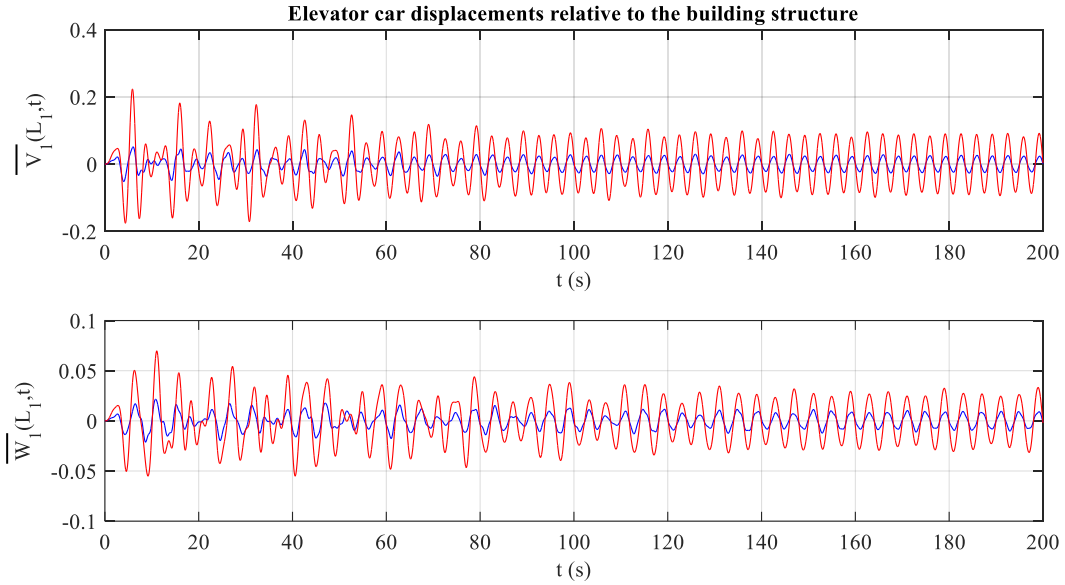

Figure 4.21 Lateral displacements of the elevator car relative to the building structure in the lateral in plane and out of plane direction for case study one comparing stiffness parameters of $k_1=k_2=80$kN/m represented as blue line and $k_1=k_2=30$kN/m represented as red line

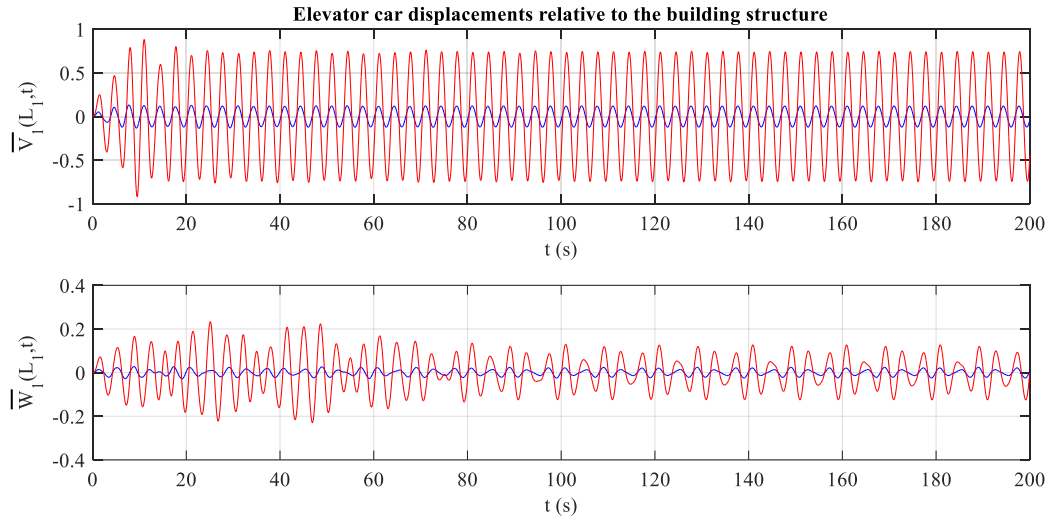

Figure 4.22 Lateral displacements of the elevator car relative to the building structure in the lateral in plane and out of plane direction for case study two comparing stiffness parameters of $k_1=k_2=80$kN/m represented as blue line and $k_1=k_2=30$kN/m represented as red line

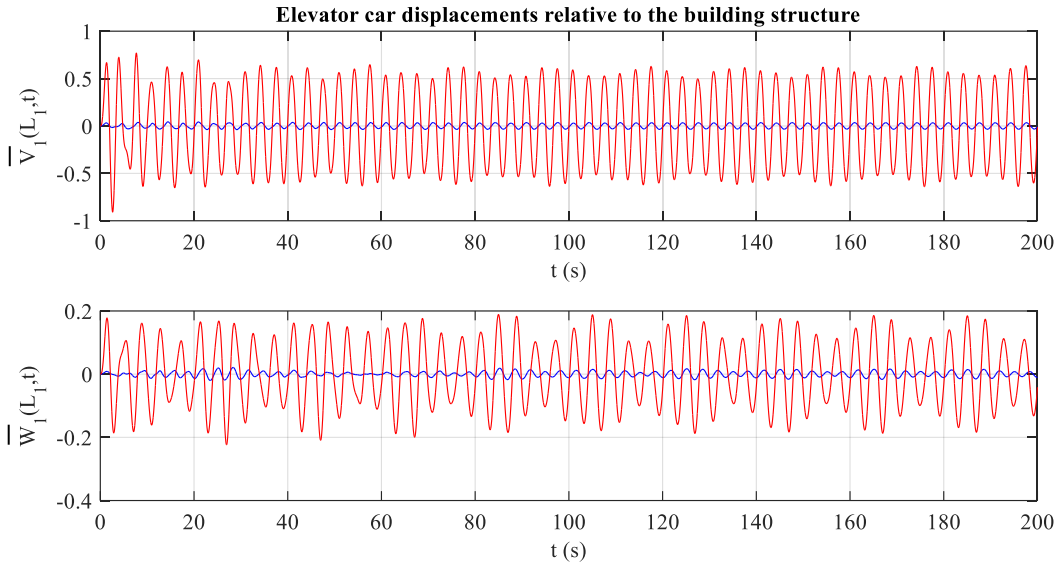

Figure 4.23 Lateral displacements of the elevator car relative to the building structure in the lateral in plane and out of plane direction for case study three comparing stiffness parameters of $k_1=k_2=80$kN/m represented as blue line and $k_1=k_2=30$kN/m represented as red line

4.3.5 Longitudinal response of the elevator car, compensating sheave, and counterweight

The longitudinal displacements of the elevator car, compensating sheave, and counterweight for case studies one, two, and three are shown in Figure 4.24, Figure 4.25, and Figure 4.26 compared when using a stiffness parameters of k_1=k_2=80kN/m represented as blue line and k_1=k_2=30kN/m represented as red line. When the elevator car is positioned at the bottom landing level and at the top landing level the longitudinal displacements of the elevator car, compensating sheave, counterweight the displacements when using high stiffness and low stiffness parameters are the same as in case studies one and three shown in Figure 4.24 and Figure 4.26. The highest displacements of the elevator car, compensating sheave, and counterweight are when the elevator car is at the veering point where the fundamental natural frequencies of the suspension and compensating ropes match as in case study two shown in Figure 4.25.

Figure 4.24 Longitudinal displacements of (a) elevator car (b) compensating sheave (c) counterweight for case study one when using a stiffness parameters of k_1=k_2=80kN/m represented as blue line and k_1=k_2=30kN/m represented as red line

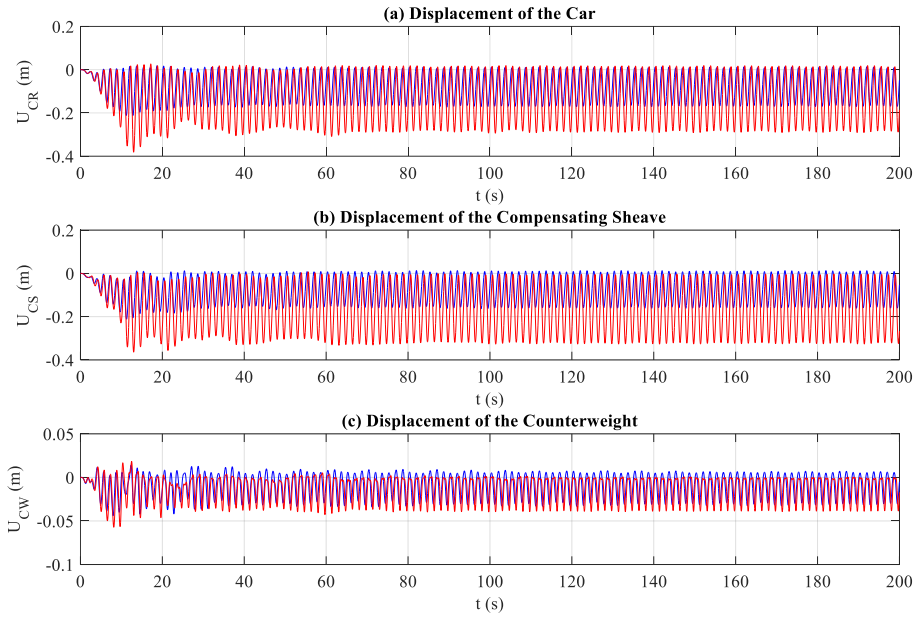

Figure 4.25 Longitudinal displacements of (a) elevator car (b) compensating sheave (c) counterweight for case study two when using a stiffness parameters of k_1=k_2=80kN/m represented as blue line and k_1=k_2=30kN/m represented as red line

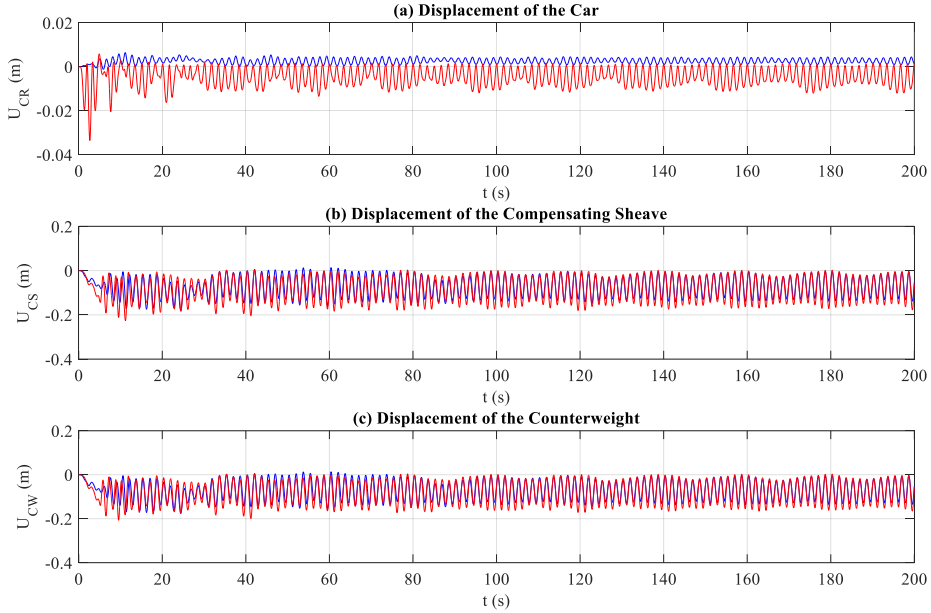

Figure 4.26 Longitudinal displacements of (a) elevator car (b) compensating sheave (c) counterweight for case study three when using a stiffness parameters of k_1=k_2=80kN/m represented as blue line and k_1=k_2=30kN/m represented as red line

The FFT frequency spectra of the elevator car, compensating sheave and counterweight over a time span of 100.0 seconds – 160.0 seconds from the longitudinal displacement response for case study one are shown in Figure 4.27 (a) (b) (c), compared when using a stiffness parameters of $k_1=k_2=80$kN/m represented as blue line and $k_1=k_2=30$kN/m represented as red line.

The predominant frequency shown Figure 4.27 is 0.60 Hz which is double the frequency of excitation in the lateral in plane direction of the building structure. This type of frequency is coming in the longitudinal direction of each mass by the coefficients f_{CR}, f_{CS}, f_{CW} that appear in equations (4.123) - (4.125) and are defined in equations (F.57), (F.67), and (F.74), respectively, and is primary external excitation.

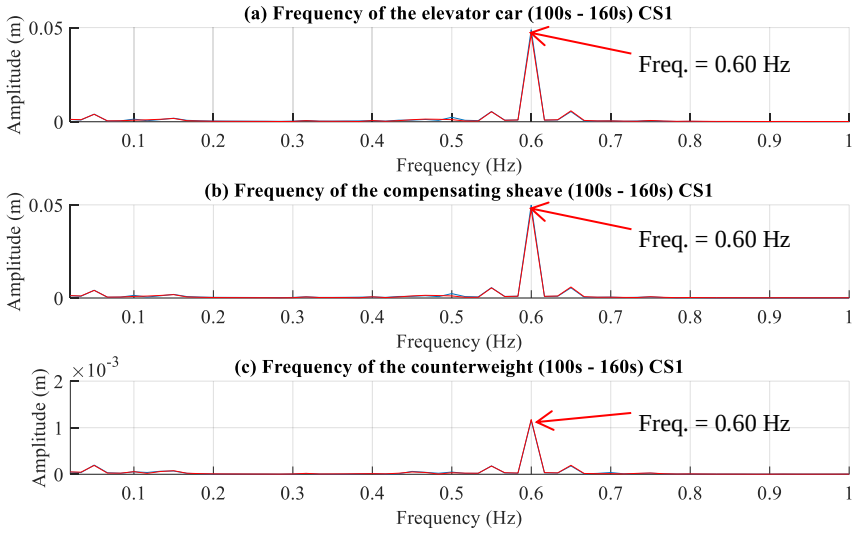

Figure 4.27 FFT frequency spectra of (a) elevator car (b) compensating sheave (c) counterweight between the time span of 100.0 seconds – 160.0 seconds for case study one with stiffness parameters of $k_1=k_2=80$kN/m represented as blue line and $k_1=k_2=30$kN/m represented as red line

The longitudinal displacements of the elevator car, compensating sheave and counterweight when the elevator car is positioned at the bottom and top landing level when compared with a high and low stiffness parameters there is no change in the displacement response of each mass. The high displacements were predicted when using a low spring parameter when compared with a high stiffness parameter when the elevator car is positioned at the height of 84.0m from the bottom landing level, which is where both the suspension and compensating ropes at the car side are excited at the fundamental natural frequency as shown in Figure 4.2.

As it was presented in this Chapter, when the elastic interface between the elevator car and the building structure in the lateral directions is considered the veering phenomena appear. The simulation results were compared when the elevator car is positioned at the bottom landing level, at a height where the eigenvalues of the suspension and compensating ropes at the car side for the fundamental natural frequency match, and when the elevator car is positioned at the top landing level, with a comparison when using a high and low stiffness parameter in the lateral direction of the elevator car. On all three case studies the lateral response of the suspension ropes, compensating ropes, and the elevator car was higher when the fundamental natural frequency of the suspension and compensating rope match.

Due to ride quality control on the elevator system, an elevator car with low lateral stiffness having high lateral vibrations as the ones shown in Figure 4.22 would not be suitable for service. This is why high stiffness springs are used in the elastic interface between the elevator car and the building structure in the lateral directions to minimize the lateral vibrations on the elevator car.

The stationary mathematical model derived in this chapter can be used to predict the response of the suspension and compensating ropes with the interaction between the elevator car, compensating sheave, and counterweight in the longitudinal direction with the lateral elastic interface between the elevator car and the building structure.

The mathematical model derived in this chapter has not yet been validated in a high rise building under wind loading. It is recommended that a full validation of the lateral displacements of the suspension and compensating ropes at the car and counterweight side be completed.

5. Nonstationary Model of a High – Rise Elevator System

5.1 Description of the vibration model

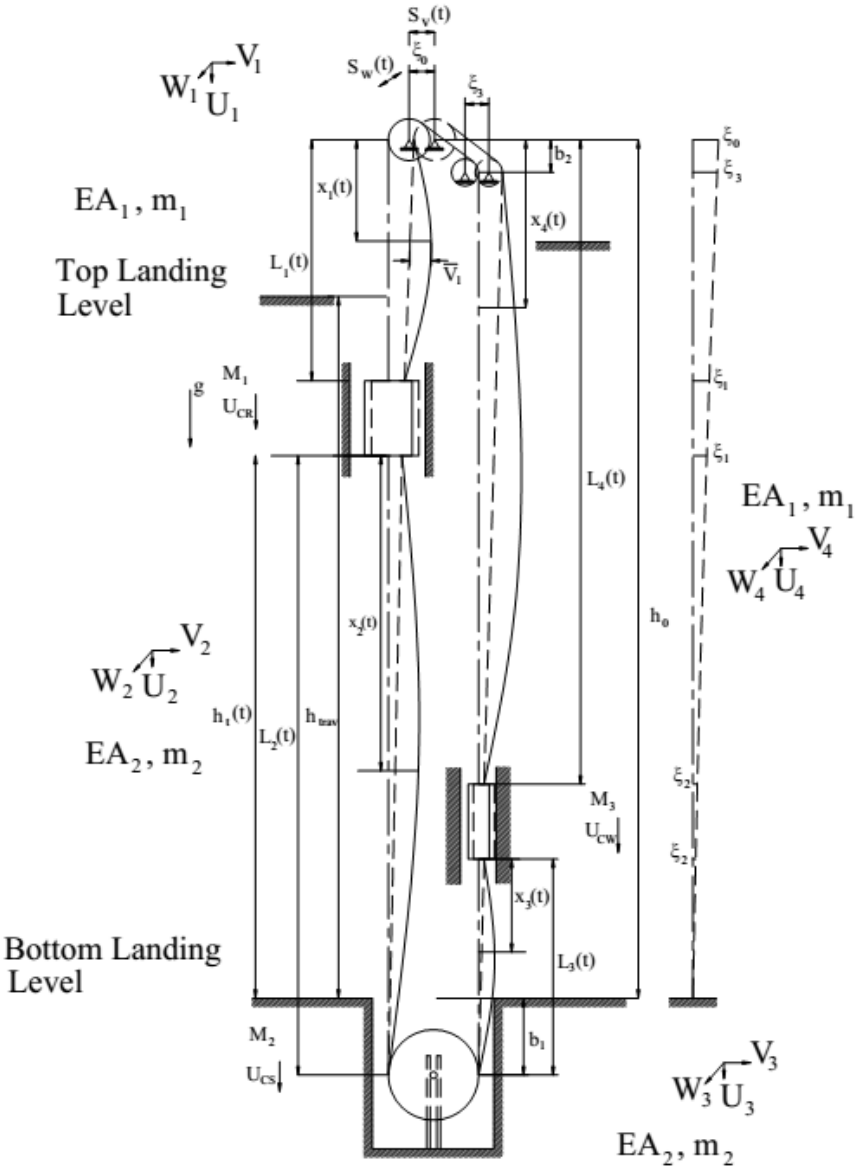

Figure 5.1 Drawing of the mathematical model taken into account.

The model of an elevator system discussed in Chapter 4 with a car of mass M_1 traveling up or down along the elevator shaft at the car side, a counterweight traveling in the opposite direction at the counterweight side, and a compensating sheave of mass M_2 positioned at the bottom of the elevator shaft and not travelling along the elevator shaft, is referred to in this chapter as nonstationary and is shown in Figure 5.1. The parameters that will change with time are the lengths of the ropes that change with the position of the elevator car and

counterweight along the height of travel. The length of the suspension ropes and of the compensating ropes of the car and counterweight side denoted by $L_1(t)$, $L_2(t)$, $L_3(t)$, and $L_4(t)$ will be varying with time according to the kinematic profile dictated by the drive control algorithm, the equations were derived in Salamaliki-Simpson (2009).

The response of the elevator ropes subjected to dynamic loading due to the building sway are represented by the lateral in-plane and lateral out of plane displacements denoted as $V_i\left(x_i(t),t\right)$ and $W_i\left(x_i(t),t\right)$ where the subscript $i=1,2,3,4$ corresponds to the sections of the ropes of length L_1, L_2, L_3, and L_4, respectively. The displacements of the ropes relative to the configuration of the ropes when they are stretched by the structure motion are represented by $\bar{V}_i\left(x(t),t\right)$ and $\bar{W}_i\left(x_i(t),t\right)$. The lateral in-plane and lateral out of plane motions of the ropes are coupled with the longitudinal motions of the ropes that are denoted as $U_i\left(x_i(t),t\right)$. The rest of the parameters remain unchanged.

As discussed by Kaczmarczyk and Iwankiewicz (2006) and in Strakosch (1998), the lateral vibrations at the elevator car are induced by irregularities and imperfections of the rail guide system resulting from the accumulation of manufacturing error, which are transmitted to the suspension and compensating ropes resulting in adverse dynamic behaviour of the elevator system. According to Lopez et al. (2010), which proposed an adaptive control for active suspension of an elevator car to improve ride quality in high-rise buildings to minimize the lateral vibrations on an elevator car are used in high rise buildings. Thus, lateral vibrations of the elevator car and counterweight during travel were not considered in the derivation of the mathematical model of a complete elevator system.

The time varying lengths of the system are represented by $L_i(t)$for $i=1,2,\ldots,4$. When the variation of $L_i(t)$ is small over a time interval corresponding to the fundamental natural frequency of the system considered as fixed values of these parameters, the length is said to vary slowly with time, according to Kaczmarczyk (1997). The variation of $L_i(t)$ is then observed on a slow time scale defined as $\tau=\bar{\varepsilon}T$, where T is a non-dimensional fast time scale and $\bar{\varepsilon}$ is a small parameter. Thus, the length of the ropes can be represented by $L_i(\tau)$ In order to represent the slow variability of L_i the fast non-dimensional time scale is defined as defined as $T=\omega_0 t$, where ω_0 is the initial fundamental natural frequency of the system and t is the time. The small parameter $\bar{\varepsilon}$ can be defined as equation (5.1).

$$\bar{\varepsilon}=\frac{v(t)}{\omega_0 L_0} \tag{5.1}$$

where L_0 is the initial lengths of the ropes corresponding to ω_0. According to Kaczmarczyk (2005), for high rise elevator system the terms identified as being of the order $0(\bar{\varepsilon})$ or higher are neglected.

The assumptions taken into account in Chapter 4 remain the same. The following assumptions were taken into account:

a) The length of the ropes $L_i = L_i(\tau)$ for i=1,2,…,4 are slowly varying in time.

b) The Coriolis and centrifugal forces of the ropes are taken into account in the lateral direction.

c) The Coriolis and centrifugal forces are not considered in the longitudinal direction for the elevator car, compensating sheave, counterweight, and all ropes.

d) The travel kinematics is prescribed and the elevator car follows the time profile dictated by the drive control system, where the acceleration at the car and counterweight side are denoted as a_{CR} and a_{CW}=-a_{CR}. When the elevator car is travelling up to the top landing level the a_{CR} is considered with positive sign and travelling down to the bottom landing level the acceleration is considered with negative sign.

e) The compensating sheave is positioned at the pit constrained to vibrate in the longitudinal direction.

f) The longitudinal velocity of the rope section is given as $\dot{U} + v(t)$ where *v(t)* is the transport velocity and $\dot{U} = U_t + v(t)U_x$. Thus, the absolute longitudinal acceleration is given as $\frac{d}{dt}\left[U_t + v(t)U_x + v(t)\right] = U_{tt} + 2v(t)U_{xt} + v^2(t)U_{xx} + a(t)U_x + a(t)$, where *a(t)* is the acceleration at the car or counterweight side.

g) The elastic interface with the building at the car and counterweight side is neglected.

5.2 Derivation of the Mathematical model

The same procedure to derive the mathematical model of Chapter 4 using Hamilton principle is used to derive the nonstationary mathematical model of an elevator system on this chapter.

The terms corresponding to the centrifugal and Coriolis effects are considered and thus total derivatives are used to express the absolute velocity in the lateral in plane and out of plane directions represented by equations (5.2) and (5.3), respectively.

$$\frac{dV_i}{dt} = \dot{V}_i = \frac{\partial V_i(x_i,t)}{\partial t} + \frac{\partial V_i(x_i,t)}{\partial x_i} v(t) \tag{5.2}$$

$$\frac{dW_i}{dt} = \dot{W}_i = \frac{\partial W_i(x_i,t)}{\partial t} + \frac{\partial W_i(x_i,t)}{\partial x_i} v(t) \tag{5.3}$$

The kinetic energy of the system is rewritten as in equation (5.4)

$$\hat{Q} = \sum_{i=1}^{4} \int_0^L \bar{Q}_i\left(\dot{U}_i, \dot{V}_i, \dot{W}_i\right) dx + Q_{M_1}\left(\dot{U}_{CR}\right) + Q_{M_2}\left(U_{CS}\right)_t + Q_{M_3}\left(\dot{U}_{CW}\right) \tag{5.4}$$

where the upper dot represents the total derivative with respect to *t*. The kinetic energy of the ropes are expressed as equation (5.5).

$$\bar{Q}_i = \frac{1}{2} m_i \left[\left(\dot{U}_i + v(t)\right)^2 + \left(\dot{V}_i\right)^2 + \left(\dot{W}_i\right)^2 \right] \tag{5.5}$$

The kinetic energy of the elevator car is rewritten as in equation (5.6).

$$Q_{M_1} = \frac{1}{2} M_1 \left[\left(\dot{U}_{CR} + v(t)\right)^2 \right] \tag{5.6}$$

The kinetic energy of the compensating sheave is the same as in equation (4.5) and the kinetic energy of the counterweight is defined as in equation (5.7).

$$Q_{M_3} = \frac{1}{2} M_3 \left[\left(\dot{U}_{CW} + v(t)\right)^2 \right] \tag{5.7}$$

Applying into (3.17) equations (5.4), (4.7), (4.12), and (4.13) the following equation results

$$\int_{t_1}^{t_2} \left(\begin{array}{l} \sum_{i=1}^{4} \int_0^{L_i} \left(\delta \bar{Q}_i\left(\dot{U}_i, \dot{V}_i, \dot{W}_i\right) - \delta \hat{I}_{ig}\left(U_i\right) - \delta \hat{I}_{ie}\left(U_{ix}, V_{ix}, W_{ix}\right) \right) dx_i + \\ \delta Q_{M_1}\left(\dot{U}_{CR}\right) + \delta Q_{M_2}\left(\left(U_{CS}\right)_t\right) + \delta Q_{M_3}\left(\dot{U}_{CW}\right) \\ + M_1 g \delta U_{CR} + M_2 g \delta U_{CS} + M_3 g \delta U_{CW} \end{array} \right) dt = 0 \tag{5.8}$$

Integrating the kinetic energy of the rope with respect to t and x the following equation is derived

$$\int_{t_1}^{t_2} \int_0^{L_i} \delta \bar{Q}_i dx_i dt = \int_{t_1}^{t_2} \int_0^{L_i} \left(\left(\frac{\partial \bar{Q}_i}{\partial\left(\dot{U}_i + v(t)\right)} \right) \delta \dot{U}_i + \left(\frac{\partial \bar{Q}_i}{\partial \dot{V}_i} \right) \delta \dot{V}_i + \left(\frac{\partial \bar{Q}_i}{\partial \dot{W}_i} \right) \delta \dot{W}_i \right) dx_i dt \tag{5.9}$$

And

$$\int_{t_1}^{t_2} \delta \bar{Q}_i dt = \int_{t_1}^{t_2} \left(\frac{\partial \bar{Q}_i}{\partial \left(\dot{U}_i + v(t) \right)} \frac{d}{dt} \left(\delta U_i \right) + \frac{\partial \bar{Q}_i}{\partial \dot{V}_i} \frac{d}{dt} \left(\delta V_i \right) + \frac{\partial \bar{Q}_i}{\partial \dot{W}_i} \frac{d}{dt} \left(\delta W_i \right) \right) dt \tag{5.10}$$

Can be written as

$$\begin{aligned} \int_{t_1}^{t_2} \delta \bar{Q}_i dt &= \left[\frac{\partial \bar{Q}_i}{\partial \left(\dot{U}_i + v(t) \right)} \delta U_i \right]_{t_1}^{t_2} - \int_{t_1}^{t_2} \frac{d}{dt} \left(\frac{\partial \bar{Q}_i}{\partial \left(\dot{U}_i + v(t) \right)} \right) \delta U_i dt \\ &+ \left[\frac{\partial \bar{Q}_i}{\partial \dot{V}_i} \delta V_i \right]_{t_1}^{t_2} - \int_{t_1}^{t_2} \frac{d}{dt} \left(\frac{\partial \bar{Q}_i}{\partial \dot{V}_i} \right) \delta V_i dt \\ &+ \left[\frac{\partial \bar{Q}_i}{\partial \dot{W}_i} \delta W_i \right]_{t_1}^{t_2} - \int_{t_1}^{t_2} \frac{d}{dt} \left(\frac{\partial \bar{Q}_i}{\partial \dot{W}_i} \right) \delta W_i dt \end{aligned} \tag{5.11}$$

According to equation (4.14) the terms in red in equation (5.11) are the virtual displacements which are 0 when evaluated between t_1 and t_2. Thus, equation (5.11) can be rewritten as equation (5.12)

$$\int_{t_1}^{t_2} \delta \bar{Q}_i dt = -\int_{t_1}^{t_2} \frac{d}{dt} \left(\frac{\partial \bar{Q}_i}{\partial \left(\dot{U}_i + v(t) \right)} \right) \delta U_i dt - \int_{t_1}^{t_2} \frac{d}{dt} \left(\frac{\partial \bar{Q}_i}{\partial \dot{V}_i} \right) \delta V_i dt - \int_{t_1}^{t_2} \frac{d}{dt} \left(\frac{\partial \bar{Q}_i}{\partial \dot{W}_i} \right) \delta W_i dt \tag{5.12}$$

Similarly, the kinetic energy of the elevator car and counterweight are integrated with respect to t and represented in equations (5.13) and (5.14), respectively.

$$\int_{t_1}^{t_2} \delta Q_{M_1} dt = -\int_{t_1}^{t_2} \frac{d}{dt} \left(\frac{\partial Q_{M_1}}{\partial \left(\dot{U}_{CR} + v(t) \right)} \right) \delta U_{CR} dt \tag{5.13}$$

$$\int_{t_1}^{t_2} \delta Q_{M_3} dt = -\int_{t_1}^{t_2} \frac{d}{dt} \left(\frac{\partial Q_{M_3}}{\partial \left(\dot{U}_{CW} + v(t) \right)} \right) \delta U_{CW} dt \tag{5.14}$$

Applying into equation (5.8) equations (4.21), (5.12) - (5.14), (4.29), (4.31) and boundary conditions (4.34) - (4.41) the following equation is obtained

$$\int_{t_1}^{t_2}\left(\begin{array}{l}\sum_{i=1}^{4}\int_{0}^{L_i}\left(\begin{array}{l}\left[-\frac{d}{dt}\left(\frac{\partial\bar{Q}_i}{\partial\dot{V}_i}\right)+\frac{\partial}{\partial x}\left(\frac{\partial\hat{\Pi}_{ie}}{\partial V_{ix}}\right)\right]\delta V_i \\ +\left[-\frac{d}{dt}\left(\frac{\partial\bar{Q}_i}{\partial\left(\dot{U}_i+v(t)\right)}\right)+\frac{\partial}{\partial x}\left(\frac{\partial\Pi_{ie}}{\partial U_{ix}}\right)+m_i g\right]\delta U_i \\ +\left[-\frac{d}{dt}\left(\frac{\partial\bar{Q}_i}{\partial\dot{W}_i}\right)+\frac{\partial}{\partial x}\left(\frac{\partial\Pi_{ie}}{\partial W_{ix}}\right)\right]\delta W_i\end{array}\right)dx \\ +\left[-\frac{d}{dt}\left(\frac{\partial Q_{M_1}}{\partial\left(\dot{U}_{CR}+v(t)\right)}\right)-\left.\frac{\partial\hat{\Pi}_{1e}}{\partial U_{1x}}\right|_{x=L_1}+\left.\frac{\partial\hat{\Pi}_{2e}}{\partial U_{2x}}\right|_{x=0}+M_1 g\right]\delta U_{CR} \\ +\left[-\frac{d}{dt}\left(\frac{\partial Q_{M_2}}{\partial\left(U_{CS}\right)_t}\right)-\left.\frac{\partial\hat{\Pi}_{2e}}{\partial U_{2x}}\right|_{x=L_2}-\left.\frac{\partial\hat{\Pi}_{3e}}{\partial U_{3x}}\right|_{x=L_3}+M_2 g\right]\delta U_{CS} \\ +\left[-\frac{d}{dt}\left(\frac{\partial Q_{M_3}}{\partial\left(\dot{U}_{CW}+v(t)\right)}\right)-\left.\frac{\partial\hat{\Pi}_{4e}}{\partial U_{4x}}\right|_{x=L_4}+\left.\frac{\partial\hat{\Pi}_{3e}}{\partial U_{3x}}\right|_{x=L_3}+M_3 g\right]\delta U_{CW}\end{array}\right)dt=0 \tag{5.15}$$

The virtual displacement $\delta U_i, \delta V_i, \delta W_i, \delta U_{CR}, \delta U_{CS}, \delta U_{CW}$ are arbitrary and the above equation can only be valid for all the values of the virtual displacement if

$$\frac{d}{dt}\left(\frac{\partial\bar{Q}_i}{\partial\dot{V}_i}\right)-\frac{\partial}{\partial x}\left(\frac{\partial\hat{\Pi}_{ie}}{\partial V_{ix}}\right)=0 \tag{5.16}$$

$$\frac{d}{dt}\left(\frac{\partial\bar{Q}_i}{\partial\left(\dot{U}_i+v(t)\right)}\right)-\frac{\partial}{\partial x}\left(\frac{\partial\Pi_{ie}}{\partial U_{ix}}\right)-m_i g=0 \tag{5.17}$$

$$\frac{d}{dt}\left(\frac{\partial\bar{Q}_i}{\partial\dot{W}_i}\right)-\frac{\partial}{\partial x}\left(\frac{\partial\Pi_{ie}}{\partial W_{ix}}\right)=0 \tag{5.18}$$

$$\frac{d}{dt}\left(\frac{\partial Q_{M_1}}{\partial\left(\dot{U}_{CR}+v(t)\right)}\right)+\left.\frac{\partial\hat{\Pi}_{1e}}{\partial U_{1x}}\right|_{x=L_1}-\left.\frac{\partial\hat{\Pi}_{2e}}{\partial U_{2x}}\right|_{x=0}-M_1 g=0 \tag{5.19}$$

$$\frac{d}{dt}\left(\frac{\partial Q_{M_2}}{\partial\left(U_{CS}\right)_t}\right)+\left.\frac{\partial\hat{\Pi}_{2e}}{\partial U_{2x}}\right|_{x=L_2}+\left.\frac{\partial\hat{\Pi}_{3e}}{\partial U_{3x}}\right|_{x=L_3}-M_2 g=0 \tag{5.20}$$

$$\frac{d}{dt}\left(\frac{\partial Q_{M_3}}{\partial\left(\dot{U}_{CW}+v(t)\right)}\right)+\left.\frac{\partial\hat{\Pi}_{4e}}{\partial U_{4x}}\right|_{x=L_4}-\left.\frac{\partial\hat{\Pi}_{3e}}{\partial U_{3x}}\right|_{x=L_3}-M_3 g \tag{5.21}$$

Equations (5.16) - (5.21) can be rewritten as equations. (5.22) - (5.27). The equations (5.22) to (5.24) describe the dynamics of the i^{th} rope in the elevator system, where *i=1,2,3, and 4.*

$$\begin{aligned} &m_i\ddot{V}_i - T_{ix}V_{ix} - EA_i\left(U_{ix} + \frac{1}{2}\left(V_{ix}^{\,2} + W_{ix}^{\,2}\right)\right)_x V_{ix} \\ &-T_iV_{ixx} - EA_i\left(U_{ix} + \frac{1}{2}\left(V_{ix}^{\,2} + W_{ix}^{\,2}\right)\right)V_{ixx} = 0 \end{aligned} \tag{5.22}$$

$$\begin{aligned} &m_i\ddot{W}_i - T_{ix}W_{ix} - EA_i\left(U_{ix} + \frac{1}{2}\left(V_{ix}^{\,2} + W_{ix}^{\,2}\right)\right)_x W_{ix} \\ &-T_iW_{ixx} - EA_i\left(U_{ix} + \frac{1}{2}\left(V_{ix}^{\,2} + W_{ix}^{\,2}\right)\right)W_{ixx} = 0 \end{aligned} \tag{5.23}$$

$$m_i\left(\ddot{U}_i + a(t)\right) - T_{ix} - EA_i\left(U_{ix} + \frac{1}{2}\left(V_{ix}^{\,2} + W_{ix}^{\,2}\right)\right)_x - m_ig = 0 \tag{5.24}$$

The equations (5.25) to (5.27) are the boundary conditions at $x_1 = L_1(\tau)$ and $x_2=0$, $x_2 = L_2(\tau)$ and $x_3 = L_3(\tau)$, $x_3=0$, and $x_4 = L_4(\tau)$ in the longitudinal direction for the elevator car, compensating sheave, and counterweight respectively.

$$\begin{aligned} &M_1\left(\ddot{U}_{CR} + a(t)\right) + T_1(\mathrm{L}_1) + EA_1\left(U_{1x} + \frac{1}{2}\left(V_{1x}^{\,2} + W_{1x}^{\,2}\right)\right)\Big|_{x_1=L_1} \\ &-T_2(0) - EA_2\left(U_{2x} + \frac{1}{2}\left(V_{2x}^{\,2} + W_{2x}^{\,2}\right)\right)\Big|_{x_2=0} - M_1g = 0 \end{aligned} \tag{5.25}$$

$$\begin{aligned} &M_2\left(U_{CS}\right)_{tt} + T_2(\mathrm{L}_2) + EA_2\left(U_{2x} + \frac{1}{2}\left(V_{2x}^{\,2} + W_{2x}^{\,2}\right)\right)\Big|_{x_2=L_2} \\ &+T_3(\mathrm{L}_3) + EA_2\left(U_{3x} + \frac{1}{2}\left(V_{3x}^{\,2} + W_{3x}^{\,2}\right)\right)\Big|_{x_3=L_3} - M_2g = 0 \end{aligned} \tag{5.26}$$

$$\begin{aligned} &M_3\left(\ddot{U}_{CW} + a(t)\right) + T_4(\mathrm{L}_4) + EA_1\left(U_{4x} + \frac{1}{2}\left(V_{4x}^{\,2} + W_{4x}^{\,2}\right)\right)\Big|_{x_4=L_4} \\ &-T_3(0) - EA_2\left(U_{3x} + \frac{1}{2}\left(V_{3x}^{\,2} + W_{3x}^{\,2}\right)\right)\Big|_{x_3=0} - M_3g = 0 \end{aligned} \tag{5.27}$$

The equations (4.59) to (4.62) of tension derived in Chapter 4 are rewritten as equations (5.28) to (5.31), which include the acceleration at the car and counterweight side.

$$T_1(x_1, t;\tau) = \left(M_1 + m_1\left(L_1(\tau) - x_1\right) + m_2L_2(\tau)\right)\left(g - a_{CR}(t)\right) + \frac{M_2}{2}g \tag{5.28}$$

$$T_2\left(x_2,t;\tau\right)=\left(m_2\left(L_2\left(\tau\right)-x_2\right)\right)\left(g-a_{CR}\left(t\right)\right)+\frac{M_2}{2}g \tag{5.29}$$

$$T_3\left(x_3,t;\tau\right)=\left(m_2\left(L_3\left(\tau\right)-x_3\right)\right)\left(g-a_{CW}\left(t\right)\right)+\frac{M_2}{2}g \tag{5.30}$$

$$T_4\left(x_4,t;\tau\right)=\left(M_3+m_1\left(L_4\left(\tau\right)-x_4\right)+m_2L_3\left(\tau\right)\right)\left(g-a_{CW}\left(t\right)\right)+\frac{M_2}{2}g \tag{5.31}$$

where the acceleration at the car and counterweight side are defined as a_{CR} and a_{CW}=-a_{CR}. Additionally of equations (4.78) to (4.91) for the partial derivatives with respect to x and t required for this model are shown in equations (5.32) to (5.35) for the lateral in plane direction.

$$V_{1xt}=\bar{V}_{1xt}+\left(\frac{\psi_1\left(\tau\right)-1}{L_1\left(\tau\right)}\right)\mathrm{A}_v\,\lambda_v\cos\left(\lambda_v t\right)=\bar{V}_{1xt}+J_1^v \tag{5.32}$$

$$V_{2xt}=\bar{V}_{2xt}-\left(\frac{\psi_2\left(\tau\right)}{L_2\left(\tau\right)}\right)\mathrm{A}_v\,\lambda_v\cos\left(\lambda_v t\right)=\bar{V}_{2xt}-J_2^v \tag{5.33}$$

$$V_{3xt}=\bar{V}_{3xt}-\left(\frac{\psi_3\left(\tau\right)}{L_3\left(\tau\right)}\right)\mathrm{A}_v\,\lambda_v\cos\left(\lambda_v t\right)=\bar{V}_{3xt}-J_3^v \tag{5.34}$$

$$V_{4xt}=\bar{V}_{4xt}+\left(\frac{\psi_4\left(\tau\right)-\psi_5\left(\tau\right)}{L_4\left(\tau\right)}\right)\mathrm{A}_v\,\lambda_v\cos\left(\lambda_v t\right)=\bar{V}_{4xt}+J_4^v \tag{5.35}$$

Similarly, the partial derivatives with respect to x and t for the lateral out of plane direction can be deducted. The deformations obtained with $\psi_1\left(\tau\right),\psi_2\left(\tau\right),\psi_3\left(\tau\right),\psi_4\left(\tau\right),\psi_5\left(\tau\right)$ change slowly in time. Thus, are determined with the same shape function as in Chapter 4. Substituting equations (5.28) to (5.31) into equation (5.24) results in equation (5.36).

$$m_i\ddot{U}_i-EA_i\left(U_{ix}+\frac{1}{2}\left(V_{ix}^{\ 2}+W_{ix}^{\ 2}\right)\right)_x=0 \tag{5.36}$$

According to Kaczmarczyk et al. (2010), the entire longitudinal inertia from equation (5.36) can be neglected. Considering the longitudinal natural frequencies of the ropes are much higher than the lateral natural frequencies, resulting in equation (5.37) where $e_i(t;\tau)$ have slowly varying terms in time corresponding to $L_i(\tau)$.

$$e\left(t;\tau\right)=U_{ix}+\frac{1}{2}\left(V_{ix}^{\ 2}+W_{ix}^{\ 2}\right) \tag{5.37}$$

For the longitudinal direction of the elevator car and counterweight equations (5.25) and (5.27) are simplified by neglecting the Coriolis and centrifugal forces in the longitudinal direction as $v(t)U_x = 0$ resulting in equations (5.38) and (5.40) respectively which are the same as equation (4.56) and (4.58) derived in Chapter 4. The equation (4.57) of the compensating sheave derived in Chapter 4 remains unchanged.

$$M_1(U_{CR})_{tt} + EA_1\left(U_{1x} + \frac{1}{2}\left(V_{1x}{}^2 + W_{1x}{}^2\right)\right)\Big|_{x_1=L_1} - EA_2\left(U_{2x} + \frac{1}{2}\left(V_{2x}{}^2 + W_{2x}{}^2\right)\right)\Big|_{x_2=0} = 0 \tag{5.38}$$

$$M_2(U_{CS})_{tt} + EA_2\left(U_{2x} + \frac{1}{2}\left(V_{2x}{}^2 + W_{2x}{}^2\right)\right)\Big|_{x=L_2} + EA_2\left(U_{3x} + \frac{1}{2}\left(V_{3x}{}^2 + W_{3x}{}^2\right)\right)\Big|_{x=L_3} = 0 \tag{5.39}$$

$$M_3(U_{CW})_{tt} + EA_1\left(U_{4x} + \frac{1}{2}\left(V_{4x}{}^2 + W_{4x}{}^2\right)\right)\Big|_{x_4=L_4} - EA_2\left(U_{3x} + \frac{1}{2}\left(V_{3x}{}^2 + W_{3x}{}^2\right)\right)\Big|_{x_3=0} = 0 \tag{5.40}$$

The absolute acceleration is derived by equations (5.2) and (5.3) given in equations (5.41) and (5.42) for the lateral in plane and lateral out of plane direction respectively.

$$\frac{d}{dt}(\dot{V}_i) = \frac{\partial^2 V_i(x_i,t)}{\partial t^2} + 2v(t)\frac{\partial^2 V_i(x_i,t)}{\partial x_i \partial t} + \frac{\partial^2 V_i(x_i,t)}{\partial x_i{}^2}v^2(t) + a(t)\frac{\partial V_i(x_i,t)}{\partial x_i} \tag{5.41}$$

$$\frac{d}{dt}(\dot{W}_i) = \frac{\partial^2 W_i(x_i,t)}{\partial t^2} + 2v(t)\frac{\partial^2 W_i(x_i,t)}{\partial x_i \partial t} + \frac{\partial^2 W_i(x_i,t)}{\partial x_i{}^2}v^2(t) + a(t)\frac{\partial W_i(x_i,t)}{\partial x_i} \tag{5.42}$$

Equations (5.22) and (5.23) can be rewritten using equations (5.41) and (5.42) represented in equations (5.43) to (5.44).

$$\begin{aligned} &m_i V_{itt} + 2m_i v(t)V_{ixt} + m_i v^2(t)V_{ixx} + m_i a(t)V_{ix} - T_{ix}V_{ix} \\ &-EA_i\left(U_{ix} + \frac{1}{2}\left(V_{ix}{}^2 + W_{ix}{}^2\right)\right)_x V_{ix} - T_i V_{ixx} - EA_i\left(U_{ix} + \frac{1}{2}\left(V_{ix}{}^2 + W_{ix}{}^2\right)\right)V_{ixx} = 0 \end{aligned} \tag{5.43}$$

$$\begin{aligned} &m_i W_{itt} + 2m_i v(t)W_{ixt} + m_i v^2(t)W_{ixx} + m_i a(t)W_{ix} - T_{ix}W_{ix} \\ &-EA_i\left(U_{ix} + \frac{1}{2}\left(V_{ix}{}^2 + W_{ix}{}^2\right)\right)_x W_{ix} - T_i W_{ixx} - EA_i\left(U_{ix} + \frac{1}{2}\left(V_{ix}{}^2 + W_{ix}{}^2\right)\right)W_{ixx} = 0 \end{aligned} \tag{5.44}$$

The Galerkin method is applied with the expansions shown in equations (5.45) and (5.46).

$$\bar{V}_i(x_i,t;\tau) = \sum_{n=1}^{N} \phi_{in}(x_i;\tau)\,\mathrm{q}_{in}(t) \tag{5.45}$$

$$\bar{W}_i(x_i,t;\tau) = \sum_{n=1}^{N} \alpha_{in}(x_i;\tau)\,\mathrm{c}_{in}(t) \tag{5.46}$$

The linear natural modes of the lateral in plane and out of plane motions for all ropes are shown in equations (5.47) and (5.48) with the slowly varying in time terms.

$$\phi_{in}\left(x_i;\tau\right)=sin\left(\frac{n\pi}{L_i\left(\tau\right)}x_i\right) \text{ for } i=1,\ldots 4. \tag{5.47}$$

$$\alpha_{in}\left(x_i;\tau\right)=sin\left(\frac{n\pi}{L_i\left(\tau\right)}x_i\right) \text{ for } i=1,\ldots 4. \tag{5.48}$$

According to Kaczmarczyk (1997), the lengths $L_i\left(\tau\right)$ are changing slowly in time, the eigenvalues for the lateral in plane and out of plane direction for the i^{th} rope can be determined as $\frac{n\pi}{L_i\left(\tau\right)}$, which are changing slowly in time.

The lateral in plane and lateral out of plane natural frequencies represented by $\hat{\omega}_{in}^{Lin}\left(\tau\right)$ and $\hat{\omega}_{in}^{Lout}\left(\tau\right)$ corresponds to a value of $L_i(\tau)$. The natural frequencies of ropes $i=1,\ldots,4$ represented by $\hat{\omega}_{in}^{Lin}\left(\tau\right)$ and $\hat{\omega}_{in}^{Lout}\left(\tau\right)$ for the lateral in plane and out of plane direction can be determined using equation (5.49) corresponding to a value of $L_i(\tau)$, respectively.

$$\hat{\omega}_{in}^{Lin}\left(\tau\right)=\hat{\omega}_{in}^{Lout}\left(\tau\right)=\frac{n\pi}{L_i\left(\tau\right)}\sqrt{\frac{T_i\left(x_i,t;\tau\right)}{m_i}} \tag{5.49}$$

Substituting expansions (5.47) and (5.48) into equation (5.37) which can be expanded into equations (5.50) to (5.53).

$$e_1\left(t;\tau\right)=\frac{U_{CR}}{L_1\left(\tau\right)}+\frac{1}{4}\sum_{j=1}^{N}\left(\frac{j\pi}{L_1\left(\tau\right)}\right)^2 q_{1j}^2\left(t\right)+\frac{\left(f_1^{v}\left(t;\tau\right)\right)^2}{2}+\frac{1}{4}\sum_{j=1}^{N}\left(\frac{j\pi}{L_1\left(\tau\right)}\right)^2 c_{1j}^2\left(t\right) + \frac{\left(f_1^{w}\left(t;\tau\right)\right)^2}{2} \tag{5.50}$$

$$e_2\left(t;\tau\right)=\frac{U_{CS}-U_{CR}}{L_2\left(\tau\right)}+\frac{1}{4}\sum_{j=1}^{N}\left(\frac{j\pi}{L_2\left(\tau\right)}\right)^2 q_{2j}^2\left(t\right)+\frac{\left(f_2^{v}\left(t;\tau\right)\right)^2}{2}+\frac{1}{4}\sum_{j=1}^{N}\left(\frac{j\pi}{L_2\left(\tau\right)}\right)^2 c_{2j}^2\left(t\right) + \frac{\left(f_2^{w}\left(t;\tau\right)\right)^2}{2} \tag{5.51}$$

$$e_3(t;\tau)=\frac{U_{CS}-U_{CW}}{L_3(\tau)}+\frac{1}{4}\sum_{j=1}^{N}\left(\frac{j\pi}{L_3(\tau)}\right)^2 q_{3j}^2(t)+\frac{\left(f_3^v(t;\tau)\right)^2}{2}+\frac{1}{4}\sum_{j=1}^{N}\left(\frac{j\pi}{L_3(\tau)}\right)^2 c_{3j}^2(t)+\frac{\left(f_3^w(t;\tau)\right)^2}{2} \tag{5.52}$$

$$e_4(t;\tau)=\frac{U_{CW}}{L_4(\tau)}+\frac{1}{4}\sum_{j=1}^{N}\left(\frac{j\pi}{L_4(\tau)}\right)^2 q_{4j}^2(t)+\frac{\left(f_4^v(t;\tau)\right)^2}{2}+\frac{1}{4}\sum_{j=1}^{N}\left(\frac{j\pi}{L_4(\tau)}\right)^2 c_{4j}^2(t)+\frac{\left(f_4^w(t;\tau)\right)^2}{2} \tag{5.53}$$

Substituting expansions (5.45) and (5.46) and equations (5.50) to (5.53) into (5.43) to (5.44) and applying the orthogonality conditions with respect to the linear modes a system of nonlinear ordinary differential equations for the i^{th} rope results as follows.

$$\ddot{\mathrm{q}}_{ir}(t)+\sum_{n=1}^{N}B_{irn}(t;\tau)\dot{\mathrm{q}}_{in}(t)+\left(\hat{\omega}_{ir}(\tau)\right)^2\mathrm{q}_{ir}(t)+\sum_{n=1}^{N}\hat{k}_{irn}(t;\tau)\mathrm{q}_{in}(t)+\sum_{n=1}^{N}\tilde{R}_{irn}(\tau)q_{in}^2(t)q_{ir}(t)+\sum_{n=1}^{N}\tilde{R}_{irn}(\tau)c_{in}^2(t)c_{ir}(t)+\hat{F}_{ir}^{Lin}(t;\tau)=0 \tag{5.54}$$

$$\ddot{c}_{ir}(t)+\sum_{n=1}^{N}B_{irn}(t;\tau)\dot{c}_{in}(t)+\left(\hat{\omega}_{ir}(\tau)\right)^2 c_{ir}(t)+\sum_{n=1}^{N}\hat{k}_{irn}(t;\tau)c_{in}(t)+\sum_{n=1}^{N}\tilde{R}_{irn}(\tau)q_{in}^2(t)c_{ir}(t)+\sum_{n=1}^{N}\tilde{R}_{irn}(\tau)c_{in}^2(t)c_{ir}(t)+\hat{F}_{ir}^{Lout}(t;\tau)=0 \tag{5.55}$$

Equations (5.54) and (5.55) represent the equations of motion of the i^{th} rope for $i=1,\ldots,4$ in the lateral in plane and out of plane directions.

The coefficients $B_{irn}, \hat{k}_{irn}$ represent the damping and stiffness matrix for the lateral in plane and out of plane direction, respectively. The coefficients $\tilde{R}_{irn}$ are the cubic nonlinear terms for the lateral in plane and out of plane directions. The coefficients $\hat{F}_{ir}^{Lin}, \hat{F}_{ir}^{Lout}$ are the excitation terms for the lateral in plane and out of plane directions of rope i^{th}. The equations (5.50) to (5.53) are substituted in equations (5.38) to (5.40) for the elevator car, compensating sheave, and counterweight resulting in equations (5.56) to (5.58).

$$M_1\left(U_{CR}(t)\right)_{tt}+\hat{k}^{1u1}(\tau)U_{CR}(t)+\hat{k}^{2u1}(\tau)U_{CS}(t)+\sum_{n=1}^{N}\tilde{R}_n^{1u1}(\tau)q_{1n}^2(t)$$
$$+\sum_{n=1}^{N}\tilde{R}_n^{1u1}(\tau)c_{1n}^2(t)+\sum_{n=1}^{N}\tilde{R}_n^{2u1}(\tau)q_{2n}^2(t)+\sum_{n=1}^{N}\tilde{R}_n^{2u1}(\tau)c_{2n}^2(t)+f_{CR}(t;\tau)=0 \quad (5.56)$$

$$M_2\left(U_{CS}(t)\right)_{tt}+\hat{k}^{1u2}(\tau)U_{CR}(t)+\hat{k}^{2u2}(\tau)U_{CS}(t)+\hat{k}^{3u2}(\tau)U_{CW}(t)+\sum_{n=1}^{N}\tilde{R}_n^{1u2}(\tau)q_{2n}^2(t)$$
$$+\sum_{n=1}^{N}\tilde{R}_n^{1u2}(\tau)c_{2n}^2(t)+\sum_{n=1}^{N}\tilde{R}_n^{2u2}(\tau)q_{3n}^2(t)+\sum_{n=1}^{N}\tilde{R}_n^{2u2}(\tau)c_{3n}^2(t)+f_{CS}(t;\tau)=0 \quad (5.57)$$

$$M_3\left(U_{CW}(t)\right)_{tt}+\hat{k}^{1u3}(\tau)U_{CS}(t)+\hat{k}^{2u3}(\tau)U_{CW}(t)+\sum_{n=1}^{N}\tilde{R}_n^{1u3}(\tau)q_{3n}^2(t)$$
$$+\sum_{n=1}^{N}\tilde{R}_n^{1u3}(\tau)c_{3n}^2(t)+\sum_{n=1}^{N}\tilde{R}_n^{2u3}(\tau)q_{4n}^2(t)+\sum_{n=1}^{N}\tilde{R}_n^{2u3}(\tau)c_{4n}^2(t)+f_{CW}(t;\tau)=0 \quad (5.58)$$

Equations (5.56) to (5.58) represent the motion in the longitudinal direction of the elevator car, compensating sheave, and counterweight with slowly varying coefficients in time corresponding to $L_i(\tau)$.

Equations (5.56) to (5.58) are transformed into the modal coordinates using the transformation $\vec{U}(t)=\left[Y(\tau)\right]\vec{S}(t)$ where $\vec{U}(t)=\left[U_{CR}(t)\quad U_{CS}(t)\quad U_{CW}(t)\right]^T$ and $\vec{S}(t)=\left[S_{CR}(t)\quad S_{CS}(t)\quad S_{CW}(t)\right]^T$ is a vector of modal-coordinates corresponding to the system comprising the car, compensating sheave, and counterweight, respectively. If $\left[Y(\tau)\right]$ is the mass-normalized mode shape matrix slowly changing in time, the following set of equations describing the vertical response of the car, compensating sheave and counterweight in terms of the modal parameters are represented in equations (5.59) to (5.61).

$$\ddot{S}_{CR}(t)+2\zeta_{CR}\omega_{CR}(\tau)\dot{S}_{CR}(t)+\omega_{CR}^2(\tau)S_{CR}(t)+\left(\vec{Y}^{(1)}(\tau)\right)^T\left(\vec{F}(t;\tau)+\vec{\eta}(t;\tau)\right)=0 \quad (5.59)$$

$$\ddot{S}_{CS}(t)+2\zeta_{CS}\omega_{CS}(\tau)\dot{S}_{CS}(t)+\omega_{CS}^2(\tau)S_{CS}(t)+\left(\vec{Y}^{(2)}(\tau)\right)^T\left(\vec{F}(t;\tau)+\vec{\eta}(t;\tau)\right)=0 \quad (5.60)$$

$$\ddot{S}_{CW}(t)+2\zeta_{CW}\omega_{CW}(\tau)\dot{S}_{CW}(t)+\omega_{CW}^2(\tau)S_{CW}(t)+\left(\vec{Y}^{(3)}(\tau)\right)^T\left(\vec{F}(t;\tau)+\vec{\eta}(t;\tau)\right)=0 \quad (5.61)$$

The longitudinal natural frequencies of the elevator car, compensating sheave and counterweight represented as $\omega_{CR}(\tau),\omega_{CS}(\tau),\omega_{CW}(\tau)$ are changing slowly in time corresponding to the lengths $L_i(\tau)$ of the i^{th} rope due to the change of position of the elevator car and counterweight. The longitudinal natural frequencies of the elevator car, compensating

sheave and counterweight can be estimated with the eigenvalues of the stiffness matrix shown in (5.62) changing slowly in time and the mass matrix represented in (4.130).

$$\begin{bmatrix} \hat{k}^{1u1}(\tau) & \hat{k}^{2u1}(\tau) & 0 \\ \hat{k}^{1u2}(\tau) & \hat{k}^{2u2}(\tau) & \hat{k}^{3u2}(\tau) \\ 0 & \hat{k}^{1u3}(\tau) & \hat{k}^{2u3}(\tau) \end{bmatrix} \tag{5.62}$$

The coefficients $\vec{F}(t;\tau), \vec{\eta}(t;\tau)$ are shown in equations (5.63) and (5.64).

$$\vec{F}(t;\tau) = \begin{bmatrix} f_{CR}(t;\tau) \\ f_{CS}(t;\tau) \\ f_{CW}(t;\tau) \end{bmatrix} \tag{5.63}$$

$$\vec{\eta}(t;\tau) = \begin{bmatrix} \eta_{CR}(t;\tau) \\ \eta_{CS}(t;\tau) \\ \eta_{CW}(t;\tau) \end{bmatrix} \tag{5.64}$$

The coefficients $\eta_{CR}(t;\tau), \eta_{CS}(t;\tau), \eta_{CW}(t;\tau)$ are the quadratic terms from the equations of motion of the elevator car, compensating sheave, counterweight represented in equations (5.65) to (5.67).

$$\eta_{CR}(t;\tau) = \sum_{n=1}^{N} \tilde{R}_n^{1u1}(\tau) q_{1n}^2(t) + \sum_{n=1}^{N} \tilde{R}_n^{1u1}(\tau) c_{1n}^2(t) + \sum_{n=1}^{N} \tilde{R}_n^{2u1}(\tau) q_{2n}^2(t) + \sum_{n=1}^{N} \tilde{R}_n^{2u1}(\tau) c_{2n}^2(t) \tag{5.65}$$

$$\eta_{CS}(t;\tau) = \sum_{n=1}^{N} \tilde{R}_n^{1u2}(\tau) q_{2n}^2(t) + \sum_{n=1}^{N} \tilde{R}_n^{1u2}(\tau) c_{2n}^2(t) + \sum_{n=1}^{N} \tilde{R}_n^{2u2}(\tau) q_{3n}^2(t) + \sum_{n=1}^{N} \tilde{R}_n^{2u2}(\tau) c_{3n}^2(t) \tag{5.66}$$

$$\eta_{CW}(t;\tau) = \sum_{n=1}^{N} \tilde{R}_n^{1u3}(\tau) q_{3n}^2(t) + \sum_{n=1}^{N} \tilde{R}_n^{1u3}(\tau) c_{3n}^2(t) + \sum_{n=1}^{N} \tilde{R}_n^{2u3}(\tau) q_{4n}^2(t) + \sum_{n=1}^{N} \tilde{R}_n^{2u3}(\tau) c_{4n}^2(t) \tag{5.67}$$

All coefficients appear in Appendix G, which are dependent of the slowly varying parameter τ for $L_i(\tau)$.

5.3 Simulation Results

Two case study results are shown to verify the proposed mathematical model of a nonstationary elevator system through a comparison of each case study results when the elevator car is travelling along the travel height at high and low velocity, to demonstrate the influence of the Coriolis and centrifugal forces.

The parameters taken to analyse the dynamic performance of an elevator system in this chapter are exactly the same as the ones presented in Chapter 4 without considering the elastic interface with the building at the car in the lateral directions. The excitation of the building structure at the machine room level is also the same as in Chapter 4.

It is assumed the elevator car is travelling at a rated acceleration of $a_{CR}(t)=1.80m/s^2$, and a rated jerk of $j(t)=1.80m/s^3$. From the Galerkin method the nonlinear ordinary differential equations are given for N number of modes for the simulation results presented in this Chapter, the number of modes taken into account are $N=4$.

According to Salamaliki-Simpson (2009), the solution for a nonstationary rope and mass mathematical model can be obtained with a stiff solver of integration algorithm. However, a non-stiff solver is used to find the solution of the dynamic response of a nonstationary full elevator system, such as ODE45.

For case study one the elevator car is traveling at a rated velocity of $v(t)=15.00m/s$ and a comparison is shown when the car is travelling from the bottom landing level to the top landing level and from the top landing level to the bottom landing level. The kinematic profile of the elevator car dictated by the drive control algorithm is shown in Figure 5.2 when the elevator is travelling from the bottom landing level to the top landing level. Similarly when the elevator car is traveling from the top landing level to the bottom landing level can be obtained.

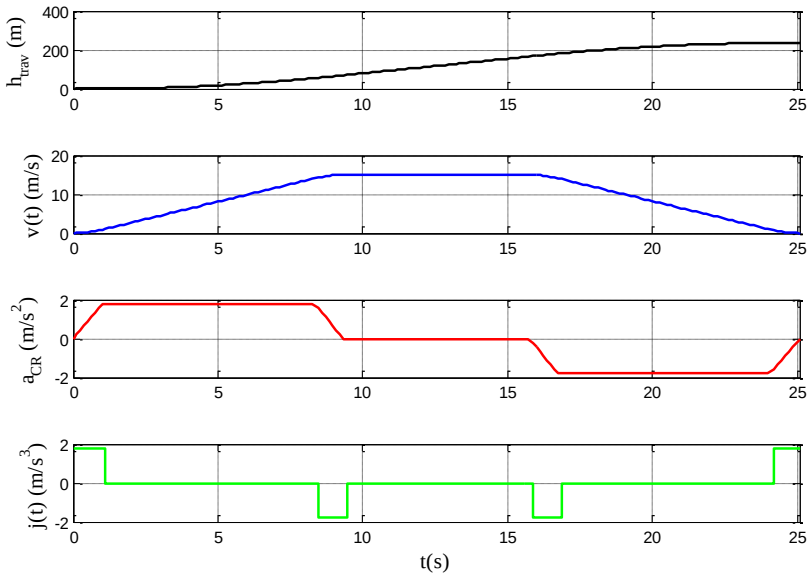

Figure 5.2 The kinematic profile of the elevator car for case study one when the car is going from the bottom landing level to the top landing level with a rated velocity of $v(t)=15.00m/s$

For case study two the elevator car is traveling at a rated velocity of *v(t)=4.00m/s* and a comparison is given when the car is travelling from the bottom landing level to the top landing level and from the top landing level to the bottom landing level. The kinematic profile of the elevator car dictated by the drive control algorithm is shown in Figure 5.3 when the elevator is travelling from the bottom landing level to the top landing level. Similarly when the elevator car is traveling from the top landing level to the bottom landing level can be obtained.

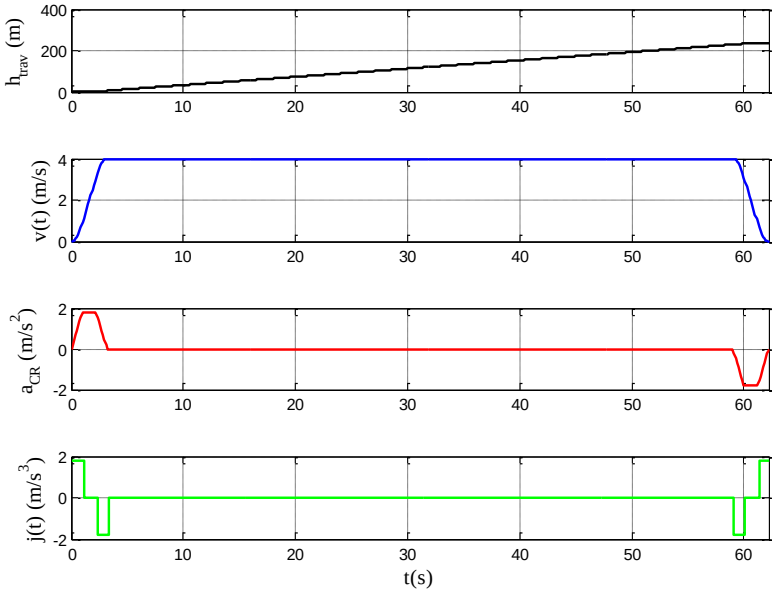

Figure 5.3 The kinematic profile of the elevator car for case study two when the car is going from the bottom landing level to the top landing level with a rated velocity of *v(t)=4.00m/s*

5.3.1 Frequency Analysis

The variation of frequency in the lateral direction of the suspension ropes at the car side according to the position of the elevator car along the travel height is determined with the eigenvalues of equation (5.68).

$$\tilde{\omega}_{1rr}(\tau)=\begin{bmatrix} \dfrac{r^2\pi^2}{L_1^{\,2}(\tau)}\left[-v^2(t)+\dfrac{M_1+m_1L_1(\tau)+m_2L_2(\tau)}{m_1}\left(g-a_{CR}(t)\right)+\dfrac{M_2}{2m_1}g-\dfrac{gL_1(\tau)}{2}\right] \\ \dfrac{2nr\left((-1)^{n+r}-1\right)}{\left(n^2-r^2\right)^2L_1(\tau)}\left(-g\left(n^2+r^2\right)+a_{CR}(t)\left(3n^2-r^2\right)\right) \end{bmatrix} \quad (5.68)$$

The variation of frequency corresponding to all lateral modes of the suspension ropes dependent of τ which are slowly changing in time due to $L_i(\tau)$ at the car side according to the position of the elevator car in the hoistway is measured from the bottom landing level are shown in Figure 5.4 with a *v(t)=15.00m/s* as in case study one and in Figure 5.5 with a *v(t)=4.00m/s* as in case study two. In Figure 5.4 and Figure 5.5 the solid red, green, cyan, and purple line are the variation of frequency of the first four lateral natural frequencies at the car side of the suspension ropes, considering the Coriolis and centrifugal forces as shown in equation (5.68). The dashed dotted red, green, cyan, and purple line is when the Coriolis and centrifugal forces are not considered as shown in equation (5.69). The small step from the curves of the natural frequencies of the suspension ropes with the Coriolis and centrifugal forces is due to the high velocity considered in case study one. When the elevator car is traveling at a low velocity there is low influence of the Coriolis and centrifugal forces in the natural frequencies of the ropes. This can be demonstrated with case study two in Figure 5.5 where the elevator car is traveling at a low velocity.

In Figure 5.4, Figure 5.5, Figure 5.6, and Figure 5.7 the dashed black, blue, and cyan lines represent the change of frequency in the longitudinal direction of the elevator car, compensating sheave, and counterweight according to the position of the elevator car, estimated by finding the eigenvalues from the stiffness matrix represented in (5.62) and mass matrix represented in (4.130).

In Figure 5.4, Figure 5.5, Figure 5.6, and Figure 5.7 the dashed magenta and blue horizontal lines represent the frequency of excitation from the building structure at 0.30 Hz and 0.25 Hz in the lateral in plane and out of plane directions.

The suspension ropes will be passing through resonance, matching the fundamental natural frequency, when the elevator car is at a height of approximately 50.0 m from the bottom landing level. The passage through resonance occur when the ropes are changing length and one of the natural frequencies of the ropes matches the external excitation frequency as discussed by Kaczmarczyk (2012), Kaczmarczyk (1997), Terumichi et al. (1997), and Terumichi et al. (2003), thus the lateral displacement response of the ropes will start to increase and then decrease. During the passage through resonance, the elevator car travelling at high velocity the lateral displacements of the ropes will be smaller when compared when the elevator car is travelling at low velocity.

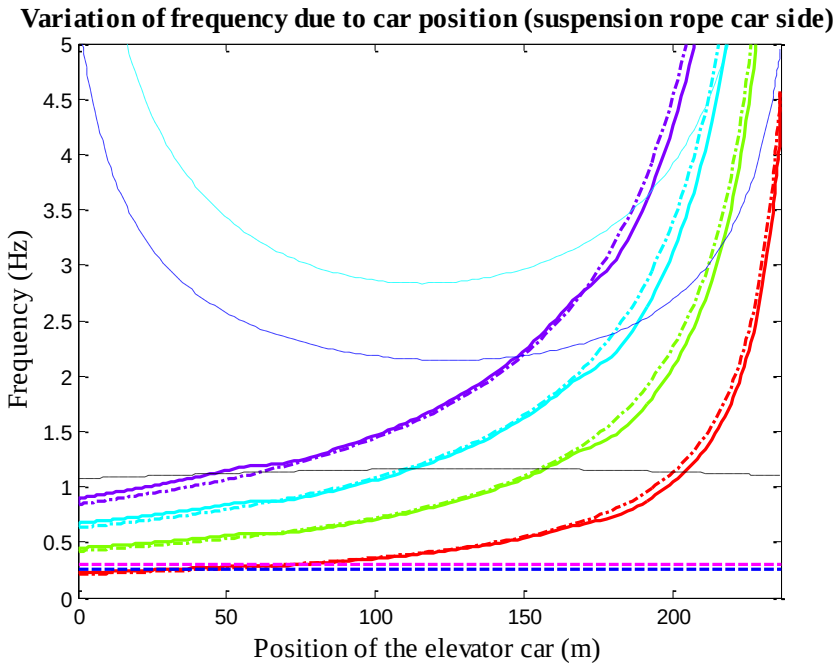

Figure 5.4 Variation of frequency of the suspension ropes according to the position of the elevator car (car side) for *v(t)=15.00m/s* for case study one

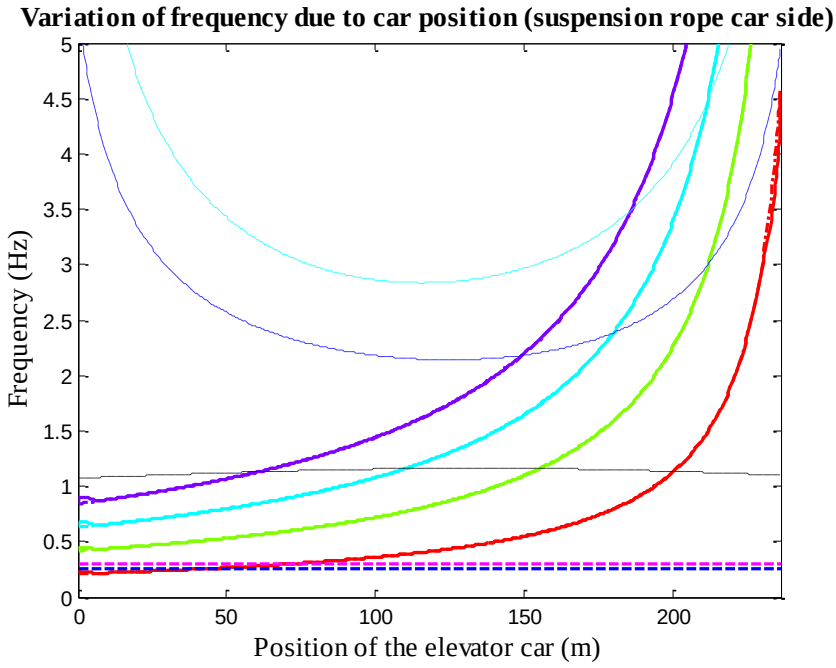

Figure 5.5 Variation of frequency of the suspension ropes according to the position of the elevator car (car side) for *v(t)=4.00m/s* for case study two

$$\tilde{\omega}_{1rr}(\tau)=\left[\begin{array}{c}\dfrac{r^2\pi^2 g}{L_1{}^2(\tau)}\left[\dfrac{M_1+m_1L_1(\tau)+m_2L_2(\tau)+\dfrac{M_2}{2}}{m_1}-\dfrac{L_1(\tau)}{2}\right]\\ -\dfrac{2gnr\left((-1)^{n+r}-1\right)}{\left(n^2-r^2\right)^2 L_1(\tau)}\left(n^2+r^2\right)\end{array}\right] \tag{5.69}$$

The variation of frequency in the lateral direction of the compensating ropes at the car side according to the positions of the elevator car along the travel height is determined with the eigenvalues of equation (5.70)

$$\tilde{\omega}_{2rr}(\tau)=\left[\begin{array}{c}\dfrac{r^2\pi^2}{L_2{}^2(\tau)}\left[-v_{CR}^2(t)+L_2(\tau)\left(g-a_{CR}(t)\right)+\dfrac{M_2}{2m_2}g-\dfrac{gL_2(\tau)}{2}\right]\\ \dfrac{2nr\left((-1)^{n+r}-1\right)}{\left(n^2-r^2\right)^2 L_2(\tau)}\left(-g\left(n^2+r^2\right)+a_{CR}(t)\left(3n^2-r^2\right)\right)\end{array}\right] \tag{5.70}$$

The variation of frequency corresponding to all lateral modes of the compensating ropes at the car side dependent of τ which are slowly changing in time due to $L_i(\tau)$ according to the position of the elevator car in the hoistway measured from the bottom landing level are shown in Figure 5.6 with a *v(t)=15.00m/s* as in case study one and in Figure 5.7 with a v(*t)=4.00m/s* as in case study two. In Figure 5.6 and Figure 5.7 the solid red, green, cyan, and purple line are the variation of frequency of the first four laterals in plane natural frequencies at the car side of the compensating ropes, considering the Coriolis and centrifugal forces as shown in equation (5.70). The dashed dotted red, green, cyan, and purple line is when the Coriolis and centrifugal forces are not considered.

The compensating ropes will be passing through resonance, matching the 1st and 2nd natural frequencies, at a height of approximately 100.0 m and 200.0 m from the bottom landing level, respectively.

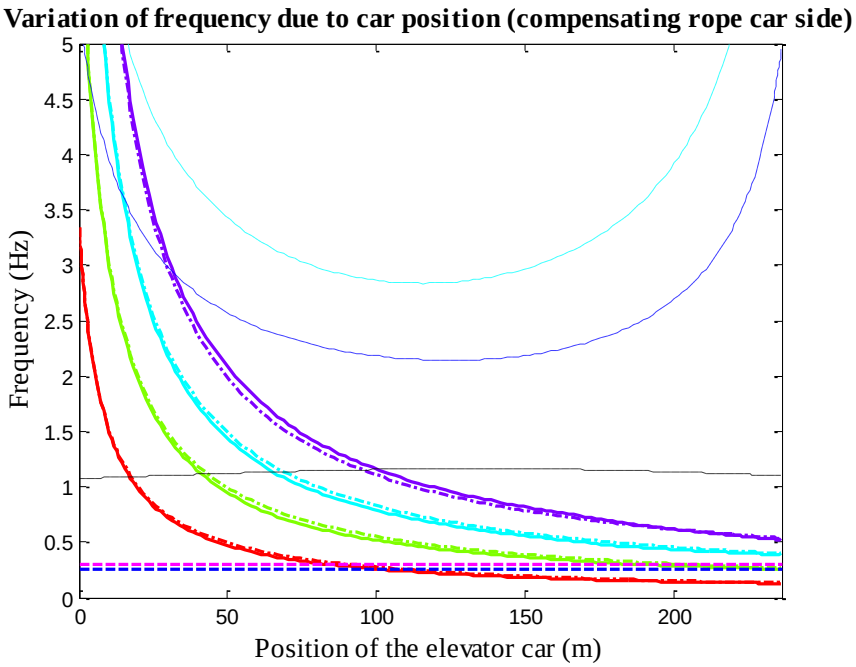

Figure 5.6 Variation of frequency of the compensating ropes according to the position of the elevator car (car side) for *v(t)=15.00m/s* for case study one

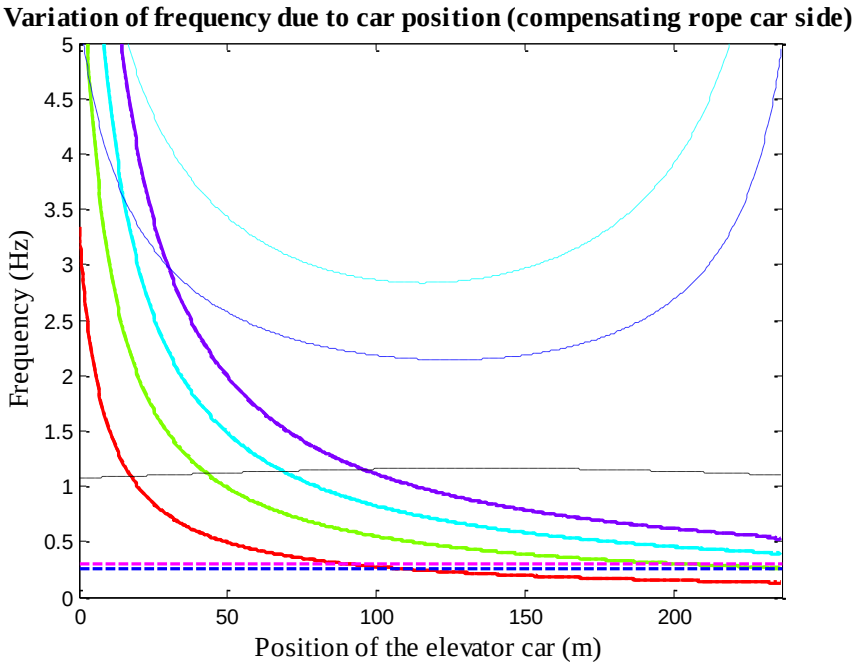

Figure 5.7 Variation of frequency of the compensating ropes according to the position of the elevator car (car side) for *v(t)=4.00m/s* for case study two

The variation of frequency of the compensating and suspension ropes at the counterweight side can be obtained from the mathematical model.

5.3.2 Mode shapes

The mode shapes of the elevator car, compensating sheave, and counterweight are dependent of τ which are slowly changing in time due to $L_i(\tau)$. In section 4.3.2 are shown the mode shapes of the elevator car, compensating sheave, and counterweight when the car is at the bottom landing level, at 84.0m from the bottom landing level, and at the top landing level.

In Figure 5.8 are shown the mode shapes of the 1st and 2nd mode shapes of the suspension ropes at the car side for case study one represented by a solid and dashed blue line, respectively. The mode shapes of the suspension rope at the car side are scaled to show the maximum amplitude as 1. Similarly, the mode shapes for all ropes have the same shape which are coming from the trial function used in the Galerkin method defined in equations (5.47) and (5.48) which are changing according to the position of the elevator car while travelling along the travel height.

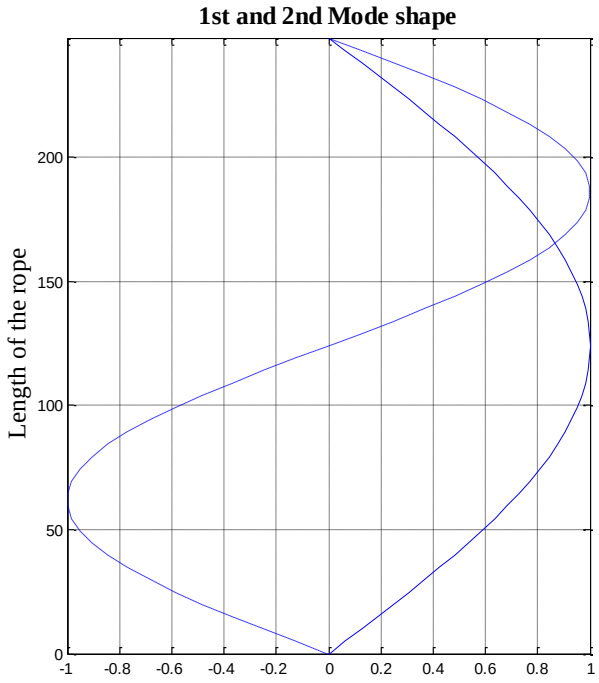

Figure 5.8 1st and 2nd mode shapes of the suspension rope at the car side

5.3.3 Response of the ropes

The behaviour of all ropes of the elevator system are obtained from the mathematical model. The displacement of the suspension ropes at the car side at the mid span length of the rope for case study one when the elevator car is travelling at a rated velocity of *v(t)=15.00m/s* when

going from the bottom landing level to the top landing level represented by a blue solid line and when traveling from the top to the bottom landing level represented by a red line are shown in Figure 5.9 for (a) in the lateral in plane direction and (b) in the lateral out of plane direction. Similarly, the displacement of the suspension ropes at the car side at the mid span length of the rope for case study two when the elevator car is travelling at a rated velocity of v(t)=4.00m/s is shown in Figure 5.10.

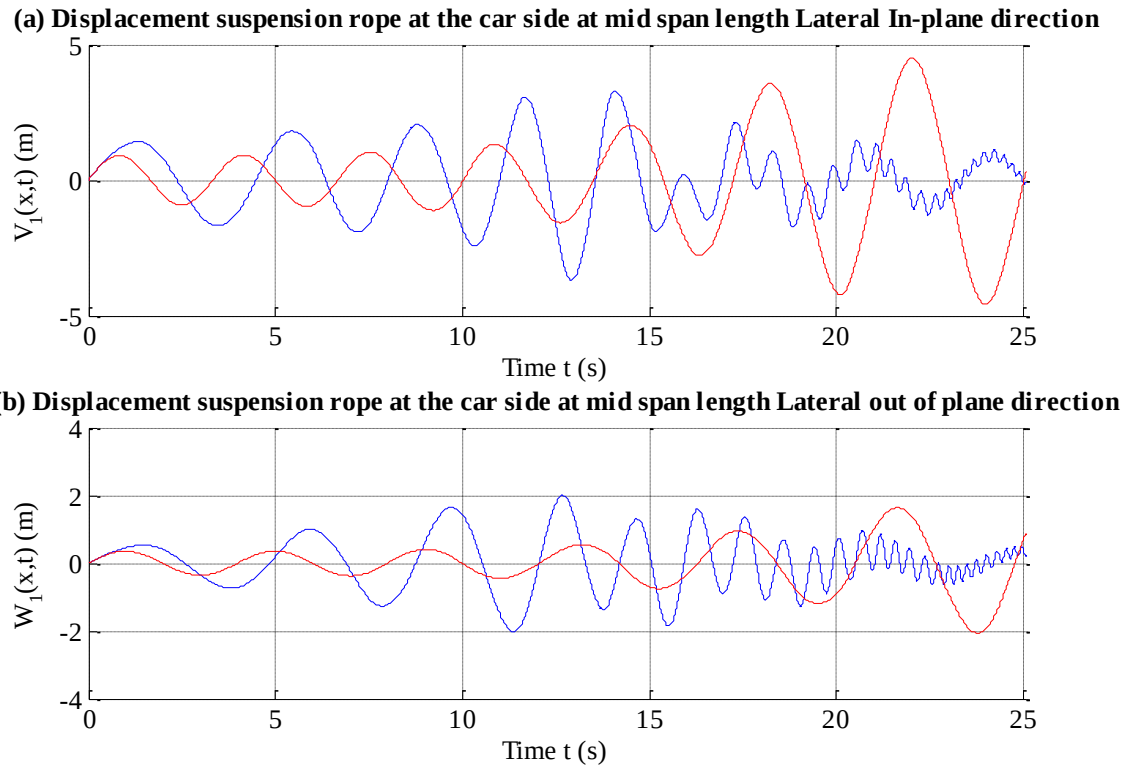

Figure 5.9 Displacement of the suspension rope at the car side at the mid span length of the ropes in (a) Lateral in plane (b) Lateral out of plane directions when the elevator car is travelling with a rated speed of *v(t)=15.00m/s* as in case study one when the car is travelling up represented by a blue line and when going down is represented by a red line.

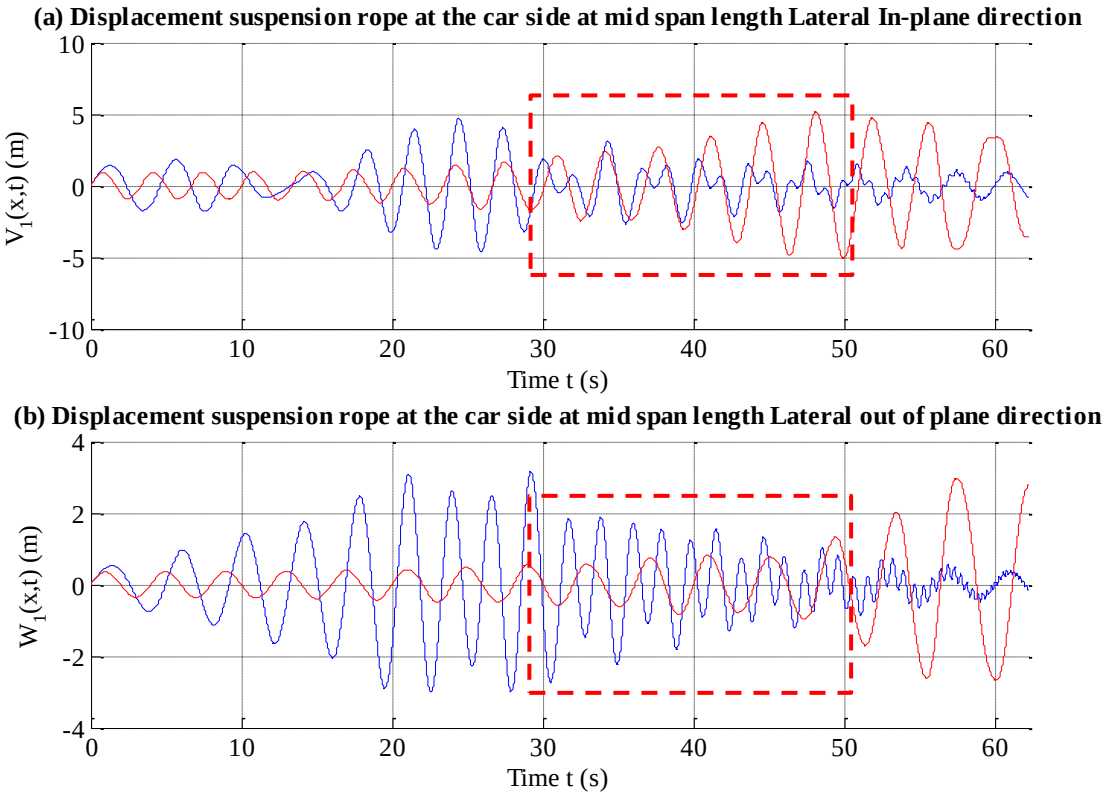

Figure 5.10 Displacement of the suspension rope at the car side at the mid span length of the ropes in (a) Lateral in plane (b) Lateral out of plane directions when the elevator car is travelling with a rated speed of *v(t)=4.00m/s* as in case study two when the car is travelling up represented by a blue line and when going down is represented by a red line

As shown in Figure 5.9 and Figure 5.10 the passage of resonance of the suspension ropes at the car side when the elevator car is traveling at a rated velocity of 15.00m/s and 4.00m/s is observed when the elevator car is at a height of approximately 50.0 m from the bottom landing level. The response of the ropes in the lateral in plane and out of plane direction are higher when the car is travelling at a rated velocity of 4.00m/s, as discussed by Terumichi et al. (2003).

The FFT frequency spectra of the lateral in plane and out of plane direction over a time span of 30.0 seconds – 50.0 seconds for case study two are shown in Figure 5.11 (a) and (b), respectively. The maximum frequencies are 0.30 Hz and 0.25 Hz which are the frequencies in which the building structure is exciting the ropes in the lateral in plane and out of plane directions shown in Figure 5.11 (a) and (b). The frequencies of 0.30 Hz and 0.25 Hz from the lateral in plane and out of plane directions are coming from the kinematic forcing terms that are exciting the ropes at the machine room level.

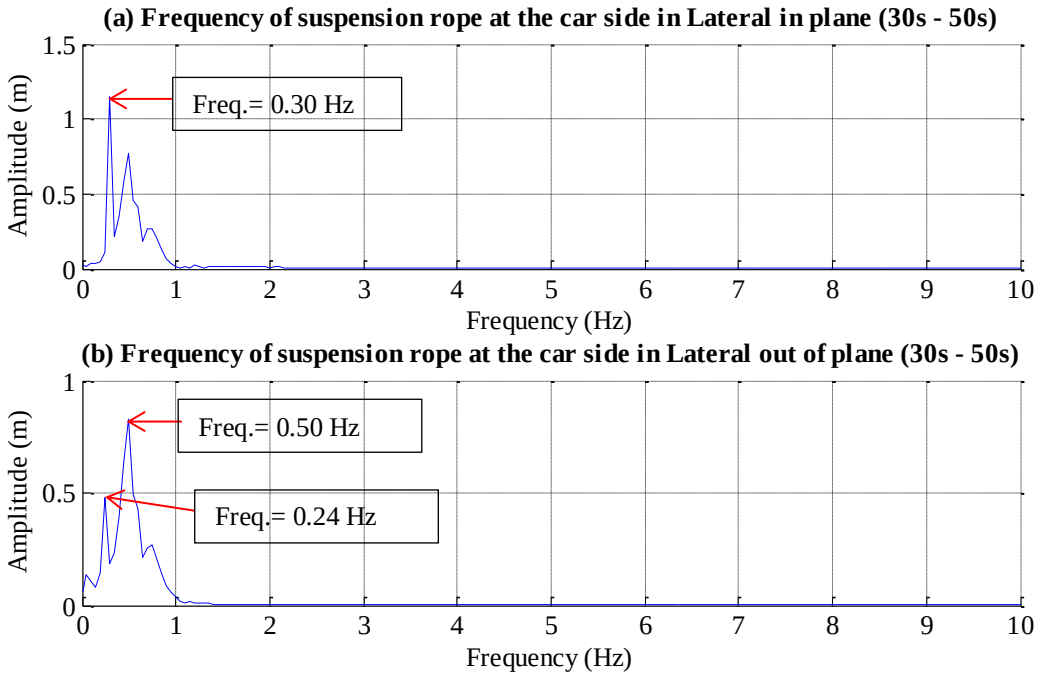

Figure 5.11 The FFT frequency spectrum of the suspension rope in the lateral in plane direction between 30 seconds and 50 seconds (a) Lateral in plane direction (b) Lateral out of plane direction for case study two when the elevator is travelling to the top landing level with *v(t)=4.00m/s*

In Figure 5.12 and Figure 5.13 show the maximum displacements of the suspension ropes at the car side in the lateral in plane when the elevator car is travelling from the bottom to the top landing level represented by a dashed blue line and when the car is travelling from the top to the bottom landing level represented by a dashed red line at a rated velocity of *v(t)=15.00m/s* and *v(t)=4.00m/s*, respectively. The suspension rope length is measured from center of the traction sheave to the top elevator car which is considered as a lumped mass where the height is neglected according to the assumption made in Chapter 4. As it can be seen maximum displacements are observed when the elevator car is travelling at a rated velocity of 4.00m/s. The suspension ropes are excited at the fundamental natural frequency thus the 1st mode shape is the maximum displacements of the suspension ropes at the car side.

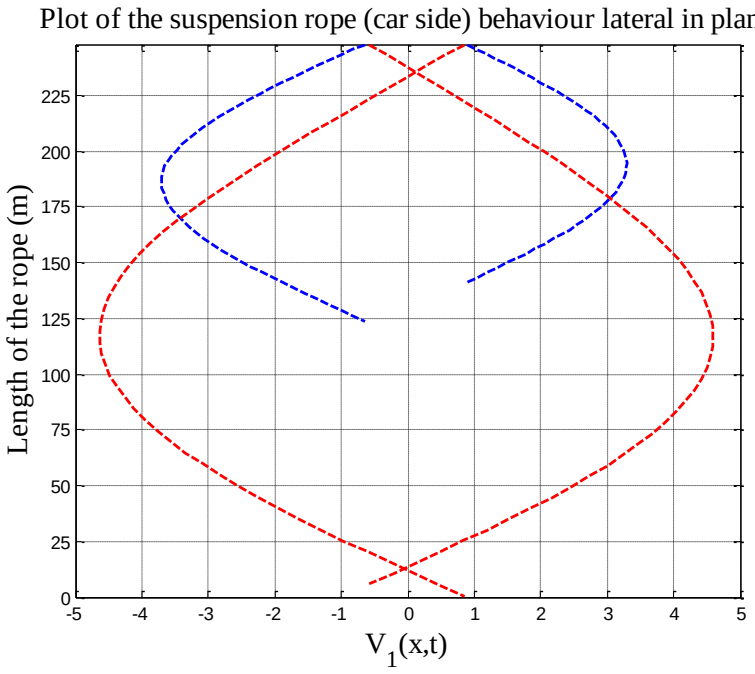

Figure 5.12 Behaviour of the suspension rope at the car side in the lateral in plane direction for case study one comparing when the elevator car is travelling with a rated velocity of *v(t)=15.00m/s* when the car is going up represented by dashed blue line and when going down represented by dashed red line

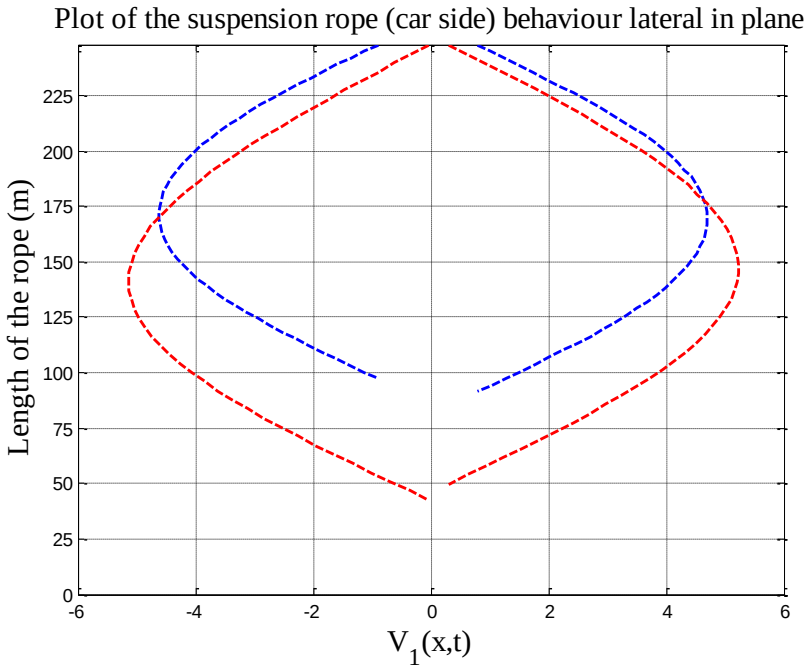

Figure 5.13 Behaviour of the suspension rope at the car side in the lateral in plane direction for case study two comparing when the elevator car is travelling with a rated velocity of *v(t)=4.00m/s* when the car is going up represented by dashed blue line and when going down represented by dashed red line

In Figure 5.14 and Figure 5.15 show the maximum displacements of the suspension ropes at the car side in the lateral out of plane when the elevator car is travelling from the bottom to the top landing level represented by a dashed blue line and when the car is travelling from the top to the bottom landing level represented by a dashed red line at a rated velocity of *v(t)=15.00m/s* and *v(t)=4.00m/s*, respectively. The maximum displacements are when the elevator car is travelling at a rated velocity of 4.00m/s. The suspension ropes are excited at the fundamental natural frequency thus the 1st mode shape is the maximum displacements of the suspension ropes at the car side.

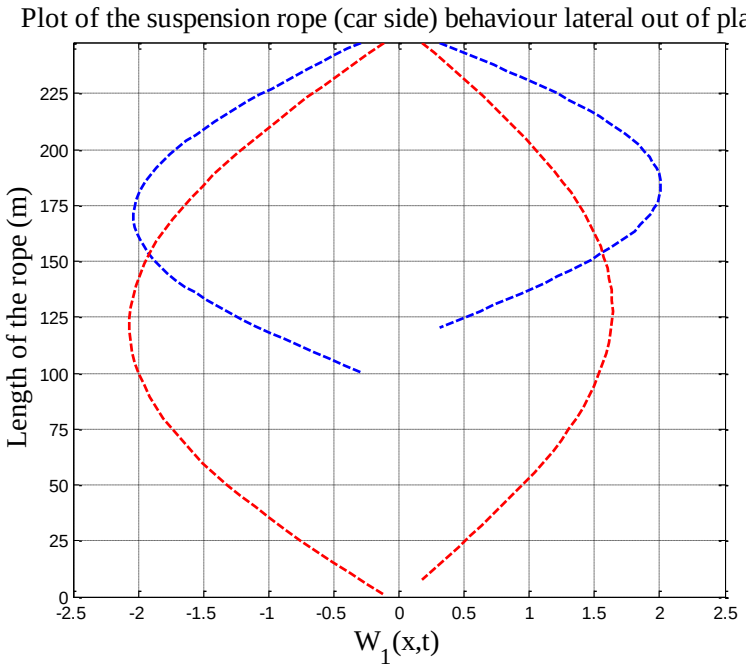

Figure 5.14 Behaviour of the suspension rope at the car side in the lateral out of plane direction for case study one comparing when the elevator car is travelling with a rated velocity of *v(t)=15.00m/s* when the car is going up represented by dashed blue line and when going down represented by dashed red line

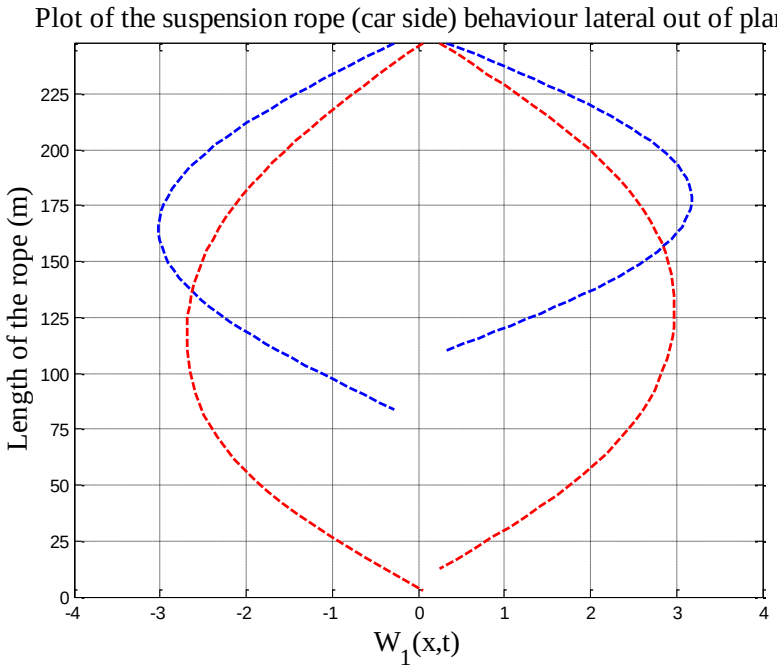

Figure 5.15 Behaviour of the suspension rope at the car side in the lateral out of plane direction for case study two comparing when the elevator car is travelling with a rated velocity of *v(t)=4.00m/s* when the car is going up represented by dashed blue line and when going down represented by dashed red line

In Figure 5.16 and Figure 5.17 show the maximum displacements of the compensating ropes at the car side in the lateral in plane when the elevator car is travelling from the bottom to the top landing level represented by a dashed blue line and when the car is travelling from the top to the bottom landing level represented by a dashed red line at a rated velocity of *v(t)=15.00m/s* and *v(t)=4.00m/s*, respectively. The compensating rope length is measured from the center of the compensating sheave to the bottom of the elevator car which is considered as a lumped mass where the height is neglected according to the assumption made in Chapter 4. The maximum displacements are when the elevator car is travelling at a rated velocity of 4.00m/s. The compensating ropes are excited at the second natural frequency thus the 2nd mode shape is the maximum displacements of the compensating ropes at the car side.

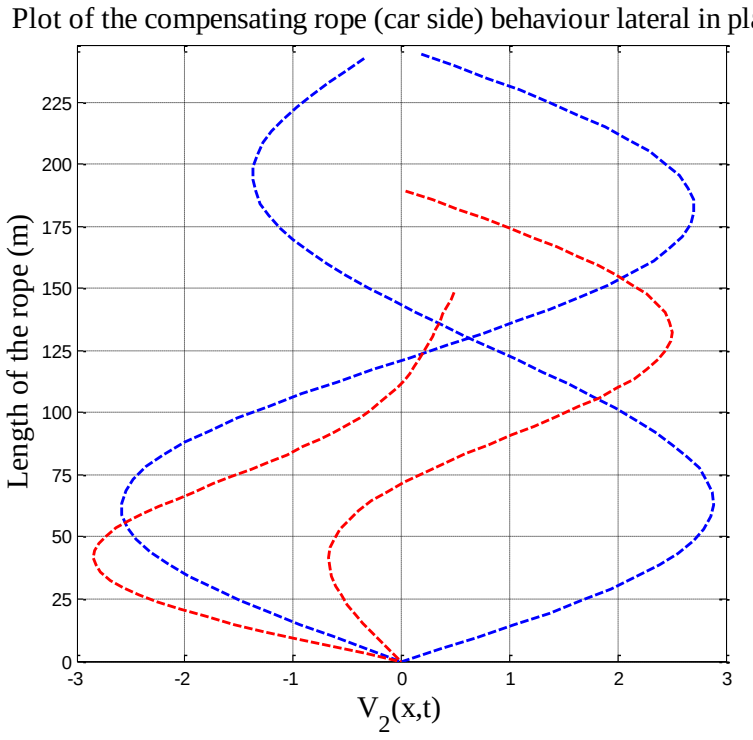

Figure 5.16 Behaviour of the compensating rope at the car side in the lateral in plane direction for case study one comparing when the elevator car is travelling with a rated velocity of *v(t)=15.00m/s* when the car is going up represented by dashed blue line and when going down represented by dashed red line

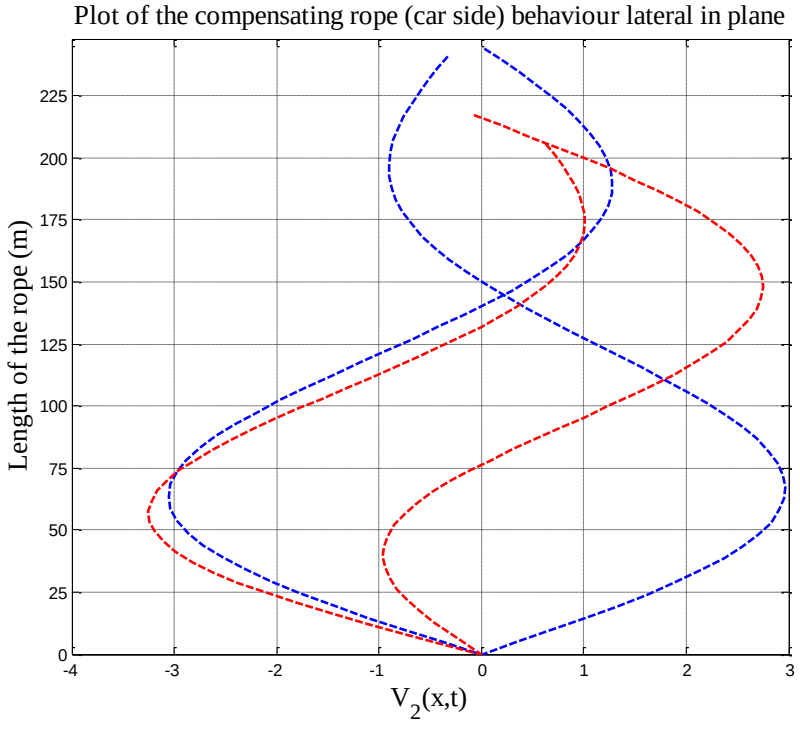

Figure 5.17 Behaviour of the compensating rope at the car side in the lateral in plane direction for case study two comparing when the elevator car is travelling with a rated velocity of *v(t)=4.00m/s* when the car is going up represented by dashed blue line and when going down represented by dashed red line

In Figure 5.18 and Figure 5.19 show the maximum displacements of the compensating ropes at the car side in the lateral out of plane when the elevator car is travelling from the bottom to the top landing level represented by a dashed blue line and when the car is travelling from the top to the bottom landing level represented by a dashed red line at a rated velocity of *v(t)=15.00m/s* and *v(t)=4.00m/s*, respectively. The maximum displacements are when the elevator car is travelling at a rated velocity of 4.00m/s. The compensating ropes are excited at the second natural frequency, thus the 2nd mode shape is the maximum displacements of the compensating ropes at the car side.

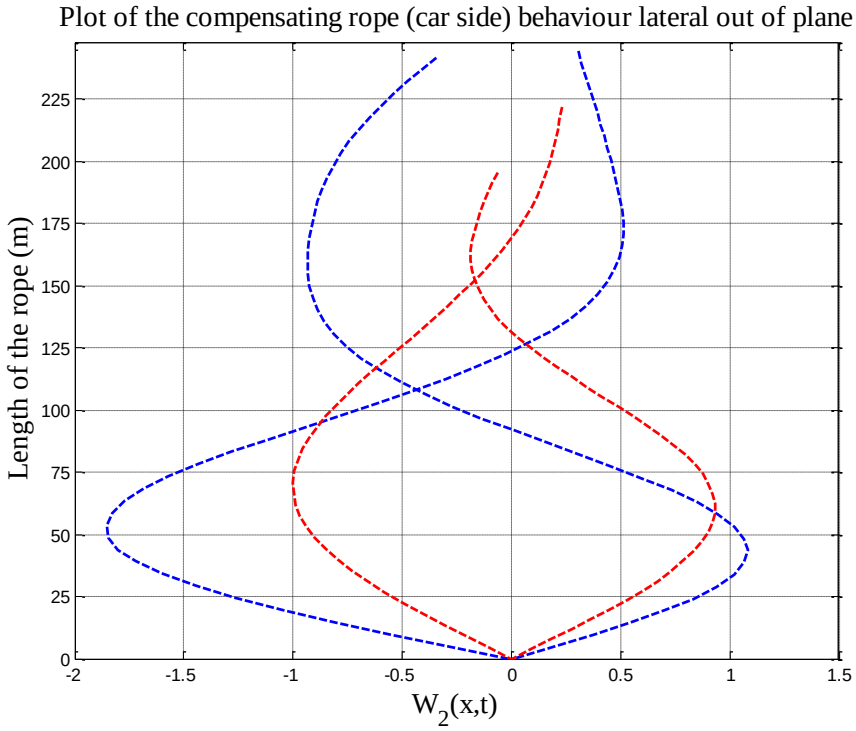

Figure 5.18 Behaviour of the compensating rope at the car side in the lateral out of plane direction for case study one comparing when the elevator car is travelling with a rated velocity of *v(t)=15.00m/s* when the car is going up represented by dashed blue line and when going down represented by dashed red line

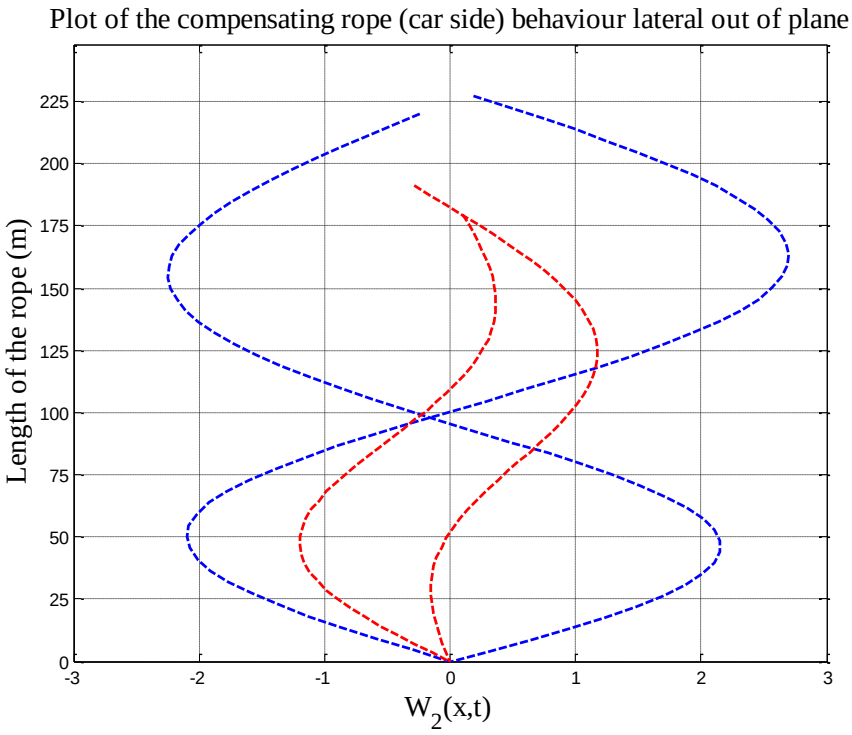

Figure 5.19 Behaviour of the compensating rope at the car side in the lateral out of plane direction for case study two comparing when the elevator car is travelling with a rated velocity of *v(t)=4.00m/s* when the car is going up represented by dashed blue line and when going down represented by dashed red line

The behaviour of the suspension and compensating ropes at the counterweight side can be obtained with the mathematical model.

5.3.4 Longitudinal response of the elevator car, compensating sheave, counterweight

The longitudinal displacements of the elevator car, compensating sheave, and counterweight when the elevator car is traveling from the bottom to the top landing level represented by a blue line and from the top to the bottom landing level represented by a red line with a rated velocity of *v(t)=15.00m/s* shown in Figure 5.20 and with a rated velocity of *v(t)=4.00m/s* Figure 5.21. The highest displacements of the elevator car, compensating sheave, and counterweight are when the elevator car is travelling at a rated velocity of *v(t)=4.00m/s*.

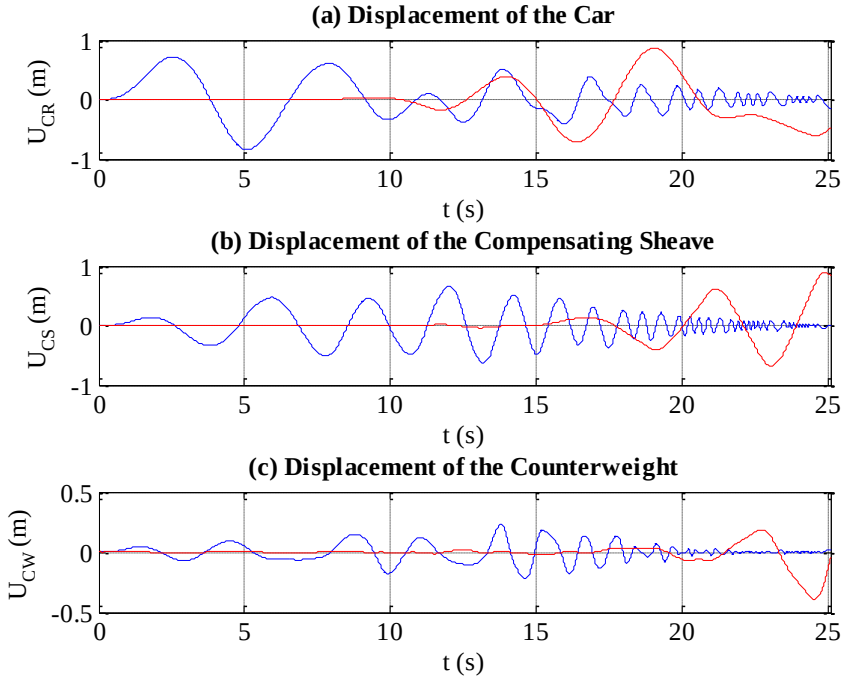

Figure 5.20 Longitudinal displacements of (a) elevator car (b) compensating sheave (c) counterweight for case study one when the elevator car is travelling with a rated velocity of *v(t)=15.00m/s* when the car is going up represented by blue line and when going down represented by red line

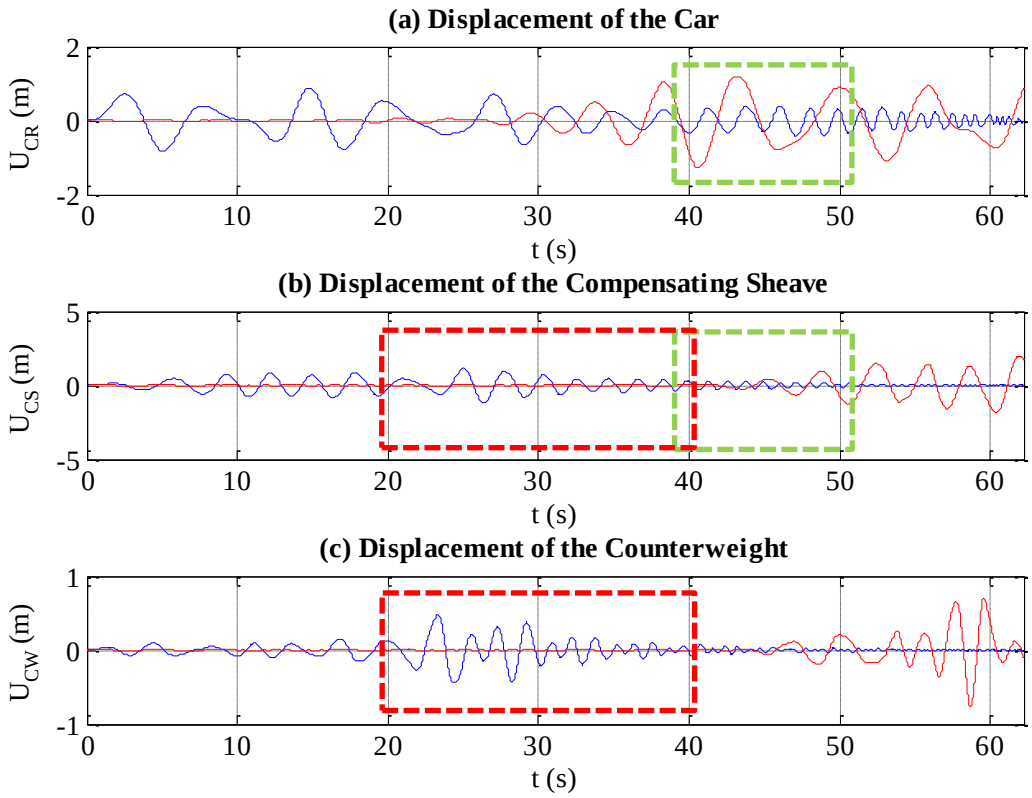

Figure 5.21 Longitudinal displacements of (a) elevator car (b) compensating sheave (c) counterweight for case study two when the elevator car is travelling with a rated velocity of *v(t)=4.00m/s* when the car is going up represented by blue line and when going down represented by red line

The FFT frequency spectra of the elevator car and compensating sheave over a time span of 40.0 seconds – 50.0 seconds from the longitudinal displacement response when the elevator car is travelling at a rated velocity of *v(t)=4.00m/s* shown in Figure 5.22 (a) and (b) when the elevator car is travelling from the bottom to the top landing level represented by a blue line and from the top to the bottom landing level represented by a red line.

The predominant frequency shown in Figure 5.22 is 0.60 Hz which is double the frequency of excitation in the lateral in plane direction of the building structure. This type of frequency is coming in the longitudinal direction of each mass by the coefficients $f_{CR}(t,\tau)$, $f_{CS}(t,\tau)$ that appear in equations (5.59) - (5.60) and are defined in equations (G.22) and (G.28), is primary external excitation.

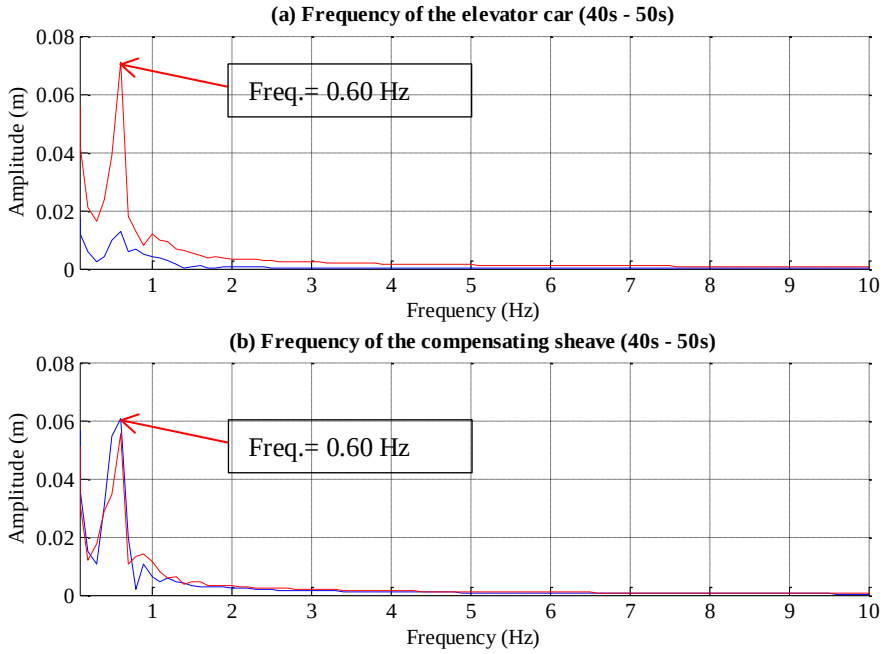

Figure 5.22 FFT frequency spectra of (a) elevator car (b) compensating sheave between the time span of 40.0 seconds – 50.0 seconds for case study two when the elevator car is travelling at *v(t)=4.00m/s* when the car is going up represented by blue line and when going down represented by red line

The FFT frequency spectra of the compensating sheave and counterweight over a time span of 20.0 seconds – 40.0 seconds from the longitudinal displacement response when the elevator car is travelling at a rated velocity of *v(t)=4.00m/s* shown in (a) and (b) when the elevator car is travelling from the bottom to the top landing level represented by a blue line and from the top to the bottom landing level represented by a red line.

The predominant frequency shown in Figure 5.23 is 0.60 Hz which is double the frequency of excitation in the lateral in plane direction of the building structure. This type of frequency is coming in the longitudinal direction of each mass by the coefficients $f_{CS}(t,\tau)$, $f_{CW}(t,\tau)$ that appear in equations (5.60) - (5.61) and are defined in equations (G.28) and (G.33), is primary external excitation.

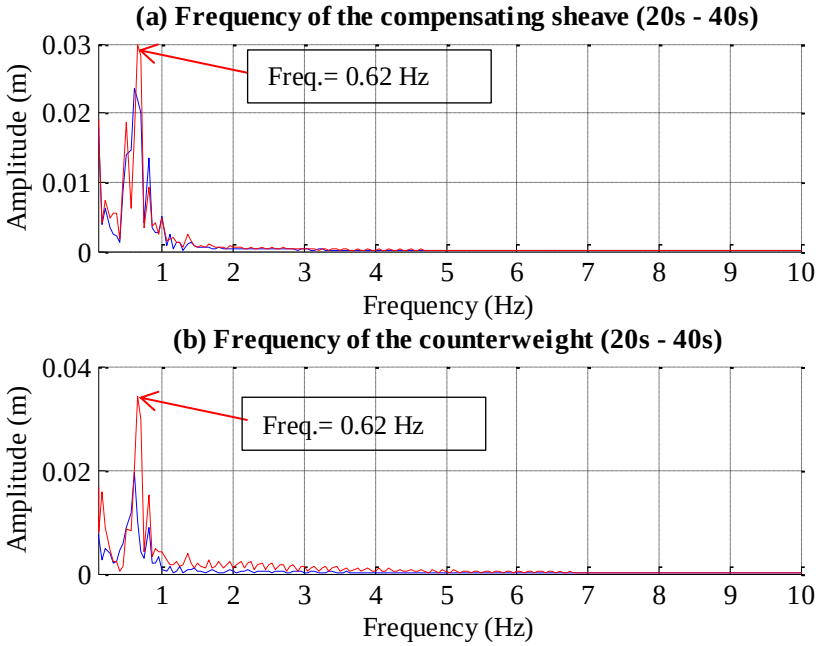

Figure 5.23 FFT frequency spectra of (a) compensating sheave (b) counterweight between the time span of 20.0 seconds – 40.0 seconds for case study two when the elevator car is travelling at *v(t)=4.00m/s* when the car is going up represented by blue line and when going down represented by red line

5.4 Autoparametric resonance 2:1

In the nonstationary mathematical model of a full elevator system which is described by the nonlinear equations (5.54) and (5.55) for the i^{th} rope and (5.59) to (5.61) for the elevator car, compensating sheave and counterweight, autoparametric (2:1) resonance may occur due to coupling between the longitudinal displacements of the elevator car, compensating sheave and counterweight and the lateral in plane and out of plane displacements of the suspension and compensating ropes.

The stiffness term of the ropes represented as $\hat{k}_{irn}(t;\tau)$ contain the longitudinal displacements of the elevator car, compensating sheave, and counterweight defined in Appendix G in equations (G-2), (G-5), (G-9), and (G-13) provides parametric excitation to the lateral modal displacements of the rope, therefore the excitation of each mass provides autoparametric excitation to the rope, which gives a 2:1 resonance, according to Nayfeh and Mook (1979).

This type of resonance was also studied by Salamaliki-Simpson and Kaczmarczyk (2006) in a rope and mass mathematical model where adverse situation arises due to the quadratic coupling between the longitudinal and lateral modes of the system. A comparison was also

done with a high and low rated velocity of the mass and concluding that at low velocity the lateral response of the rope is higher.

In the following simulation the autoparametric (2:1) resonance has been studied in respect to the tuning between the longitudinal and lateral modes. In order for this type of resonance to take place the longitudinal natural frequency of the elevator car should be twice the lateral natural frequency of the suspension ropes at the car side ($\omega_{CR} = 2\tilde{\omega}_{1rr}$) and also the external excitation frequency of the building structure should coincide with the longitudinal natural frequency ($\Omega_v = \omega_{CR}$).

A four mode approximation in each direction of motion is applied. In order to demonstrate the principle features of the dynamic behaviour of the system, the first four lateral in plane and lateral out of plane modes are considered. Since the longitudinal natural frequency of the elevator car is the lowest between the elevator car, compensating sheave and counterweight. Thus, the longitudinal natural frequency of the elevator car was tuned to be $\omega_{CR} = 2\tilde{\omega}_{1rr}$.

To demonstrate a 2:1 resonance through the autoparametric excitation terms of the elevator car. The mass of the compensating sheave is assumed to be $M_2 = 20000\,\text{kg}$, the elevator car is assumed to have a rated velocity of *v(t)=2.00m/s*, a rated acceleration of $a_{CR}(t)=1.00\text{m/s}^2$, and a rated jerk of $j(t)=1.00\text{m/s}^3$. The rest of the parameters of the building and elevator ropes remain unchanged as defined in Chapter 4.

It is assumed the fundamental natural frequency of the building structure is $\Omega_v = 5.4475\,\text{rad/s}$ (0.867 Hz) in the lateral in plane direction, where $\Omega_v = \omega_{CR}(\tau) = 2\tilde{\omega}_{1rr}(\tau)$ and in the lateral out of plane direction is $\Omega_w = 1.6336\,\text{rad/s}$ (0.26 Hz). Assuming, the high rise building is excited by wind harmonically, the displacement at the machine room level in the lateral in plane direction is $A_v = 0.90\,\text{m}$ and in the lateral out of plane direction is $A_w = 0.35\,\text{m}$.

A comparison is shown when the car is travelling from the bottom landing level to the top landing level and vice versa.

The kinematic profile of the elevator car dictated by the drive control algorithm when traveling at a rated velocity of *v(t)=2.00m/s* from the bottom landing level to the top landing level is shown in Figure 5.24. Similarly when the elevator car is traveling from the top landing level to the bottom landing level can be obtained.

The variation of frequency corresponding to all lateral modes of the suspension ropes dependent of τ which are slowly changing in time due to $L_i(\tau)$ at the car side according to the position of the elevator car in the hoistway is measured from the bottom landing level are shown in Figure 5.25 with a *v(t)=2.00m/s*. In Figure 5.25 the solid red, green, cyan, and purple line are the variation of frequency of the first four lateral natural frequencies at the car side of the suspension ropes, considering the Coriolis and centrifugal forces as shown in equation (5.68).

In Figure 5.25 the dashed black, blue, and cyan lines represent the change of frequency in the longitudinal direction of the elevator car, compensating sheave, and counterweight according to the position of the elevator car, estimated by finding the eigenvalues from the stiffness matrix represented in (5.62) and mass matrix represented in (4.130).

In Figure 5.25 the dashed magenta and blue horizontal lines represent the frequency of excitation from the building structure at 0.867 Hz and 0.26 Hz in the lateral in plane and out of plane directions. The lateral in plane excitation frequency of the building structure will $\Omega_v = \omega_{CR}(\tau) = 2\tilde{\omega}_{1rr}(\tau)$ when the elevator car is approximately at a height of 100.0m from the bottom landing level, shown with a dashed yellow circle in Figure 5.24 and Figure 5.25.

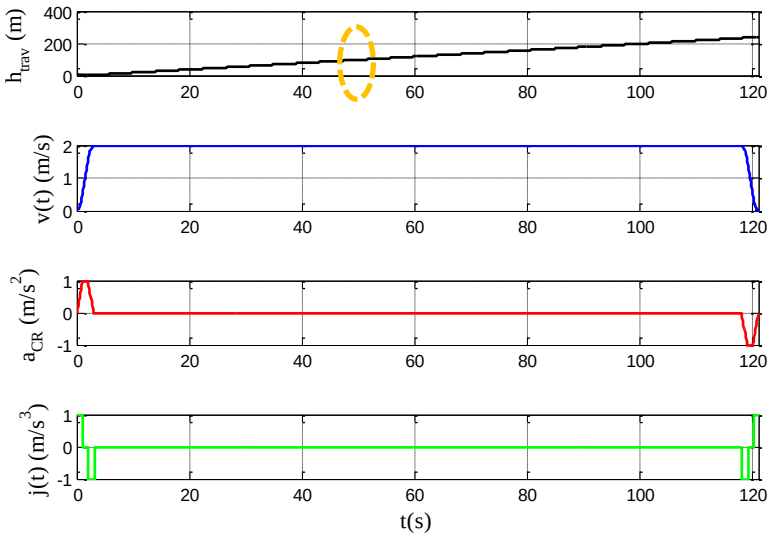

Figure 5.24 The kinematic profile of the elevator car when the car is going from the bottom landing level to the top landing level with a rated velocity of *v(t)=2.00m/s*

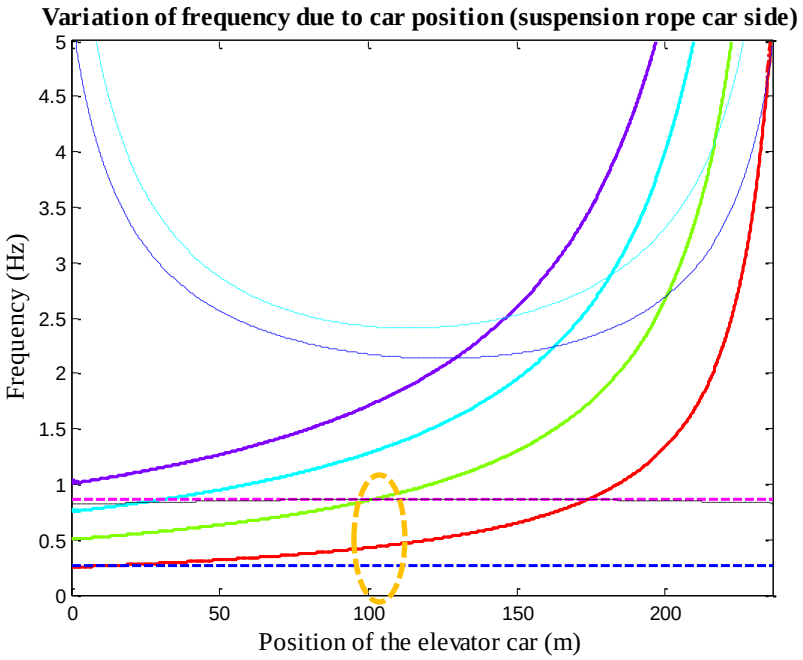

Figure 5.25 Variation of frequency of the suspension ropes according to the position of the elevator car (car side) for *v(t)=2.00m/s*

5.4.1 Lateral response of the suspension ropes

The displacement of the suspension ropes at the car side at the mid span length of the rope when the elevator car is travelling at a rated velocity of *v(t)=2.00m/s* when going from the bottom landing level to the top landing level shown in Figure 5.26 where (a) in the lateral in plane direction and (b) in the lateral out of plane direction.

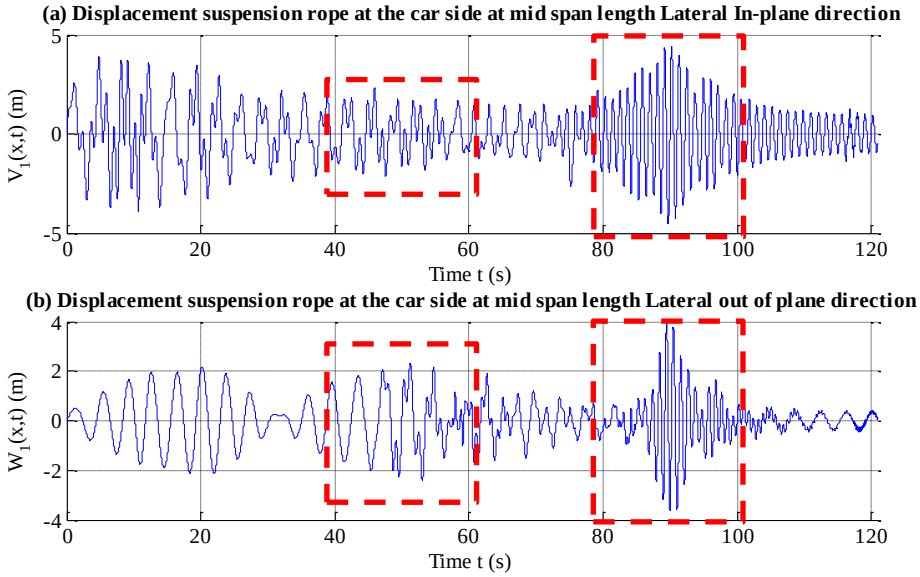

Figure 5.26 Displacement of the suspension rope at the car side at the mid span length of the ropes in (a) Lateral in plane (b) Lateral out of plane directions when the elevator car is travelling with a rated velocity of *v(t)=2.00m/s* from the bottom landing level to top landing level

The FFT frequency spectra of the lateral in plane and out of plane direction over a time span of 40.0 seconds – 60.0 seconds when the elevator car is travelling from the bottom landing level to the top landing level is shown in Figure 5.27 (a) and (b), respectively. The maximum frequencies are 0.30 Hz and 0.89 Hz which are approximately the frequencies in which the building structure is exciting the ropes in the lateral in plane and out of plane directions shown in Figure 5.27 (a) and (b). The frequencies of 0.30 Hz and 0.89 Hz from the lateral in plane and out of plane directions are coming from the kinematic forcing terms that are exciting the ropes at the machine room level. The two frequencies appear on both directions due to the coupling between the lateral in plane and out of plane direction from the terms $\tilde{R}_{irn}$ which are the cubic nonlinear terms of equations (5.54) and (5.55) defined for the i^{th} rope. To better demonstrate the 2:1 auto parametric resonance of the suspension ropes at the car side, the response of the suspension ropes at the car side are shown when the elevator car is going down.

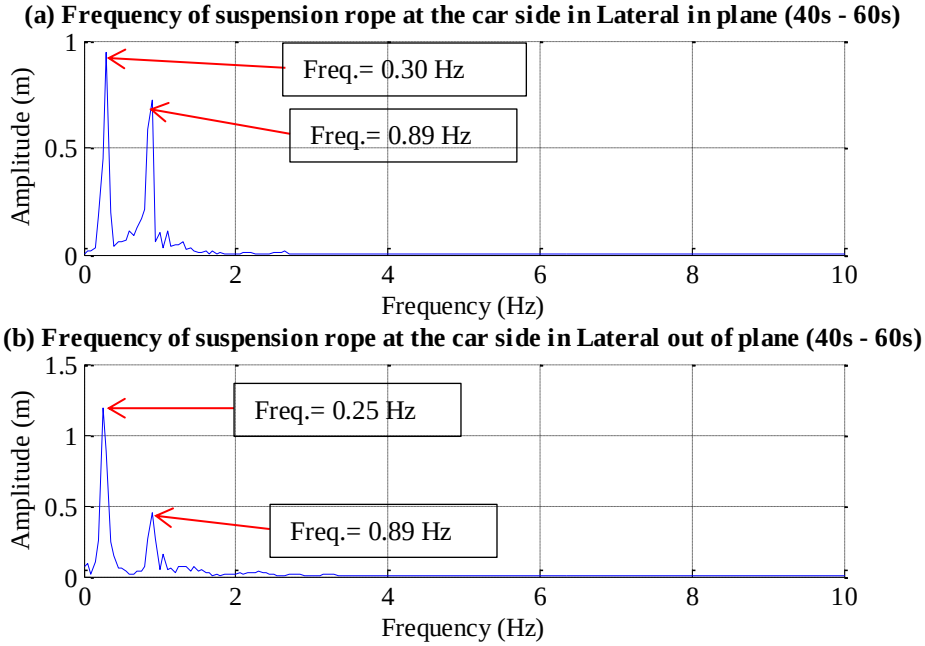

Figure 5.27 FFT frequency spectra of suspension ropes at the car side (a) Lateral in plane (b) Lateral out of plane between a time span of 40.0 seconds – 60.0 seconds when the elevator car is travelling at *v(t)=2.00m/s* when the car is going up.

The FFT frequency spectra of the lateral in plane and out of plane direction over a time span of 100.0 seconds – 120.0 seconds when the elevator car is travelling from the bottom landing level to the top landing level is shown in Figure 5.28 (a) and (b), respectively. The maximum frequencies are 0.30 Hz and 0.88 Hz which are approximately the frequencies in which the building structure is exciting the ropes in the lateral in plane and out of plane directions shown in Figure 5.28 (a) and (b). The frequencies of 0.30 Hz and 0.88 Hz from the lateral in plane and out of plane directions are coming from the kinematic forcing terms that are exciting the ropes at the machine room level. Due to the short length of the suspension rope the expected frequency from the building structure in the lateral in plane and out of plane direction are shown by the suspension rope in each direction and the transfer of energy from both directions is not present.

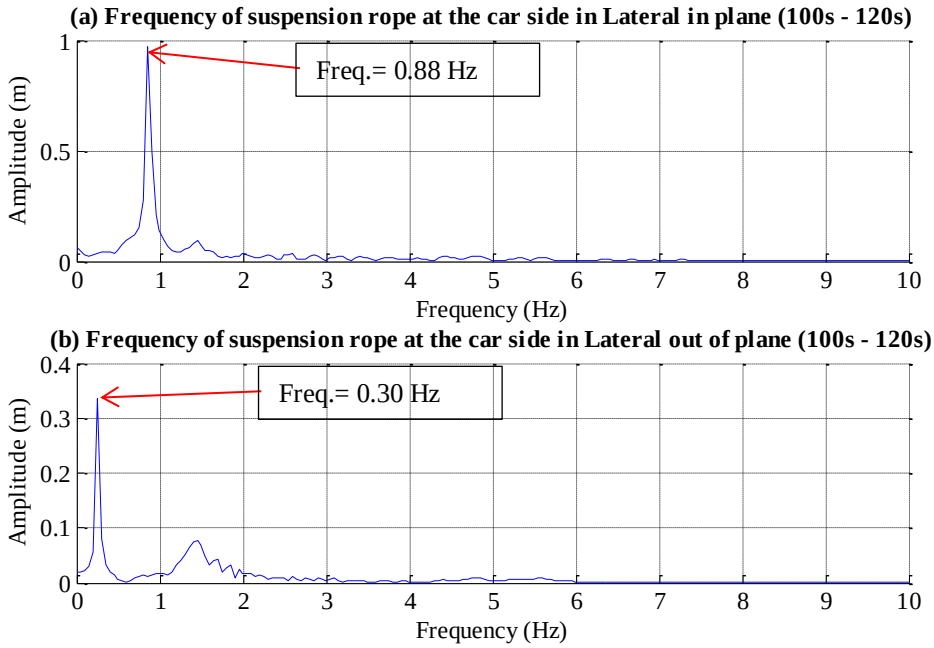

Figure 5.28 FFT frequency spectra of suspension ropes at the car side (a) Lateral in plane (b) Lateral out of plane between a time span of 100.0 seconds – 120.0 seconds when the elevator car is travelling at *v(t)=2.00m/s* when the car is going up.

The displacement of the suspension ropes at the car side at the mid span length of the rope when the elevator car is travelling at a rated velocity of *v(t)=2.00m/s* when going from the top landing level to the bottom landing level is shown in Figure 5.29 in (a) the lateral in plane direction and (b) the lateral out of plane direction.

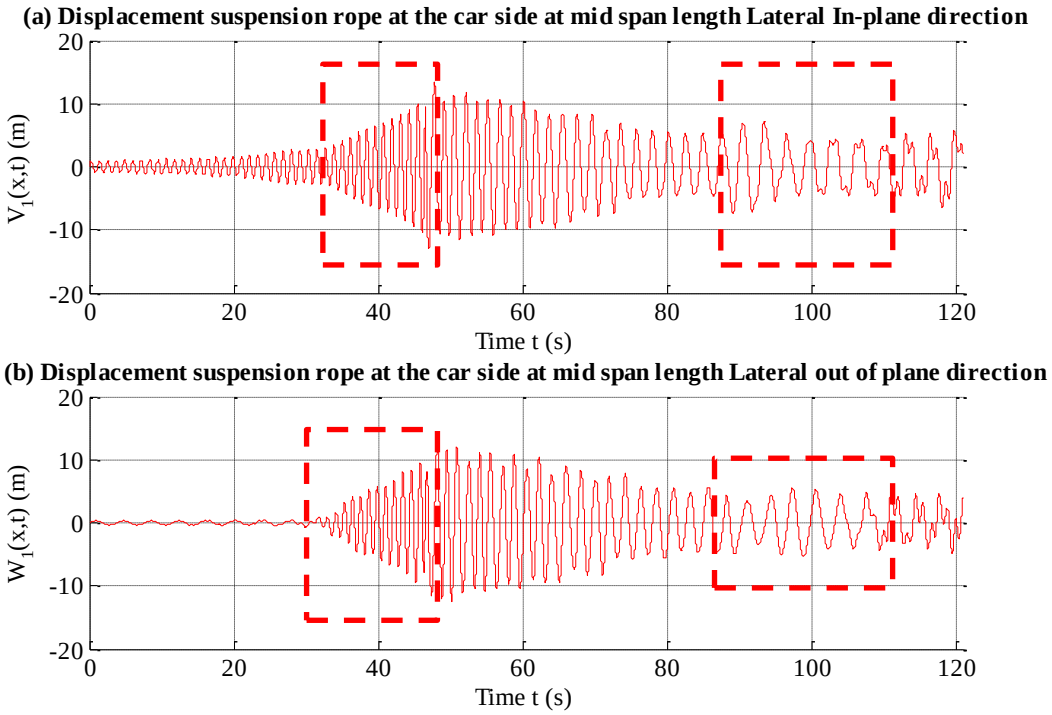

Figure 5.29 Displacement of the suspension rope at the car side at the mid span length of the ropes in (a) Lateral in plane (b) Lateral out of plane directions when the elevator car is travelling with a rated velocity of *v(t)=2.00m/s* from the top landing level to bottom landing level

The FFT frequency spectra of the lateral in plane and out of plane direction over a time span of 35.0 seconds – 45.0 seconds when the elevator car is travelling from the top landing level to the bottom landing level is shown in Figure 5.30 (a) and (b), respectively. The maximum frequency is 0.89 Hz which is approximately the frequency in which the building structure is exciting the suspension ropes in the lateral in plane direction shown in Figure 5.30 (a) and (b). The frequency of 0.89 Hz appear on both directions due to the coupling between the longitudinal direction with the lateral in plane and out of plane direction which are found at the stiffness term $\hat{k}_{irn}(t;\tau)$ of equations (5.54) and (5.55) of the lateral in plane and out of plane direction of the suspension ropes at the car side defined in equation (G.2). Energy from the high frequency longitudinal direction is transferred to the low frequency lateral modes and the lower modes are strongly excited at half the frequency of the excitation in the lateral in plane direction, as discussed by Salamaliki-Simpson and Kaczmarczyk (2006).

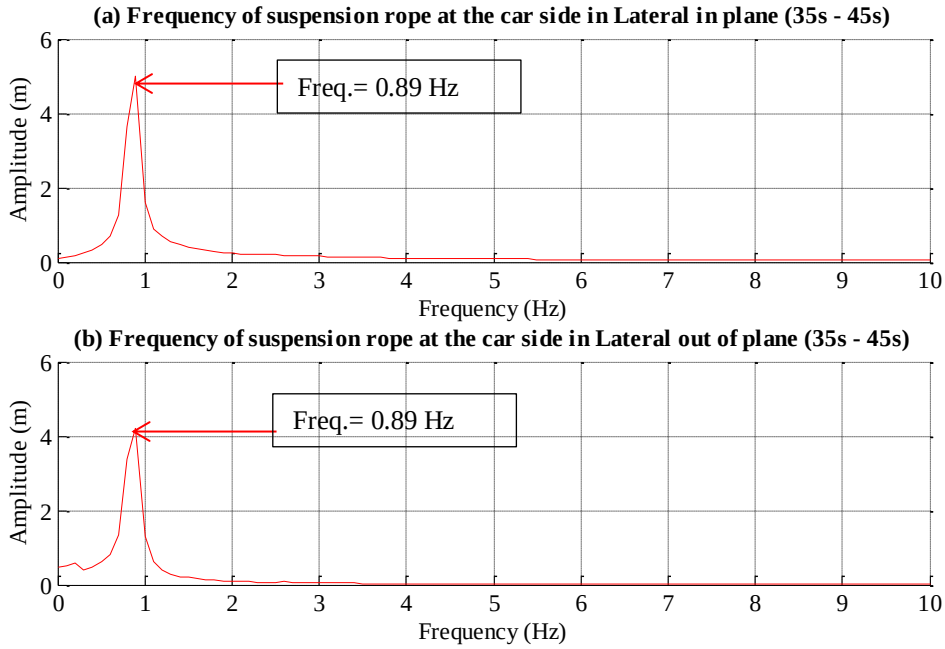

Figure 5.30 FFT frequency spectra of suspension ropes at the car side (a) Lateral in plane (b) Lateral out of plane between a time span of 35.0 seconds – 45.0 seconds when the elevator car is travelling at *v(t)=2.00m/s* when the car is going down.

The FFT frequency spectra of the lateral in plane and out of plane direction over a time span of 90.0 seconds – 120.0 seconds when the elevator car is travelling from the top landing level to the bottom landing level is shown in Figure 5.31 (a) and (b), respectively. The maximum frequencies are 0.30 Hz and 0.89 Hz which are approximately the frequencies in which the building structure is exciting the ropes in the lateral in plane and out of plane directions shown in Figure 5.31 (a) and (b). The frequencies of 0.30 Hz and 0.89 Hz from the lateral in plane and out of plane directions are coming from the kinematic forcing terms that are exciting the ropes at the machine room level. The two frequencies appear on both directions due to the coupling between the lateral in plane and out of plane direction from the terms $\tilde{R}_{irn}$ which are the cubic nonlinear terms of equations (5.54) and (5.55) defined for the suspension rope at the car side. As the elevator car is going down the natural frequency of the suspension rope at the car side is lowered, thus the transfer of energy from the lateral in plane and out of plane direction is present.

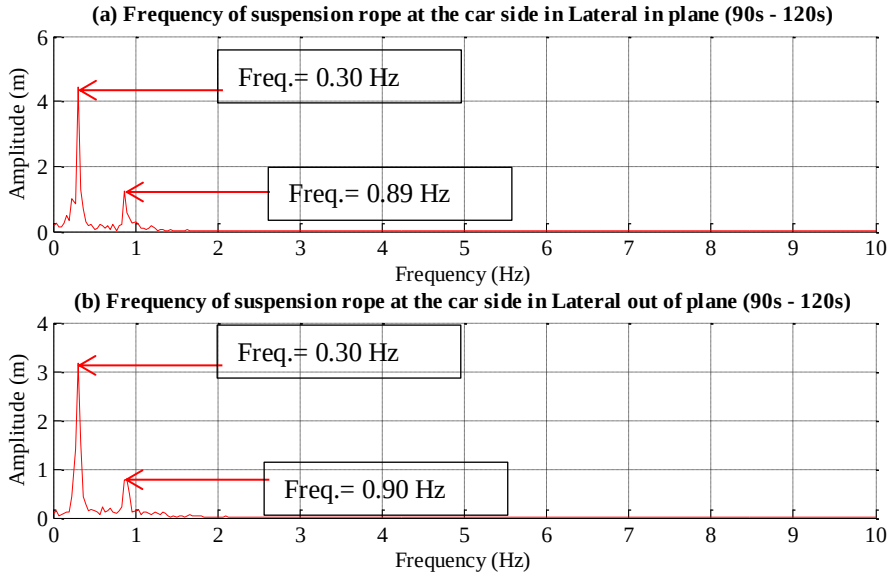

Figure 5.31 FFT frequency spectra of suspension ropes at the car side (a) Lateral in plane (b) Lateral out of plane between a time span of 90.0 seconds – 120.0 seconds when the elevator car is travelling at *v(t)=2.00m/s* when the car is going down.

5.4.2 Longitudinal response of the elevator car, compensating sheave, and counterweight

The longitudinal displacements of the elevator car, compensating sheave, and counterweight when the elevator car is going up is shown in Figure 5.32 when the elevator car is travelling at a rated velocity of *v(t)=2.00m/s.*

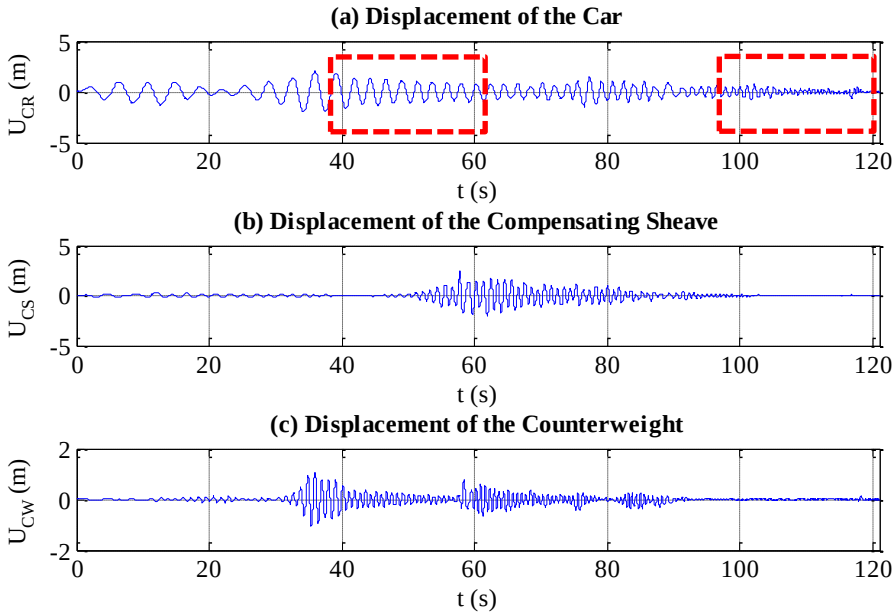

Figure 5.32 Longitudinal displacements of (a) elevator car (b) compensating sheave (c) counterweight when the elevator car is travelling at a rated velocity of *v(t)=2.00m/s* when going up

The FFT frequency spectra of the elevator car between a time span of 40.0 seconds – 60.0 and 100.0 seconds – 120.0 seconds when the elevator car is travelling from the bottom landing level to the top landing level is shown in Figure 5.33 (a) and (b), respectively. The frequency of 1.75 Hz is approximately twice the frequency of excitation in the lateral in plane direction coming from the excitation term $f_{CR}(t;\tau)$ in the longitudinal direction which is defined in equation (G.22), which is primary external excitation. The frequency of 0.85 Hz is the frequency of excitation in the lateral in plane direction of the building structure at the machine room level.

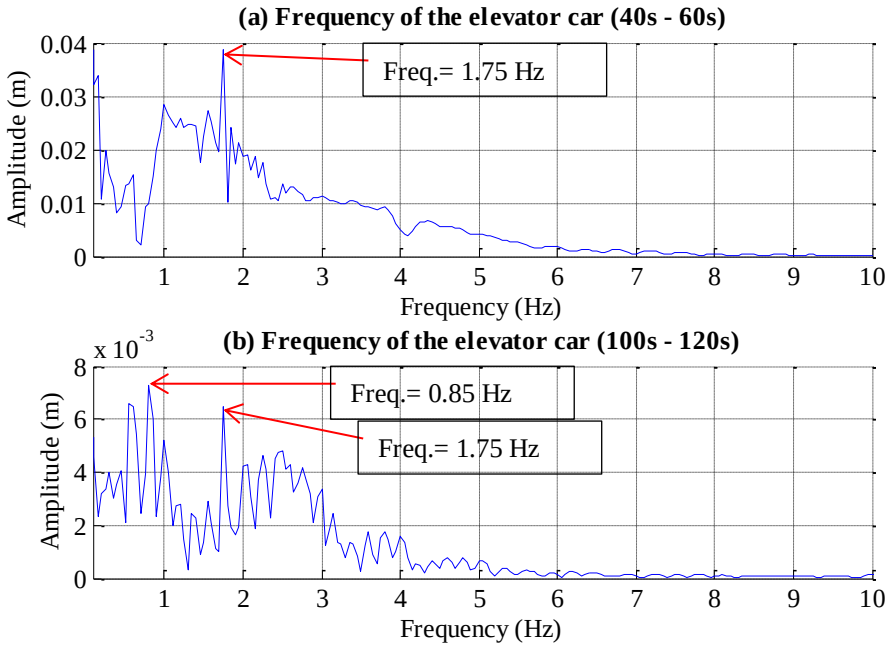

Figure 5.33 FFT frequency spectra of the elevator car between the time span (a) 40.0s to 60.0s (b) 100.0s to 120.0s when the elevator car is travelling at *v(t)=2.00m/s* when the car is going up.

Similarly, the response in the longitudinal direction of the elevator car, compensating sheave, and counterweight when the elevator car is travelling from the top landing level to the bottom landing level can be determined.

According to the simulation results presented in this Chapter by comparing when the elevator is travelling at a high and low rated velocity and when the elevator car is traveling from the bottom landing level to the top landing level and vice versa from the top landing level to the bottom landing level. As the elevator car is travelling at a low rated velocity the response of

the ropes and of the elevator car, compensating sheave, and counterweight are higher as the elevator is passing through resonance with a low rated velocity.

The nonstationary mathematical model derived in this chapter has not yet been validated in a high rise building under wind loading. It is recommended that a full validation of the lateral displacements of the suspension and compensating ropes at the car and counterweight side be completed.

A special case was shown where the longitudinal natural frequency of the elevator car is equal to twice the lateral natural frequencies of the suspension ropes at the car side, where this type resonance is called 2:1 autoparametric resonance. The excitation frequency in which the high rise building is exciting the elevator system is equal to the longitudinal natural frequency of the elevator car. In this case study the longitudinal mode of the elevator car excited the lateral modes of the suspension ropes due to the quadratic coupling in the coefficient $\hat{k}_{irn}(t;\tau)$ in the equations of motion of the suspension rope at the car side ($i=1$) in equations (5.54) and (5.55) shown in Appendix G. The results showed better correlation when the elevator car was travelling at a very low rated velocity from the top landing level to the bottom landing level.

6. Conclusions

This research addresses the linear and nonlinear phenomena that occur in the vibration problem of an elevator system in high rise buildings. The aim of this study was to develop and to validate a computer model of the elevator system to predict the dynamic responses of ropes and cables in an elevator system due to the vibrations of a high-rise building which is excited by the action of wind loading, when the elevator system is stationary and in motion. The wind loading is not represented in the mathematical models of the elevator system, due to considerable amount of time and resources during experimental testing. The vibrations of a high-rise building are considered as displacements which are caused by the wind loading on a high-rise building.

The mathematical methodology defined in Chapter 2 to predict the responses of the elevator steel wire ropes has been validated through experimental tests conducted using an experimental test rig described in Chapter 3. The mathematical model predictions have shown a good agreement with the experimental results.

In Chapter 3 the techniques validated through the experimental tests were used to model the rope and mass assembly of an experimental test rig. A set of experiments were developed to estimate the modal damping ratio of the rope and mass assembly, the lateral natural frequencies, and the modulus of elasticity of the rope. The torsional linear stiffness of the steel frame used to restrict the mass to move in the longitudinal and lateral in plane direction was estimated. A methodology was developed to derive the mathematical model of the rope and mass assembly taking into account the stationary and nonlinear behaviour of the system. Linear and nonlinear resonances were predicted through simulation. The lateral and longitudinal natural frequencies of the rope and mass system obtained from the mathematical model agreed when compared with the natural frequencies obtained from the experimental testing. The whirling motion of the rope took place, due to the transfer of energy between the lateral in plane motion to the lateral out of plane motion. The numerical simulation was compared with experimental results and a good agreement was found for the displacements of the rope. However the rotation of the mass in the experimental testing has influence in the lateral in plane and longitudinal displacements of the mass. The imperfections or misalignment at the mass assembly, that are responsible for any additional looseness or misalignment were difficult to eliminate and to accommodate in the current model due to project constraints.

Due to good comparison of the rope lateral displacements between the experimental and numerical simulation results under different input parameters. The methodology used to derive the mathematical model of a rope and mass system was used to derive the mathematical model of a full elevator system for a high rise building to predict the motions of the ropes and the interaction between its components.

In Chapter 4 a stationary mathematical model of a high rise elevator system that predicts the behaviour of the suspension and compensating ropes at the car and counterweight side with the influence of the lateral in plane and out of plane displacements of the elevator car and longitudinal displacements of the elevator car, compensating sheave, and counterweight was derived. The equations of motion for the entire system were derived. The stationary and nonlinear vibrations of the suspension and compensating ropes were taken into account. The numerical results were compared with a high and low lateral stiffness of the elevator car.

When the elastic interface between the elevator car and the building structure in the lateral directions is considered the veering phenomena was discussed. The simulation results were compared when the elevator car is positioned at the bottom landing level, at a height where the eigenvalues of the suspension and compensating ropes for the fundamental natural frequency becomes equal, and when the elevator car is positioned at the top landing level. Among all three case studies the lateral response of the suspension ropes, compensating ropes, and the elevator car was higher when the elevator car is positioned at a height where the fundamental natural frequency of the suspension and compensating rope becomes equal. Due to good ride quality on the elevator car, an elevator car with lateral low stiffness of the guiding system and having lateral vibrations as the ones shown in Chapter 4 would not be suitable for service. This is why the lateral high stiffness of the guiding system are used in the elastic interface between the elevator car and the building structure in the lateral directions to minimize the lateral vibrations on the elevator car. Thus, the mathematical model derived in Chapter 5 the lateral stiffness of the elevator car was neglected. The mathematical model derived in Chapter 4 can be used to predict the response of the suspension and compensating ropes and the interaction between its components.

In Chapter 5 an efficient nonstationary mathematical model of a high rise elevator system that predicts the behaviour of the suspension and compensating ropes at the car and counterweight side with the influence of the longitudinal displacements of the elevator car, compensating sheave, and counterweight while the elevator car is going up or down in the elevator shaft was derived. The equations of motion for the entire system were derived taking into account the kinematic profile of an elevator system dictated by the drive control algorithm. The equations

of motion of the entire system accommodate the Coriolis and centrifugal forces due to the nonstationary behaviour of the system. The nonstationary and nonlinear vibrations when the suspension and compensating ropes are changing length were taken into account. The change of length of the ropes was treated as slowly varying in time.

The numerical results were discussed by comparing when the elevator is travelling at a high and low rated velocity and when the elevator car is traveling from the bottom landing level to the top landing level and vice versa. As the elevator car is travelling at a low rated velocity the response of the ropes and of the elevator car, compensating sheave, and counterweight are higher as slow passage through the resonance regions takes place. A special case was shown where the first longitudinal natural frequency equal to twice the lateral fundamental natural frequency of the suspension ropes at the car side leading to the nonlinear 2:1 autoparametric resonance. The external excitation frequency of the high rise building is equal to the first longitudinal natural frequency. In this case study the first longitudinal mode excited the lateral modes of the suspension ropes due to the quadratic coupling in the equations of motion of the suspension rope at the car side. The 2:1 autoparametric resonance was more evident when the elevator car was travelling at a very low rated velocity and when travelling from the top landing level to the bottom landing level.

The mathematical models of a high rise elevator system presented in this research are the basis for the development of computer simulation tools for designers to predict unwanted resonance vibration by using the parameters of the elevator system such as number of steel wire suspension and compensating ropes, the mass per unit length, the elastic modulus, and the lateral modal damping ratios of the ropes, the height of the building structure at the machine room level, the travel height, the elevator car, compensating sheave, and counterweight full mass, with the longitudinal modal damping ratio of each mass. Designers would be able to configure the high rise elevator system and study which arrangements are better to prevent unwanted vibrations of the ropes and the components of the elevator system.

6.1 Future work

There is scope for further developments in modelling and prediction of the dynamic behaviour of a full elevator system and experimental testing, such as:

- The validation of the full elevator model presented in chapters 4 and 5 can be completed considering the stationary and nonstationary behaviour of the elevator system in a high rise building under wind loading. The full validation of the lateral displacements of the suspension and compensating ropes at the car and counterweight side can be accomplished.

- As new elevator systems are being installed in open elevator shaft (without elevator shaft walls) the influence of aerodynamic effects on the dynamics of ropes in a full elevator system should be studied.

- To expand the mathematical model derived in Chapter 4 future mathematical models could include the elastic interface between the building structure and the counterweight.

- In the modern high-rise systems elevator cars are equipped with active roller guides when installed in high rise buildings, to mitigate the lateral vibrations from misalignment of the guide rails and to suppress the lateral vibrations of the elevator car. The new mathematical models of a high rise elevator system could be incorporated active roller guides, to predict the behaviour of the suspension and compensating ropes in a stationary and nonstationary elevator system and to predict the effects at the elevator car.

- Impact between the shaft walls and the ropes and the interaction between the ropes of the elevator system should be included as this is another excitation to the elevator car during operation and stationary.

- As it was presented in Chapter 3 the lateral damping ratios of the ropes were determined experimentally of a steel wire rope and were considered constant throughout all modes for a constant length of rope. A new research could arise to determine the damping ratios for different modes during travel of the elevator car and for different travel directions.

- For the mathematical model derived in Chapter 3, a future mathematical model could be derived by adding a rotational degree of freedom to the mass/car assembly dynamics in the lateral in plane direction.

- A new type of sensor to monitor the vibrations of the ropes in the elevator system stationary and during travel should be studied. As it was reported in Chapter 1, a fibre optic sensor based on Fibre Bragg Grating technology could be used to measure the vibrations of the ropes.

- The existing mathematical model results could be verified through the development of another model using an alternative software platform such as MSc Software Adams which is multibody dynamic software. A single rope can be characterized by segments of a specified length linked all together by joints and a mass can be attached at the bottom restricted to vibrate only in the longitudinal and lateral in plane directions.

- The effects of the rope vibrations on the elevator car structure can be developed. The models could accommodate the geometry of the elevator car, compensating sheave, and counterweight. A more in depth analysis of the elevator car components in particular the deformations of the car frame/body and the materials being used can be developed. As certain components can be excited at their natural frequency.

- High rise buildings are often being constructed in seismic areas. The mathematical models of a full elevator system in a high rise building with the excitation of wind loading can be included seismic excitation. To predict the behaviour of the suspension and compensating ropes at the car and counterweight side with the interaction of the elevator car, compensating sheave and counterweight, when the high rise building is being excited by wind and seismic loading.

Appendix A

Orthogonality of Modes of one rope and a mass

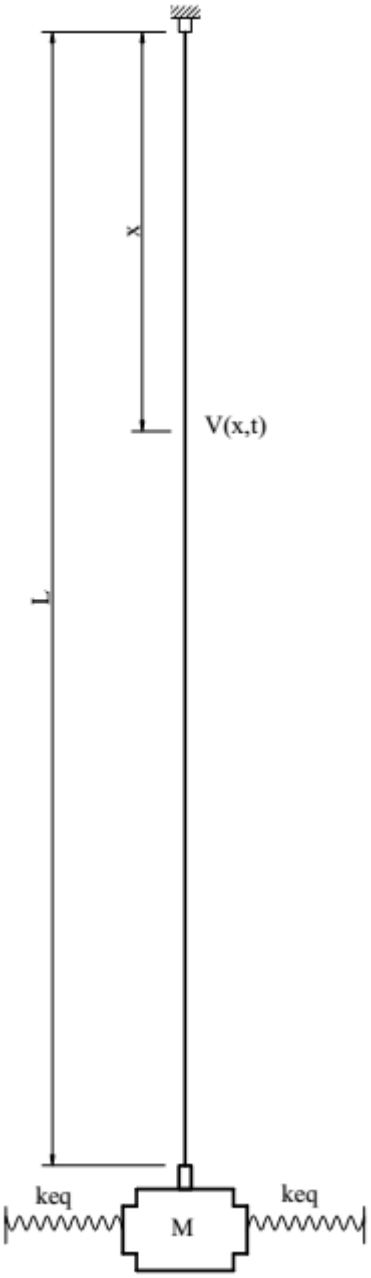

Figure A.1 Drawing of the model taken into account

For the lateral in plane and out of plane motion of the model of Figure A.1, the differential equation of the stationary, unconstrained system can be written as:

$$mV_{tt} - T_0 V_{xx} = 0 \qquad \text{(A.1)}$$

Which must be satisfied in the domain $0 \le x \le L$.

In addition V must satisfy the boundary conditions at $x = 0$ and $x = L$ which are described by the equations A.2 and A.3, respectively.

$$V(0,t) = 0 \tag{A.2}$$

$$MV(L,t) + 2k_{eq}V(L,t) + T_0 V_x(L,t) = 0 \tag{A.3}$$

Using the separation of variables technique the displacement V can be expressed as:

$$V(x,t) = \phi(x)q(t) \tag{A.4}$$

where $q(t)$ is a harmonic function with frequency ω, so that

$$V_{tt}(x,t) = -\omega^2 \phi(x)q(t) \tag{A.5}$$

where $\omega = \beta^{Lin}\sqrt{\frac{T_0}{m}}$. The Eigenvalue problem of (A.1) is then reduced to

$$\phi''(x) + (\beta^{Lin})^2 \phi(x) = 0 \tag{A.6}$$

where the prime designates differentiation with respect to x. Equation A.6 can be re-written as

$$T_0 \phi_n''(x) = -m\omega^2 \phi_n(x) \tag{A.7}$$

The orthogonality property of (A.7) can be examined by considering modes n and r of the Eigenvalue problem as the following equations:

$$T_0 \phi_n''(x) = -m\omega_n^2 \phi_n(x) \tag{A.8a}$$

$$T_0 \phi_r''(x) = -m\omega_r^2 \phi_r(x) \tag{A.8b}$$

Multiplying the (A.8a) by $\phi_r(x)$ and (A.8b) by $\phi_n(x)$ and integrating over the entire interval $[0 - L]$.

$$\int_0^L T_0 \phi_n''(x)\phi_r(x)dx = -m\omega_n^2 \int_0^L \phi_n(x)\phi_r(x)dx \tag{A.9a}$$

$$\int_0^L T_0 \phi_r''(x)\phi_n(x)dx = -m\omega_r^2 \int_0^L \phi_r(x)\phi_n(x)dx \tag{A.9b}$$

The second boundary condition at $x = L$, for modes n and r can be written as the following expressions:

$$-\omega_n M\phi_n(L)\phi_r(L) = (-T_0\phi_n'(L) - k_{eq}\phi_n(L))\phi_r(L) \tag{A.10a}$$

$$-\omega_n M\phi_r(L)\phi_n(L) = (-T_0\phi_r'(L) - k_{eq}\phi_r(L))\phi_n(L) \tag{A.10b}$$

Subtracting (A.9a) and (A.9b) from the expressions (A.10a) and (A.10b)

$$\int_0^L T_0\phi_n''(x)\phi_r(x)dx + \omega_n M\phi_n(L)\phi_r(L) = -m\omega_n^2\int_0^L \phi_n(x)\phi_r(x)dx + T_0\phi_n'(L)\phi_r(L) + k_{eq}\phi_n(L)\phi_r(L) \tag{A.11a}$$

$$\int_0^L T_0\phi_r''(x)\phi_n(x)dx + \omega_r M\phi_r(L)\phi_n(L) = -m\omega_r^2\int_0^L \phi_r(x)\phi_n(x)dx + T_0\phi_r'(L)\phi_n(L) + k_{eq}\phi_r(L)\phi_n(L) \tag{A.11b}$$

Evaluating the integrals of (A.11a) and (A11b) with the method of integration by parts the following equations are produced:

$$T_0\phi_n'(L)\phi_r(L) - T_0\int_0^L \phi_n'(x)\phi_r'(x)dx + \omega_n M\phi_n(L)\phi_r(L) = -m\omega_n^2\int_0^L \phi_n(x)\phi_r(x)dx + T_0\phi_n'(L)\phi_r(L) + k_{eq}\phi_n(L)\phi_r(L) \tag{A.12a}$$

$$T_0\phi_r'(L)\phi_n(L) - T_0\int_0^L \phi_r'(x)\phi_n'(x)dx + \omega_r M_1\phi_r(0)\phi_n(0) = -m_2\omega_r^2\int_0^L \phi_r(x)\phi_n(x)dx + T_0\phi_r'(L)\phi_n(L) + k_{eq}\phi_r(L)\phi_n(L) \tag{A.12b}$$

Subtracting Equations (A.12a) and (A.12b), the resulting equation is

$$M\phi_r(L)\phi_n(L) + m\int_0^L \phi_r(x)\phi_n(x)dx = \begin{cases} m_{2r} & \text{if } n = r \\ 0 & \text{if } n \neq r \end{cases} \tag{A.13}$$

Applying (A.12a) into (A.9a)

$$T_0\int_0^L \phi_n''(x)\phi_r(x)dx - T_0\phi_n'(L)\phi_r(L) - k_{eq}\phi_n(L)\phi_r(L) = \begin{cases} -m_{2rr}\omega_{2rr}^2 & \text{if } n = r \\ 0 & \text{if } n \neq r \end{cases} \tag{A.14}$$

Appendix B

Lateral Eigenvalue Problem of one rope and a mass

In the lateral motion the rope is being treated as a string governed by the equation

$$mV_{tt} - T_0 V_{xx} = 0 \tag{B.1}$$

The equation of the string (B.1) is solved using the technique of the separation of variables in order to determine the equation for the mode shapes. It is assumed that the displacement $V(x,t)$ can be written as a product of two functions one depending on length *(x)* and the other on time *(t)*.

$$V(x,t) = \phi(x) q(t) \tag{B.2}$$

and each function can be written separately as following

$$\phi''(x) + (\beta^{Lin})^2 \phi(x) = 0 \tag{B.3}$$

$$q''(t) + \omega^2 q(t) = 0 \tag{B.4}$$

The solution for each function is defined in Equations (B.5) and (B.6) respectively

$$q(t) = A\cos\omega t + B\sin\omega t \tag{B.5}$$

$$\phi(x) = C\cos\beta^{Lin}(x) + D\sin\beta^{Lin}(x) \tag{B.6}$$

where A,B,C,D are constants of integration. The boundary condition at $x = 0$ is

$$V(0,t) = 0 \tag{B.7}$$

From the boundary condition (B.7) $q(t)\phi(0) = 0$ and $C\cos\beta^{Lin}(x) + D\sin\beta^{Lin}(x) = 0$ and thus $C = 0$

Consequently

$$\phi(x) = D\sin\beta^{Lin}(x) \tag{B.8}$$

at $x = L$ the boundary condition is

$$M V(x,t)_{tt}\big|_{x=L} + T_0 V(x,t)_x\big|_{x=L} + K_{eq} V(x,t)\big|_{x=L} = 0 \tag{B.9}$$

Equations (B.2), (B.4) are applied into Equation (B.9) resulting into a new Equation (B.10).

$$(K_{eq} - M\omega^2)\sin\beta^{Lin} L + T_0 \beta^{Lin}\cos\beta^{Lin} L = 0 \tag{B.10}$$

applying Equation (B.2), (B.3), (B.4) into (B.1)

$$\omega^2 = \left(\frac{T_0}{m}\right)(\beta^{Lin})^2 \tag{B.11}$$

using Equation (B.11) into Equation (B.10)

$$T_0\beta^{Lin}\cos\beta^{Lin}L + \left(k_{eq} - \frac{MT_0}{m}\left(\beta^{Lin2}\right)^2\right)\sin\beta^{Lin}L = 0 \tag{B.12}$$

Appendix C

Simulation Results for the Experimental Testing

Running a simulation with a number of mode of *N=1*.

A comparison between the experimental testing and the mathematical model of the displacements in the lateral in plane and out of plane direction is shown in Figure C.1 and the whirling motion of the rope appears in Figure C.2.

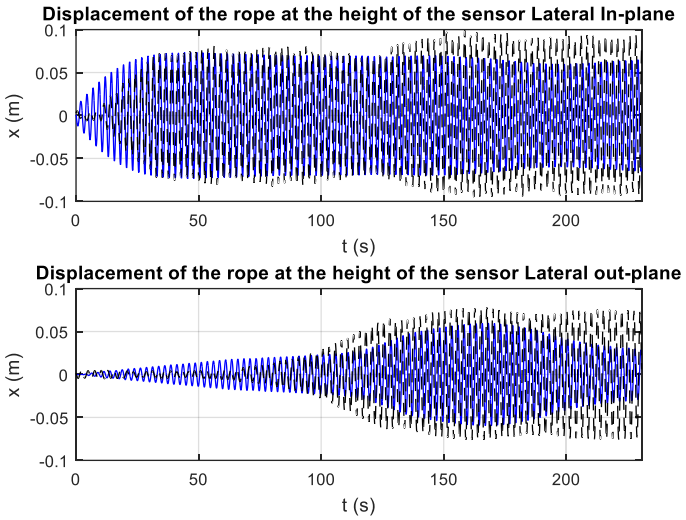

Figure C.1 Comparison of the rope displacement at sensor height from the experiment and the mathematical model

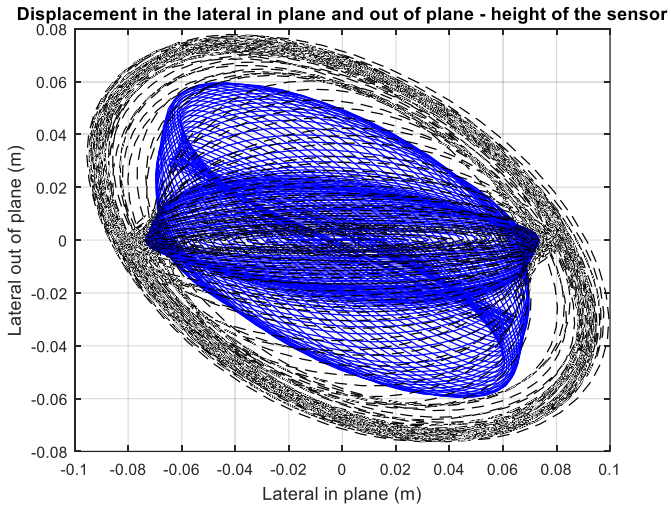

Figure C.2 Comparison of the displacements in the Lateral in plane and out of plane direction

Running a simulation with a number of mode of *N=2*.

A comparison between the experimental testing and the mathematical model of the displacements in the lateral in plane and out of plane direction is shown in Figure C.3 and the whirling motion of the rope appears in Figure C.4.

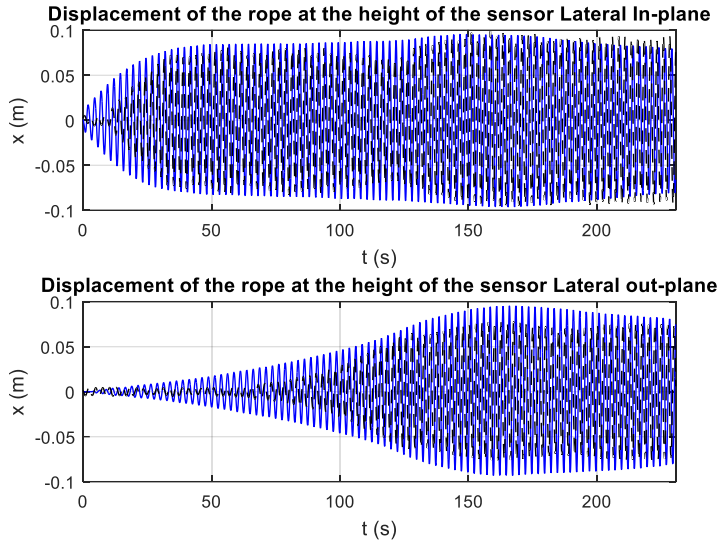

Figure C.3 Comparison of the rope displacement at sensor height from the experiment and the mathematical model

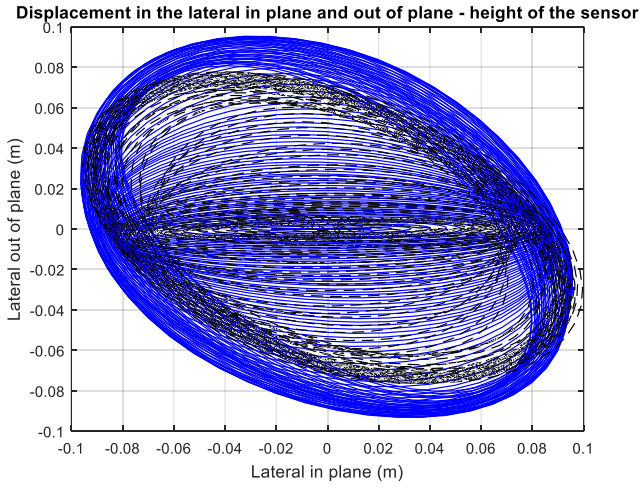

Figure C.4 Comparison of the displacements in the Lateral in plane and out of plane direction

Running a simulation with a number of mode of *N=3*.

A comparison between the experimental testing and the mathematical model of the displacements in the lateral in plane and out of plane direction is shown in Figure C.5 and the whirling motion of the rope appears in Figure C.6.

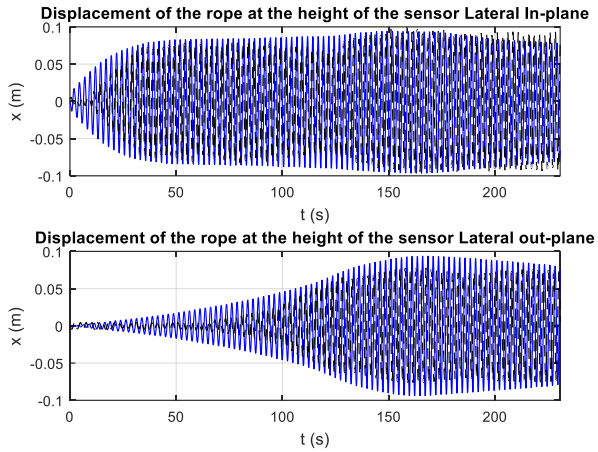

Figure C.5 Comparison of the rope displacement at sensor height from the experiment and the mathematical model

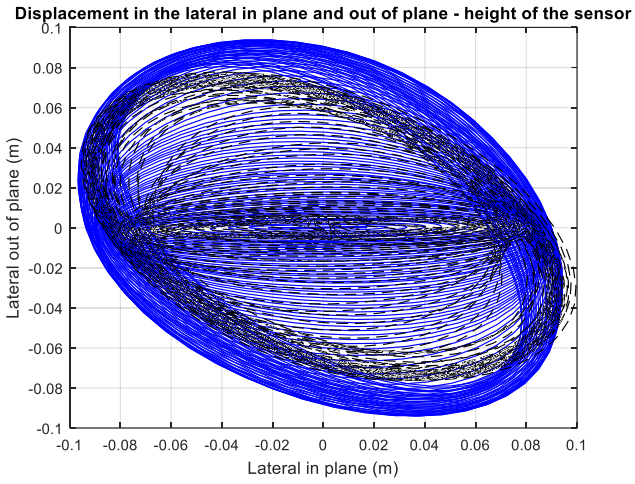

Figure C.6 Comparison of the displacements in the Lateral in plane and out of plane direction.

As it can be seen the simulation with higher number of modes for the Galerkin method agrees better with the experimental testing. The contribution of the first three modes to compare the results with the experimental testing agrees better. Thus, the number of modes chosen in Chapter 3 to compare the simulation with the experimental testing will give an acceptable correlation.

Appendix D

Lateral Eigenvalue Problem of two ropes and a mass

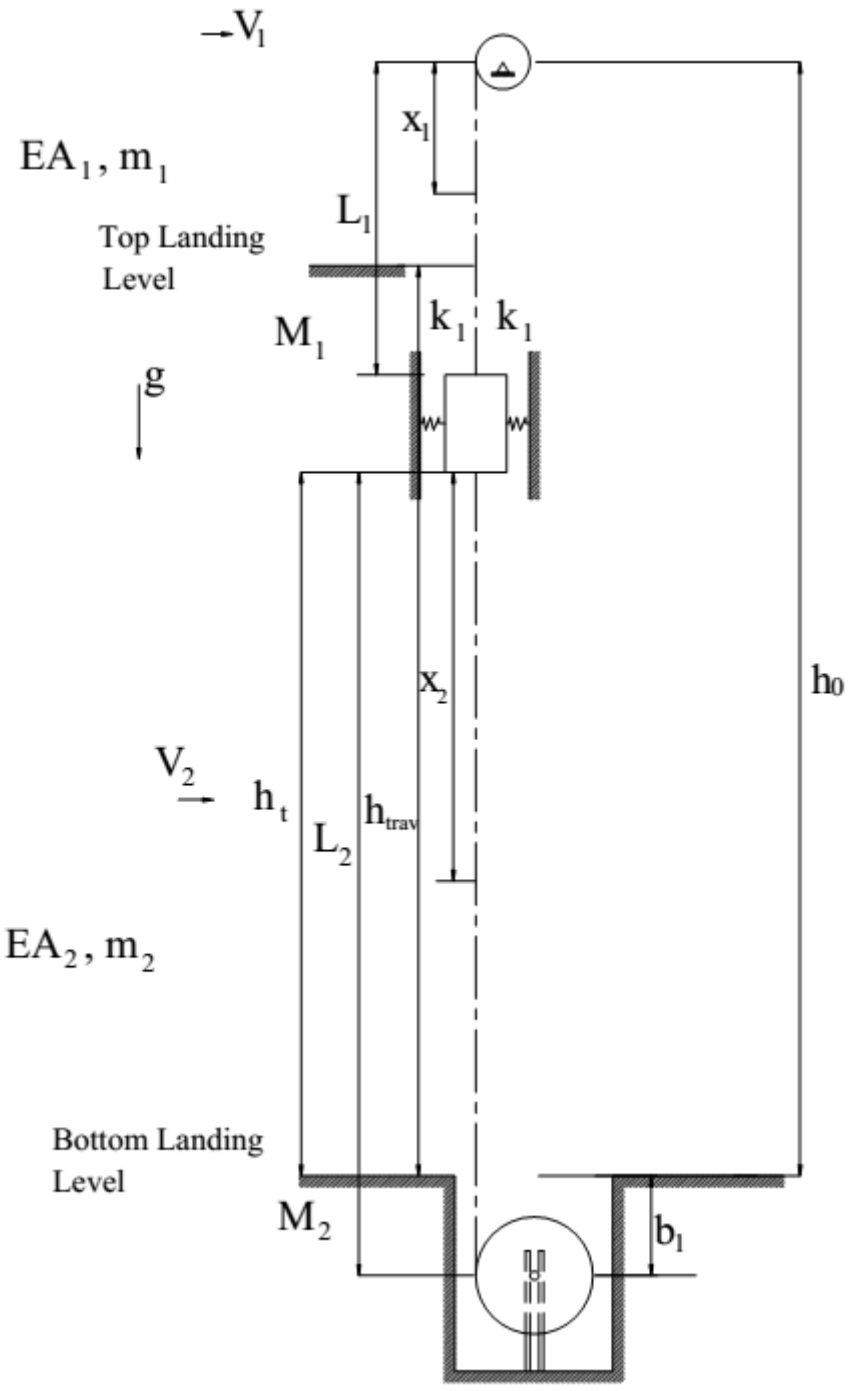

Figure D.1. Drawing of the mathematical model taken into account.

The lateral motion of the mathematical model of the ropes of Figure D.1, which are being treated as a string, are governed by the following equations

$$m_1 V_{1tt} - T_1 V_{1xx} = 0 \tag{D.1}$$

$$m_2 V_{2tt} - T_2 V_{2xx} = 0 \tag{D.2}$$

$$V_1(0,t) = 0 \tag{D.3}$$

$$V_1(\mathrm{L}_1,t) = V_2(0,t) \tag{D.4}$$

$$V_2(\mathrm{L}_2,t) = 0 \tag{D.5}$$

$$M_1 V_{1tt}(L_1,t) + T_1 V_{1x}(L_1,t) - T_2 V_{2x}(0,t) + 2k_1 V_1(L_1,t) = 0 \tag{D.6}$$

The equation of the string (D.1) and (D.2) are solved using the technique of the separation of variables in order to determine the equation for the mode shapes. The boundary conditions are defined from equations (D.3) to (D.5). It is assumed that the displacement $V_1(x,t)$ and $V_2(x,t)$ can be written as a product of two functions one depending on length *(x)* and the other on time *(t)*.

$$V_1(x,t) = \phi_1(x_1)q(t) \tag{D.7}$$

$$V_2(x,t) = \phi_2(x_2)q(t) \tag{D.8}$$

The solution for each function is defined in equations (D.9) and (D.10) respectively

$$\phi_1(x) = A_1 \cos\beta_1 x_1 + B_1 \sin\beta_1 x_1 \tag{D.9}$$

$$\phi_2(x) = A_2 \cos\beta_2 x_2 + B_2 \sin\beta_2 x_2 \tag{D.10}$$

Where β_1 and β_2 are defined as equations (D.11) and (D.12)

$$\beta_1 = \omega\sqrt{\frac{m_1}{T_1}} \tag{D.11}$$

$$\beta_2 = \omega\sqrt{\frac{m_2}{T_2}} \tag{D.12}$$

From the boundary condition (D.3).

$A_1 = 0$ Thus, equation (D.9) can be rewritten as

$$\phi_1(x) = B_1 \sin\beta_1 x_1 \tag{D.13}$$

From boundary condition (D.4)

$$A_2 - B_1 \sin \beta_1 L_1 = 0 \tag{D.14}$$

From boundary condition (D.5)

$$A_2 \cos \beta_2 L_2 + B_2 \sin \beta_2 L_2 = 0 \tag{D.15}$$

From boundary condition (D.6) and using equations (D.14) and (D.15)

$$-M_1 \omega^2 B_1 \sin \beta_1 L_1 + T_1 B_1 \beta_1 \cos \beta_1 L_1 - T_2 B_2 \beta_2 + k_1 B_1 \sin \beta_1 L_1 = 0 \tag{D.16}$$

Placing equations (D.14) to (D.15) in a matrix and finding the determinant of the matrix gives equation (D.17)

$$\begin{aligned} &\omega \sqrt{T_2 m_2} \cos\left(\omega L_2 \sqrt{\frac{m_2}{L_2}}\right) \sin\left(\omega L_1 \sqrt{\frac{m_1}{L_1}}\right) + 2k_1 \sin\left(\omega L_2 \sqrt{\frac{m_2}{L_2}}\right) \sin\left(\omega L_1 \sqrt{\frac{m_1}{L_1}}\right) \\ &+ \omega \sqrt{T_1 m_1} \sin\left(\omega L_2 \sqrt{\frac{m_2}{L_2}}\right) \cos\left(\omega L_1 \sqrt{\frac{m_1}{L_1}}\right) - M_1 \omega^2 \sin\left(\omega L_2 \sqrt{\frac{m_2}{L_2}}\right) \sin\left(\omega L_1 \sqrt{\frac{m_1}{L_1}}\right) = 0 \end{aligned} \tag{D.17}$$

To determine B_1, A_2, *and* B_2, assuming

$$B_1 = 1 \tag{D.18}$$

Thus using B_1 in equation (D.13) and (D.14) results in equation (D.19) and (D.20)

$$A_2 = \sin \beta_1 L_1 \tag{D.19}$$

$$B_2 = -\frac{\sin \beta_1 L_1 \cos \beta_2 L_2}{\sin \beta_2 L_2} \tag{D.20}$$

Using equations (D.18) to (D.20) in (D.13) and (D.10) gives equations (D.21) and (D.22)

$$\phi_1(x) = \sin \beta_1 x_1 \tag{D.21}$$

$$\phi_2(x) = \sin \beta_1 L_1 \cos \beta_2 x_2 - \frac{\sin \beta_1 L_1 \cos \beta_2 L_2}{\sin \beta_2 L_2} \sin \beta_2 x_2 \tag{D.22}$$

Appendix E

Orthogonality of Modes of two ropes and a mass

For the lateral in plane and out of plane motion of the mathematical model of Figure D.1, the differential equation of the stationary, unconstrained system can be written as:

$$m_1 V_{1tt} - T_1 V_{1xx} = 0 \text{ in the domain } 0 \le x_1 \le L_1 \tag{E.1}$$

$$m_2 V_{2tt} - T_2 V_{2xx} = 0 \text{ in the domain } 0 \le x_2 \le L_2 \tag{E.2}$$

In addition V_1 must satisfy the boundary conditions at $x_1 = 0$ and $x_1 = L_1$ and V_2 must satisfy boundary conditions at $x_2 = 0$ and $x_2 = L_2$ which are described by the equations (E.3) to (E.6), respectively.

$$V_1(0,t) = 0 \tag{E.3}$$

$$V_1(\mathrm{L}_1,t) = V_2(0,t) \tag{E.4}$$

$$V_2(\mathrm{L}_2,t) = 0 \tag{E.5}$$

$$M_1 V_{1tt}(L_1,t) + T_1(L_1) V_{1x}(L_1,t) - T_2(0) V_{2x}(0,t) + 2k_1 V_1(L_1,t) = 0 \tag{E.6}$$

Using the separation of variables technique the displacement V_1 and V_2 can be expressed as

$$V_1(x,t) = \phi_1(x_1) q(t) \tag{E.7}$$

$$V_2(x,t) = \phi_2(x_2) q(t) \tag{E.8}$$

$$-\omega^2 = \frac{\ddot{q}(t)}{q(t)} \tag{E.9}$$

where the prime designates differentiation with respect to *x*. Equations (E.1) and (E.2) can be rewritten as

$$m_1 \omega^2 \phi_1(x) = -T_1 \phi_1''(x_1) \tag{E.10}$$

$$m_2 \omega^2 \phi_2(x) = -T_2 \phi_2''(x_2) \tag{E.11}$$

The orthogonality property of equations (E.10) and (E.11) can be examined by considering modes *n* and r of the Eigenvalue problem as the following equations:

$$m_1 \omega_n^2 \phi_{1n}(x) = -T_1 \phi_{1n}''(x_1) \tag{E.12}$$

$$m_2\omega_n^2\phi_{2n}(x) = -T_2\phi''_{2n}(x_2) \tag{E.13}$$

$$m_1\omega_r^2\phi_{1r}(x) = -T_1\phi''_{1r}(x_1) \tag{E.14}$$

$$m_2\omega_r^2\phi_{2r}(x) = -T_2\phi''_{2r}(x_2) \tag{E.15}$$

Multiplying Equations (E.12) and (E.13) by $\phi_{1r}(x)$ and $\phi_{2r}(x)$ respectively and (E.14) and (E.15) by $\phi_{1n}(x)$ and $\phi_{2n}(x)$ and integrating over the interval $[0-L_1]$ Equations (E.12) and (E.14) and $[0-L_2]$ equations (13) and (15).

$$m_1\omega_n^2\int_0^{L_1}\phi_{1n}(x)\phi_{1r}(x)dx = -T_1\int_0^{L_1}\phi''_{1n}(x)\phi_{1r}(x)dx \tag{E.16}$$

$$m_2\omega_n^2\int_0^{L_2}\phi_{2n}(x)\phi_{2r}(x)dx = -T_2\int_0^{L_2}\phi''_{2n}(x)\phi_{2r}(x)dx \tag{E.17}$$

$$m_1\omega_r^2\int_0^{L_1}\phi_{1n}(x)\phi_{1r}(x)dx = -T_1\int_0^{L_1}\phi''_{1r}(x)\phi_{1n}(x)dx \tag{E.18}$$

$$m_2\omega_r^2\int_0^{L_2}\phi_{2n}(x)\phi_{2r}(x)dx = -T_2\int_0^{L_2}\phi''_{2r}(x)\phi_{2n}(x)dx \tag{E.19}$$

The boundary condition equation (E.6) and using equations (E.7), (E.8), (E.9), for modes *n* and *r* and multiplying by $\phi_{1r}(x)$ and $\phi_{1n}(x)$ respectively, can be written as the following expressions:

$$-M_1\phi_{1n}(L_1)\phi_{1r}(L_1)\omega_n^2 = -T_1\phi'_{1n}(L_1)\phi_{1r}(L_1) + T_2\phi'_{2n}(0)\phi_{1r}(L_1) - 2k_1\phi_{1n}(L_1)\phi_{1r}(L_1) \tag{E.20}$$

$$-M_1\phi_{1r}(L_1)\phi_{1n}(L_1)\omega_r^2 = -T_1\phi'_{1r}(L_1)\phi_{1n}(L_1) + T_2\phi'_{2r}(0)\phi_{1n}(L_1) - 2k_1\phi_{1r}(L_1)\phi_{1n}(L_1) \tag{E.21}$$

Evaluating the integrals of (E.16) to (E.19) by parts the following equations are produced:

$$m_1\omega_n^2\int_0^{L_1}\phi_{1n}(x)\phi_{1r}(x)dx = -T_1\phi'_{1n}(\mathrm{L}_1)\phi_{1r}(\mathrm{L}_1) + T_1\int_0^{L_1}\phi'_{1n}(x_1)\phi'_{1r}(x_1)dx \tag{E.22}$$

$$m_2\omega_n^2\int_0^{L_2}\phi_{2n}(x)\phi_{2r}(x)dx = T_2\phi'_{2n}(0)\phi_{2r}(0) + T_2\int_0^{L_2}\phi'_{2n}(x_2)\phi'_{2r}(x_2)dx \tag{E.23}$$

$$m_1\omega_r^2\int_0^{L_1}\phi_{1n}(x)\phi_{1r}(x)dx = -T_1\phi'_{1r}(\mathrm{L}_1)\phi_{1n}(\mathrm{L}_1) + T_1\int_0^{L_1}\phi'_{1n}(x_1)\phi'_{1r}(x_1)dx \tag{E.24}$$

$$m_2\omega_r^2\int_0^{L_2}\phi_{2n}(x)\phi_{2r}(x)dx = T_2\phi'_{2r}(0)\phi_{2n}(0) + T_2\int_0^{L_2}\phi'_{2n}(x_2)\phi'_{2r}(x_2)dx \tag{E.25}$$

Summing equation (E.22) and (E.23) and subtracting equations (E.20) for *n*. For *r* summing equations (E.24) and (E.25) and subtracting equation (E.21), and using the transformation $\phi_1(\mathrm{L}_1) = \phi_2(0)$ gives equations (E.26) and (E.27)

$$m_1\omega_n^2\int_0^{L_1}\phi_{1n}(x)\phi_{1r}(x)dx + m_2\omega_n^2\int_0^{L_2}\phi_{2n}(x)\phi_{2r}(x)dx + M_1\phi_{1r}(L_1)\phi_{1n}(L_1)\omega_n^2 = T_1\int_0^{L_1}\phi'_{1n}(x_1)\phi'_{1r}(x_1)dx + 2k\phi_{1n}(L_1)\phi_{1r}(L_1) + T_2\int_0^{L_2}\phi'_{2n}(x_2)\phi'_{2r}(x_2)dx \tag{E.26}$$

$$m_1\omega_r^2\int_0^{L_1}\phi_{1n}(x)\phi_{1r}(x)dx + m_2\omega_r^2\int_0^{L_2}\phi_{2n}(x)\phi_{2r}(x)dx + M_1\phi_{1r}(L_1)\phi_{1n}(L_1)\omega_r^2 = T_1\int_0^{L_1}\phi'_{1n}(x_1)\phi'_{1r}(x_1)dx + T_2\int_0^{L_2}\phi'_{2n}(x_2)\phi'_{2r}(x_2)dx + 2k\phi_{1r}(L_1)\phi_{1n}(L_1) \tag{E.27}$$

Substracting equation (E.26) and (E.27) gives the following solution

$$m_1\int_0^{L_1}\phi_{1n}(x)\phi_{1r}(x)dx + m_2\int_0^{L_2}\phi_{2n}(x)\phi_{2r}(x)dx + M_1\phi_{1r}(L_1)\phi_{1n}(L_1) = \begin{cases} m_{1rr} & \text{if } n = r \\ 0 & \text{if } n \neq r \end{cases} \tag{E.28}$$

Applying (E.28) into (E.27)

$$T_1\int_0^{L_1}\phi'_{1n}(x_1)\phi'_{1r}(x_1)dx + T_2\int_0^{L_2}\phi'_{2n}(x_2)\phi'_{2r}(x_2)dx + 2k_1\phi_{1r}(L_1)\phi_{1n}(L_1) \begin{cases} m_{1rr}\omega_r^2 & \text{if } n = r \\ 0 & \text{if } n \neq r \end{cases} \tag{E.29}$$

Appendix F

Coefficients for the Stationary Model of a High Rise Elevator System

Where G_{jp}^{1Lin} and G_{jp}^{2Lin} are represented as equations (F.1) to (F.4)

$$G_{jp}^{1Lin}=\begin{cases} j=p;\dfrac{\left(\beta_{1j}^{Lin}\right)^2 L_1}{2}+\dfrac{\beta_{1j}^{Lin}\sin\left(2\beta_{1j}^{Lin}L_1\right)}{4} \\ j\neq p;\beta_{1j}^{Lin}\beta_{1p}^{Lin}\left[\dfrac{\sin\left(L_1\left(\beta_{1j}^{Lin}-\beta_{1p}^{Lin}\right)\right)}{2\left(\beta_{1j}^{Lin}-\beta_{1p}^{Lin}\right)}+\dfrac{\sin\left(L_1\left(\beta_{1j}^{Lin}+\beta_{1p}^{Lin}\right)\right)}{2\left(\beta_{1j}^{Lin}+\beta_{1p}^{Lin}\right)}\right] \end{cases} \tag{F.1}$$

$$G_{jp}^{2Lin}=\begin{cases} j=p;\left(\begin{array}{l}\dfrac{L_2\left(\beta_{2j}^{Lin}\right)^2\sin^2\beta_{1j}^{Lin}L_1}{2\sin^2\beta_{2j}^{Lin}L_2}+\dfrac{\beta_{2j}^{Lin}\sin^2\beta_{1j}^{Lin}L_1\cos 2\beta_{2j}^{Lin}L_2\sin 2\beta_{2j}^{Lin}L_2}{4\sin^2\beta_{2j}^{Lin}L_2} \\ +\beta_{2j}^{Lin}\sin^2\beta_{1j}^{Lin}L_1\cos\beta_{2j}^{Lin}L_2\sin\beta_{2j}^{Lin}L_2\end{array}\right) \\ j\neq p;\dfrac{1}{\left(\beta_{2p}^{Lin}\right)^2-\left(\beta_{2j}^{Lin}\right)^2}\left(\begin{array}{l}\sin\beta_{2p}^{Lin}L_2\left(\begin{array}{l}\sin\beta_{2j}^{Lin}L_2\left(\beta_{2p}^{Lin}C_{2p}^{v}C_{1j}^{v}-\beta_{2j}^{Lin}C_{1p}^{v}C_{2j}^{v}\right)\\ +\cos\beta_{2j}^{Lin}L_2\left(\beta_{2p}^{Lin}C_{2p}^{v}C_{2j}^{v}+\beta_{2j}^{Lin}C_{1p}^{v}C_{1j}^{v}\right)\end{array}\right)+ \\ \cos\beta_{2p}^{Lin}L_2\left(\begin{array}{l}\cos\beta_{2j}^{Lin}L_2\left(\beta_{2j}^{Lin}C_{2p}^{v}C_{1j}^{v}-\beta_{2p}^{Lin}C_{1p}^{v}C_{2j}^{v}\right)\\ -\sin\beta_{2j}^{Lin}L_2\left(\beta_{2p}^{Lin}C_{1p}^{v}C_{1j}^{v}+\beta_{2j}^{Lin}C_{2p}^{v}C_{2j}^{v}\right)\end{array}\right)- \\ \left(\beta_{2j}^{Lin}C_{2p}^{v}C_{1j}^{v}-\beta_{2p}^{Lin}C_{1p}^{v}C_{2j}^{v}\right)\end{array}\right) \end{cases} \tag{F.2}$$

Where $C_{1p}^{v}=\beta_{2p}^{Lin}\sin\beta_{1p}^{Lin}L_1$, $C_{1j}^{v}=\beta_{2j}^{Lin}\sin\beta_{1j}^{Lin}L_1$, $C_{2j}^{v}=\dfrac{\beta_{2j}^{Lin}\sin\beta_{1j}^{Lin}L_1\cos\beta_{2j}^{Lin}L_2}{\sin\beta_{2j}^{Lin}L_2}$, and $C_{2p}^{v}=\dfrac{\beta_{2p}^{Lin}\sin\beta_{1p}^{Lin}L_1\cos\beta_{2p}^{Lin}L_2}{\sin\beta_{2p}^{Lin}L_2}$.

Similarly G_{jp}^{1Lout} and G_{jp}^{2Lout} can be deducted.

The coefficients for the first rope in the lateral in plane direction are the following:

$$m_{1rr}^{Lin}=m_1\int_0^{L_1}\phi_{1r}^2\left(x_1\right)dx_1+M_1\phi_{1r}^2\left(L_1\right)+m_2\int_0^{L_2}\phi_{2r}^2\left(x_2\right)dx_2 \tag{F.3}$$

$$\left(\omega_{1rr}^{Lin}\right)^2 = \left[\begin{array}{l} -\left(M_1 + m_1 L_1 + m_2 L_2 + \frac{M_2}{2}\right) g \int_0^{L_1} \phi_{1r}''(x_1)\phi_{1r}(x_1)dx_1 \\ +\left(M_1 + m_2 L_2 + \frac{M_2}{2}\right) g \phi_{1r}'(\mathrm{L}_1)\phi_{1r}(\mathrm{L}_1) \\ +2k_1\phi_{1r}(\mathrm{L}_1)^2 - \left(m_2 L_2 + \frac{M_2}{2}\right) g \int_0^{L_2} \phi_{2r}''(x_2)\phi_{2r}(x_2)dx_2 \\ -\left(m_2 L_2 + \frac{M_2}{2}\right) g \phi_{2r}'(0)\phi_{1r}(\mathrm{L}_1) \end{array}\right] / m_{1rr}^{Lin} \tag{F.4}$$

$$k_{1rn}^{Lin1} = \left[\begin{array}{l} m_1 g \int_0^{L_1} x\phi_{1n}''(x_1)\phi_{1r}(x_1)dx_1 + m_1 g \int_0^{L_1} \phi_{1n}'(x_1)\phi_{1r}(x_1)dx_1 \\ -\frac{EA_1\left(\left(f_1^{\,v}\right)^2 + \left(f_1^{\,w}\right)^2\right)}{2} \int_0^{L_1} \phi_{1n}''(x_1)\phi_{1r}(x_1)dx_1 \\ -\frac{EA_1 U_{CR}}{L_1}\left(\int_0^{L_1} \phi_{1n}''(x_1)\phi_{1r}(x_1)dx_1 - \phi_{1n}'(\mathrm{L}_1)\phi_{1r}(\mathrm{L}_1)\right) \\ +\frac{EA_1\left(\left(f_1^{\,v}\right)^2 + \left(f_1^{\,w}\right)^2\right)}{2}\phi_{1n}'(\mathrm{L}_1)\phi_{1r}(\mathrm{L}_1) + \frac{EA_1\left(f_1^{\,v}\right)^2}{L_1}\phi_{1n}(\mathrm{L}_1)\phi_{1r}(\mathrm{L}_1) \\ -\frac{EA_2\left(U_{CS} - U_{CR}\right)}{L_2}\left(\int_0^{L_2} \phi_{2n}''(x_2)\phi_{2r}(x_2)dx_2 - \phi_{2n}'(0)\phi_{1r}(L_1)\right) \\ -\frac{EA_2\left(\left(f_2^{\,v}\right)^2 + \left(f_2^{\,w}\right)^2\right)}{2} \int_0^{L_2} \phi_{2n}''(x_2)\phi_{2r}(x_2)dx_2 \\ -\frac{EA_2\left(\left(f_2^{\,v}\right)^2 + \left(f_2^{\,w}\right)^2\right)}{2}\phi_{2n}'(0)\phi_{1r}(\mathrm{L}_1) + \frac{EA_2\left(f_2^{\,v}\right)^2}{L_2}\phi_{1n}(\mathrm{L}_1)\phi_{1r}(\mathrm{L}_1) \\ +m_2 g \int_0^{L_2} x_2\phi_{2n}''(x_2)\phi_{2r}(x_2)dx_2 + m_2 g \int_0^{L_2} \phi_{2n}'(x_2)\phi_{2r}(x_2)dx_2 \end{array}\right] / m_{1rr}^{Lin} \tag{F.5}$$

$$k_{1rn}^{Lin2} = \frac{EA_1 f_1^{\,v} f_1^{\,w}}{L_1 m_{1rr}^{Lin}}\alpha_{1n}\left(L_1\right)\phi_{1r}(\mathrm{L}_1) + \frac{EA_2 f_2^{\,v} f_2^{\,w}}{L_2 m_{1rr}^{Lin}}\alpha_{1n}\left(L_1\right)\phi_{1r}(\mathrm{L}_1) \tag{F.6}$$

$$k_{1r}^{Lin3} = \left(\frac{EA_1 f_1^{\,v}}{L_1} - \frac{EA_2 f_2^{\,v}}{L_2}\right)\frac{\phi_{1r}(\mathrm{L}_1)}{m_{1rr}^{Lin}} \tag{F.7}$$

$$k_{1r}^{Lin4} = \left(\frac{EA_2 f_2^{\,v}}{L_2}\right)\frac{\phi_{1r}(\mathrm{L}_1)}{m_{1rr}^{Lin}} \tag{F.8}$$

$$D_{1nr}^{Lin1}=\left(\begin{array}{l}-\dfrac{EA_1 f_1^{v}}{L_1}\phi_{1r}(\mathrm{L}_1)\int_0^{L_1}\phi_{1n}''(x_1)\phi_{1r}(x_1)dx_1+\dfrac{EA_1 f_1^{v}}{L_1}\phi_{1j}(\mathrm{L}_1)\phi_{1r}(\mathrm{L}_1)\phi_{1n}'(\mathrm{L}_1)\\ +\dfrac{EA_1 f_1^{v}}{2L_1}G_{jp}^{1Lin}\phi_{1r}(\mathrm{L}_1)-\dfrac{EA_2 f_2^{v}}{L_2}\phi_{1r}(\mathrm{L}_1)\int_0^{L_2}\phi_{2n}''(x_2)\phi_{2r}(x_2)dx_2\\ -\dfrac{EA_2 f_2^{v}}{L_2}\phi_{1j}(\mathrm{L}_1)\phi_{1r}(\mathrm{L}_1)\phi_{2n}'(0)+\dfrac{EA_2 f_2^{v}}{2L_2}G_{jp}^{2Lin}\phi_{1r}(\mathrm{L}_1)\end{array}\right)/m_{1rr}^{Lin} \tag{F.9}$$

$$D_{1nr}^{Lin2}=\left(\begin{array}{l}-\dfrac{EA_1 f_1^{w}}{L_1}\alpha_{1n}(\mathrm{L}_1)\int_0^{L_1}\phi_{1n}''(x_1)\phi_{1r}(x_1)dx_1+\dfrac{EA_1 f_1^{w}}{L_1}\alpha_{1j}(\mathrm{L}_1)\phi_{1r}(\mathrm{L}_1)\phi_{1n}'(\mathrm{L}_1)\\ -\dfrac{EA_2 f_2^{w}}{L_2}\alpha_{1n}(\mathrm{L}_1)\int_0^{L_2}\phi_{2n}''(x_2)\phi_{2r}(x_2)dx_2-\dfrac{EA_2 f_2^{w}}{L_2}\alpha_{1j}(\mathrm{L}_1)\phi_{1r}(\mathrm{L}_1)\phi_{2n}'(0)\end{array}\right)/m_{1rr}^{Lin} \tag{F.10}$$

$$D_{1nr}^{Lin3}=\frac{EA_1 f_1^{v}}{2m_{1rr}^{Lin}L_1}G_{jp}^{1Lout}\phi_{1r}(\mathrm{L}_1)+\frac{EA_2 f_2^{v}}{2m_{1rr}^{Lin}L_2}G_{jp}^{2Lout}\phi_{1r}(\mathrm{L}_1) \tag{F.11}$$

$$\begin{aligned}R1_{1jnr}^{Lin}&=-\frac{EA_1G_{jp}^{1Lin}}{2m_{1rr}^{Lin}L_1}\int_0^{L_1}\phi_{1n}''(x_1)\phi_{1r}(x_1)dx_1+\frac{EA_1G_{jp}^{1Lin}}{2L_1m_{1rr}^{Lin}}\phi_{1n}'(\mathrm{L}_1)\phi_{1r}(\mathrm{L}_1)\\ &-\frac{EA_2G_{jp}^{2Lin}}{2m_{1rr}^{Lin}L_2}\int_0^{L_2}\phi_{2n}''(x_2)\phi_{2r}(x_2)dx_2-\frac{EA_2G_{jp}^{2Lin}}{2L_2m_{1rr}^{Lin}}\phi_{2n}'(0)\phi_{1r}(\mathrm{L}_1)\end{aligned} \tag{F.12}$$

$$\begin{aligned}R2_{1jnr}^{Lin}&=-\frac{EA_1G_{jp}^{1Lout}}{2m_{1rr}^{Lin}L_1}\int_0^{L_1}\phi_{1n}''(x_1)\phi_{1r}(x_1)dx_1+\frac{EA_1G_{jp}^{1Lout}}{2L_1m_{1rr}^{Lin}}\phi_{1n}'(\mathrm{L}_1)\phi_{1r}(\mathrm{L}_1)\\ &-\frac{EA_2G_{jp}^{2Lout}}{2m_{1rr}^{Lin}L_2}\int_0^{L_2}\phi_{2n}''(x_2)\phi_{2r}(x_2)dx_2-\frac{EA_2G_{jp}^{2Lout}}{2L_2m_{1rr}^{Lin}}\phi_{2n}'(0)\phi_{1r}(\mathrm{L}_1)\end{aligned} \tag{F.13}$$

$$F_{1r}^{Lin}=\left[\begin{array}{l}-m_1S_1^{v}\int_0^{L_1}\phi_{1r}(x_1)dx_1-m_1S_2^{v}\int_0^{L_1}x_1\phi_{1r}(x_1)dx_1+m_1gf_1^{v}\int_0^{L_1}\phi_r(x_1)dx_1+\\ \left(\begin{array}{l}\left(M_1+m_2L_2+\dfrac{M_2}{2}\right)gf_1^{v}+\left(\dfrac{M_2}{2}+m_2L_2\right)gf_2^{v}\\ -M_1S_7^{v}+\dfrac{EA_1}{2}\left(\left(f_1^{v}\right)^3+f_1^{v}\left(f_1^{w}\right)^2\right)+\dfrac{EA_2}{2}\left(\left(f_2^{v}\right)^3+f_2^{v}\left(f_2^{w}\right)^2\right)\end{array}\right)\phi_{1r}(\mathrm{L}_1)\\ -m_2S_3^{v}\int_0^{L_2}\phi_{2r}(x_2)dx_2+m_2S_4^{v}\int_0^{L_2}x_2\phi_{2r}(x_2)dx_2-m_2gf_2^{v}\int_0^{L_2}\phi_{2r}(x_2)dx_2\end{array}\right]/m_{1rr}^{Lin} \tag{F.14}$$

The coefficients for the first rope in the lateral out of plane direction are the following

$$m_{1rr}^{Lout}=m_1\int_0^{L_1}\alpha_{1r}^2\left(x_1\right)dx_1+m_2\int_0^{L_2}\alpha_{2r}^2\left(x_2\right)dx_2+M_1\alpha_{1r}^2\left(L_1\right) \tag{F.15}$$

$$\left(\omega_{1rr}^{Lout}\right)^2 = \begin{bmatrix} -\left(M_1 + m_1 L_1 + m_2 L_2 + \dfrac{M_2}{2}\right) g \int_0^{L_1} \alpha_{1r}''(x_1)\alpha_{1r}(x_1)dx_1 \\ +\left(M_1 + m_2 L_2 + \dfrac{M_2}{2}\right) g \alpha_{1r}'(\mathrm{L}_1)\alpha_{1r}(\mathrm{L}_1) \\ +2k_2\alpha_{1r}(\mathrm{L}_1)^2 - \left(m_2 L_2 + \dfrac{M_2}{2}\right) g \int_0^{L_2} \alpha_{2r}''(x_2)\alpha_{2r}(x_2)dx_2 \\ -\left(m_2 L_2 + \dfrac{M_2}{2}\right) g \alpha_{2r}'(0)\alpha_{1r}(\mathrm{L}_1) \end{bmatrix} / m_{1rr}^{Lout} \tag{F.16}$$

$$k_{1rn}^{Lout1} = \begin{bmatrix} m_1 g \int_0^{L_1} x_1 \alpha_{1n}''(x_1)\alpha_{1r}(x_1)dx_1 + m_1 g \int_0^{L_1} \alpha_{1n}'(x_1)\alpha_{1r}(x_1)dx_1 \\ -\dfrac{EA_1\left(\left(f_1^{\,v}\right)^2 + \left(f_1^{\,w}\right)^2\right)}{2} \int_0^{L_1} \alpha_{1n}''(x_1)\alpha_{1r}(x_1)dx_1 \\ -\dfrac{EA_1 U_{CR}}{L_1}\left(\int_0^{L_1} \alpha_{1n}''(x_1)\alpha_{1r}(x_1)dx_1 - \alpha_{1n}'(\mathrm{L}_1)\alpha_{1r}(\mathrm{L}_1)\right) \\ +\dfrac{EA_1\left(\left(f_1^{\,v}\right)^2 + \left(f_1^{\,w}\right)^2\right)}{2}\alpha_{1n}'(\mathrm{L}_1)\alpha_{1r}(\mathrm{L}_1) - \dfrac{EA_1\left(f_1^{\,w}\right)^2}{L_1}\alpha_{1n}(\mathrm{L}_1)\alpha_{1r}(\mathrm{L}_1) \\ -\dfrac{EA_1\left(U_{CS} - U_{CR}\right)}{L_1}\left(\int_0^{L_2} \alpha_{2n}''(x_2)\alpha_{2r}(x_2)dx_2 - \alpha_{2n}'(0)\alpha_{1r}(\mathrm{L}_1)\right) \\ -\dfrac{EA_2\left(\left(f_2^{\,v}\right)^2 + \left(f_2^{\,w}\right)^2\right)}{2} \int_0^{L_2} \alpha_{2n}''(x_2)\alpha_{2r}(x_2)dx_2 \\ -\dfrac{EA_2\left(\left(f_2^{\,v}\right)^2 + \left(f_2^{\,w}\right)^2\right)}{2}\alpha_{2n}'(0)\alpha_{1r}(\mathrm{L}_1) + \dfrac{EA_2\left(f_2^{\,w}\right)^2}{L_2}\alpha_{1n}(L_1)\alpha_{1r}(\mathrm{L}_1) \\ +m_2 g \int_0^{L_2} x_2 \alpha_{2n}''(x_2)\alpha_{2r}(x_2)dx_2 + m_2 g \int_0^{L_2} \alpha_{2n}'(x_2)\alpha_{2r}(x_2)dx_2 \end{bmatrix} / m_{1rr}^{Lout} \tag{F.17}$$

$$k_{1r}^{Lout3} = \left(\frac{EA_1 f_1^{\,w}}{L_1} - \frac{EA_2 f_2^{\,w}}{L_2}\right)\frac{\alpha_{1r}(\mathrm{L}_1)}{m_{1rr}^{Lout}} \tag{F.18}$$

$$k_{1r}^{Lout4} = \left(\frac{EA_2 f_2^{\,w}}{L_2}\right)\frac{\alpha_{1r}(\mathrm{L}_1)}{m_{1rr}^{Lout}} \tag{F.19}$$

$$k_{1rn}^{Lout5} = \frac{EA_1 f_1^{\,v} f_1^{\,w}}{L_1 m_{1rr}^{Lout}}\phi_{1n}(\mathrm{L}_1)\alpha_{1r}\left(L_1\right) + \frac{EA_2 f_2^{\,v} f_2^{\,w}}{L_2 m_{1rr}^{Lout}}\phi_{1n}(\mathrm{L}_1)\alpha_{1r}\left(L_1\right) \tag{F.20}$$

$$D_{1nr}^{Lout1} = \begin{pmatrix} -\dfrac{EA_1 f_1^{\,v}}{L_1}\phi_{1j}(\mathrm{L}_1)\int_0^{L_1} \alpha_{1n}''(x_1)\alpha_{1r}(x_1)dx_1 - \dfrac{EA_1 f_1^{\,v}}{L_1}\phi_{1j}(\mathrm{L}_1)\alpha_{1r}(\mathrm{L}_1)\alpha_{1n}'(\mathrm{L}_1) \\ -\dfrac{EA_2 f_2^{\,v}}{L_2}\phi_{1j}(\mathrm{L}_1)\int_0^{L_2} \alpha_{2n}''(x_2)\alpha_{2r}(x_2)dx_2 - \dfrac{EA_2 f_2^{\,v}}{L_2}\phi_{1j}(\mathrm{L}_1)\alpha_{1r}(\mathrm{L}_1)\alpha_{2n}'(0) \end{pmatrix} / m_{1rr}^{Lout} \tag{F.21}$$

$$D_{1nr}^{Lout2}=\left(\begin{array}{l}\dfrac{EA_1 f_1^{\,w}}{L_1}\left(\begin{array}{l}-\alpha_{1j}(\mathrm{L}_1)\int_0^{L_1}\alpha_{1n}''(x_1)\alpha_{1r}(x_1)dx_1\\+\alpha_{1j}(\mathrm{L}_1)\alpha_{1r}(\mathrm{L}_1)\alpha_{1n}'(\mathrm{L}_1)+\dfrac{1}{2}G_{jp}^{1Lout}\alpha_{1r}(\mathrm{L}_1)\end{array}\right)\\+\dfrac{EA_2 f_2^{\,w}}{L_2}\left(\begin{array}{l}-\alpha_{1j}(\mathrm{L}_1)\int_0^{L_2}\alpha_{2n}''(x_2)\alpha_{2r}(x_2)dx_2\\-\alpha_{1j}(\mathrm{L}_1)\alpha_{1r}(\mathrm{L}_1)\alpha_{2n}'(0)+\dfrac{1}{2}G_{jp}^{2Lout}\alpha_{1r}(\mathrm{L}_1)\end{array}\right)\end{array}\right)/m_{1rr}^{Lout} \tag{F.22}$$

$$D_{1nr}^{Lout5}=\frac{EA_1 f_1^{\,w}}{2m_{1rr}^{Lout}L_1}G_{jp}^{1Lin}\alpha_{1r}(\mathrm{L}_1)+\frac{EA_2 f_2^{\,w}}{2m_{1rr}^{Lout}L_2}G_{jp}^{2Lin}\alpha_{1r}(\mathrm{L}_1) \tag{F.23}$$

$$\begin{aligned}R1_{1jnr}^{Lout}&=-\frac{EA_1G_{jp}^{1Lin}}{2m_{1rr}^{Lout}L_1}\int_0^{L_1}\alpha_{1n}''(x_1)\alpha_{1r}(x_1)dx_1+\frac{EA_1G_{jp}^{1Lin}}{2L_1m_{1rr}^{Lout}}\alpha_{1n}'(\mathrm{L}_1)\alpha_{1r}(\mathrm{L}_1)\\&-\frac{EA_2G_{jp}^{2Lin}}{2m_{1rr}^{Lout}L_2}\int_0^{L_2}\alpha_{2n}''(x_2)\alpha_{2r}(x_2)dx_2-\frac{EA_2G_{jp}^{2Lin}}{2L_2m_{1rr}^{Lout}}\alpha_{2n}'(0)\alpha_{1r}(\mathrm{L}_1)\end{aligned} \tag{F.24}$$

$$\begin{aligned}R2_{1jnr}^{Lout}&=-\frac{EA_1G_{jp}^{1Lout}}{2m_{1rr}^{Lout}L_1}\int_0^{L_1}\alpha_{1n}''(x)\alpha_{1r}(x)dx+\frac{EA_1G_{jp}^{1Lout}}{2L_1m_{1rr}^{Lout}}\alpha_{1n}'(\mathrm{L}_1)\alpha_{1r}(\mathrm{L}_1)\\&-\frac{EA_2G_{jp}^{2Lout}}{2m_{1rr}^{Lout}L_2}\int_0^{L_2}\alpha_{2n}''(x_2)\alpha_{2r}(x_2)dx_2-\frac{EA_2G_{jp}^{2Lout}}{2L_2m_{1rr}^{Lout}}\alpha_{2n}'(0)\alpha_{1r}(\mathrm{L}_1)\end{aligned} \tag{F.25}$$

$$F_{1r}^{Lout}=\left[\begin{array}{l}-m_1S_1^{\,w}\int_0^{L_1}\alpha_{1r}(x_1)dx_1-m_1S_2^{\,w}\int_0^{L_1}x_1\alpha_{1r}(x_1)dx_1+m_1gf_1^{\,w}\int_0^{L_1}\alpha_{1r}(x_1)dx_1+\\\left(\begin{array}{l}\left(M_1+m_2L_2+\dfrac{M_2}{2}\right)gf_1^{\,w}+\left(\dfrac{M_2}{2}+m_2L_2\right)gf_2^{\,w}\\-M_1S_7^{\,w}+\dfrac{EA_1}{2}\left(\left(f_1^{\,w}\right)^3+f_1^{\,w}\left(f_1^{\,v}\right)^2\right)+\dfrac{EA_2}{2}\left(\left(f_2^{\,w}\right)^3+f_2^{\,w}\left(f_2^{\,v}\right)^2\right)\end{array}\right)\alpha_{1r}(\mathrm{L}_1)\\-m_2S_3^{\,w}\int_0^{L_2}\alpha_{2r}(x_2)dx_2+m_2S_4^{\,w}\int_0^{L_2}x_2\alpha_{2r}(x_2)dx_2-m_2gf_2^{\,w}\int_0^{L_2}\alpha_{2r}(x_2)dx_2\end{array}\right]/m_{1rr}^{Lout} \tag{F.26}$$

The coefficients for the third rope in the lateral in plane direction are the following

$$m_{3rr}^{Lin}=m_2\int_0^{L_3}\phi_{3r}^2(x_3)\,dx_3 \tag{F.27}$$

$$\begin{aligned}\left(\omega_{3rr}^{Lin}\right)^2&=-\left(m_2L_3+\frac{M_2}{2}\right)\frac{g}{m_{3rr}^{Lin}}\int_0^{L_3}\phi_{3r}''(x_3)\phi_{3r}(x_3)dx_3\\&+\frac{m_2g}{m_{3rr}^{Lin}}\left(\int_0^{L_3}\phi_{3r}'(x_3)\phi_{3r}(x_3)dx_3+\int_0^{L_3}x_3\phi_{3r}''(x_3)\phi_{3r}(x_3)dx_3\right)\end{aligned} \tag{F.28}$$

$$k_{3rn}^{Lin}=\begin{bmatrix}-\dfrac{EA_2}{L_3}\left(U_{CS}-U_{CW}\right)\int_0^{L_3}\phi_{3n}''(x_3)\phi_{3r}(x_3)dx_3\\ -\dfrac{EA_2\left(\left(f_3^{v}\right)^2+\left(f_3^{w}\right)^2\right)}{2}\int_0^{L_3}\phi_{3n}''(x_3)\phi_{3r}(x_3)dx_3\end{bmatrix}/m_{3rr}^{Lin} \tag{F.29}$$

$$R1_{3\,jnr}^{Lin}=-\frac{EA_2}{4m_{3rr}^{Lin}}\left(\frac{j\pi}{L_3}\right)^2\int_0^{L_3}\phi_{3n}''(x_3)\phi_{3r}(x_3)dx_3 \tag{F.30}$$

$$R2_{3\,jnr}^{Lin}=-\frac{EA_2}{4m_{3rr}^{Lin}}\left(\frac{j\pi}{L_3}\right)^2\int_0^{L_3}\phi_{3n}''(x_3)\phi_{3r}(x_3)dx_3 \tag{F.31}$$

$$F_{3r}^{Lin}=\left[-m_2\left(S_9^{v}+gf_3^{v}\right)\int_0^{L_3}\phi_{3r}(x_3)dx_3+m_2S_{10}^{v}\int_0^{L_3}x_3\phi_{3r}(x_3)dx_3\right]/m_{3rr}^{Lin} \tag{F.32}$$

The coefficients for the fourth rope in the lateral in plane direction are the following

$$m_{4rr}^{Lin}=m_1\int_0^{L_4}\phi_{4r}^2\left(x_4\right)dx_4 \tag{F.33}$$

$$\begin{aligned}\left(\omega_{4rr}^{Lin}\right)^2=&-\left(M_3+m_1L_4+m_2L_3+\frac{M_2}{2}\right)\frac{g}{m_{4rr}^{Lin}}\int_0^{L_4}\phi_{4r}''(x)\phi_{4r}(x)dx\\ &+\frac{m_1g}{m_{4rr}^{Lin}}\left(\int_0^{L_4}x\phi_{4n}''(x)\phi_{4r}(x)dx+\int_0^{L_4}\phi_{4n}'(x)\phi_{4r}(x)dx\right)\end{aligned} \tag{F.34}$$

$$k_{4rn}^{Lin}=\begin{bmatrix}-\dfrac{EA_1}{L_4}U_{CW}\int_0^{L_4}\phi_{4n}''(x_4)\phi_{4r}(x_4)dx_4\\ -\dfrac{EA_1\left(\left(f_4^{v}\right)^2+\left(f_4^{w}\right)^2\right)}{2}\int_0^{L_4}\phi_{4n}''(x_4)\phi_{4r}(x_4)dx_4\end{bmatrix}/m_{4rr}^{Lin} \tag{F.35}$$

$$R1_{4\,jnr}^{Lin}=-\frac{EA_1}{4m_{4rr}^{Lin}}\left(\frac{j\pi}{L_4}\right)^2\int_0^{L_4}\phi_{4n}''(x_4)\phi_{4r}(x_4)dx_4 \tag{F.36}$$

$$R2_{4\,jnr}^{Lin}=-\frac{EA_1}{4m_{4rr}^{Lin}}\left(\frac{j\pi}{L_4}\right)^2\int_0^{L_4}\phi_{4n}''(x_4)\phi_{4r}(x_4)dx_4 \tag{F.37}$$

$$F_{4r}^{Lin}=\left[m_1\left(-S_5^{v}+gf_4^{v}\right)\int_0^{L_4}\phi_{4r}(x_4)dx_4-m_1S_6^{v}\int_0^{L_4}x_4\phi_{4r}(x_4)dx_4\right]/m_{4rr}^{Lin} \tag{F.38}$$

The coefficients for the third rope in the lateral out of plane direction are the following

$$m_{3rr}^{Lout} = m_2 \int_0^{L_3} \alpha_{3r}^2 \left(x_3\right) dx_3 \tag{F.39}$$

$$\begin{aligned}\left(\omega_{3rr}^{Lout}\right)^2 &= -\left(m_2 L_2 + \frac{M_2}{2}\right)\frac{g}{m_{3rr}^{Lout}} \int_0^{L_3} \alpha_{3r}''(x_3)\alpha_{3r}(x_3)dx_3 \\ &+ \frac{m_2 g}{m_{3rr}^{Lout}}\left(\int_0^{L_3} x_3 \alpha_{3n}''(x_3)\alpha_{3r}(x_3)dx_3 + \int_0^{L_3} \alpha_{3n}'(x_3)\alpha_{3r}(x_3)dx_3\right)\end{aligned} \tag{F.40}$$

$$k_{3rn}^{Lout} = \left[\left(-\frac{EA_2\left(U_{CS} - U_{CW}\right)}{L_3} - \frac{EA_2\left(\left(f_3^{\,v}\right)^2 + \left(f_3^{\,w}\right)^2\right)}{2}\right)\int_0^{L_3} \alpha_{3n}''(x_3)\alpha_{3r}(x_3)dx_3\right] / m_{3rr}^{Lout} \tag{F.41}$$

$$R1_{3\,jnr}^{Lout} = -\frac{EA_2}{4m_{3rr}^{Lout}}\left(\frac{j\pi}{L_3}\right)^2 \int_0^{L_3} \alpha_{3n}''(x_3)\alpha_{3r}(x_3)dx_3 \tag{F.42}$$

$$R2_{3\,jnr}^{Lout} = -\frac{EA_2}{4m_{3rr}^{Lout}}\left(\frac{j\pi}{L_3}\right)^2 \int_0^{L_3} \alpha_{3n}''(x_3)\alpha_{3r}(x_3)dx_3 \tag{F.43}$$

$$F_{3r}^{Lout} = \left[-m_2\left(S_9^w + gf_3^{\,w}\right)\int_0^{L_3} \alpha_{3r}(x_3)dx_3 + m_2 S_{10}^w \int_0^{L_3} x_3 \alpha_{3r}(x_3)dx_3\right] / m_{3rr}^{Lout} \tag{F.44}$$

The coefficients for the fourth rope in the lateral out of plane direction are the following

$$m_{4rr}^{Lout} = m_1 \int_0^{L_4} \alpha_{4r}^2 \left(x_4\right) dx_4 \tag{F.45}$$

$$\begin{aligned}\left(\omega_{4rr}^{Lout}\right)^2 &= -\left(M_3 + m_1 L_4 + m_2 L_3 + \frac{M_2}{2}\right)\frac{g}{m_{4rr}^{Lout}} \int_0^{L_4} \alpha_{4r}''(x_4)\alpha_{4r}(x_4)dx_4 \\ &+ \frac{m_1 g}{m_{4rr}^{Lout}}\left(\int_0^{L_4} x_4 \alpha_{4n}''(x_4)\alpha_{4r}(x_4)dx_4 + \int_0^{L_4} \alpha_{4n}'(x_4)\alpha_{4r}(x_4)dx_4\right)\end{aligned} \tag{F.46}$$

$$k_{4rn}^{Lout} = \frac{1}{m_{4rr}^{Lout}}\left(-\frac{EA_1 U_{CW}}{L_4} - \frac{EA_1\left(\left(f_4^{\,v}\right)^2 + \left(f_4^{\,w}\right)^2\right)}{2}\right)\int_0^{L_4} \alpha_{4n}''(x_4)\alpha_{4r}(x_4)dx_4 \tag{F.47}$$

$$R1_{4\,jnr}^{Lout} = -\frac{EA_1}{4m_{4rr}^{Lout}}\left(\frac{j\pi}{L_4}\right)^2 \int_0^{L_3} \alpha_{4n}''(x_4)\alpha_{4r}(x_4)dx_4 \tag{F.48}$$

$$R2_{4\,jnr}^{Lout} = -\frac{EA_1}{4m_{4rr}^{Lout}}\left(\frac{j\pi}{L_4}\right)^2 \int_0^{L_4} \alpha_{4n}''(x_4)\alpha_{4r}(x_4)dx_4 \tag{F.49}$$

$$F_{4r}^{Lout}=\left[m_1\left(-S_5^w+gf_4^w\right)\int_0^{L_4}\alpha_{4r}(x_4)dx_4-m_1S_6^w\int_0^{L_4}x_4\alpha_{4r}(x_4)dx_4\right]/m_{4rr}^{Lout} \tag{F.50}$$

The coefficients of the elevator car in the longitudinal direction are the following

$$k1^{u1}=\frac{EA_1}{L_1}+\frac{EA_2}{L_2} \tag{F.51}$$

$$k2^{u1}=-\frac{EA_2}{L_2} \tag{F.52}$$

$$k3_n^{u1}=\frac{EA_1f_1^v}{L_1}\phi_{1n}\left(L_1\right)-\frac{EA_2f_2^v}{L_2}\phi_{1n}\left(L_1\right) \tag{F.53}$$

$$k4_n^{u1}=\frac{EA_1f_1^w}{L_1}\alpha_{1n}\left(L_1\right)-\frac{EA_2f_2^w}{L_2}\alpha_{1n}\left(L_1\right) \tag{F.54}$$

$$R1_{jp}^{u1}=\frac{EA_1}{2L_1}G_{jp}^{1Lin}-\frac{EA_2}{2L_2}G_{jp}^{2Lin} \tag{F.55}$$

$$R2_{jp}^{u1}=\frac{EA_1}{2L_1}G_{jp}^{1Lout}-\frac{EA_2}{2L_2}G_{jp}^{2Lout} \tag{F.56}$$

$$f_{CR}=\frac{EA_1}{2}\left(\left(f_1^v\right)^2+\left(f_1^w\right)^2\right)-\frac{EA_2}{2}\left(\left(f_2^v\right)^2+\left(f_2^w\right)^2\right) \tag{F.57}$$

The coefficients of the compensating sheave in the longitudinal direction are the following

$$k1^{u2}=-\frac{EA_2}{L_2} \tag{F.58}$$

$$k2^{u2}=EA_2\left(\frac{1}{L_2}+\frac{1}{L_3}\right) \tag{F.59}$$

$$k3^{u2}=-\frac{EA_2}{L_3} \tag{F.60}$$

$$k4_n^{u2}=-\frac{EA_2f_2^v}{L_2}\phi_{2n}\left(L_2\right) \tag{F.61}$$

$$k5_n^{u2}=-\frac{EA_2f_2^w}{L_2}\alpha_{2n}\left(L_2\right) \tag{F.62}$$

$$R1_{jp}^{u2} = -\frac{EA_2}{2L_2} G_{jp}^{2Lin} \tag{F.63}$$

$$R2_{jp}^{u2} = -\frac{EA_2}{2L_2} G_{jp}^{2Lout} \tag{F.64}$$

$$R3_{n}^{u2} = \frac{EA_2}{4}\left(\frac{n\pi}{L_3}\right)^2 \tag{F.65}$$

$$R4_{n}^{u2} = \frac{EA_2}{4}\left(\frac{n\pi}{L_3}\right)^2 \tag{F.66}$$

$$f_{CS} = \frac{EA_2}{2}\left(\left(f_2^v\right)^2 + \left(f_2^w\right)^2 + \left(f_3^v\right)^2 + \left(f_3^w\right)^2\right) \tag{F.67}$$

The coefficients of the counterweight in the longitudinal direction are the following

$$k1^{u3} = -\frac{EA_2}{L_3} \tag{F.68}$$

$$k2^{u3} = \frac{EA_2}{L_3} + \frac{EA_1}{L_4} \tag{F.69}$$

$$R1_{n}^{u3} = -\frac{EA_2}{4}\left(\frac{n\pi}{L_3}\right)^2 \tag{F.70}$$

$$R2_{n}^{u3} = -\frac{EA_2}{4}\left(\frac{n\pi}{L_3}\right)^2 \tag{F.71}$$

$$R3_{n}^{u3} = \frac{EA_1}{4}\left(\frac{n\pi}{L_4}\right)^2 \tag{F.72}$$

$$R4_{n}^{u3} = \frac{EA_1}{4}\left(\frac{n\pi}{L_4}\right)^2 \tag{F.73}$$

$$f_{CW} = \frac{EA_1}{2}\left(\left(f_4^v\right)^2 + \left(f_4^w\right)^2\right) - \frac{EA_2}{2}\left(\left(f_3^v\right)^2 + \left(f_3^w\right)^2\right) \tag{F.74}$$

Appendix G

Coefficients for the Nonstationary Model of a High Rise Elevator System

The modified coefficients for the nonstationary model of a high rise elevator system are shown from equations (G.1) to (G.35).

For rope *i=1* in the lateral in plane direction

$$B_{1rn}(t;\tau)=\begin{bmatrix} 2\zeta_r\hat{\omega}_{1r}(\tau) \\ \dfrac{4v(t)nr\left((-1)^{n+r}-1\right)}{L_1(\tau)\left(n^2-r^2\right)} \end{bmatrix} \tag{G.1}$$

$$\hat{k}_{1rn}(t;\tau)=\begin{bmatrix} \dfrac{r^2\pi^2}{L_1^{\,2}(\tau)}\left[-v^2(t)-\dfrac{gL_1(\tau)}{2}+\dfrac{EA_1}{m_1}\left(\dfrac{\left(U_{CR}(t)\right)}{L_1(\tau)}+\dfrac{\left(\psi_1(\tau)-1\right)^2}{2L_1^{\,2}(\tau)}\left(S_v^2(t)+S_w^2(t)\right)\right)\right] \\ \dfrac{2nr\left((-1)^{n+r}-1\right)}{\left(n^2-r^2\right)^2L_1(\tau)}\left(-g\left(n^2+r^2\right)+a_{CR}(t)\left(3n^2-r^2\right)\right) \end{bmatrix} \tag{G.2}$$

$$\tilde{R}_{1rn}(\tau)=-\frac{EA_1r^2\pi^2}{4m_1L_1^{\,2}(\tau)}\left(\frac{n\pi}{L_1(\tau)}\right)^2 \tag{G.3}$$

$$\hat{F}_{1r}^{Lin}(t;\tau)=\frac{2S_v(t)}{L_1(\tau)r\pi}\begin{bmatrix} \left(\lambda_V{}^2L_1(\tau)-(g+a_{CR})\left(\psi_1(\tau)-1\right)\right) \\ +(-1)^r\left(-\lambda_V{}^2L_1(\tau)+\left(\psi_1(\tau)-1\right)\left(-\lambda_V{}^2L_1(\tau)+g+a_{CR}(t)\right)\right) \end{bmatrix} \tag{G.3}$$

$$+\frac{4v(t)}{L_1(\tau)r\pi}\left(\psi_1(\tau)-1\right)\lambda_V\,\mathrm{A}_v\cos\left(\lambda_V t\right)\left((-1)^r-1\right)$$

For rope *i=2* in the lateral in plane direction

$$B_{2rn}(t;\tau)=\begin{bmatrix} 2\zeta_r\hat{\omega}_{2r}(\tau) \\ \dfrac{4v(t)nr\left((-1)^{n+r}-1\right)}{L_2(\tau)\left(n^2-r^2\right)} \end{bmatrix} \tag{G.4}$$

$$\hat{k}_{2rn}(t;\tau)=\begin{bmatrix}\dfrac{r^2\pi^2}{L_2{}^2(\tau)}\left[\begin{array}{l}-v_{CR}^2(t)-\dfrac{gL_2(\tau)}{2}\\ +\dfrac{EA_2}{m_2}\left(\dfrac{\left(U_{CS}(t)-U_{CR}(t)\right)}{L_2(\tau)}+\dfrac{\left(\psi_2(\tau)\right)^2}{2L_2{}^2(\tau)}\left(S_v^2(t)+S_w^2(t)\right)\right)\end{array}\right]\\ \dfrac{2nr\left((-1)^{n+r}-1\right)}{\left(n^2-r^2\right)^2L_2(\tau)}\left(-g\left(n^2+r^2\right)+a_{CR}(t)\left(3n^2-r^2\right)\right)\end{bmatrix} \tag{G.5}$$

$$\tilde{R}_{2rn}(\tau)=-\frac{EA_2r^2\pi^2}{4m_2L_2{}^2(\tau)}\left(\frac{n\pi}{L_2(\tau)}\right)^2 \tag{G.6}$$

$$\begin{aligned}\hat{F}_{2r}^{Lin}(t;\tau)&=\frac{2\psi_2(\tau)S_v(t)}{L_2(\tau)r\pi}\left[\left(\lambda_V{}^2L_2(\tau)+g+a_{CR}(t)\right)+(-1)^r\left(-g-a_{CR}(t)\right)\right]\\ &-\frac{4v_{CR}(t)\psi_2(\tau)}{L_2(\tau)r\pi}\lambda_V\,\mathrm{A}_v\cos(\lambda_Vt)\left((-1)^r-1\right)\end{aligned} \tag{G.7}$$

For rope *i=3* in the lateral in plane direction

$$B_{3rn}(t;\tau)=\begin{bmatrix}2\zeta_r\hat{\omega}_{3r}(\tau)\\ \dfrac{4v(t)nr\left((-1)^{n+r}-1\right)}{L_3(\tau)\left(n^2-r^2\right)}\end{bmatrix} \tag{G.8}$$

$$\hat{k}_{3rn}(t;\tau)=\begin{bmatrix}\dfrac{r^2\pi^2}{L_3{}^2(\tau)}\left[\begin{array}{l}-v_{CW}^2(t)-\dfrac{gL_3(\tau)}{2}\\ +\dfrac{EA_2}{m_2}\left(\dfrac{\left(U_{CS}(t)-U_{CW}(t)\right)}{L_3(\tau)}+\dfrac{\left(\psi_3(\tau)\right)^2}{2L_3{}^2(\tau)}\left(S_v^2(t)+S_w^2(t)\right)\right)\end{array}\right]\\ \dfrac{2nr\left((-1)^{n+r}-1\right)}{\left(n^2-r^2\right)^2L_3(\tau)}\left(-g\left(n^2+r^2\right)+a_{CW}(t)\left(3n^2-r^2\right)\right)\end{bmatrix} \tag{G.9}$$

$$\tilde{R}_{3rn}(\tau)=-\frac{EA_2r^2\pi^2}{4m_2L_3{}^2(\tau)}\left(\frac{n\pi}{L_3(\tau)}\right)^2 \tag{G.10}$$

$$\begin{aligned}\hat{F}_{3r}^{Lin}(t;\tau)&=\frac{2\psi_3(\tau)S_v(t)}{L_3(\tau)r\pi}\left[\left(\lambda_V{}^2L_3(\tau)+g+a_{CW}(t)\right)+(-1)^r\left(-g-a_{CW}(t)\right)\right]\\ &-\frac{4v_{CW}(t)\psi_3(\tau)}{L_3(\tau)r\pi}\lambda_V\,\mathrm{A}_v\cos(\lambda_Vt)\left((-1)^r-1\right)\end{aligned} \tag{G.11}$$

For rope *i=4* in the lateral in plane direction

$$B_{4rn}(t;\tau)=\begin{bmatrix} 2\zeta_r\hat{\omega}_{4r}(\tau) \\ \dfrac{4v(t)nr\left((-1)^{n+r}-1\right)}{L_4(\tau)\left(n^2-r^2\right)} \end{bmatrix} \tag{G.12}$$

$$\hat{k}_{4rn}(t;\tau)=\begin{bmatrix} \dfrac{r^2\pi^2}{L_4{}^2(\tau)}\left[\begin{matrix} -v_{CW}^2(t)-\dfrac{gL_4(\tau)}{2} \\ +\dfrac{EA_1}{m_1}\left(\dfrac{U_{CW}(t)}{L_4(\tau)}+\dfrac{\left(\psi_4(\tau)-\psi_5(\tau)\right)^2}{2L_4{}^2(\tau)}\left(S_v^2(t)+S_w^2(t)\right)\right)\end{matrix}\right] \\ \dfrac{2nr\left((-1)^{n+r}-1\right)}{\left(n^2-r^2\right)^2L_4(\tau)}\left(-g\left(n^2+r^2\right)+a_{CW}(t)\left(3n^2-r^2\right)\right) \end{bmatrix} \tag{G.13}$$

$$\tilde{R}_{4rn}(\tau)=-\frac{EA_1r^2\pi^2}{4m_1L_4{}^2(\tau)}\left(\frac{n\pi}{L_4(\tau)}\right)^2 \tag{G.14}$$

$$\begin{aligned}\hat{F}_{4r}^{Lin}(t;\tau)=&\frac{2S_v(t)}{L_4(\tau)r\pi}\left[\begin{matrix}\left(\lambda_V{}^2L_4(\tau)\psi_5(\tau)-\left(g+a_{CW}(t)\right)\left(\psi_4(\tau)-\psi_5(\tau)\right)\right) \\ +(-1)^r\left(\begin{matrix}-\lambda_V{}^2L_4(\tau)\psi_5(\tau)+ \\ \left(\psi_4(\tau)-\psi_5(\tau)\right)\left(-\lambda_V{}^2L_4(\tau)+g+a_{CW}(t)\right)\end{matrix}\right)\end{matrix}\right] \\ &+\frac{4v_{CW}}{L_4(\tau)r\pi}\left(\psi_4(\tau)-\psi_5(\tau)\right)\lambda_V\,\mathrm{A}_v\cos(\lambda_V t)\left((-1)^r-1\right)\end{aligned} \tag{G.15}$$

For rope *i=1* in the lateral out of plane direction

$$\begin{aligned}\hat{F}_{1r}^{Lout}(t;\tau)=&\frac{2S_w(t)}{L_1(\tau)r\pi}\left[\begin{matrix}\left(\lambda_w{}^2L_1(\tau)-\left(g+a_{CR}\right)\left(\psi_1(\tau)-1\right)\right) \\ +(-1)^r\left(-\lambda_w{}^2L_1(\tau)+\left(\psi_1(\tau)-1\right)\left(-\lambda_w{}^2L_1(\tau)+g+a_{CR}(t)\right)\right)\end{matrix}\right] \\ &+\frac{4v(t)}{L_1(\tau)r\pi}\left(\psi_1(\tau)-1\right)\lambda_w\,\mathrm{A}_w\cos(\lambda_w t)\left((-1)^r-1\right)\end{aligned} \tag{G.16}$$

For rope *i=2* in the lateral out of plane direction

$$\begin{aligned}\hat{F}_{2r}^{Lout}(t;\tau)=&\frac{2\psi_2(\tau)S_w(t)}{L_2(\tau)r\pi}\left[\left(\lambda_w{}^2L_2(\tau)+g+a_{CR}(t)\right)+(-1)^r\left(-g-a_{CR}(t)\right)\right] \\ &-\frac{4v_{CR}(t)\psi_2(\tau)}{L_2(\tau)r\pi}\lambda_w\,\mathrm{A}_w\cos(\lambda_w t)\left((-1)^r-1\right)\end{aligned} \tag{G.17}$$

For rope *i=3* in the lateral out of plane direction

$$\hat{F}_{3r}^{Lout}(t;\tau)=\frac{2\psi_3(\tau)S_w(t)}{L_3(\tau)r\pi}\left[\left(\lambda_w{}^2L_3(\tau)+g+a_{CW}(t)\right)+(-1)^r\left(-g-a_{CW}(t)\right)\right]$$
$$-\frac{4v_{CW}(t)\psi_3(\tau)}{L_3(\tau)r\pi}\lambda_w\,\mathrm{A}_w\cos(\lambda_w t)\left((-1)^r-1\right) \qquad \text{(G.18)}$$

For rope *i=4* in the lateral out of plane direction

$$\hat{F}_{4r}^{Lout}(t;\tau)=\frac{2S_w(t)}{L_4(\tau)r\pi}\left[\begin{array}{l}\left(\lambda_w{}^2L_4(\tau)\psi_5(\tau)-\left(g+a_{CW}(t)\right)\left(\psi_4(\tau)-\psi_5(\tau)\right)\right)\\+(-1)^r\left(\begin{array}{l}-\lambda_w{}^2L_4(\tau)\psi_5(\tau)+\\\left(\psi_4(\tau)-\psi_5(\tau)\right)\left(-\lambda_w{}^2L_4(\tau)+g+a_{CW}(t)\right)\end{array}\right)\end{array}\right] \qquad \text{(G.19)}$$
$$+\frac{4v_{CW}}{L_4(\tau)r\pi}\left(\psi_4(\tau)-\psi_5(\tau)\right)\lambda_w\,\mathrm{A}_w\cos(\lambda_w t)\left((-1)^r-1\right)$$

For the elevator car

$$\hat{k}^{1u1}(\tau)=\frac{EA_1}{L_1(\tau)}+\frac{EA_2}{L_2(\tau)} \qquad \text{(G.20)}$$

$$\hat{k}^{2u1}(\tau)=-\frac{EA_2}{L_2(\tau)} \qquad \text{(G.21)}$$

$$f_{CR}(t;\tau)=-\frac{EA_1}{2}\left[\left(\frac{\psi_1(\tau)-1}{L_1(\tau)}\right)^2\left(S_v^2(t)+S_w^2(t)\right)\right]+\frac{EA_2}{2}\left[\left(\frac{\psi_2(\tau)}{L_2(\tau)}\right)^2\left(S_v^2(t)+S_w^2(t)\right)\right] \qquad \text{(G.22)}$$
$$+\left(M_1+\frac{m_1L_1(\tau)}{2}-\frac{m_2L_2(\tau)}{2}\right)a_{CR}(t)$$

$$\tilde{R}_n^{1u1}=-\frac{EA_1}{4}\left(\frac{n\pi}{L_1(\tau)}\right)^2 \qquad \text{(G.23)}$$

$$\tilde{R}_n^{2u1}=\frac{EA_2}{4}\left(\frac{n\pi}{L_2(\tau)}\right)^2 \qquad \text{(G.24)}$$

For the compensating sheave

$$\hat{k}^{1u2}(\tau) = -\frac{EA_2}{L_2(\tau)} \tag{G.25}$$

$$\hat{k}^{2u2}(\tau) = EA_2\left(\frac{1}{L_2(\tau)} + \frac{1}{L_3(\tau)}\right) \tag{G.26}$$

$$\hat{k}^{3u2}(\tau) = -\frac{EA_2}{L_3(\tau)} \tag{G.27}$$

$$f_{CS}(t;\tau) = -\frac{EA_2}{2}\left(\left(\frac{\psi_2(\tau)}{L_2(\tau)}\right)^2 + \left(\frac{\psi_3(\tau)}{L_3(\tau)}\right)^2\right)\left(S_v^2(t) + S_w^2(t)\right) + \frac{m_2 a_{CR} L_2(\tau)}{2} - \frac{m_2 a_{CR} L_3(\tau)}{2} \tag{G.28}$$

$$\tilde{R}_n^{1u2} = -\frac{EA_2}{4}\left(\frac{n\pi}{L_2(\tau)}\right)^2 \tag{G.29}$$

$$\tilde{R}_n^{2u2} = -\frac{EA_2}{4}\left(\frac{n\pi}{L_3(\tau)}\right)^2 \tag{G.30}$$

For the counterweight

$$\hat{k}^{1u3}(\tau) = -\frac{EA_2}{L_3(\tau)} \tag{G.31}$$

$$\hat{k}^{2u3}(\tau) = \frac{EA_2}{L_3(\tau)} + \frac{EA_1}{L_4(\tau)} \tag{G.32}$$

$$f_{CW}(t;\tau) = \left(S_v^2(t) + S_w^2(t)\right)\left(-\frac{EA_1\left(\psi_4(\tau) - \psi_5(\tau)\right)^2}{2L_4(\tau)} + \frac{E_2A_2\left(\psi_3(\tau)\right)^2}{2L_3(\tau)}\right) + \left(M_3 + \frac{m_1 L_4(\tau)}{2} - \frac{m_2 L_3(\tau)}{2}\right)a_{cw}(t) \tag{G.33}$$

$$\tilde{R}_n^{1u3} = \frac{EA_2}{4}\left(\frac{n\pi}{L_3(\tau)}\right)^2 \tag{G.34}$$

$$\tilde{R}_n^{2u3} = -\frac{EA_1}{4}\left(\frac{n\pi}{L_4(\tau)}\right)^2 \tag{G.35}$$

References

Ahn, J. (2007) A vibrating string with dynamic frictionless impact. *Journal Applied Numerical Mathematics.* **57**(8), 861–884.

Alsahlani, A. and Mukherjee, R. (2010). Vibration of a string wrapping and unwrapping around an obstacle. *Journal of Sound and Vibration*. **329**(14), 2707–2715.

Amerio, L. (1978) Continous solutions of the problem of a string vibraing against an obtacle. *In: Seminario Matematico della Universita di Padova, Padova*. 67 – 96.

Anderson, K. (2015) *Compenstation Rope Test Unit Operations Guide*. Memphis, USA: ThyssenKrupp Elevator AG.

Andrew, J. P. and Kaczmarczyk, S. (2011) *Systems Engineering of Elevators.* Mobile, Alabama, USA: Elevator World, Inc.

Arrasate, X., Kaczmarczyk, S., Almandoz, G., Abete, J.M., and Isasa, I. (2013) Measurement and Simulation of Machine-Borne Vertical Vibration in Elevator Systems. *In: 11th International Conference on Vibration Problems.* Lisbon.

Arrasate, X., Kaczmarczyk, S., Almandoz, G., Abete, J.M., and Isasa, I. (2012) The modelling, simulation and experimental testing of vertical vibrations in an elevator system with 1:1 roping configuration. *In: 2nd Symposium on Lift and Escalator Technologies.* Northampton.

Auciello, N.M. (1996) Tapered Cantilever Beam with Tip Mass of Rotatory Inertia and Eccentricity. *Journal of Sound and Vibration*, **194**(1), 25–34.

Avitabile, P. (2002) Experimental Modal Analysis. *Journal of Sound and Vibration.* (January, 2002). pp.1–11.

Bamberger, A. and Schatzman, M. (1983) New results on the vibrating string with continous obstacle. *Society for Industrial and Applied Mathematics*. **14**(3), 560 – 595.

Barker, F.H. and Erlandsen, P.O. (1999) *System and Method for Minimizing Horizontal Vibration of Elevator Compensating Ropes.* Patent Applicant: Otis Elevator Company. USA patent application 5861084, 19 January 1999.

Bashor, R., Bobby, S., Kijewski-Correa, T., and Kareem, A. (2012) Full-scale performance evaluation of tall buildings under wind. *Journal of Wind Engineering and Industrial Aerodynamics*. **104-106**, 88–97.

Bendiksen, O.O. (2000) Localization phenomena in structural dynamics. *Journal of Chaos, solitons and fractals,* **11**, 1621–1660.

du Bois, J.L., Adhikari, S. and Lieven, N. a. J. (2011) On the Quantification of Eigenvalue Curve Veering: A Veering Index. *Journal of Applied Mechanics*. **78**(4).

Brüel & Kjær (2013) *LAN-XI Data Acquisition Hardware*. Denmark: Brüel & Kjær.

Brüel & Kjær (2015) *Transducers and Conditioning.* Denmark: Brüel & Kjær.

Burton, M.D., Kwok, K.C.S. and Abdelrazaq, A. (2015) Wind-Induced Motion of Tall Buildings: Designing for Occupant Comfort. *International Journal of High-Rise Buildings*. **4**(1), pp.1–8.

Cunha, A. and Caetano, E. (1999) Dynamic Measurements on Stay Cables of Cable-Stayed Bridges Using an Interferometry Laser System. *Journal of Experimental Techniques*. **23**(3) pp. 38–43.

Dauhoo, M.Z. and Soobhug, M. (2003) An Adaptive Weighted Bisection Method For Finding Roots Of Non-Linear Equations. *International Journal of Computer Mathematics.* **80**(7) pp.897–906.

Drako, P. (2011) *Elevator Ropes*. Germany: Pfeifer Drako.

Emory, B.H., Zhu, W.D., Kaczmarczyk, S. (2009) Modal Testing and Modeling of a Simplified Elevator System. *In: Society for Experimental Mechanics Inc.*

Ewins, D.J. (1994) *Modal Testing: Theory, Practice, and Application.* 2nd ed. Jon Wiley and Sons, UK.

Foss, G.C. (2006) Modal Damping Estimates from Static Load-Deflection Curves. *In: Society for Experimental Mechanics.*

Frontini, M. and Gotusso, L. (1990). Numerical study of the motion of a string vibrating against an obstacle by physical discretization. *Journal of Applied Mathematical Modelling*. **14**(9) 489–494.

Gade, S., Herlufsen, H. and Konstantin-hansen, H. (2005) *How to Determine the Modal Parameters of Simple Structures*. Denmark: Brüel & Kjær.

Galindez-Jamioy, C. a. and López-Higuera, J.M. (2012) Brillouin Distributed Fiber Sensors: An Overview and Applications. *Journal of Sensors.* **2012**, 1–17.

Giannini, O. and Sestieri, A. (2015) Experimental characterization of veering crossing and lock-in in simple mechanical systems. *Journal of Mechanical Systems and Signal Processing.* 1–19.

Han, S.M. and Grosenbaugh, M. a. (2004) Non-linear free vibration of a cable against a straight obstacle. *Journal of Sound and Vibration*. **273**(1-25), 337–361.

Herlufsen, H. (2012) *Modal Analysis using Multi-reference and Multiple-Input Multiple-Output Techniques.* Denmark: Brüel & Kjær.

Inman, D.J. (2001) *Engineering Vibrations.* 2nd ed. Pearson PLC, UK.

Kaczmarczyk, S. (2010) *Active Control System to Minimize Compensating Rope Sway in a High-Rise Elevator Installation.* Northampton, UK: University of Northampton.

Kaczmarczyk, S., Mirhadizadeh, S., Picton, P., Salamaliki-Simpson, R., and Turner, S. (2013) Modelling, simulation and experimental validation of nonlinear dynamic interactions in an aramid rope system. *In: 11th International Conference on Vibration Problems*. Lisbon.

Kaczmarczyk, S. (2011) Nonlinear Sway and Active Stiffness Control of Long Moving Ropes in High-Rise Vertical Transportation Systems. *In: International Conference on Vibration Problems.* Prague.

Kaczmarczyk, S. (2005) Prediction of the Influence of Vibration on Structural Integrity of Elevator Suspension Ropes. *Journal of Key Engineering Materials.* **293-294**, 761–768.

Kaczmarczyk, S. (2012) The nonstationary, nonlinear dynamic interactions in slender continua deployed in high-rise vertical transportation systems in the modern built environment. *Journal of Physics: Conference Series*, **382**.

Kaczmarczyk, S. (1997) The passage through resonance in a catenary-vertical cable hoisting system with slowly varying length. *Journal of Sound and Vibration*. **208**(2), 243–269.

Kaczmarczyk, S. and Iwankiewicz, R. (2006) Dynamic response of an elevator car due to stochastic rail excitation. *Proceeding Estonian Academy of Sciences, Physics, and Mathematics.* **55**(1), 58.

Kaczmarczyk, S., Iwankiewicz, R. and Terumichi, Y. (2009) The dynamic behaviour of a non-stationary elevator compensating rope system under harmonic and stochastic excitations. *Journal of Physics: Conference Series*. **181**.

Kaczmarczyk, S., Iwankiewicz, R. and Terumichi, Y. (2010) The responses of long moving vertical ropes and cables subjected to dynamic loading due to the host structure sway. *Symposium on the Mechanics of Slender Structures* (MoSS 2010), University of Mondragon, San Sebastian, Spain, 21-23 July 2010, 21–23.

Kaczmarczyk, S. and Ostachowicz, W. (2003) Transient vibration phenomena in deep mine hoisting cables. Part 1: Mathematical model. *Journal of Sound and Vibration*. **262**(2), 219–244.

Kaczmarczyk, S. and Picton, P. (2012) The Prediction of Nonlinear Responses and Active Stiffness Control of Moving Slender Continua Subjected to Dynamic Loadings in a Vertical Host Structure. *International Journal of Accoustics and Vibration*. **18**(1), 39–44.

Kawaguti, K. Terumichi, Y., Takehara, S., Kaczmarczyk, S., and Sogabe, K. (2007) The Study of the Tether Motion with Time-Varying Length Using the Absolute Nodal Coordinate Formulation with Multiple Nonlinear Time Scales. *Journal of System Design and Dynamics*. **1**(3), 491–500.

Kijewski-Correa, T. and Kochly, M. (2007) Monitoring the wind-induced response of tall buildings: GPS performance and the issue of multipath effects. *Journal of Wind Engineering and Industrial Aerodynamics*. **95**(9-11), 1176–1198.

Kijewski-correa, T.L. (2003a) *Full-Scale Measurements and System Identificatiion: A Time-Frequency Perspective (Volume I).* Ph. D. Thesis, University of Notre Dame.

Kijewski-correa, T.L. (2003b) *Full-Scale Measurements and System Identification: A Time-Frequency Perspective (Volume II).* Ph. D. Thesis, University of Notre Dame.

Kohut, P., Holak, K., Uhl, T., Ortyl, L., Owerko, T., Kuras, P., and Kocierz, R. (2013) Monitoring of a civil structure's state based on noncontact measurements. *Journal of Structural Health Monitoring*. **12**(5-6), 411–429.

Kollmorgen. (2014) *Kollmorgen Electric Cylinder Catalog.* USA: Kollmorgen.

KONE. (2013) *The Next Leap KONE high-rise solutions.* Finland: KONE.

Kwon, D., Kijewski-correa, T. and Kareem, A. (2008) E-Analysis of High-Rise Buildings Subjected to Wind Loads. *Journal of Structural Engineering (ASCE)*. 1139 – 1153.

Lee, H. and Rhee, H. (2013) 3-D measurement of structural vibration using digital close-range photogrammetry. *Journal of Sensors and Actuators A: Physical*. **196**, 63–69.

Lopez, S., Perondi, E., and Sobrinho, M. (2010) Adaptive Control for an Active Suspension of an Elevator. *In: Symposium Series in Mechatronics*. **4**, 62–71.

Maiz, S., Bambill, D., Rossit, C., and Laura, P. Lauraa. (2007) Transverse vibration of Bernoulli–Euler beams carrying point masses and taking into account their rotatory inertia: Exact solution. *Journal of Sound and Vibration*, **303**(3-5), 895–908.

Martín-Pérez, B., Delf, A., Cousin, B., Zhang, C., Bao, X., and Li, W. (2010) Strain monitoring in a reinforced concrete slab sustaining service loads by distributed Brillouin fibre optic sensors. *Canadian Journal of Civil Engineering*. **37**(10), 1341–1349.

Mas, D., Espinosa, J., Perez, J., Ilueca, C., Ferrer, B., and Roig, A. (2011) High speed imaging and algorithms for non-invasive vibrations measurement. *In: Experimental Vibration Analysis for Civil Engineering Structures.* 531 – 538.

Mcdonald, P.C. and Iosifescu, C. (1998) Use of a LVDT displacement transducer in measurements at low temperatures. *Journal of Measurement Science and Technology*. **9**, 563–569.

Meirovitch, L. (2001) *Fundamentals of Vibrations.* Singapore: McGraw-Hill Book Co.

Mendis, P., Ngo, T., Haritos, N., Hira, A., Samali, B., Cheung, J. (2007) Wind Loading on Tall Buildings. *Electronic Journal of Structural Engineering: Loading on Structures.*

Möhring, H.-C. and Bertram, O. (2012) Integrated autonomous monitoring of ball screw drives. *CIRP Annals - Manufacturing Technology*. **61**(1), 355–358.

Nakazawa, D. Watanabe, S., Fukui, D., Okawa, T. (2013) Lateral vibration analysis for elevator compensation rope. *In: 11th International Conference on Vibration Problems.* Lisbon.

Nassif, H.H., Gindy, M. and Davis, J. (2005) Comparison of laser Doppler vibrometer with contact sensors for monitoring bridge deflection and vibration. *Journal of Nondestructive Testing and Evaluation International*. **38**(3), 213–218.

National Instruments. (2009) *NI 9263, Operating instructions and specifications*. Austin, USA: National Instruments.

National Instruments. (2010) *CompactRIO NI cRIO-9024, Operating instructions and specifications.* Austin, USA: National Instruments.

National Instruments. (2009) *NI 9219, Operating instructions and specifications*. Austin, USA: National Instruments.

National Instruments. (2014) *Reconfigurable Chassis for NI CompactRIO NI cRIO-9111, operating instructions and specifications*. Austin, USA: National Instruments.

National Lift Tower. (2015) *The National Lift Tower* [online]. Northampton, The National Lift Tower. Available from: http://www.nationallifttower.co.uk/ [Accessed 11th August 2015].

Nayfeh, A. and Mook, D. (1979) *Nonlinear Oscillations*. USA: Jon Wiley and Sons.

Pierre, C. and Plaut, R.H. (1989) Curve veering and mode localization in a buckling problem. *Journal of Applied Mathematics and Physics*. **40**(5), 758–761.

Preumont, A. and Seto, K. (2008) *Active Control of Structures*. UK: Jon Wiley and Sons.

Qiu, Y.Z. and Maji, a. K. (2014) Experimental and Analytical Investigation of Carbon Fiber Cable Vibration Damping. *Journal of Experimental Mechanics*. **54**(6), 1087–1097.

Rao, S.S. (2005) *Mechanical Vibrations* 4th ed. Singapore: Prentice Hall.

RDP Electronics (2014). *Displacement DCTH Series DC to DC LVDT Displacement Transducer Captive Guided* [online]. Wolverhampton, RDP Electronics. Available from http://www.rdpe.com/uk/dcth.htm [Accessed 21th October 2014].

Ren, H. & Zhu, W.D. (2013) An Accurate Spatial Discretization and Substructure Method With Application to Moving Elevator Cable-Car Systems - Part II: Application. *Journal of Vibration and Acoustics*. **135**(5).

Robertson, L.E. (1992) *Sway Minimization System for Elevator Cables*. USA patent application 5103937, April 14, 1992

Rosa, M. A. de and Auciello, N. M. (1996) Free Vibrations of Tapered Beams with Flexible Ends. *Journal of Computers and Structures*, **60**(2), 197–202.

Salamaliki-Simpson, R. (2009). *The Modelling and Simulation of the Dynamic Behaviour of a Lift Car-Rope Suspension System.* Ph. D Thesis, The University of Northampton.

Salamaliki-Simpson, R. and Kaczmarczyk, S. (2006) Non-Linear Modal Interactions in a Suspension Rope System with Time-Varying Length. *Journal of Modern Practices in Stress and Vibration Analysis*, **5-6**, 217–224.

Sandilo, S.H., 2013. *On Aspects of Asymptotics for Axially Moving Continua.* Ph. D. Thesis, Technical University of Delft.

Silva, T.A.N. et al. (2015) A Hybrid Procedure to Identify the Optimal Stiffness Coefficients of Elastically Restrained Beams. *International Journal of Applied Mathematics and Computer Science*, 25(2), pp.245–257.

Silva, T., Maria, L., Maia, N., and Barbosa, J. (2011) Elastically Restrained Bernoulli-Euler Beams Applied to Rotary Machinery Modelling. *Acta Mechanica Sinica*, **27**(1), 56–62.

Smith, R., Kaczmarczyk, S. Nickerson, J., and Bass, P. (2012) *Elevator rope positioning apparatus.* Patent Applicant: ThyssenKrupp Elevator AG. USA Patent Application 8123002B2 February 28, 2012.

Smith, R. and Kaczmarczyk, S. (2012) *Actively damped tension member*. Patent Applicant: ThyssenKrupp Elevator Capital Corporation. USA Patent Application 8110050B2 February 07, 2012.

Söderlind, G., Jay, L. and Calvo, M. (2014) Stiffness 1952–2012: Sixty years in search of a definition. *Journal of BIT Numerical Mathematics*. **55**, 531–558.

Strakosch, G.R. (1998) *The Vertical Transportation Handbook*. 3rd ed. New York: Jon Wiley and Sons, Inc

Terumichi, Y., Kaczmarczyk, S., Yoshizawa, M., Turner, S., and Ostachowicz, W. (2003) Modelling , Simulation and Analysis Techniques in the Prediction of Non-stationary Vibration Response of Hoist Ropes in Lift Systems. *Journal of Modern Practices in Stress and Vibration Analysis*, **440-441**, 497–504.

Terumichi, Y., Ohtsuka, M., Yoshizawa, M., Fukawa, and Tsujioka, Y. (1997) Nonstationary vibrations of a string with time-varying length and a mass-spring system attached at the lower end. *Journal of Nonlinear Dynamics*, **12**.

Thyssenkrupp Elevator AG. (2014) *MULTI History*. [online]. Germany, ThyssenKrupp Elevator AG. Available from: http://www.thyssenkruppelevator.co.uk/multi/ [Accessed 05th October 2015].

Valkering, T.P. (1994) Non-trivial Dynamics in a Driven String with Impact Non-linearity. *Journal of Sound and Vibration*. **175**(3), 397–422.

Watanabe, S., Okawa, T., Nakazawa, D., and Fukui, D. (2013) Vertical vibration analysis for elevator compensating sheave. *Journal of Physics: Conference Series*. **448**.

Watanabe, S. and Higashinaka, T. (2012) Dynamic Simulation of Rope for High-speed Elevators. *Mitsubishi Electric Advance*. **137**, 17 – 19.

Wilcoxon_Research. (2009) Piezoelectric accelerometer design. USA: Meggit.

Yamaguchi, H. and Adhikari, R. (1995) Energy-Based Evaluation of Modal Damping in Structural Cables with and without Damping Treatment. *Journal of Sound and Vibration*. **181**, 71–83.

Zhang, P., Bao, J.H. and Zhu, C.M. (2013) Dynamic analysis of hoisting viscous damping string with time-varying length. *Journal of Physics: Conference Series*. **448**.

Zhou, Y., Kijewski, T. and Kareem, A. (2003) Aerodynamic Loads on Tall Buildings : Interactive Database. *Journal of Structural Engineering (ASCE)*. **129**(3), 394–404.

Zhu, W.D. and Ren, H. (2013) An Accurate Spatial Discretization and Substructure Method With Application to Moving Elevator Cable-Car Systems - Part I: Methodology. *Journal of Vibration and Acoustics*. **135**(5).

Zhu, Y., Zhu, Y., Hui, L., and Krishnaswamy, S. (2011). Damage detection in FRP structures using fiber Bragg grating dynamc strain sensing systems. *International Society for Optics and photonics.* **7982**.